PhD dissertation

Collaborative Beamforming Schemes for Wireless Sensor Networks with Energy Harvesting Capabilities

Author

Lazar Berbakov

PhD Advisors

Dr. Carles Antón-Haro
Dr. Javier Matamoros
Centre Tecnològic de Telecomunicacions de Catalunya

Universitat Politècnica de Catalunya

Para ella, que me dio la vida
y
para ella, el amor de mi vida.

Abstract

In recent years, wireless sensor networks have attracted considerable attention in the research community. Their development, induced by technological advances in microelectronics, wireless networking and battery fabrication, is mainly motivated by a large number of possible applications such as environmental monitoring, industrial process control, goods tracking, healthcare applications, to name a few.

Due to the unattended nature of wireless sensor networks, battery replacement can be either too costly or simply not feasible. In order to cope with this problem and prolong the network lifetime, energy efficient data transmission protocols have to be designed. Motivated by this ultimate goal, this PhD dissertation focuses on the design of collaborative beamforming schemes for wireless sensor networks with energy harvesting capabilities. On the one hand, by resorting to collaborative beamforming, sensors are able to convey a common message to a distant base station, in an energy efficient fashion. On the other, sensor nodes with energy harvesting capabilities promise virtually infinite network lifetime. Nevertheless, in order to realize collaborative beamforming, it is necessary that sensors align their transmitted signals so that they are coherently combined at the destination. Moreover, sensor nodes have to adapt their transmissions according to the amounts of harvested energy over time.

First, this dissertation addresses the scenario where two sensor nodes (one of them capable of harvesting ambient energy) collaboratively transmit a common message to a distant base station. In this setting, we show that the optimal power allocation policy at the *energy harvesting* sensor can be computed independently (i.e., without the knowledge of the optimal policy at the battery operated one). Furthermore, we propose an iterative algorithm that allows us to compute the optimal policy at the *battery operated* sensor, as well. The insights gained by the aforementioned scenario allow us to generalize the analysis to a system with *multiple* energy harvesting sensors. In particular, we develop an iterative algorithm which *sequentially* optimizes the policies for all the sensors until some convergence criterion is satisfied. For the previous scenarios, this PhD dissertation evaluates the impact of total energy harvested, number of sensors and limited energy storage capacity on the system performance.

Finally, we consider some practical schemes for carrier synchronization, required in order to implement collaborative beamforming in wireless sensor networks. To that end, we analyze two algorithms for decentralized *phase synchronization*: (i) the one bit of feedback algorithm previously proposed in the literature; and (ii) a decentralized phase synchronization algorithm that we propose. As for the former, we analyze the impact of additive noise on the beamforming gain and algorithm's convergence properties, and, subsequently, we propose a variation that performs sidelobe control. As for the latter, the sensors are allowed to choose their respective training timeslots randomly, relieving the base station of the burden associated with centralized coordination. In this context, this PhD dissertation addresses the impact of number of timeslots and additive noise on the achieved received signal strength and throughput.

Resumen

En los últimos años, las redes de sensores inalámbricas han atraído considerable atención en la comunidad investigadora. Su desarrollo, impulsado por recientes avances tecnológicos en microelectrónica y radio comunicaciones, está motivado principalmente por un gran abanico de aplicaciones, tales como: Monitorización ambiental, control de procesos industriales, seguimiento de mercancías, telemedicina, entre otras.

En las redes de sensores inalámbricas, es primordial el diseño de protocolos de transmisión energéticamente eficientes ya que no se contempla el reemplazo de baterías debido a su coste y/o complejidad. Motivados por esta problemática, esta tesis doctoral se centra en el diseño de esquemas de conformación de haz distribuidos para redes de sensores, en el que los nodos son capaces de almacenar energía del entorno, lo que en inglés se denomina energy harvesting.

En primer lugar, esta tesis doctoral aborda el escenario en el que dos sensores (uno de ellos capaz de almacenar energía del ambiente) transmiten conjuntamente un mensaje a una estación base. En este contexto, se demuestra que la política de asignación de potencia óptima en el sensor con energy harvesting puede ser calculada de forma independiente (es decir, sin el conocimiento de la política óptima del otro sensor). A continuación, se propone un algoritmo iterativo que permite calcular la política óptima en el sensor que funciona con baterías. Este esquema es posteriormente generalizado para el caso de múltiples sensores. En particular, se desarrolla un algoritmo iterativo que optimiza las políticas de todos los sensores secuencialmente. Para los escenarios anteriormente mencionados, esta tesis evalúa el impacto de la energía total cosechada, número de sensores y la capacidad de la batería.

Por último, se aborda el problema de sincronización de fase en los sensores con el fin de poder realizar la conformación de haz de forma distribuida. Para ello, se analizan dos algoritmos para la sincronización de fase descentralizados: (i) el algoritmo "one bit of feedback" previamente propuesto en la literatura, y (ii) un algoritmo de sincronización de fase descentralizado que se propone en esta tesis. En el primer caso, se analiza el impacto del ruido aditivo en la ganancia y la convergencia del algoritmo. Además, se propone una variación que realiza el control de lóbulos secundarios. En el segundo esquema, los sensores eligen intervalos de tiempo de forma aleatoria para transmitir y posteriormente reciben información de la estación base para ajustar sus osciladores. En este escenario, esta tesis doctoral aborda el impacto del número de

intervalos de tiempo y el ruido aditivo sobre la ganancia de conformación.

Resum

En els darrers anys, les xarxes de sensors sense fils han estat objecte d'atenció per la comunitat investigadora. El seu desenvolupament, impulsat pels recents avenços tecnològics en microelectrònica i ràdio comunicacions, està motivat principalment per un gran ventall d'aplicacions, com ara: Monitorització ambiental, control de processos industrials, seguiment de mercaderies i telemedicina, entre altres.

A les xarxes de sensors sense fils és primordial el disseny de protocols de transmissió energèticament eficients, ja que no es contempla la substitució de bateries a causa del seu cost i / o complexitat. Motivats per aquesta problemàtica, aquesta tesi doctoral es centra en el disseny d'esquemes de conformació de feix distribuïts per xarxes de sensors capaços d'obtenir i emmagatzemar energia de l'entorn, el que en anglès s'anomena energy harvesting.

En primer lloc, aquesta tesi doctoral aborda l'escenari en el qual dos sensors (un d'ells capaç d'emmagatzemar energia de l'ambient) conjuntament transmeten un mateix missatge a la estació base. En aquest context, es demostra que la òptima política d'assignació de potència en el sensor amb energy harvesting pot ser calculada de forma independent (és a dir, sense el coneixement de la política òptima de l'altre sensor). A continuació, es proposa un algoritme iteratiu que permet calcular la política òptima en el sensor que funciona amb únicament amb bateries. Aquest esquema és posteriorment generalitzat per al cas de múltiples sensors. En particular, es desenvolupa un algoritme iteratiu que optimitza les polítiques de tots els sensors seqüencialment. Pels escenaris anteriorment esmentats, aquesta tesi avalua l'impacte de l'energia total recollida, nombre de sensors i la capacitat de la bateria.

Finalment, es considera el problema de sincronització de fase entre els sensors necessari per tal de poder realitzar la conformació de feix de forma distribuïda. Per aquest escenari, s'analitzen dos algorismes de sincronització de fase descentralitzats: (i) l'algoritme "one bit of feedback" prèviament proposat en la literatura, i (ii) un algoritme de sincronització de fase descentralitzat que es proposa en aquesta tesi. En el primer cas, s'analitza l'impacte del soroll additiu en el guany i la convergència de l'algoritme. A més, es proposa una variació que realitza el control de lòbuls secundaris. En el segon esquema, els sensors trien intervals de temps de forma aleatòria per transmetre i posteriorment reben informació de l'estació base per ajustar els seus oscil·ladors. En aquest escenari, aquesta tesi doctoral aborda l'impacte del nombre d'intervals

de temps i el soroll additiu sobre el guany de conformació.

Acknowledgements

En primer lugar, querría dar mis gracias al CTTC, por ofrecerme la oportunidad de continuar mis estudios y realizar esta tesis doctoral en un entorno profesional y amigable. Aunque estuviera lejos de mi tierra, aquí me he sentido como en casa durante estos años.

Quisiera dar mis gracias a mis mentores Carles Antón y Javier Matamoros. Ambos han estado apoyándome durante estos años con mucha paciencia, proporcionándome la motivación tan necesaria en algunos momentos difíciles, cuando las cosas no salían como yo me lo esperaba.

Gracias a toda la gente del CTTC. Gracias, a mis compañeros doctorandos, especialmente a la comunidad serbia: Anica, Biljana y Tatjana, con las que he pasado muchas horas charlando y que me han apoyado durante mi camino hacía la tesis doctoral. También, quisiera dar mis agradecimientos a Angelos, quien ha tenido mucha paciencia con mi griego, que espero que haya mejorado durante estos años. Por último, pero con misma importancia, quisiera dar mis gracias a toda la gente de administración, especialmente a Carme por su comprensión y apoyo.

Желео бих да се захвалим свима онима који су ме подржавали на мом путу ка Докторату. Не би било у реду да не споменем чланове Радио Клуба “Нови Сад”: Милана, Бркића, Горана, Марка, Милослава, Донета, Мирка, Меги, Рацу, Кобца, Љубишу и остале. Захваљујем се такође и друговима са факултета: Лети, Млађи, Свети, Николи, Жиги, Лугоњи, Пајчину, Јањи, Ивани, Драгани, Николини... који су учинили да студије на ФТН буду нешто више од интеграла и радио таласа, и помогли да ових 5 година далеко од Новог Сада прођу много лакше.

Хвала мајка Дари, деда Лази, Чики, Тањи, Николи, Ивани, Снежи, Уји, Ујни, Секи, Данилу, Драгани, тетка Ради, Ујни Јагоди, Аци, Боби, и свима осталима који су веровали у мене.

И на крају, желим да се посебно захвалим мојој мама Нади и мојој Ивани. Обе сте ми пружиле безграничну љубав и разумевање кроз све изазове на које сам наилазио током ових година. Сви неизвесни и тешки дани су ми много лакше падали, знајући да постоји неко чија ће реч подршке помоћи да нови дан започнем са више снаге и вере у боље сутра.

Lazar Berbakov

Contents

List of acronyms

ADC	Analog-to-Digital Converter
ASLC	All Sensors, Last Cluster
AWGN	Additive White Gaussian Noise
BO	Battery Operated
BS	Base Station
CbC	Cluster-by-Cluster
cEH	Cumulative Energy Harvesting
cES	Cumulative Energy Storage
CSI	Channel State Information
DBF	Distributed beamforming
DBF-SC	Distributed beamforming with Sidelobe Control
EC	Energy Consumption
EH	Energy Harvesting
ES	Energy Storage
JO	Joint Optimization
KKT	Karush-Kuhn-Tucker
LoS	Line of Sight
MAC	Multiple-Access Channel
ML	Maximum Likelihood
pdf	Probability Density Function
SINR	Signal-to-Interference plus Noise Ratio
SNR	Signal-to-Noise Ratio
RSS	Received Signal Strength
SO	Separate Optimization
WSN	Wireless Sensor Network

Notation

$\mathbf{X}$	Matrix
$\mathsf{diag}\left[\mathbf{X}\right]$	Vector constructed with the elements in the diagonal of matrix $\mathbf{X}$
$\mathbf{X}^{-1}$	Inverse of matrix $\mathbf{X}$
$\mathbf{x}$	Column vector
^{T}	Transpose operator
^{H}	Hermitian transpose operator
*	Complex conjugate operator
$\lVert \cdot \rVert$	Euclidean norm
$\mathbf{I}_N$	Identity matrix of dimension $N \times N$
$\sim$	Distributed according to / scale as
$\triangleq$	Definition
$\lim$	Limit
$\log\left(\cdot\right)$	base-2 logarithm
$\arg$	Argument
$\max, \min$	Maximum, minimum operator
$\mathbb{E}\left[\cdot\right]$	Mathematical expectation
$\mathrm{I}\left(\cdot;\cdot\right)$	Mutual information
dom	Domain of a function
$\mathcal{R}(\cdot)$	Real part
$\mathcal{I}(\cdot)$	Imaginary part
$\mathcal{O}(\cdot)$	Order of

Chapter 1

Introduction

1.1 Motivation

Recent improvements in wireless networking, microfabrication and embedded microprocessors have enabled the production of low-cost sensor nodes. Wireless Sensor Networks (WSNs), which typically consist of a large number of sensor nodes, are used in many commercial and military applications, these including industrial process control, environmental monitoring (e.g., measuring temperature, humidity, air pressure, etc.), healthcare (patient's vital parameter monitoring), battlefield surveillance (enemy localization and tracking), and many others. In a near future, it is foreseen that in the "Internet of Things", the objects in our environment will be able to communicate among themselves without human intervention. This could potentially result in reduction of cost and losses, greatly improving the quality of life as we know it. All these promises and potentially huge future markets have driven research in decentralized signal processing, cooperative communications, energy harvesting technologies, and microelectronics.

In contrast to ordinary data networks, mainly used for human communications, wireless sensor networks pose new challenges to the research community. Constraints, such as size and production cost, result in wireless sensor nodes which have limited computational capabilities, this requiring new data processing and communication schemes to be developed. Moreover, replacing depleted sensor batteries might not be affordable or simply not feasible (e.g. when sensors are deployed in remote places). Harvesting ambient energy, however, makes it possible to overcome this drawback, resulting in a virtually infinite network lifetime. Still, the optimal allocation of such harvested energy can be quite challenging due to the random nature and variability of ambient energy sources. This, in turn, requires new approaches to problem solving, different from those used in battery-operated communication systems.

In some scenarios (e.g. remote area monitoring), sensor nodes need to communicate to a distant Base Station (BS). This turns out to be particularly challenging for low-power sensor nodes. In such situations, Distributed Beamforming (DBF), a technique by which sensors coordinate their transmissions to collaboratively send information, may become a viable solution. However, distributed beamforming requires precise carrier phase and frequency synchronization among all the sensor nodes, which turns out to be particularly difficult, due to the distributed nature of wireless sensor networks.

This PhD dissertation revolves around the design of collaborative beamforming schemes in wireless sensor networks with energy harvesting capabilities. In particular, it attempts to find the answer to the questions such as: How to allocate the available energy over time when energy harvesting and battery operated sensor collaborate? How the energy allocation changes when multiple energy harvesting sensors are used? What is the impact of energy storage constraints and/or battery aging? What is the influence of different amounts of energy at sensor nodes on the achieved throughput? As for distributed synchronization schemes, this dissertation addresses questions such as: What is the impact of the number of base stations and their location? How does interference impact on the the algorithm's convergence rate? And many others.

In the following section, we outline the contents of this PhD Dissertation. Next, we provide the list of journal and conference papers that have resulted of this work.

1.2 Outline

This PhD dissertation focuses on the design and analysis of distributed beamforming schemes for wireless sensor networks with energy harvesting capabilities. It is organized as follows:

Chapter 2 provides the reader with some background on the concepts to be used throughout this PhD dissertation. First, we provide a general overview of wireless sensor networks. Second, we revisit channel models for different wireless communication scenarios. Then, we briefly revisit the concept of antenna arrays and distributed beamforming. Next, we discuss a number of energy harvesting concepts, highlighting particularities related to wireless sensor networks. Finally, we outline some basic concepts in convex optimization.

In Chapter 3, we consider a scenario where one energy harvesting (EH) and one battery operated (BO) sensors cooperate to transmit (beamform) a common message to a distant base station. Our goal is to find the jointly optimal power allocation strategy which maximizes the total throughput for a given deadline. We initially assume that the energy harvesting sensor is equipped with a re-chargeable battery of infinite storage capacity. In this context, we identify the necessary conditions for the jointly optimal transmission policy. This leads to convex optimization problem. Furthermore, we prove that the optimal policy for the EH node can be computed independently from that of the BO one, and propose an algorithm to compute the latter from the former. Next, we generalize the analysis for a scenario in which the storage capacity of the EH sensor is finite. In addition, we analyze the computational complexity associated with the proposed optimization method. We also consider imperfections in the re-chargeable battery of the EH sensor. More specifically, we focus on the impact of long-term capacity degradation. The performance of the proposed algorithm is assessed in a scenario where solar energy is harvested from the environment.

Chapter 4 generalizes the scenario addressed in Chapter 3, by considering a setting where *multiple* energy harvesting sensors transmit a common message using collaborative beamforming. Again, the aim is to identify the jointly optimal transmission policy which maximizes the total throughput for a given deadline. In this setup, as opposed to Chapter 3, the policy at each EH sensor node cannot be computed independently. Therefore, we derive a semi-analytical solution which leverages on the coordinate descent method and an iterative algorithm, on which basis one can compute the optimal policy for one sensor whilst the policies for the remaining sensors are held fixed. We rigorously prove the optimality of the proposed method for a virtual array with an arbitrary number of EH sensor nodes, and, for the sake of completeness, we analyze its computational complexity. Besides, we extensively assess the performance of the proposed method in a realistic system scenario where vibrational energy is harvested from the environment.

Chapter 5 addresses the problem of distributed carrier synchronization. More specifically, we generalize the so-called one bit of feedback carrier synchronization algorithm to encompass sidelobe control mechanisms. The performance of the proposed algorithm is assessed in terms of Received Signal Strength (RSS) as well as the algorithm's convergence rate. Next, we consider a more realistic scenario with Additive White Gaussian Noise (AWGN). More specifically, we assess the impact of noise on the achievable beamforming gain and initial convergence rate. In order to maximize the received signal strength after algorithm's convergence, complementarily, we also investigate the optimal number of samples per iteration, as a function of the noise variance.

Furthermore, we propose a decentralized phase synchronization scheme where sensor randomly choose their respective training timeslots. In this context, we ask ourselves whether there exists an optimal number of training timeslots, and about the optimal split for the training and data transmission periods. To answer this question, we analytically derive upper bounds of the resulting beamforming gain in two scenarios of interest: ideal, and noisy phase shift estimation. Computer simulation results are mainly given in terms of (normalized) beamforming gain and achievable throughput.

Chapter 6 concludes this PhD dissertation with a summary and discussion of the main results of this work. A number of topics for future work in this research area are outlined, as well.

1.3 Contribution

Chapter 3

Contributions of Chapter 3 have resulted in 1 journal paper and 1 conference paper.

- L. Berbakov, C. Anton-Haro, and J. Matamoros, Optimal Transmission Policy for Cooperative Transmisssion with Energy Harvesting and Battery Operated Sensor Nodes. To appear in Elsevier Signal Processing Journal, pp. 1-30, submission date: Jun. 15th 2012, (accepted for publication).
- L. Berbakov, J. Matamoros, and C. Anton-Haro, Optimal Transmission Policy for Distributed Beamforming with Energy Harvesting and Battery Operated Sensor Nodes, in Proceedings of International Symposium on Wireless Communication Systems (ISWCS 2012), Aug. 2012, Paris (France).

Chapter 4

Contributions of Chapter 4 have resulted in 1 journal paper and 2 conference papers.

- L. Berbakov, C. Anton-Haro, and J. Matamoros, Joint optimization of transmission policies for collaborative beamforming with energy harvesting sensors. Submitted to IEEE Transactions on Wireless Communications, pp. 1-13, submission date: Nov. 11th 2012 (second review round).
- L. Berbakov, J. Matamoros, and C. Anton-Haro, Greedy transmission strategies for collaborative beamforming with energy harvesting sensors, in Proceedings of 7th International ITG Workshop on Smart Antennas (WSA 2013), March 2013, Stuttgart (Germany).
- L. Berbakov, C. Anton-Haro and J. Matamoros, Optimal Transmission Policy for Collaborative Beamforming with Finite Energy Storage Capacity, submitted to IEEE International Symposium on Personal, Indoor and Mobile Radio Communications (PIMRC 2013), Sep. 2013, London (UK).

Chapter 5

Contributions of Chapter 5 have resulted in 4 conference papers.

- L. Berbakov, C. Anton-Haro, and J. Matamoros, Distributed beamforming with sidelobe control using one bit of feedback, in Proceedings of 73rd Vehicular Technology Conference (VTC Spring 2011), May 2011, Budapest (Hungary).
- L. Berbakov, J. Matamoros, and C. Anton-Haro, Decentralized phase synchronization scheme for collaborative beamforming in wireless sensor networks, in Proceedings of 19th European Signal Processing Conference (EUSIPCO 2011), Sep. 2011, Barcelona (Spain).
- L. Berbakov, C. Anton-Haro, and J. Matamoros, Distributed beamforming using one bit of feedback: AWGN analysis, in Proceedings of 18th European Wireless Conference (EW 2012), Apr. 2012, Poznan (Poland).
- L. Berbakov, C. Anton-Haro, and J. Matamoros, Decentralized phase synchronization scheme for distributed beamforming in WSN with quantized phase feedback, in Proceedings of Future Network Mobile Summit (FUNEMS 2012), July 2012, Berlin (Germany).

Chapter 2

Background

In this chapter, we provide an overview of a number of concepts and tools which will be used throughout this PhD dissertation. First, in Section 2.1, we discuss some important hardware- and communication-related issues in wireless sensor networks. Then, in Sections 2.2 and 2.3, we provide some background on channel models for wireless communications. Next, in Section 2.4, we present an overview of distributed antenna arrays and beamforming, and its applicability in wireless sensor network contexts. Then, in Section 2.5, we briefly introduce energy harvesting technologies. Finally, in Section 2.6, we provide some necessary background on convex optimization tools.

2.1 Wireless sensor networks

Wireless sensor networks have become very popular in recent years, especially in areas where timely information about the physical world is crucial. This trend is expected to continue in coming years, mainly due to recent advances in microelectronics and the reduction of sensor fabrication costs. In a near future, it will be possible to incorporate hundreds or even thousands of sensors into various systems, to improve their performance and decrease the maintenance costs. A sensor node is usually composed of one sensing unit (one or more sensors with an A/D converter), one microprocessor, some memory, one RF transceiver, some energy storage

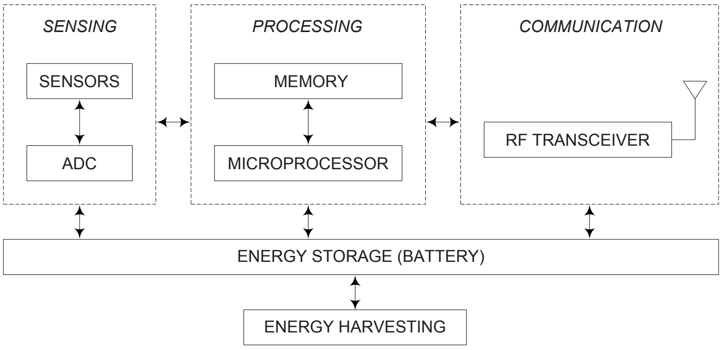

Figure 2.1: Block diagram of a wireless sensor node.

capacity and, possibly, an energy harvesting device (see Figure 2.1). The sensing unit may consist of many different types of sensor such as: thermal, seismic, acoustic, infrared, radar, etc. which, in turn, are able to monitor a variety of physical parameters such as: temperature, humidity, concentration of pollutants, object proximity, mechanical stress, etc. This motivates a range of possible applications for wireless sensor networks such as: environmental monitoring, industrial process control, military surveillance, healhcare monitoring, space exploration, among others.

In some applications, the exact location of individual sensors is not of great importance. This allows their random deployment (e.g., from an airplane) in remote areas. In these scenarios, however, the replacement of depleted batteries is quite often either costly, difficult or simply impossible to accomplish. Consequently, energy efficiency becomes of a great importance in wireless sensor networks, this being in stark contrast with Wireless Data Networks (WDN) where more emphasis is given to traditional Quality of Service (QoS) requirements such as achievable throughput and/or maximum communication delay. Energy efficiency aspects must be addressed at every layer of the protocol stack: from the modulation scheme and power allocation at the physical layer to the upper-layer protocols.

Until now, many different platforms have been developed for wireless sensor networks. Cheaper, low-end nodes such as Mica, Mica2, MicaZ [1], BTnodes, etc. are equipped with Atmel AVR microcontrollers with a CPU speed of 8-16 MHz and 128-256 kB of programmable flash memory. These sensor nodes operate on different ISM frequency bands such as 868 MHz, 915 MHz and 2.4 GHz, achieving data rates from 10 - 250 kbps. As long as some advanced functions, such as network management, are considered, the low-end devices might be out of game. To provide these functions, high-end nodes have also been developed. To name a few, Stargate, Netbridge NB-100 and Imote2, are equipped with more memory (8-32 MB), faster processors (13-400 MHz), and additional communication modules such as 802.11 and bluetooth.

To ensure inter-platform compatibility and specify a technology for low-data-rate wireless transceiver technology with low complexity and long battery lifetime, the IEEE 802.15.4 working group was formed. The resulting standard specifies three different operating frequency bands: 868 MHz (1 channel, Europe), 915 MHz (10 channels, America) and 2.4 GHz (16 channels, global availability). Physical layer supports ASK and BPSK modulation schemes for the 868 and 915 MHz bands, and O-QPSK for all three frequency bands. The transmission range of individual sensor nodes is typically 10-100 m with data rates ranging from 20 to 250 kbps. IEEE 802.15.4 only standardizes the Physical and MAC layers, leaving the standardization of the upper layers to other standard bodies, such as ZigBee, WirelessHART, and WINA.

2.2 Information theoretical channel models

In this section, we provide a brief introduction to channel models. The definition of a channel model mainly depends on the number of users involved in the communication. In terms of information theory, the channel models are divided into two groups:

- **Single-user channel model:** This channel model is used to provide an analytical framework for analyzing scenarios where one user sends data to another user. In the particular case where the noise is Gaussian, the resulting channel is usually referred to as a *Gaussian point-to-point channel* model.
- **Multi-user channel models:** These channel models are used to model communication scenarios where multiple users exchange data. A more general multi-user channel model can be built by combining the following, simpler multi-user channel models, namely: *Gaussian Multiple Access Channel* (MAC) [2, Section 15.1.2], which is used to model a scenario where two or more transmitters send information to a common receiver; *Gaussian broadcast channel* [2, Section 15.1.3], where one transmitter sends data to two or more receivers; *Gaussian relay channel* [2, Section 15.1.4], where transmitter sends data to a receiver with the help of relays; and *Gaussian interference channel* [2, Section 15.1.5], where two (or more) transmitters transmit data to two (or more) receivers at the same time and cause interference to one another.

For the reader's convenience, in the sequel, we only provide a more detailed description of those channel models which are particularly relevant to this dissertation.

2.2.1 Gaussian point-to-point channel

Here, we consider the discrete-time and memoryless[1] Gaussian channel. In this channel, given an input X_i, the output Y_i is given as the sum of the input X_i and the noise Z_i, as shown

---

[1] The output probability distribution at time i only depends on the current channel input and the noise.

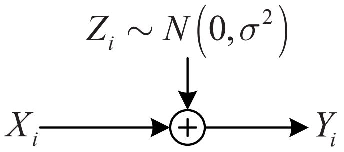

Figure 2.2: Gaussian channel.

in Figure 2.2. Noise realizations are i.i.d. and Gaussian distributed random variables with variance σ^2, whereas $\{X_i\}_{i=1}^n$ denotes the transmitted codeword of length n with probability density function $f(x)$. Therefore, according to Figure 2.2, the output Y_i is given by

$$Y_i = X_i + Z_i,\ Z_i \sim \mathcal{N}(0, \sigma^2), \tag{2.1}$$

where the noise Z_i is assumed to be independent of the signal X_i.

In real communication systems, the transmitter has limited transmit power. Consider an average power constraint P, i.e. for any codeword $\{X_i\}_{i=1}^n$ transmitted over the channel, we have that

$$\mathrm{E}\{X^2\} = \frac{1}{n}\sum_{i=1}^{n} X_i^2 \leq P. \tag{2.2}$$

Bearing this in mind, the capacity of this channel, C, defined as the maximum of the mutual information between the input and output, is given as follows

$$C = \max_{f(x):\mathrm{E}\{X^2\}\leq P} I(X;Y), \tag{2.3}$$

where $f(x)$ denotes the probability density function of the input X and the mutual information $I(X;Y)$ is defined [2] as follows

$$I(X;Y) \triangleq \int_X \int_Y p_{X,Y}(x,y) \log \frac{p_{X,Y}(x,y)}{p_X(x)p_Y(y)} dxdy, \tag{2.4}$$

with $p_{X,Y}(x,y)$ denoting the joint probability density function. It can be shown [2], that the optimal input is Gaussian distributed as $X_i \sim \mathcal{N}(0, P)$, and hence, the capacity reads

$$C = \frac{1}{2}\log\left(1 + \frac{P}{\sigma^2}\right) \text{ bits/channel use.} \tag{2.5}$$

2.2.2 Gaussian multiple-access channel

The Multiple-Access Channel (MAC) models a scenario in which two or more transmitters send data to a common receiver, as shown in Figure 2.3. In this scenario, in addition to noise, the interference from the other transmitters must be considered as well. In the sequel, we consider

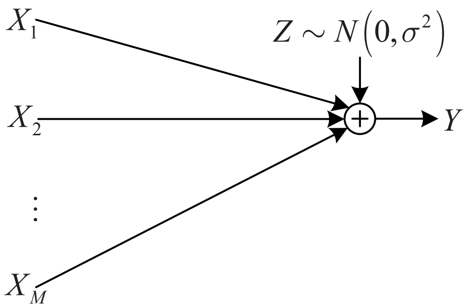

Figure 2.3: Gaussian Multiple-Access channel.

a Gaussian MAC channel with M transmitters, each subject to an average power constraint P. The received signal is given by

$$Y = \sum_{i=1}^{M} X_i + Z,\ Z \sim \mathcal{N}(0, \sigma^2). \tag{2.6}$$

The maximum achievable rates region for the MAC Gaussian channel must satisfy [2, Section 15.1.2]:

$$R_i < C_G\left(\frac{P}{\sigma^2}\right), \tag{2.7}$$

$$R_i + R_j < C_G\left(\frac{2P}{\sigma^2}\right), \tag{2.8}$$

$$\vdots$$

$$\sum_{i=1}^{M} R_i < C_G\left(\frac{MP}{\sigma^2}\right), \tag{2.9}$$

where $C_G\left(x\right) = \frac{1}{2}\log\left(1 + x\right)$ denotes the capacity of a single user Gaussian channel.

In the case where the codebooks of all the transmitters are fully correlated, i.e. when all the transmitters transmit the information with the same codeword using *beamforming*, the capacity is given by

$$C = \frac{1}{2}\log\left(1 + \frac{M^2 P}{\sigma^2}\right), \tag{2.10}$$

where the M^2 factor is the so-called beamforming gain.

2.2.3 Gaussian interference channel

In Figure 2.4, we depict a Gaussian interference channel comprising two transmitters and two receivers. In the given setup, the transmitter 1 wants to send information to receiver 1; likewise, transmitter 2 sends information to receiver 2. The channel gains to the intended receivers are

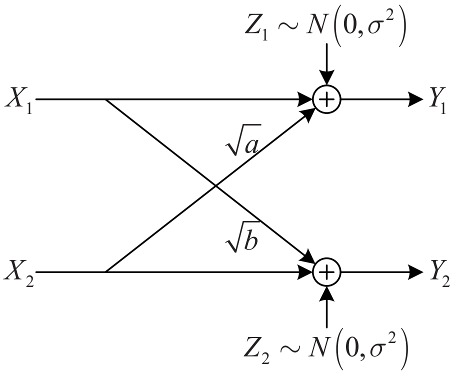

Figure 2.4: Gaussian interference channel.

normalized, whereas $\sqrt{a}$ and $\sqrt{b}$ denote the gains for crossover channels. For the given model, the received signals can thus be expressed as follows:

$$Y_1 = X_1 + \sqrt{a}X_2 + Z_1 \tag{2.11}$$

$$Y_2 = X_2 + \sqrt{b}X_1 + Z_2 \tag{2.12}$$

where Z_1 and Z_2 are modeled as independent Gaussian random variables. The capacity region of interference channel is not known in general. However, in some particular scenarios, it can be found. For strong interference scenarios (when the signal received from unintended transmitter is stronger), the capacity region is characterized in [3]. In addition, the results regarding the capacity region and low interference sum capacity are given in [4].

2.3 Fading channels

In wireless channels, in addition to noise and interference, which might be present in wired channel as well, there exist some additional challenges, such as multipath fading and shadowing, which often change over time in an unpredictable manner. For communication scenarios where the location, number and dielectric characteristics of scatterers are not known, statistical models must be used. In scenarios without a Line-of-Sight (LoS) component, only signals reflected from the surrounding objects are combined at the receiver. Let us assume that the signal transmitted is the unmodulated carrier $s(t) = \mathcal{R}\left\{e^{j(2\pi f_c t + \phi_0)}\right\}$. Then, the signal received will correspond to a sum of N multipath components:

$$r(t) = \mathcal{R}\left\{\left(\sum_{n=1}^{N} a_n(t)e^{j\phi_n(t)}\right)e^{j2\pi f_c t}\right\}, \tag{2.13}$$

where the phase term $\phi_n(t)$ includes the initial phase offset ϕ_0 and the delay associated with each multipath component, and $a_n(t)$ stands for the corresponding path loss. Alternatively, the received signal can also be rewritten as:

$$r(t) = r_I(t)\cos 2\pi f_c t + r_Q(t)\sin 2\pi f_c t, \tag{2.14}$$

where the in-phase and quadrature components are given by:

$$\begin{aligned} r_I(t) &= \sum_{n=1}^{N} a_n(t)\cos\phi_n(t), \\ r_Q(t) &= \sum_{n=1}^{N} a_n(t)\sin\phi_n(t). \end{aligned} \tag{2.15}$$

By considering N large, and by resorting to the central limit theorem [2], $r_I(t)$ and $r_Q(t)$ can be well approximated as jointly Gaussian random processes. Then, if both $r_I(t)$ and $r_Q(t)$ have variance equal to σ^2, the signal envelope

$$z(t) = |r(t)| = \sqrt{r_I^2(t) + r_Q^2(t)}, \tag{2.16}$$

is *Rayleigh*-distributed, namely

$$p_Z(z) = \frac{z}{\sigma^2} e^{-\frac{z^2}{2\sigma^2}}, \tag{2.17}$$

and, the phase $\theta = \arctan(r_Q(t)/r_I(t))$ is uniformly distributed, i.e. $\theta \sim \mathcal{U}(0, 2\pi)$.

Conversely, in a channel with a strong LoS component, $r_I(t)$ and $r_Q(t)$ are not zero-mean. In this case, the received signal can be found as the sum of an LoS component and a complex Gaussian component. Consequently, the signal envelope is shown to be a *Rician*-distributed random variable, where the Rician distribution is given by:

$$p_Z(z) = \frac{z}{\sigma^2} e^{-\frac{(z^2+s^2)}{2\sigma^2}} I_0(\frac{zs}{\sigma^2}), \tag{2.18}$$

with $2\sigma^2$ accounting for the average power of the non-LoS multipath components, s^2 standing for the power of the LoS component, and the function I_0 denoting the modified Bessel function of 0-th order.

2.4 Distributed beamforming techniques for wireless sensor networks

A technique where two or more antennas align their carrier signals in such a way that, after propagation, they combine coherently at the destination is known as transmit beamforming. On the one hand, this technique has clear benefits when compared to single antenna systems,

---

[2] Note that $a_n(t)$ and $\phi_n(t)$ are stationary and ergodic random processes.

such as: increased gain in received power, reduced interference levels to unintended directions and improved security. On the other hand, wireless transmitters with multiple antennas usually require a more complex circuitry, which is not suitable for wireless sensor network applications due to cost and size constraints.

Bearing in mind the advantages of transmit beamforming, one could wonder whether it can be implemented in a distributed scenario such as wireless sensor network. Until now, several research groups have conducted research on scenarios where sensor nodes cooperatively transmit a common message. They have shown that such collaborative transmission result in all the advantages of multi-antenna systems and, at the same time, the individual node complexity can be kept sufficiently low. However, in order to put this idea into a practical scenario, one has to face a variety of challenges such as information sharing, carrier and time synchronization, which can be difficult to accomplish, because of the distributed nature of wireless sensor networks.

Next, we outline a number of important issues in distributed beamforming contexts, namely, distributed carrier synchronization, beampattern analysis, and sidelobe control.

2.4.1 Distributed carrier synchronization

In *centralized* antenna arrays, frequency and phase synchronization can be assumed at all antenna elements. This assumption, however, does not hold in *distributed* antenna arrays (see Fig 2.5) since, here, each sensor is equipped with its own (low-quality) oscillator, which works independently from the others. Consequently, the signals transmitted by each sensor will have different initial phase. The transmitted signal, furthermore, may exhibit a significant drift, especially in temperature varying environments (i.e., in outdoor WSNs). Moreover, the exact locations of individual nodes are usually not known, this resulting in unknown phase change of the signal, due to different distances between each sensor and the destination. All the aforementioned effects pose serious obstacles to achieve coherent reception at the destination. Thus, before dealing with more complex concepts, such as beampattern analysis and sidelobe control, it is of a paramount importance to solve the problem of distributed carrier synchronization first.

One way for sensors to determine the common time scale is by resorting to mutual synchronization techniques. Since all the sensors are assumed to have the same role in synchronization, mutual synchronization is preferred in networks where sensors are equipped with oscillators of same accuracy. This method, however, usually entails large overhead. Moreover, some sort of multiple access scheme is necessary in order to differentiate one clock from the other. These issues must be particularly taken into account, especially in scenarios with large number of nodes, where a long synchronization overhead may diminish the energy savings due to beam-

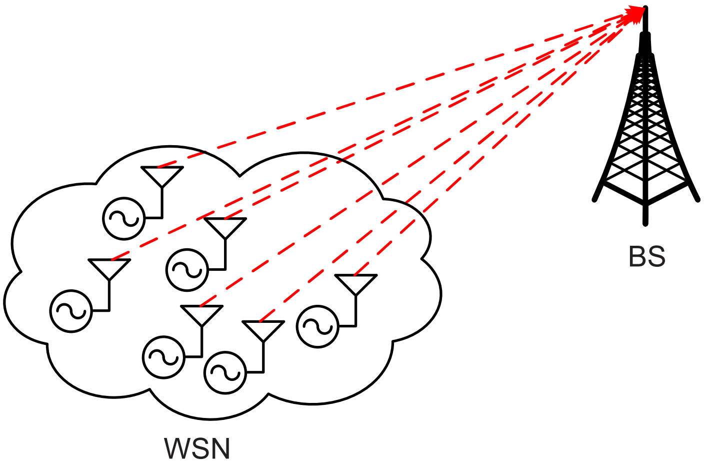

Figure 2.5: Distributed Beamforming in WSN.

forming.

Another possibility is to have a so called *master* node, which is used to help *slave* nodes to synchronize. Since propagation delays from master to slaves and from slaves to the destination are different, in order to account for these different delays, the oscillators at the slaves must precompensate their initial phase shifts. In [5], the authors propose a scheme where multiple transmitters adjust their carrier frequency and phase by tracking the clock of the destination. More specifically, the BS sends a common master beacon to all the sensor nodes. Each node "bounces" the master beacon back to the BS using a frequency different from that of the master beacon. In the proposed scheme, sensor nodes are distinguished by different direct-sequence codes at the BS. After receiving node transmissions, the BS estimates received phase of each sensor node relative to the transmitted master beacon. Next, the base station quantizes these estimates and sends them to the source nodes in a phase compensation message. Finally, after receiving the phase compensation message, each sensor node extracts its own phase compensation estimate and adjusts its carrier phase.

In [6], the authors consider a scenario where two sensor nodes S_1 and S_2 act as a distributed antenna array in order to send a common message to a destination D (see Figure 2.6). Similarly to [5], the destination sends a beacon at frequency f_0 to source nodes. However, this beacon is not directly used for carrier synchronization. Instead, each sensor generates a secondary sinusoidal beacon that is phase locked to the master beacon, but at different frequency, namely $f_1 = \frac{N_1}{M_1} f_0$. The secondary beacons propagate between the sensors, and, upon being received by the other sensor node, they are used to generate a carrier signal at frequency $f_c = \frac{N_2}{M_2} f_1$, that is phase locked to the received secondary beacon signal. In the proposed scheme, the authors assume that the overall propagation delay in both $D \rightarrow S_1 \rightarrow S_2 \rightarrow D$ and $D \rightarrow S_2 \rightarrow S_1 \rightarrow D$ directions is the same (see Figure 2.6). With this assumption, and by preserving the phase of the corresponding beacon signal when using frequency synthesis, the overall phase shift for both directions turns out to be the same. As a consequence, when the carrier signals

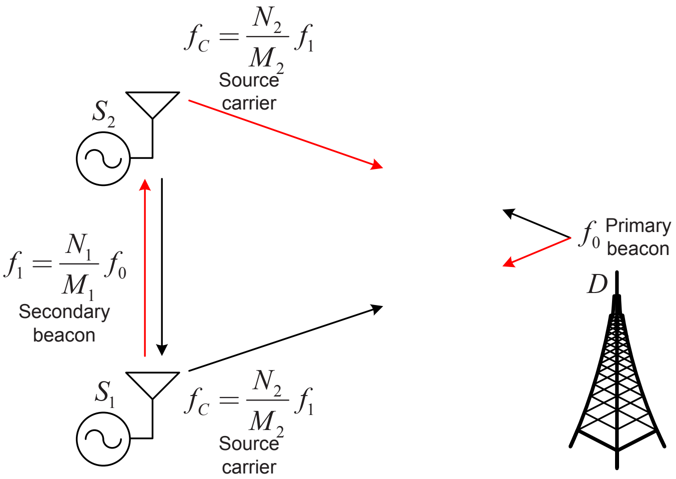

Figure 2.6: Time-slotted round-trip carrier synchronization.

arrive at the destination D, they will have the same phase. This work is further generalized in [7], by considering a scenario where multiple source nodes form a distributed antenna array. The proposed schemes, unfortunately, require multiple PLL loops at source nodes in order to accomplish simultaneous beacon receiving and data transmission. This, in turn, requires some additional complexity at individual nodes, that, in some cases, might not be affordable in wireless sensor network contexts.

A carrier synchronization scheme, suitable for simple hardware usually found on cheap sensor nodes, is proposed in [8]. In particular, the authors propose a simple carrier phase synchronization algorithm requiring only one bit of feedback per iteration. In the proposed scheme, all the sensors make random phase perturbations of their carriers in each algorithm's iteration. The sum received signal strength Y is measured at the destination and compared to the received signal strength from the previous iteration. The outcome of this comparison is then fedback to all the sensors, telling them to either retain or discard the last phase perturbation, according to the following rule:

$$\text{Feedback} = \begin{cases} \text{“1” - keep the perturbation} & \text{if } Y[n] > Y[n-1] \\ \text{“0” - discard the perturbation} & \text{if } Y[n] \leq Y[n-1] \end{cases}, \tag{2.19}$$

where n denotes the iteration index. This procedure is repeated until some prescribed level of the received signal strength is achieved. The main result of this paper is the analytical expression modelling the evolution of the normalized received signal strength as a function of algorithm's iteration, as shown in Figure 2.7. Although the proposed scheme does not require a complex hardware at individual sensors, it has some drawbacks. Namely, it is shown that the algorithm's convergence time scales linearly with the number of sensors. As a consequence, for large networks, the energy spent for carrier synchronization might be much higher than the energy saved due to distributed beamforming.

In [9], the authors extend the work in [8] by explicitly including *carrier frequency* synchroniza-

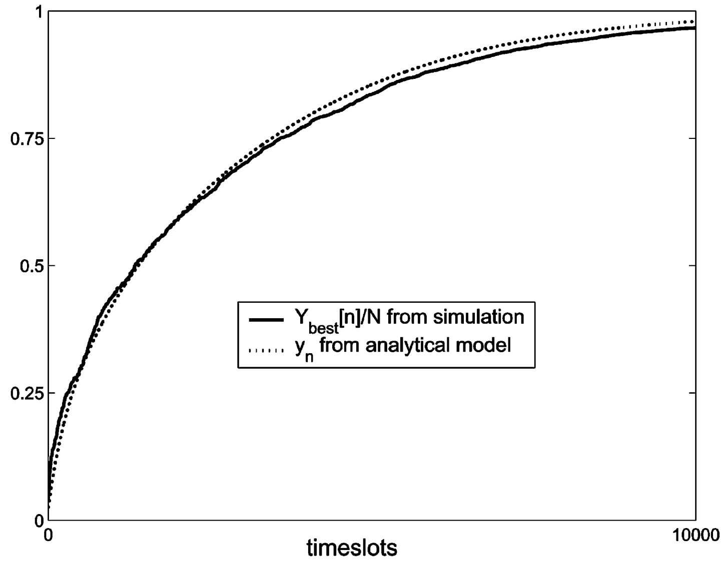

Figure 2.7: Monte Carlo simulation of optimized beamforming algorithm with $N = 1000$ transmitters, where the pdf of phase perturbations is numerically optimized, [8].

tion as well. In addition, in [9], the authors provide the experimental verification of the proposed distributed beamforming scheme. It is important to note that the scheme proposed in [8] assumes an ideal scenario, with only one destination and perfect estimation of the received signal strength. In practice, however, many different WSNs can be deployed in neighboring areas, making inter-network interference an important challenge. In addition, the noise at the receiver results in non-perfect received signal strength estimates. This, in turn, may lead to a wrong decision on whether to keep or discard the phase perturbation. In order to evaluate the algorithm's behavior in realistic scenarios, in Chapter 5, we study a scenario with multiple destinations. Furthermore, we also include the analysis of the impact of noise on the algorithm's convergence properties.

When wireless sensor networks consist of a *large* number of nodes, sometimes, it is not necessary that all of them cooperate. In contrast to all previous approaches, in [10] the author do not employ phase precompensation techniques. Instead, inspired by the observation that bandpass signals with even moderate phase offsets can still combine to provide beamforming gain, they develop a scheme which *opportunistically* selects a subset of available source nodes whose transmitted signals combine in a quasi-constructive manner at the destination. Since the computation of the optimal selection vector is exponentially complex, the authors resort to several suboptimal selection rules. The simplest one is referred to as a *sector-based* selection method (see Figure 2.8). The selection region is defined by two parameters: γ corresponding to a minimum amplitude; and α corresponding to a maximum angle. In order to be selected, a node s_k must satisfy both the minimum amplitude and maximum angle conditions, i.e.

$$s_k = \begin{cases} 1 \text{ - node selected} & \text{if } a_k \geq \gamma \text{ and } |\phi_k| \leq \alpha \\ 0 \text{ - node not selected} & \text{otherwise.} \end{cases} \tag{2.20}$$

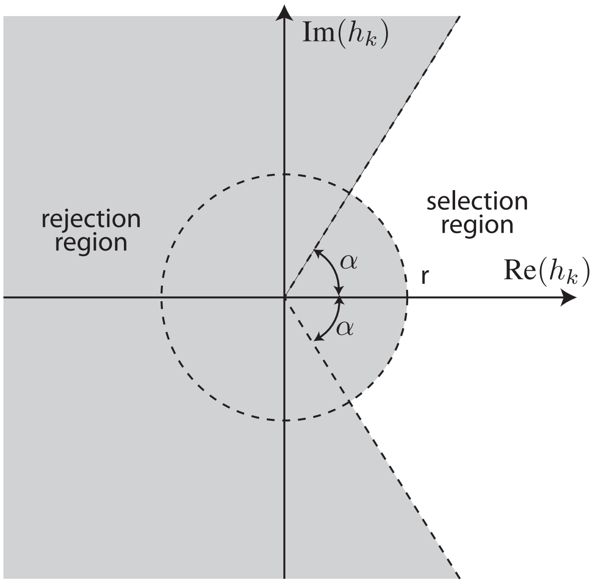

Figure 2.8: Sector-based selection region, [10].

with a_k and ϕ_k accounting for sensor-to-destination channel magnitude and phase shift (with Rayleigh and uniform distributions respectively). The optimal values of γ and α are found by maximizing the lower bound on expected normalized received power, and according to [10], they equal $\breve{\alpha} = 1.1656$ radians and $\breve{\gamma} = 0.5316$.

2.4.2 Beampattern analysis

When considering distributed antenna arrays, one can ask whether a beampattern with a narrow mainlobe and sufficient beamforming gain can be formed. One of the challenges associated with this question lies in the fact that, often, sensor node locations are not precisely known. Since the resulting beampattern strongly depends on the particular realization of the sensor locations, it is quite reasonable to address this question in a probabilistic framework. In fact, given a particular antenna geometry, spatial distribution of sensor location, and the distribution of the phase offsets at the sensor nodes, it is possible to compute the average beampattern (over different network realizations), in order to determine its mainlobe width, sidelobe characteristics, etc.

In the antenna arrays literature, the interest on stochastic analysis of random antenna arrays is not new. In [11], the authors build a random array theory based on linear non-uniform arrays. They show that a random linear array with a large number of nodes can indeed form a beampattern where the directivity approaches N, with N accounting for the number of antennas. Furthermore, it is shown that the width of the main lobe strongly depends on the array size, i.e. the larger the array, the narrower the main lobe. In other words, when the number of antenna elements is fixed, it is possible to reduce the width of mainlobe by spreading these elements

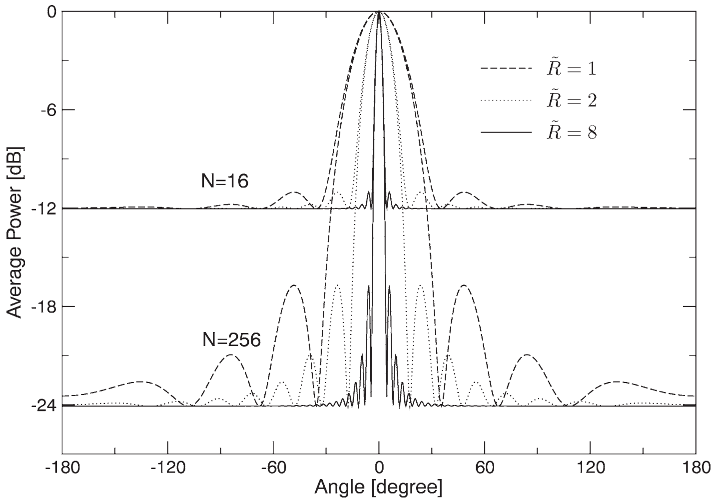

Figure 2.9: Average beampattern with different normalized network radii $\tilde{R}$ and number of sensors $N = 16, 256$, [12].

over larger distances without risking the increase in sidelobe levels.

More recently, in the context of wireless sensor networks, in [12], the authors derive the statistical average beampattern (see Figure 2.9) and probability distribution of the beampattern for sensor nodes *uniformly* distributed over a disk of radius R. All the sensor nodes are assumed to be located on the x - y plane. Each sensor node has only one ideal isotropic antenna, and all sensor nodes transmit with identical powers. Path losses are assumed to be identical as well, and multipath and shadowing effects are not considered. The authors show that the average far-field beampattern for an N-node distributed beamformer is given by:

$$P_{\mathrm{av}}(\phi) = \frac{1}{N} + \left(1 - \frac{1}{N}\right) \left| \frac{J_1(4\pi\tilde{R}\sin(\phi/2))}{2\pi\tilde{R}\sin(\phi/2)} \right|^2 \tag{2.21}$$

where $\tilde{R} = R/\lambda$ stands for the radius of the disk normalized by the wavelength of the carrier, ϕ accounts for the angle with respect to the BS, and $J_1(x)$ denotes the first-order Bessel function of the first kind. From (2.21), we see that with N sensor nodes uniformly distributed over a disk, the directivity approaches N. Furthermore, for $N \to \infty$, the authors show that the width of the main lobe turns out to be proportional to the inverse of the disk radius $\tilde{R}$.

In some deployment scenarios, a uniform sensor distribution cannot be guaranteed. Indeed, to cover a wide area, a large number of sensor nodes must be deployed simultaneously in an ad hoc way. An example of such application is rural areas monitoring where the deployment is done by dropping a group of sensor nodes from an airplane. In this particular scenario, the actual location of the sensor nodes are affected by different factors such as wind, the releasing mechanism, speed, etc. The bias from the targeted location due to each of these multiple factors can be modeled as a random variable being the effective bias the result of all these random variables. Therefore, according to the central limit theorem, the actual x and y locations will

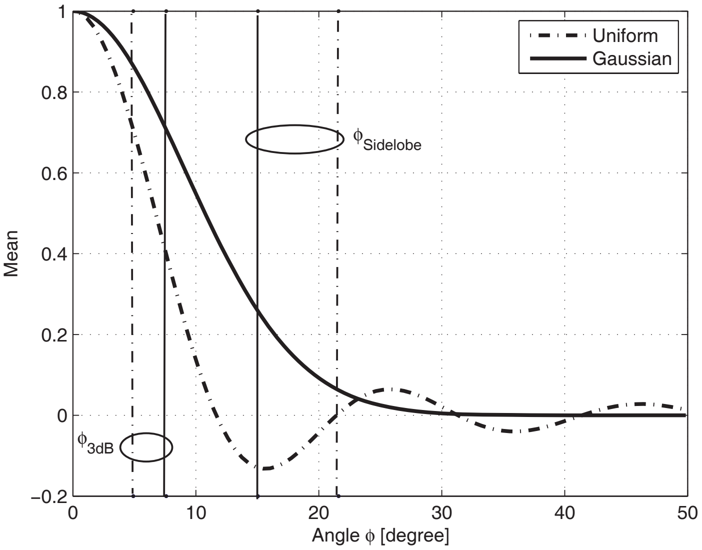

Figure 2.10: The mean of the array factor for both uniform and Gaussian spatial distributions: $N = 16$, $\sigma^2 = 1$, $\tilde{R} = 3\sigma$, [13].

follow a Gaussian distribution. In [13], the authors use the beampattern analysis framework from [12], and derive the average beampattern, which is, in the case for N Gaussian distributed sensor nodes, given by:

$$P_{\text{av}}(\phi) = \frac{1}{N} + \left(1 - \frac{1}{N}\right) \left| e^{-\frac{\alpha^2\sigma^2}{2}} \right|^2 \tag{2.22}$$

where $\alpha = \alpha(\phi) = 4\pi \sin\left(\frac{\phi}{2}\right)$ and $\tilde{R} = 3\sigma$. They show that both uniform and Gaussian sensor node deployments behave in a similar way with respect to the relation between the beamwidth and the network diameter. However, the Gaussian deployment was shown to result in wider mainlobe, and to have lower chance of large sidelobes, as can be observed in Figure 2.10.

In [12] and [13], the authors showed that after achieving phase alignment, a beampattern with a stable mainlobe is formed. However, the sidelobes of such beampattern strongly depend on the set of actual node locations. In scenarios with multiple wireless sensor networks deployed in neighboring areas, high sidelobes may cause an unacceptable level of interference to the unintended base stations. If, somehow, we manage to control sidelobes in order to keep the interference below some prescribed threshold, this could result in the increase of network capacity and wireless channel availability. To that end, in [14] the authors propose a node selection algorithm. The algorithm is based on the iterative selection of the group of sensors, which results in sidelobe level that is below some prescribed threshold. It is designed to overcome simple node's hardware limitations and avoid complex central weight design and signalling. Node selection is carried out when the network is deployed for the first time and can be repeated when configuration of the network changes.

Table 2.1: Typical Data for Various Energy Harvesting Sources. [15]

Energy kind	Conditions	Power density	Area/Volume
Vibration	1 m/s^2	100 μW/cm^3	1 cm^3
Solar	Outdoors	7500 μW/cm^2	1 cm^2
Solar	Indoors	100 μW/cm^2	1 cm^2
Thermal	$\Delta T = 5°$C	60 μW/cm^2	1 cm^2

2.5 Energy harvesting

In deployment scenarios where non-rechargeable batteries are difficult or impossible to replace (e.g., in remote areas), network lifetime is severely constrained by battery capacity. A natural way to overcome this drawback is to extract energy from the environment, convert it into electrical energy and effectively recharge such batteries. This concept, usually referred to as *energy harvesting*, has attracted considerable attention in the research community in recent years. Depending on the application, the energy is available in solar, thermal or mechanical form, which, in turn, require different transducers: solar panels, Peltier element for thermal harvesting along with piezoelectric, or electromagnetic harvesters for vibrational energy. The amount of energy harvested strongly depends on the kind of energy source used. In Table 2.1, we provide typical power density levels for aforementioned kinds of harvested energy and the conditions assumed. The harvested energy needs to be *stored*, so that it can be used when needed by the sensor node. Energy storage devices usually come in the form of rechargeable batteries (e.g., Li-Ion, NiMH) or supercapacitors. Although rechargeable batteries have higher capacities than supercapacitors, they loose some of their capacity with each recharge cycle. Moreover, their peak power output is much more limited than in the case of supercapacitors. On the contrary, supercapacitors suffer from higher energy leakage rate. In order to take advantage of both, one can resort to an intelligent hybrid storage device, as suggested in [16]. In the proposed architecture, the instantaneous power demand is supplied by the supercapacitor, whenever the power generated by the energy harvesting traducer is less than the power required for the load and battery charge.

In the sequel, we provide an overview of design challenges to be faced when dealing with the EH communication systems. Communication scenarios can be categorized into two main groups, namely, those with *single* or *multiple* energy harvesting sensor(s).

2.5.1 Single energy-harvesting sensor

In order to make the analysis tractable, it is often assumed that energy and data packets are generated at discrete time instants, as shown in Figure 2.11. Furthermore, the information on

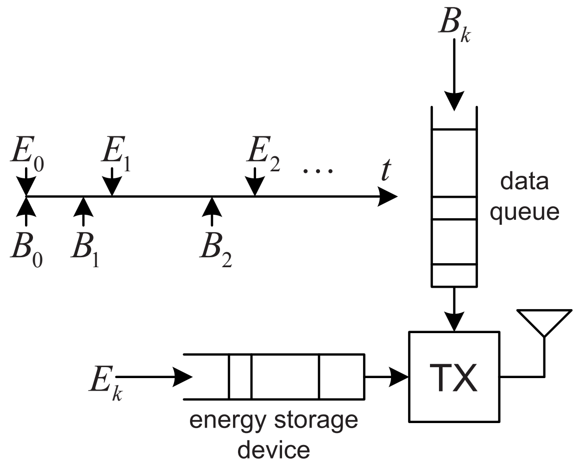

Figure 2.11: Energy harvesting transmitter with discrete energy and data arrivals.

energy and data amounts, i.e. E_k and B_k, along with the exact time instants is assumed to be known either in advance (non-causal information), or that the knowledge is acquired during the transmission (causal information). When compared to a battery operated communication system, with total power/energy constraint, energy harvesting systems include an additional set of causality constraints. In other words, energy cannot be spent before it is harvested (and, thus, the Energy Consumption (EC) curve must lie below the cumulative Energy Harvesting (cEH) constraint at all times), as shown in Figure 2.12 (left). Likewise, data cannot be transmitted before it is generated.

For single-sensor scenarios, in [17], the authors derive the optimal transmission (power allocation) policy which minimizes the time T needed to deliver all data packets to the destination subject to causality constraints on energy E_k and data packet B_k arrivals. They consider a scenario in which energy and data packet arrivals are non-causally known. In addition, the energy storage capacity is assumed to be *infinite*. For the data packet arrivals, the authors consider two scenarios: first, where all the packets have arrived before the transmission starts; second, where the packets arrive during the transmission. For the former scenario, they show that the power only potentially changes (increases) in time instants where some energy is harvested, i.e. the transmission policy is *nondecreasing*. Furthermore, they develop an algorithm that finds the optimal policy, which turns out to be the one that yields the tightest piecewise linear energy consumption curve, lying below the energy harvesting curve at all times and touching the energy harvesting curve at $t = T$, as shown in Figure 2.12 (right). For the later scenario, i.e. when data arrive during transmission, the authors identify the new set of optimality conditions that require that the transmission power remains constant between two events , i.e., the power only potentially changes when new energy is harvested or a new packet arrives. Furthermore, they show that the optimal policy is such that whenever the power changes at an energy harvesting event, then the energy consumed up to that event equals the energy harvested up to that event. In addition, it is shown that when the power changes at a packet arrival event, the

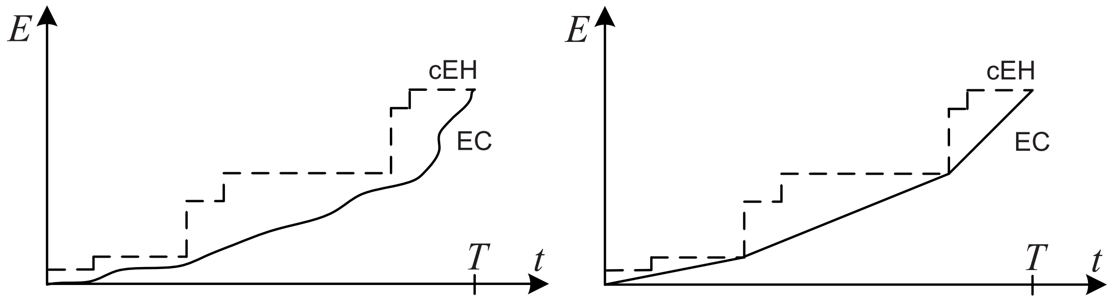

Figure 2.12: Feasible and optimal transmission policy for an EH transmitter with *infinite* battery capacity.

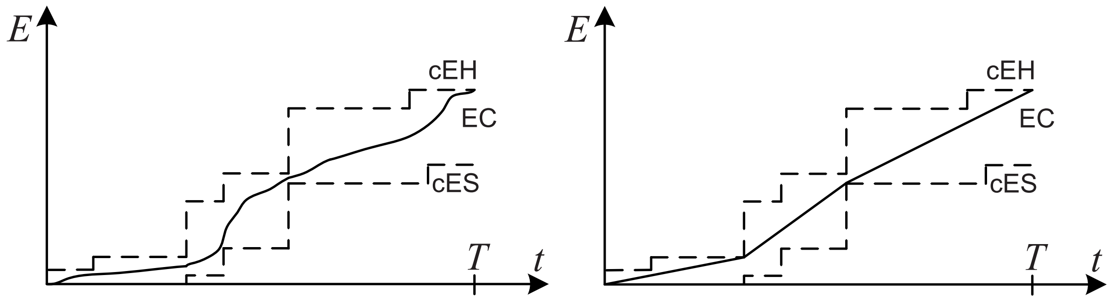

Figure 2.13: Feasible and optimal transmission policy for an EH transmitter with *finite* battery capacity.

number of packets transmitted until that event equals the number of packets generated up to that event. Finally, if the power changes at an event that has both energy and data arrivals at the same time, then, one of the two causality constraints (either energy or data constraint) must be satisfied with equality.

In [18], the authors go one step beyond [17], by considering *finite* energy storage capacity effects in a scenario where all data packets are available before the transmission starts. Now, the transmission policy must be such, that there is always enough free space in the energy storage device to accommodate the next energy arrival (i.e., any policy causing a battery overflow is strictly suboptimal). This translates into a set of cumulative Energy Storage (cES) constraints, as those shown in Figure 2.13 (left). Consequently, the EC curve of the optimal policy must lie inside the tunnel defined by cEH and cES curves. Furthermore, the authors show that in contrast with [17], transmit powers are not anymore nondecreasing over time. As a matter of fact, the optimal policy requires that the power decreases only at energy harvesting instants when the energy storage device is full and increases only at energy harvesting instants when the energy storage device is completely discharged. The optimal policy is such that it yields the tightest piecewise linear energy consumption curve, lying inside the tunnel defined by cEH and cES curves at all times and touching the energy harvesting curve at $t = T$ (see Figure 2.13 (right)).

Ozel *et al* generalize the previous analysis to Rayleigh fading channels (instead of Gaussian)

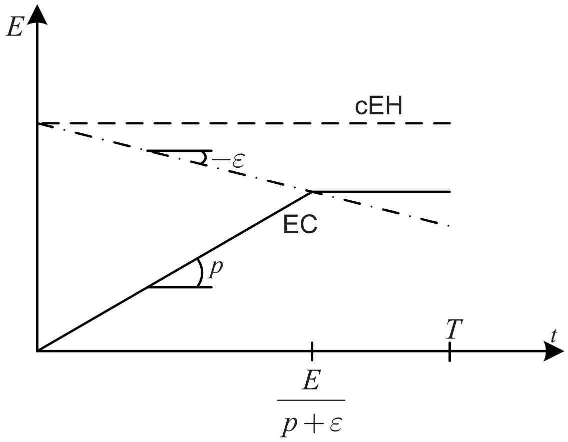

Figure 2.14: Optimal transmission policy for an EH transmitter with *battery leakage*.

and for the case in which the information on the harvested energy and channel gains is either causally or non-causally known [19]. For the non-causal case, the approach from [17] and [18] cannot be used, since the knowledge of energy arrivals/fading coefficients is acquired during transmission. Instead, a dynamic programming approach is considered. In order to further reduce the computational complexity, inherent in dynamic programming, the authors propose several suboptimal policies.

In [17–19], the authors consider that the harvested energy is exclusively used for data transmission. In practice, however, a fraction of the harvested energy will be unavoidably spent in the sensor's circuitry for data processing. In order to further investigate this issue, in [20] and [21], the authors explicitly take into account both transmission and processing energy consumption in a system with energy harvesting capabilities.

In real-world communication systems, batteries lose a portion of stored energy over time. This is due to unwanted chemical reactions, resulting into an internal current leakage between positive and negative electrode of a cell. Besides, batteries may also loose some capacity, because of aging and repetitive recharging cycles. All these effects have a major impact on performance. In order to facilitate the analysis of energy harvesting communication systems with battery imperfections, the authors in [22] propose a general optimization framework. Furthermore, they derive the optimal transmission policy for a wireless system with constant energy leakage rate. They show that, in contrast to previous works, it is not optimal to transmit with constant power until deadline T anymore, since some energy will be wasted until then (see Figure 2.14, dash-dotted curve). Instead, the authors show that there exists an optimal power p and transmission time $\frac{E}{p+\epsilon}$, which depends on the energy leakage rate ϵ. Similarly, in [23], the authors derive a throughput-optimal transmission policy for a transmitter with energy storage losses, in point-to-point and broadcast channels scenarios. They show that the optimal policies for these models are threshold policies. More specifically, energy is stored when harvesting power is above an upper threshold, energy is retrieved when harvested power is below a lower

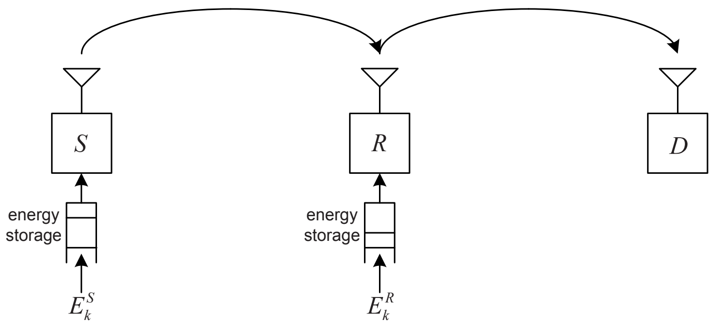

Figure 2.15: Two-hop communication system with energy-harvesting source and relay terminals.

threshold, and the transmitter transmits when the harvested power is in between.

2.5.2 Multiple energy-harvesting sensors

Communication scenarios involving *multiple* sensors, in general render the computation of the optimal transmission policy more involved and often, coupled.

In [24], the authors consider a two-hop network model, in which the source S and the relay R are capable of harvesting energy from the environment, as shown in Figure 2.15. Depending on whether the relay can simultaneously transmit and receive data, the authors consider two communication scenarios, namely, full-duplex and half-duplex relaying scenarios. The goal in both scenarios is to identify the transmission policy that departs the maximum number of bits until a given deadline. In a scenario with *full*-duplex relaying, the authors show that the transmission policies are to some extent decoupled. In other words, it is optimal that source S adopts the transmission policy that maximizes the total number of bits transmitted to the relay. Likewise, the bit arrival profile from the source transmission along with the energy harvesting profile at relay are used to compute the optimal transmission policy at relay. Consequently, both policies can be computed by employing the algorithm proposed in [17]. This approach, however, cannot be used in a *half*-duplex relay scenario, due to the fact the relay cannot transmit and receive data at the same time. This, in turn, renders the transmission policies coupled. However, in the case of a *single energy arrival* at the source, the numerical solution can be efficiently computed. Furthermore, in [25], the authors generalize the half-duplex scenario in [24], by considering the case of *multiple-energy arrivals* for both the source and the relay. More specifically, they identify the optimal policy for the case of two energy arrivals at the source, delegating the multi-arrival case for future work.

In [26], the authors investigate the optimal packet scheduling and power allocation in a two-user *multiple access* communication system, where both transmitters have energy harvesting capabilities. They assume that all data, i.e. B_1 and B_2, have arrived before the transmission

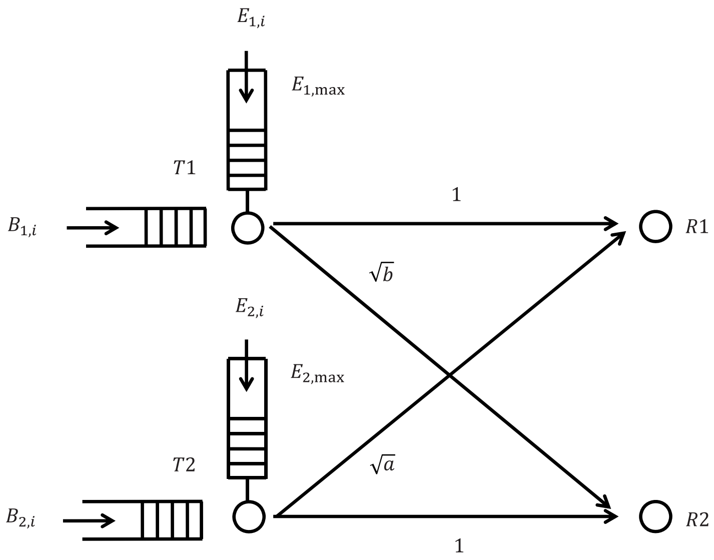

Figure 2.16: Interference channel model with energy harvesting and data arrivals, [27].

starts, and that the information on energy harvesting arrivals is non-causally known. The goal is to identify the optimal transmission policies, such that the time, by which all packets from both users are delivered to the destination, is minimized. In order to solve this problem, the authors consider a *dual* problem, i.e. the problem of maximizing the number of bits transmitted for a given deadline T.

A two-user Gaussian *interference* channel with energy harvesting transmitters is considered in [27] (see Figure 2.16). The focus of this paper is on the transmission policy which maximizes the total number of bits transmitted from T_1 and T_2 to R_1 and R_2 respectively, for a given deadline. The authors show that the iterative *coordinate descent method*, optimizing individual transmission policies at each iteration, converges to the optimal solution when all data is available before the transmission starts. Namely, in each iteration, the network utility function, i.e. the sum data throughput, is *maximized* over the transmission policy of one transmitter, whilst the policy of the other one is *fixed*, until both policies converge to the optimal solution. Furthermore, this solution is extended to the scenario where data arrive during the transmission, Besides, it is observed that, in some cases, the single-user subproblems can further be simplified by considering them independently from each other.

In [28], the authors consider an AWGN *broadcast* channel. The transmitter has a fixed number of packets to deliver to each receiver. The goal is to minimize the time by which all the packets are delivered to their respective destinations. To gain some insight into the problem, the authors first consider a two-receiver broadcast channel. They show that the optimal total transmit power allocation has the the same structure as the optimal single user transmit power allocation in [17]. In addition, they prove that the total transmit power must be split among all the users based on a cut-off power level. Furthermore, the analysis is extended to an M user broadcast channel, where it is shown to be optimal to split the total power among M users according to $M - 1$

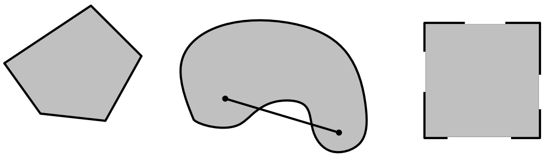

Figure 2.17: Convex and nonconvex sets. Left: Pentagon including its border is convex; Middle: The kidney shape is not convex; Right: Square, which does not contain some border points, is not convex [32].

cut-off levels. This problem is further generalized in [29] and [30] for scenarios with finite battery capacity and fading broadcast channel respectively.

All the previous work assume that receivers require much less energy than transmitters, and hence, it can be neglected. However, the *receiving energy* can be comparable to the energy required by transmitter, especially in scenarios where complex coding and modulation schemes are employed. To address these scenarios, a general framework for utility function maximization in a wireless network with energy harvesting transmitters and receivers is proposed in [31].

2.6 Convex optimization

In some parts of this PhD dissertation, we assume that the wireless sensor nodes are capable of harvesting energy from the environment. In these scenarios, it turns out that the problem of optimal power allocation can be cast into a convex program. To provide the necessary mathematical background, in this section, we review some important concepts of convex optimization along with the necessary and/or sufficient optimality conditions.

2.6.1 Convex sets

A set $\mathcal{C}$ is said to be convex if the line segment between any two points in $\mathcal{C}$ lies in $\mathcal{C}$, that is, if for any $\mathbf{x}_1, \mathbf{x}_2 \in \mathcal{C}$ and any θ such that $0 \leq \theta \leq 1$, the following holds:

$$\theta \mathbf{x}_1 + (1-\theta)\mathbf{x}_2 \in \mathcal{C} \tag{2.23}$$

Figure 2.17 presents some simple convex and nonconvex sets in $\mathbb{R}^2$. A point of the form $\theta_1\mathbf{x}_1 + \theta_2\mathbf{x}_2 + \ldots + \theta_k\mathbf{x}_k$, where $\theta_1 + \theta_2 + \ldots + \theta_k = 1$ and $\theta_i \geq 0$ for $i = 1, \ldots, k$, is called a convex combination of the points $\mathbf{x}_1, \ldots, \mathbf{x}_k$. It can be shown that a set is convex if and only if it contains every convex combination of its points.

In the sequel, we list the operations that preserve convexity of sets. In other words, they allow us to construct the convex sets from others, and help us to determine convexity of sets.

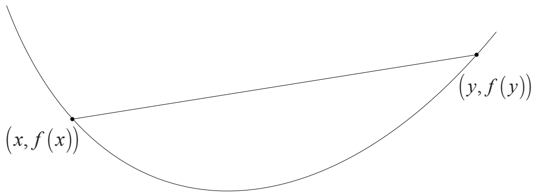

Figure 2.18: Convex function. The cord between any two point lies above the graph of convex function [32].

- Intersection preserves convexity: if $\mathcal{S}_1$ and $\mathcal{S}_2$ are convex, then $\mathcal{S}_1 \bigcap \mathcal{S}_2$ is also convex. This property extends to the intersection of an infinite number of sets: if $\mathcal{S}_k$ is convex for every $k \in K$, then the set $\bigcap_{k \in K} \mathcal{S}_k$ is convex, as well.
- An affine function of a convex set is convex. In other words, for a convex set $\mathcal{S} \subseteq \mathbb{R}^n$ and affine function $f(\mathbf{x}) = \mathbf{A}\mathbf{x} + \mathbf{b}$, the image of $\mathcal{S}$ under f, i.e. $f(\mathcal{S}) = \{f(\mathbf{x}) | \mathbf{x} \in \mathcal{S}\}$, is convex.
- Perspective function preserves convexity. Recall that the perspective function scales or normalizes vectors so the last component is one, and then discards the last component. Therefore, if $\mathcal{C} \subseteq \mathbf{dom} P$ is convex, than its image $P(\mathcal{C}) = \{P(\mathbf{x}) | \mathbf{x} \in \mathcal{C}\}$ is convex, as well.

2.6.2 Convex functions

A function $f : \mathbb{R}^n \rightarrow R$ is convex if $\mathbf{dom} f$ is a convex set and if for all $\mathbf{x}, \mathbf{y} \in \mathbf{dom} f$, and θ such that $0 \leq \theta \leq 1$, we have:

$$f(\theta\mathbf{x} + (1-\theta)\mathbf{y}) \leq \theta f(\mathbf{x}) + (1-\theta) f(\mathbf{y}). \tag{2.24}$$

In other words, this means that the line segment between $(\mathbf{x}, f(\mathbf{x}))$ and $(\mathbf{y}, f(\mathbf{y}))$, which is the chord from $\mathbf{x}$ to $\mathbf{y}$, lies above the graph of function f, as show in Figure 2.18 . A function f is called strictly convex if strict inequality holds in (2.24) for $\mathbf{x} \neq \mathbf{y}$ and $0 < \theta < 1$. We call the function f concave if $-f$ is convex, and strictly concave if $-f$ is strictly convex.

For a function f that is differentiable (i.e. its gradient ∇f exists at each point in $\mathbf{dom} f$ which is open), we have that if the following holds:

$$f(\mathbf{y}) \geq f(\mathbf{x}) + \nabla f(\mathbf{x})^T (\mathbf{y} - \mathbf{x}) \tag{2.25}$$

for all $\mathbf{x}, \mathbf{y} \in \mathbf{dom} f$, then the function f is convex. This is the so-called *first-order condition*.

In the same vein, let us consider a twice differentiable function f (i.e. its Hessian $\nabla^2 f$ exists on each point in $\mathbf{dom} f$, which is open). Then f is convex, if and only if $\mathbf{dom} f$ is convex and its

Hessian is positive semidefinite. In other words, for all $\mathbf{x} \in \mathbf{dom} f$ the following *second-order condition* holds:

$$\nabla^2 f(\mathbf{x}) \succeq 0. \tag{2.26}$$

Likewise, f is concave if and only if $\mathbf{dom} f$ is convex and $\nabla^2 f(\mathbf{x}) \preceq 0$ for all $\mathbf{x} \in \mathbf{dom} f$. However, for strict convexity if and only if relation does not hold anymore. In fact, if $\nabla^2 f(\mathbf{x}) \succ 0$ for all $\mathbf{x} \in \mathbf{dom} f$, then f is strictly convex. Nevertheless, the converse is not true.

Similarly to convex sets, the operations that preserve convexity might help us prove convexity or concavity of some particular function. A list of operations includes:

- *Nonnegative weighted sum* of convex functions, i.e $f = w_1 f_1 + \ldots + w_k f_k$ is convex.
- *Composition with an affine mapping* is convex function, i.e. if f is convex, than $g(\mathbf{x}) = f(\mathbf{A}\mathbf{x} + \mathbf{b})$ is complex as well.
- *Pointwise maximum*: If functions f_1 and f_2 are convex functions, then their pointwise maximum defined by $f(\mathbf{x}) = \max\{f_1(\mathbf{x}), f_2(\mathbf{x})\}$, is also convex.
- *Composition*: Consider two functions $h : \mathbb{R}^k \rightarrow \mathbb{R}$ and $g : \mathbb{R}^n \rightarrow \mathbb{R}^k$ and their composition $f = h \circ g : \mathbb{R}^n \rightarrow \mathbb{R}$, defined by:

  $$f(\mathbf{x}) = h(g(\mathbf{x})), \quad \mathbf{dom}\ f = \{\mathbf{x} \in \mathbf{dom}\ g | g(\mathbf{x}) \in \mathbf{dom}\ h\}. \tag{2.27}$$

  By assuming that $k = 1$ and $n = 1$, the following rules for *scalar composition* hold:

  - function f is convex if h is convex and nondecreasing, and g is convex,
  - function f is convex if h is convex and nonincreasing, and g is concave,
  - function f is concave if h is concave and nondecreasing, and g is concave,
  - function f is concave if h is concave and nonincreasing, and g is convex.

2.6.3 Convex optimization problems

In general, optimization problems can be posed as follows:

$$\begin{aligned} &\min_{\mathbf{x}}\ f_0(\mathbf{x}) \\ &\text{s.t. } f_i(\mathbf{x}) \leq 0, && i = 1, \ldots, m \\ &\qquad h_i(\mathbf{x}) = 0, && i = 1, \ldots, p, \end{aligned} \tag{2.28}$$

where $\mathbf{x} \in \mathbb{R}^n$ accounts for the *optimization variable* whereas the function $f_0 : \mathbb{R}^n \rightarrow \mathbb{R}$ stands for the *objective* or *cost function*. The inequalities $f_i(\mathbf{x}) \leq 0$ denote *inequality constraints*, while the equations $h_i(\mathbf{x}) = 0$ stand for the *equality constraints*. If there are no constraints we say the problem is *unconstrained*.

The set of points for which objective as well as all constraints are defined is called the domain $\mathcal{D}$ of the optimization problem. A given point $\mathbf{x} \in \mathcal{D}$ is called *feasible* if it satisfies all equality and inequality constraints. The problem is called feasible if there exists at least one feasible point, and infeasible otherwise. The set of all feasible points is called the *feasible set*.

We define the *optimal value* $\breve{p}$ of the problem (2.28) as

$$\breve{p} = \inf_{\mathbf{x}} \{ f_0(\mathbf{x}) | f_i(\mathbf{x}) \leq 0, i = 1, \ldots, m, h_i(\mathbf{x}) = 0, i = 1, \ldots, p \} \tag{2.29}$$

We say that $\breve{\mathbf{x}}$ is an *optimal solution*, if $\breve{\mathbf{x}}$ is feasible and $f_0(\breve{\mathbf{x}}) = \breve{p}$. The set of all optimal solutions is denoted as optimal set. A feasible point $\mathbf{x}$ is *locally optimal* if it minimizes f_0 over nearby points in the feasible set. In this dissertation, we will sometimes refer to optimal solution as *globally optimal* in order to distinguish between *locally optimal* and *optimal*. If point $\mathbf{x}$ is feasible and $f_i(\mathbf{x}) = 0$, we say that i-th inequality constraint is *active*. On the contrary, if $f_i(\mathbf{x}) < 0$, we say that i-th inequality constraint is *inactive*.

A problem of the form (2.28) is a *convex optimization problem* when the following holds:

- the objective function $f_0(\mathbf{x})$ is convex,
- the inequality constraint functions $f_i(\mathbf{x}), i = 1, \ldots, m$ are convex,
- the equality constraint functions $h_i(\mathbf{x}), i = 1, \ldots, p$ are affine, i.e. $h_i(\mathbf{x}) = \mathbf{a}_i^T \mathbf{x} - b_i$.

An important property of convex optimization problems is that any locally optimal point is also *globally optimal*.

2.6.4 The Lagrange dual function

Consider an optimization problem in the standard form (2.28). Assume that its domain $\mathcal{D} = \bigcap_{i=0}^{m} \textbf{dom}\, f_i \cap \bigcap_{i=1}^{p} \textbf{dom}\, h_i$ is nonempty. To recall, we do not assume that the problem is convex. The Lagrangian duality results from augmenting the objective function with a weighted sum of the constraint functions. The *Lagrangian* $L : \mathbb{R}^n \times \mathbb{R}^m \times \mathbb{R}^p \rightarrow \mathbb{R}$ associated with the problem (2.28) is defined as:

$$\mathcal{L}(\mathbf{x}, \boldsymbol{\lambda}, \boldsymbol{\nu}) = f_0(\mathbf{x}) + \sum_{i=1}^{m} \lambda_i f_i(\mathbf{x}) + \sum_{i=1}^{p} \nu_i h_i(\mathbf{x}), \tag{2.30}$$

with domain $\textbf{dom}\, \mathcal{L} = \mathcal{D} \times \mathbb{R}^m \times \mathbb{R}^p$. The variables λ_i account for *Lagrangian multipliers* associated with the i-th inequality constraint $f_i(\mathbf{x}) \leq 0$. In the same vein, ν_i denote Lagrange multipliers associated with the i-th equality constraint $h_i(\mathbf{x}) = 0$. The vectors $\boldsymbol{\lambda} = \{\lambda_i\}_{i=1}^{m}$ and $\boldsymbol{\nu} = \{\nu_i\}_{i=1}^{p}$ stand for the dual variables.

The Lagrangian dual function $g : \mathbb{R}^m \times \mathbb{R}^p \to \mathbb{R}$ can be defined as:

$$g(\boldsymbol{\lambda}, \boldsymbol{\nu}) = \inf_{\mathbf{x}} \mathcal{L}(\mathbf{x}, \boldsymbol{\lambda}, \boldsymbol{\nu}) = \inf_{\mathbf{x}} \left(f_0(\mathbf{x}) + \sum_{i=1}^{m} \lambda_i f_i(\mathbf{x}) + \sum_{i=1}^{p} \nu_i h_i(\mathbf{x}) \right). \tag{2.31}$$

When the Lagrangian (2.30) is not lower-bounded in $\mathbf{x}$, the Lagrange dual function equals $-\infty$. Note that the dual function is the pointwise infimum of a family of affine functions of $(\boldsymbol{\lambda}, \boldsymbol{\nu})$, and, hence, it is concave, even when the problem (2.28) is not convex.

An important property of the Lagrangian dual function is that yields a lower bound on the optimal value $\breve{p}$ of the problem (2.28). In other words, for any $\boldsymbol{\lambda} \succeq 0$ and any $\boldsymbol{\nu}$, we have that $g(\boldsymbol{\lambda}, \boldsymbol{\nu}) \leq \breve{p}$

The Lagrange dual problem

For each pair $(\boldsymbol{\lambda}, \boldsymbol{\nu})$ with $\boldsymbol{\lambda} \succeq 0$, we know that the Lagrange dual function gives us a lower bound on the optimal value $\breve{p}$. Therefore, the tightest lower-bound can be obtained by solving the so-called Lagrange dual problem, namely

$$\begin{aligned} &\max_{\boldsymbol{\lambda}, \boldsymbol{\nu}} \; g(\boldsymbol{\lambda}, \boldsymbol{\nu}) \\ &\text{s.t. } \boldsymbol{\lambda} \succeq 0. \end{aligned} \tag{2.32}$$

which, from (2.31) is a convex optimization problem.

The optimal dual variables are usually denoted by $(\breve{\boldsymbol{\lambda}}, \breve{\boldsymbol{\nu}})$ and the optimal value of the Lagrange dual problem (2.32) is denoted by $\breve{d}$, which turns out to be the tightest lower bound on $\breve{p}$. It is worth noting that the inequality $\breve{d} \leq \breve{p}$ also holds true for nonconvex problems. This property is well known as *weak duality*.

KKT optimality conditions for convex problems

The so-called Karush-Kuhn-Tucker (KKT) conditions [32] are sufficient for the points $\mathbf{x}, \boldsymbol{\lambda}, \boldsymbol{\nu}$ to be primal and dual optimal. In other words, any solution $(\mathbf{x}, \boldsymbol{\lambda}, \boldsymbol{\nu})$ satisfying the KKT conditions:

$$f_i(\breve{\mathbf{x}}) \leq 0, i = 1 \ldots m \tag{2.33}$$

$$h_i(\breve{\mathbf{x}}) = 0, i = 1 \ldots p \tag{2.34}$$

$$\breve{\lambda}_i \geq 0, i = 1 \ldots m \tag{2.35}$$

$$\breve{\lambda}_i f_i(\breve{\mathbf{x}}) = 0, i = 1 \ldots m \tag{2.36}$$

$$\nabla f_0(\breve{\mathbf{x}}) + \sum_{i=1}^{m} \breve{\lambda}_i \nabla f_i(\breve{\mathbf{x}}) + \sum_{i=1}^{p} \breve{\nu}_i \nabla h_i(\breve{\mathbf{x}}) = 0, \tag{2.37}$$

is known to be optimal. KKT conditions play a pivotal role in this PhD dissertation. They will be extensively used in Chapters 3 and 4, for various proofs.

Chapter 3

Collaborative Beamforming with Energy Harvesting and Battery Operated Sensors

In this chapter, we focus on the scenario where one energy harvesting and one battery operated sensor cooperatively transmit a common message to a distant base station. The goal is to find the *jointly* optimal transmission (power allocation) policy which maximizes the total throughput for a given deadline. First, we address the case in which the storage capacity of the energy harvesting sensor is assumed to be *infinite*. In this case, we identify the necessary conditions for such optimal transmission policy. Based on these conditions, we first show that the problem is convex. Then, we go one step beyond and prove that (i) the optimal power allocation for the energy harvesting sensor can be computed independently (i.e. without taking into account the policy at the battery operated sensor); and that (ii) it unequivocally determines (and allows to compute) that of the battery operated one. Finally, we generalize the analysis for the case were the energy harvesting sensor is assumed to have *finite* storage capacity. For both infinite and finite storage capacity cases, we prove the optimality of the proposed algorithm. Furthermore, we provide detailed analysis of algorithms complexity. Finally, we assess the performance by means of computer simulations, where a particular attention is paid to the impact of total energy harvested, finite storage capacity and long-term battery degradation on the achievable throughput.

3.1 Introduction

Although battery-operated sensor nodes can be deployed in remote or inaccessible areas, their limited energy storage capabilities severely constraint the wireless sensor network operation lifetime. In order to overcome this drawback, energy harvesting has been proposed as a viable solution. Namely, sensor nodes equipped with an energy harvesting device are able to extract the energy available in the surrounding (e.g., solar, thermal or vibrational energy), convert it into electrical energy and recharge the battery. However, since the ambient energy sources are usually unpredictable, it is very important to develop novel energy management and communication schemes, which particularly take into account the randomness and variability of the energy harvesting process.

Recently, the research community has shown a great interest on how to optimally allocate such harvested energy for efficient communication by wireless transmitters in various communication scenarios. Although from a completely different context (optimal rate control with QoS constraints), the approach to problem solving in [33] has extensively been used in analysis of different energy harvesting communication settings. In [17], a *single*-transmitter scenario with *infinite* energy storage capacity is considered. In order to facilitate analysis, the authors assume that the full knowledge on energy harvesting and data arrivals is available before the transmission starts. For the given setting, the authors derive the optimal power allocation policy such that the time needed to deliver all data packets to the destination is minimized, subject to constraints imposed by energy and data packet arrivals. They show that the optimal transmission policy has a so-called majorization structure, i.e. the power allocation is piece-wise constant non-decreasing function of time. Besides, it is shown that the battery must be empty at the time instants where the power changes.

In [18], the authors further generalize the scenario in [17], by considering an energy harvesting wireless transmitter with *finite* energy storage capacity. The authors show that the optimal transmission policy must be such that there is always enough available energy storage capacity to accommodate a new energy arrival (i.e., no energy is lost due to battery overflows). This finding, as a consequence, introduces a new set of *battery capacity constraints* that have to be fulfilled. In contrast to [17], the optimal policy is not non-decreasing anymore. Instead, the optimal transmission policy is such that the power is allowed to increase/decrease when the energy storage is empty/full at some energy harvesting time instant. Further generalizing the scenarios with *Gaussian* channels, considered in [17] and [18], Ozel *et al* address a setting where single node transmits data over a *Rayleigh-fading* channel and for the case in which the information on the harvested energy and channel gains is either causally or non-causally known [19].

Departing from single transmitter - single receiver scenario, other works in the literature address scenarios with *multiple* energy harvesting terminals. This includes studies for the multiple-access [26], interference [27], relay [24] and broadcast [28–30] channels.

Multi-antenna transceivers are proven to be very useful for wireless communication, especially because of improving the overall energy efficiency and decreasing the interference levels to unintended directions. However, using sensor nodes equipped with multiple antennas would increase the overall complexity and cost, which might not always be affordable in wireless sensor network contexts. In order to overcome individual node's complexity while still providing the benefits of antenna arrays, distributed beamforming techniques have been proposed as a viable solution. Namely, by employing these techniques, the set of nodes in a wireless sensor network emulate a virtual antenna array, this allowing them to reach a distant base station or data sink in a more energy efficient manner. Nevertheless, distributed nature of virtual antenna arrays renders the accurate frequency and phase synchronization, naturally assumed in centralized arrays, more involved. In order to cope with these challenges, different schemes have been proposed, such as iterative synchronization scheme with one-bit of feedback in [8, 9], or opportunistic sensor selection schemes [10].

3.1.1 Contribution

In this chapter, we consider a scenario where one energy harvesting and one battery operated transmitter cooperatively transmit a previously shared, *common message* to a distant base station. We assume that the sensors have their oscillators perfectly synchronized, this resulting in a coherent sum of received signals at the base station[1]. Besides, as in [17, 18], the information on harvested energy arrivals and amounts is assumed to be perfectly known in advance. In addition, the Gaussian model is adopted for the channel between each sensor and the BS. Our goal is to find the *jointly* optimal transmission (power allocation) policy at both the energy harvesting and battery operated sensors, such that the total data throughput for a given deadline is maximized. The problem of interest is similar to the one addressed in [17, 18], but here we consider a more general scenario with *multiple* transmitters. Besides, and unlike the Multiple-Access channel scenarios in [26], sensors here attempt to convey a *common* message to the destination. We also go one step beyond the distributed beamforming approaches in [8–10] where, implicitly, all sensors were assumed to be battery operated, and investigate the impact of *energy harvesting* constraints on performance.

As in [17], we initially assume that the energy harvesting sensor is equipped with an energy storage of *infinite* capacity. For this scenario, we identify the necessary conditions for the transmission policy to be jointly optimal. These conditions allow us to pose the problem in a convex optimization framework. Furthermore, we prove that the optimal policy for the EH node can be computed independently from that of the BO one by using the algorithm proposed

---

[1] This assumption will be justified in Chapter 5, where we provide a more detailed analysis of distributed carrier synchronization schemes.

in [17]. Subsequently, we show that the knowledge of the optimal policy at EH sensor allows us to compute the optimal policy at BO sensor by employing an iterative algorithm based on the KKT conditions. Next, we generalize the analysis for a scenario in which, as in [18], the storage capacity of the EH sensor is assumed to be *finite*. Surprisingly, this assumption only modifies the way of computing the optimal policy at the EH sensor (by using the algorithm proposed in [18]), whereas the optimal policy for the BO sensor can be computed with the same iterative algorithm proposed before. The system performance is evaluated in a scenario with solar energy harvesting. For the finite storage capacity case, we also consider imperfections in the re-chargeable battery of the EH sensor. More specifically, we focus on the impact of *long-term* capacity degradation, as opposed to the (short-time) battery leakage effects addressed in [22], and find the loss in throughput if the information on degraded battery capacity is not available.

The contents of this chapter have been partly published in references [34] and [35].

The chapter is organized as follows. First, in Section 3.2, we introduce the signal model. Next, in Section 3.3, we consider a scenario where battery capacity of EH sensor is assumed to be infinite. Then, in Section 3.4, we generalize the previous analysis to a scenario in which the energy storage capacity of EH sensor is finite. Subsequently, in Section 3.5 we analyze the computational complexity of proposed scheme. Finally, we conclude the chapter by summarizing the main findings in Section 3.6.

3.2 Signal model

Let us consider one energy harvesting and one battery operated sensor that cooperate to transmit a common message signal $m(t)$ to a distant base station, as shown in Figure 3.1. The received signal reads

$$r(t) = m(t)\left(\sum_{i=1}^{2} g_i^*(t)e^{j\psi_i(t)}\right) + w(t) \tag{3.1}$$

where the common message is given by $m(t) = \sum_l x_l u(t - lT_s)$, with $\{x_l\}$ standing for a sequence of zero-mean complex Gaussian symbols with unit variance (T_s is the symbol period) and $u(t)$ denoting the impulse response of a bandlimited pulse (unit bandwidth); $g_i(t) = \sqrt{p_i(t)}e^{-j\theta_i(t)}$ accounts for the time-varying complex transmit weights in polar notation (to be designed); $e^{j\psi_i(t)}$ stands for the phase shift of the (Gaussian) sensor-to-base station channels; and $w(t)$ is zero-mean complex additive white Gaussian noise with unit variance (i.e. $w(t) \sim \mathcal{CN}(0,1)$). In the sequel, we assume that by properly designing $\theta_i(t)$ the channel phase and, where relevant, oscillator offsets can be ideally pre-compensated (for details on actual implementation, see Chapter 5). Frequency and time synchronization is assumed, as well. Hence, the sensor network behaves as a virtual antenna array capable of *beamforming*

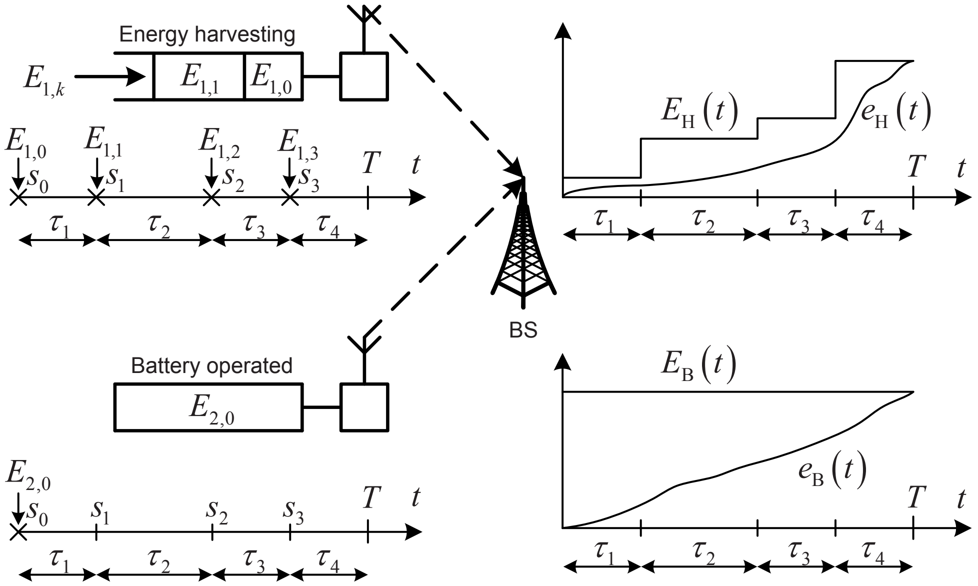

Figure 3.1: Network with energy harvesting and battery operated sensors (left); cumulative energy harvesting constraints and energy consumption curves (right).

the message to the base station. Without loss of generality, we let the first sensor be the one with energy harvesting capabilities, and the second one to be battery operated. Consequently, we hereinafter denote by $p_{\mathrm{H}}(t) \triangleq p_1(t)$ and $p_{\mathrm{B}}(t) \triangleq p_2(t)$ the instantaneous transmit power at the energy *harvesting* and *battery* operated sensors, respectively. Bearing all this in mind, the instantaneous received power at the base station is given by $p_{\mathrm{BF}}(t) = (\sqrt{p_{\mathrm{H}}(t)} + \sqrt{p_{\mathrm{B}}(t)})^2$. The total throughput for a given deadline T then reads

$$G_T\big(p_{\mathrm{H}}(t), p_{\mathrm{B}}(t)\big) = \int_0^T \log\big(1 + p_{\mathrm{BF}}(t)\big)\,dt. \tag{3.2}$$

Our goal is to find the *jointly* optimal transmission (power allocation) policies $p_{\mathrm{H}}(t)$ and $p_{\mathrm{B}}(t)$ such that G_T is maximized subject to the causality constraints imposed by the energy harvesting process, namely[2],

$$e_{\mathrm{H}}(t) \leq E_{\mathrm{H}}(t) \triangleq \sum_{k:s_k<t} E_{1,k} \tag{3.3}$$

$$e_{\mathrm{B}}(t) \leq E_{\mathrm{B}}(t) \triangleq E_{2,0}, \tag{3.4}$$

for $0 \leq t \leq T$, where $e_{\mathrm{H}}(t) = \int_0^t p_{\mathrm{H}}(\tau)d\tau$ and $e_{\mathrm{B}}(t) = \int_0^t p_{\mathrm{B}}(\tau)d\tau$ denote the energy *consumption* (EC) curves; and $E_{\mathrm{H}}(t)$, $E_{\mathrm{B}}(t)$ stand for the cumulative energy *harvesting* (cEH) constraints (see Figure 3.1, right). In the above expression, $E_{i,k}$ accounts for the amount of energy harvested[3] by sensor i in the k^{th} event ($k = 0 \ldots N-1$). We define *event* s_k as the time instant in which some energy is harvested by *any* of the sensors in the network ($E_{i,k} = 0$ for the sensor

---

[2] For scenarios where the storage capacity of the EH sensor is finite, additional constraints must be introduced (see Section 3.4).

[3] Discrete energy arrival process will be justified in Section 3.3.3.

not harvesting any energy in that event). Both the events and the amounts of energy harvested $E_{i,k}$ are assumed to be known a priori. Further, we impose $E_{i,0} > 0$ for all i (sensors) so that collaborative transmission can start immediately, that is, from $t = 0$. For battery operated sensors, we have $E_{i,k} = 0$ for $k > 0$ and, thus, the cumulative energy harvesting function is constant for the whole period. For the EH sensor, on the contrary, it is given by a staircase function, as shown in Figure 3.1, right. Finally, we define k^{th} *epoch* as the time elapsed between two consecutive events s_{k-1} and s_k. Its duration is given by $\tau_k \triangleq s_k - s_{k-1}$ for $k = 1 \dots N-1$ and, likewise, we define $\tau_N \triangleq T - s_{N-1}$. A given transmission policy is said to be *feasible* (yet, perhaps, not optimal) if, as imposed by (3.3) and (3.4), the energy consumption curves lie below cumulative energy harvesting ones at all times (or occasionally hit them).

3.3 Infinite battery capacity

In this section, we consider a scenario where the energy storage capacity of EH sensor is infinite. This, in turn, means that the transmission policy at the EH sensor is only constrained by the energy availability due to energy harvesting process. In the following lemmas, we give the necessary conditions for a transmission policy to be optimal. Furthermore, the insights gained into the problem structure allow us to compute the jointly optimal policies in a computationally efficient manner. Unless otherwise stated, the lemmas hold for *both* the energy harvesting and battery operated sensor nodes.

3.3.1 Necessary conditions for the optimality of the transmission policy

Lemma 3.1 *The transmit power in each sensor remains constant between consecutive events.*

In other words, the power/rate in *each* sensor only potentially changes when new energy arrives to *any* of them [4]. The proof of this lemma, which is based on Jensen's and Cauchy's inequalities, can be found in Appendix 3.A.1. This lemma implies that $p_{\mathrm{H}}(t) = p_{\mathrm{H},k}$, $p_{\mathrm{B}}(t) = p_{\mathrm{B},k}$ for $s_{k-1} \leq t < s_k$. That is, the power allocation curves $p_{\mathrm{H}}(t)$ and $p_{\mathrm{B}}(t)$ are necessarily staircase functions and, hence, the energy consumption curves $e_{\mathrm{H}}(t)$ and $e_{\mathrm{B}}(t)$ are piecewise linear. This observation allows us to pose the original problem (3.2)-(3.4) in a tractable convex optimization framework in which a numerical (or analytical) solution is easier to find. This will be accomplished in Section 3.3.2.

Lemma 3.2 *All the harvested/stored energy must be consumed by the given deadline T.*

---

[4] In our scenario, only one sensor harvests energy. Still, this lemma holds for a more general case with multiple energy harvesters.

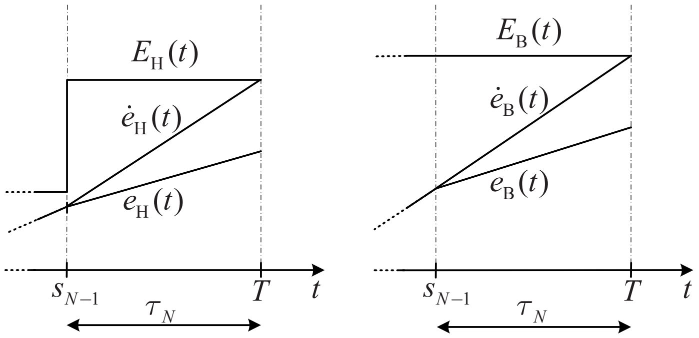

Figure 3.2: All available energy must be consumed by the deadline, (Lemma 3.2).

This means that, necessarily, the energy consumption curves reach the cumulative energy harvesting constraints at time instant T.

Proof: Lemma 3.2 can be easily proved by contradiction. Assume that the optimal transmission policy $p_{\mathrm{H}}(t)$, $p_{\mathrm{B}}(t)$ does not fulfill such condition. We could think of a different *feasible* policy $\dot{p}_{\mathrm{H}}(t)$, $\dot{p}_{\mathrm{B}}(t)$ (see Figure 3.2) such that (i) the set of curves $\dot{e}_{\mathrm{H}}(t)$ and $\dot{e}_{\mathrm{B}}(t)$ differ from the *optimal* ones in the last epoch only, namely, for $t \in [s_{N-1} \dots T)$; and (ii) it verifies $\dot{e}_{\mathrm{H}}(T) = E_{\mathrm{H}}(T)$ and $\dot{e}_{\mathrm{B}}(T) = E_{\mathrm{B}}(T)$. Being piecewise linear (and continuous), these curves would necessarily lie *above* the optimal ones during the last epoch, this resulting in a higher received power and throughput. This contradicts the optimality of the original transmission policy. ∎

Lemma 3.3 *If feasible, a transmission policy with constant transmit power in each sensor between any two (i.e. not necessarily consecutive) events turns out to be optimal for the period of time elapsed between these two events.*

This lemma goes one step beyond and states that Lemma 3.1 also holds for *non-consecutive* events, as long as a constant transmit power policy in *both* sensors is feasible[5] for this period. This follows directly from the proof of Lemma 3.1 but, since one or more energy harvests might take place in between the initial and final events, feasibility needs to be ensured (clearly, this is not needed in Lemma 3.1).

3.3.2 Computation of the optimal transmission policy

Lemma 3.1 allows us to re-write the original optimization problem given by the score function (3.2) and the causality constraints (3.3) and (3.4) as follows (to recall, our focus here is on

---

[5] In our setting, this can only be constrained by the cEH curve of the EH sensor.

scenarios where the storage capacity of the EH sensor is *infinite*):

$$\max_{\{p_{\mathrm{H},k}\}_{k=1}^{N},\{p_{\mathrm{B},k}\}_{k=1}^{N}} \sum_{k=1}^{N} \tau_k \log\left(1+(\sqrt{p_{\mathrm{H},k}}+\sqrt{p_{\mathrm{B},k}})^2\right) \tag{3.5}$$

s.t.:

$$\sum_{k=1}^{n} \tau_k p_{\mathrm{H},k} \le E_{\mathrm{H}}^{n} = \sum_{k=0}^{n-1} E_{1,k} \ \text{ for } n = 1\dots N \tag{3.6}$$

$$\sum_{k=1}^{n} \tau_k p_{\mathrm{B},k} \le E_{\mathrm{B}}^{n} = E_{2,0} \ \text{ for } n = 1\dots N \tag{3.7}$$

$$p_{\mathrm{H},k} \ge 0 \ \text{ for } k = 1\dots N \tag{3.8}$$

$$p_{\mathrm{B},k} \ge 0 \ \text{ for } k = 1\dots N \tag{3.9}$$

where we have defined $E_{\mathrm{H}}^{n} \triangleq E_{\mathrm{H}}(t)$ and $E_{\mathrm{B}}^{n} \triangleq E_{\mathrm{B}}(t)$ for $t \in [s_{n-1}, s_n)$. The problem is convex since all the constraints are affine and linear, and the objective function is concave (composition of concave nondecreasing and concave function, [32, Section 3.2.4]). Furthermore, it can be proven that the utility function is indeed strictly concave (see Appendix 3.A.2). Since the optimization problem is strictly convex, its *unique* solution can at least be found numerically (e.g. by resorting to interior point methods). However, this task is computationally intensive, in particular when the number of energy harvesting events N is large. This motivates the following analysis from which a semi-analytical and less computationally intensive solution to the optimization problem can be obtained.

The Lagrangian of the optimization problem (3.5)-(3.9) is given by

$$\begin{aligned}
\mathcal{L}_1 = &-\sum_{k=1}^{N} \tau_k \log\left(1+(\sqrt{p_{\mathrm{H},k}}+\sqrt{p_{\mathrm{B},k}})^2\right) \\
&+\sum_{n=1}^{N} \lambda_n \left(\sum_{k=1}^{n} \tau_k p_{\mathrm{H},k} - E_{\mathrm{H}}^{n}\right) + \sum_{n=1}^{N} \nu_n \left(\sum_{k=1}^{n} \tau_k p_{\mathrm{B},k} - E_{\mathrm{B}}^{n}\right) \\
&-\sum_{k=1}^{N} \mu_k p_{\mathrm{H},k} - \sum_{k=1}^{N} \xi_k p_{\mathrm{B},k}
\end{aligned} \tag{3.10}$$

and, hence, the corresponding Karush-Kuhn-Tucker conditions read

$$\frac{\partial \mathcal{L}_1}{\partial \breve{p}_{\mathrm{H},k}}, \frac{\partial \mathcal{L}_1}{\partial \breve{p}_{\mathrm{B},k}} = 0 \tag{3.11}$$

$$\sum_{k=1}^{n} \tau_k \breve{p}_{\mathrm{H},k} \le E_{\mathrm{H}}^{n} \text{ for } n = 1\dots N \tag{3.12}$$

$$\sum_{k=1}^{n} \tau_k \breve{p}_{\mathrm{B},k} \le E_{\mathrm{B}}^{n} \text{ for } n = 1\dots N \tag{3.13}$$

$$\breve{p}_{\mathrm{H},k}, \breve{p}_{\mathrm{B},k} \geq 0 \tag{3.14}$$

$$\breve{\lambda}_n, \breve{\nu}_n, \breve{\mu}_k, \breve{\xi}_k \geq 0 \tag{3.15}$$

$$\breve{\lambda}_n \left(\sum_{k=1}^{n} \tau_k \breve{p}_{\mathrm{H},k} - E_{\mathrm{H}}^n \right) = 0 \text{ for } n = 1 \ldots N \tag{3.16}$$

$$\breve{\nu}_n \left(\sum_{k=1}^{n} \tau_k \breve{p}_{\mathrm{B},k} - E_{\mathrm{B}}^n \right) = 0 \text{ for } n = 1 \ldots N \tag{3.17}$$

$$-\breve{\mu}_k \breve{p}_{\mathrm{H},k} = 0 \text{ for } k = 1 \ldots N \tag{3.18}$$

$$-\breve{\xi}_k \breve{p}_{\mathrm{B},k} = 0 \text{ for } k = 1 \ldots N. \tag{3.19}$$

where the partial derivatives in (3.11) can be expressed as

$$\frac{\partial \mathcal{L}_1}{\partial \breve{p}_{\mathrm{H},k}} = -\tau_k \frac{\sqrt{\breve{p}_{\mathrm{H},k}} + \sqrt{\breve{p}_{\mathrm{B},k}}}{\sqrt{\breve{p}_{\mathrm{H},k}} \left(1 + (\sqrt{\breve{p}_{\mathrm{H},k}} + \sqrt{\breve{p}_{\mathrm{B},k}})^2\right)} + \tau_k \sum_{n=k}^{N} \breve{\lambda}_n - \breve{\mu}_k \tag{3.20}$$

$$\frac{\partial \mathcal{L}_1}{\partial \breve{p}_{\mathrm{B},k}} = -\tau_k \frac{\sqrt{\breve{p}_{\mathrm{H},k}} + \sqrt{\breve{p}_{\mathrm{B},k}}}{\sqrt{\breve{p}_{\mathrm{B},k}} \left(1 + (\sqrt{\breve{p}_{\mathrm{H},k}} + \sqrt{\breve{p}_{\mathrm{B},k}})^2\right)} + \tau_k \sum_{n=k}^{N} \breve{\nu}_n - \breve{\xi}_k \tag{3.21}$$

By considering (3.11) and by introducing the change of variables $\breve{A}_k = \sum_{n=k}^{N} \breve{\lambda}_n - \frac{\breve{\mu}_k}{\tau_k}$ and $\breve{B}_k = \sum_{n=k}^{N} \breve{\nu}_n - \frac{\breve{\xi}_k}{\tau_k}$, equations (3.20) and (3.21) can be rewritten as follows:

$$-\frac{\sqrt{\breve{p}_{\mathrm{H},k}} + \sqrt{\breve{p}_{\mathrm{B},k}}}{\sqrt{\breve{p}_{\mathrm{H},k}} \left(1 + (\sqrt{\breve{p}_{\mathrm{H},k}} + \sqrt{\breve{p}_{\mathrm{B},k}})^2\right)} + \breve{A}_k = 0 \tag{3.22}$$

$$-\frac{\sqrt{\breve{p}_{\mathrm{H},k}} + \sqrt{\breve{p}_{\mathrm{B},k}}}{\sqrt{\breve{p}_{\mathrm{B},k}} \left(1 + (\sqrt{\breve{p}_{\mathrm{H},k}} + \sqrt{\breve{p}_{\mathrm{B},k}})^2\right)} + \breve{B}_k = 0 \tag{3.23}$$

From [32, Section 5.5.3], we know that for *any* optimization problem with differentiable objective and constraint functions for which strong duality holds[6], any pair of primal and dual optimal points *must* satisfy the KKT conditions. This is very important property, since it allows us to identify various optimality conditions which, in turn, help us to compute the optimal solution more efficiently.

Lemma 3.4 *Transmit powers are strictly positive.*

Proof: Again, this can be proved by contradiction. Assume that the power allocation policy before s_{k-1} and after s_{k+1} is optimal. Assume that, as shown in Figure 3.3, the optimal policy for the $[s_{k-1}, s_{k+1})$ period verifies $p_{\mathrm{H},k} = 0$ and $p_{\mathrm{H},k+1} > 0$. One could think of a new (and feasible) transmission policy given by $\dot{p}_{\mathrm{H},k} = \frac{\Delta e_{\mathrm{H}}}{\dot{s}_k - s_{k-1}}$ and $\dot{p}_{\mathrm{B},k} = \frac{\Delta e_{\mathrm{B}}}{\dot{s}_k - s_{k-1}}$ for $t \in [s_{k-1}, \dot{s}_k)$; and $\dot{p}_{\mathrm{H},k+1} = p_{\mathrm{H},k+1}$ along with $\dot{p}_{\mathrm{B},k+1} = p_{\mathrm{B},k+1}$ for $t \in [\dot{s}_k, s_{k+1})$. From the proof[7] of Lemma

---

[6] For convex optimization problem given by (3.5)-(3.9), the strong duality reduces to feasibility, since all the constraints are linear, [32, Section 5.2.3].

[7] Although Lemma 3.1 holds for EH *events*, its *proof* has a broader scope and encompasses *any* time instant, such as s'_k. See Appendix 3.A.1.

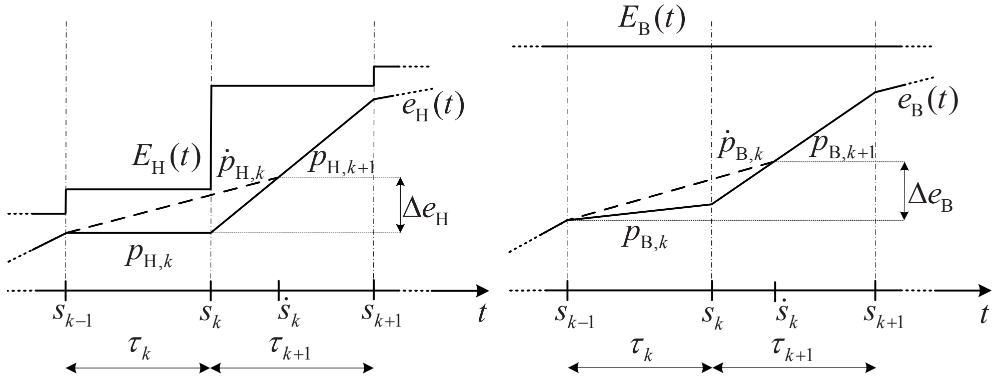

Figure 3.3: Transmit powers are strictly positive (Lemma 3.4).

3.1, we know that the new policy achieves higher throughput than the original one in $[s_{k-1}, \dot{s}_k)$ and, thus, in $[s_{k-1}, s_{k+1})$ too. Yet not optimal (since this new policy e.g. contradicts Lemma 3.1), this proves that the original policy given by $p_{\mathrm{H},k} = 0$ and $p_{\mathrm{H},k+1} > 0$ was not optimal either.

Next, in order to prove that the optimal powers at the BO sensor are strictly positive as well, we employ the KKT conditions associated with the problem (3.5)-(3.9). Namely, from (3.22) and (3.23), and by taking the first term in both sums, it can be shown that these terms are strictly negative. This, in turn, means that, in order for both (3.22) and (3.23) to vanish, the corresponding variables $\breve{A}_k$ and $\breve{B}_k$ must be strictly positive, i.e. $\breve{A}_k, \breve{B}_k > 0$. Next, by combining equations (3.22) and (3.23), we get the following relation between the optimal primal and dual variables:

$$\breve{p}_{\mathrm{B},k} = \left(\frac{\breve{A}_k}{\breve{B}_k}\right)^2 \breve{p}_{\mathrm{H},k} \tag{3.24}$$

By further replacing (3.24) into (3.22) and (3.23), and solving them for $\breve{p}_{\mathrm{H},k}$, $\breve{p}_{\mathrm{B},k}$, we get

$$\breve{p}_{\mathrm{H},k} = \frac{\breve{B}_k(\breve{A}_k + \breve{B}_k - \breve{A}_k\breve{B}_k)}{\breve{A}_k(\breve{A}_k + \breve{B}_k)^2} \tag{3.25}$$

$$\breve{p}_{\mathrm{B},k} = \frac{\breve{A}_k(\breve{A}_k + \breve{B}_k - \breve{A}_k\breve{B}_k)}{\breve{B}_k(\breve{A}_k + \breve{B}_k)^2}. \tag{3.26}$$

From the first part of this proof, we know that the optimal powers at the EH sensor node must be strictly positive, i.e. $\breve{p}_{\mathrm{H},k} > 0$. From this, the fact that $\breve{A}_k, \breve{B}_k > 0$, along with equation (3.24), we conclude that the corresponding power at BO sensor must be strictly positive, as well. This concludes our proof. ■

Lemma 3.5 *The transmit powers for an energy harvesting sensor with infinite storage capacity are monotonically increasing, i.e.* $p_{\mathrm{H},1} \leq p_{\mathrm{H},2} \leq \ldots \leq p_{\mathrm{H},N}$

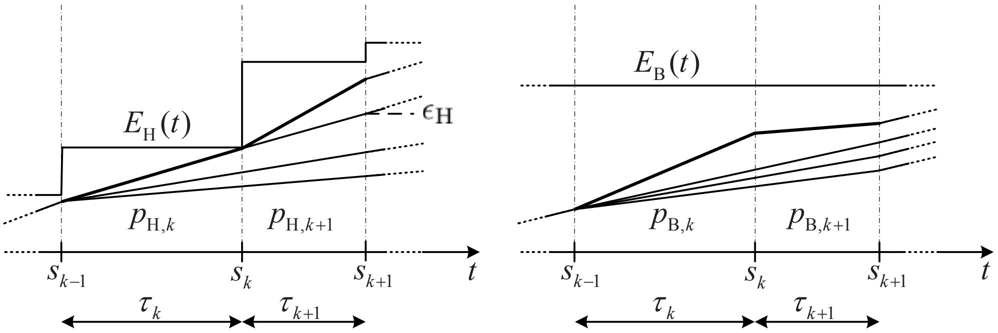

Figure 3.4: Transmit powers at the EH sensor are monotonically increasing (Lemma 3.5).

Proof: This property follows from the fact that $E_H(t)$ is a staircase function. Assume that the power allocation policy before s_{k-1} and after s_{k+1} is optimal. As shown in Figure 3.4, the optimal EC curve verifies $e_H(s_{k+1}) \in (e_H(s_{k-1}), E_H(s_{k+1})]$. For $e_H(s_{k+1}) \in (e_H(s_{k-1}), \epsilon_H]$, we know from Lemma 3.3 that a constant power allocation for the energy harvesting *and* battery operated sensors turns out to be optimal for $[s_{k-1}, s_{k+1})$ (and, hence, for $[0, T]$). In particular, this implies that $p_{H,k+1} = p_{H,k}$. For $e_H(s_{k+1}) \in (\epsilon_H, E_H(s_{k+1})]$, on the contrary, the fact that $e_H(t)$ is continuous and piecewise linear can only be ensured if (and only if) $p_{H,k+1} > p_{H,k}$. By repeatedly applying this reasoning to all consecutive epoch pairs the proof follows. As for the relationship between $p_{B,k+1}$ and $p_{B,k}$, nothing can be said yet. Still, the fact that $E_B(t)$ is a *constant* function does not impose any additional restrictions to the power allocation policy of the BO sensor in $[s_{k-1}, s_{k+1}]$. ■

Lemma 3.6 *The jointly optimal power allocation policy is such that, whenever the transmit power changes, the energy consumed by the energy harvesting sensor up to that time instant, equals the energy harvested by such sensor up to that instant (i.e, the stored energy is zero).*

The proof of this Lemma is based on the Karush-Kuhn-Tucker (KKT) conditions associated with the (joint) optimization problem (3.5)-(3.9). Details can be found in Appendix 3.A.4.

The next theorems state the main result of this paper since they allow to effectively compute the optimal transmissions policies for the EH and BO sensors, respectively.

Theorem 3.1 *The optimal transmission policy for the energy harvesting sensor, $\{\breve{p}_{H,k}\}_{k=1}^{N}$, can be computed independently from that of the battery operated one. The associated energy consumption curve turns out to be the shortest string starting in $t = 0$, ending in $t = T$, and lying below the cumulative energy harvesting curve.*

Proof: As we will prove next, Lemmas 3.1 to 3.6 unequivocally determine the optimal transmission policy for the EH sensor. First note that, in order to satisfy the energy causality constraint, the corresponding EC curve must lie below the cEH curve. From Lemma 3.2, it follows

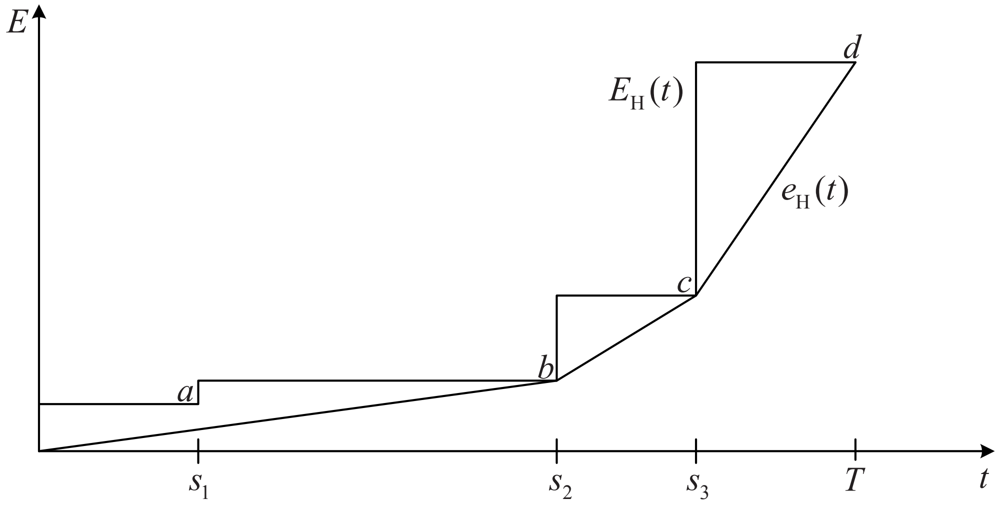

Figure 3.5: The optimal energy consumption curve for the EH sensor is given by the shortest string below the cumulative EH curve (Theorem 3.1).

that the EC curve reaches the cEH curve at $t = T$. Besides, from Lemmas 3.1 and 3.3, we know that the transmit power only potentially changes at the energy harvesting events. Consequently, the optimal EC curve must be linear between them (i.e. piecewise linear). Moreover, Lemma 3.6 dictates that, whenever the transmit power (slope) changes at an energy harvesting event, the EC curve hits the cEH curve. Based on these facts, we conclude that the first linear part of EC curve must connect the origin with some corner point on the cEH curve (see Fig 3.5). Because of Lemma 3.5, we must choose the one with the minimal slope, since otherwise the constraint on energy causality (point c) or monotonicity property of Lemma 3.5 (point a) would not be satisfied. Clearly, in Fig 3.5 this corresponds to point b. Once this point is identified, the algorithm can be iteratively applied until we find the optimal policy until deadline T. As a result, the EC curve is given by the shortest string below the cEH curve. It must be noted that this algorithm is equivalent to the one presented in [17]. However, the interesting points are that (i) we have proved that it continues to be optimal in a scenario where *two* sensors, one of them battery operated, collaborate to send the message (vs. one sensor in [17]); and that (ii) no information on the BO sensor (i.e. its optimal EC curve) is needed to determine it. ■

Theorem 3.2 *Upon finding the optimal transmission policy for the energy harvesting sensor, the optimal transmission policy for the battery operated one,* $\{\breve{p}_{B,k}\}_{k=1}^{N}$, *can be computed with the iterative procedure given by Algorithm 1.*

Proof: This algorithm stems from (3.22), (3.23), and the proof of Lemma 3.6 in Appendix 3.A.4 (see *Remark*). The real-valued variable B_k (or its counterpart for iteration m, namely, $B_k^{(m)}$) is a linear function of the Lagrange multipliers associated with the constraint (3.7). Therefore, the equation in Step 8 provides a connection between the primal and dual solutions of the problem. Since $\breve{p}_{H,k}$ is already known from Theorem 3.1, for each value of $B_k^{(m)}$

Algorithm 1 Optimal policy for the battery operated sensor

```
1: choose some small $\delta > 0$                                  ▷ Step for searching
2: $m \leftarrow 0$                                                ▷ Iteration index
3: $E_{\mathrm{B}}(T) \leftarrow E_{2,0}$                          ▷ Energy stored in the battery
4: repeat
5:     $m \leftarrow m + 1$
6:     for all $k = 1 \ldots N$ do
7:         $B_k^{(m)} \leftarrow m\delta$,
8:         solve $-\frac{\sqrt{\breve{p}_{\mathrm{H},k}}+\sqrt{\breve{p}_{\mathrm{B},k}^{(m)}}}{\sqrt{\breve{p}_{\mathrm{B},k}^{(m)}}\left(1+(\sqrt{\breve{p}_{\mathrm{H},k}}+\sqrt{\breve{p}_{\mathrm{B},k}^{(m)}})^2\right)} + B_k^{(m)} = 0$ for $p_{\mathrm{B},k}^{(m)}$
9:     end for
10:    $E_{\mathrm{B},T}^{(m)} \leftarrow \sum_k \tau_k p_{\mathrm{B},k}^{(m)}$
11: until $E_{\mathrm{B},T}^{(m)} = E_{\mathrm{B}}(T)$
12: $\breve{p}_{\mathrm{B},k} \leftarrow p_{\mathrm{B},k}^{(m)} \; \forall k$
```

to be tested (from Appendix 3.A.4 we know that all the B_ks are identical and equal to the largest Lagrange multiplier associated with (3.7), which is enforced in Step 7), the associated $\breve{p}_{\mathrm{B},k}^{(m)}$ can be found by solving the corresponding third order equation (a single real-valued root exists, as it is shown in Appendix 3.A.3). If the total energy consumed until time instant T by the battery operated sensor, computed in Step 10, equals the energy (initially) stored in it, $E_{\mathrm{B}}(T)$, the iterative algorithm stops. The stopping condition not only ensures that Lemma 3.2 is fulfilled but also, it implies that the *whole* transmission policy for the battery operated sensor $\{\breve{p}_{\mathrm{B},k}\}_{k=1}^{N}$ is feasible. In summary, we have found the optimal transmission policy for the BO sensor by (i) conducting a grid search over one variable of the dual solution; and (ii) checking in each iteration whether the unknown part of the primal solution resulting from the algorithm is feasible. Clearly, the choice of δ leads to a number of trade-offs in terms of accuracy and number of iterations needed. ■

As for algorithmic convergence, one can easily prove that each element in the set of transmit powers $\{p_{\mathrm{B},k}\}_{k=1}^{N}$ is a *monotonically decreasing* function in ν_N (the only non-zero element in the dual solution). Namely, by considering (3.23), and taking the derivative of the first term with respect to $p_{\mathrm{B},k}$, i.e.

$$\frac{\partial\left(-\frac{\sqrt{\breve{p}_{\mathrm{H},k}}+\sqrt{\breve{p}_{\mathrm{B},k}}}{\sqrt{\breve{p}_{\mathrm{B},k}}\left(1+(\sqrt{\breve{p}_{\mathrm{H},k}}+\sqrt{\breve{p}_{\mathrm{B},k}})^2\right)}\right)}{\partial\breve{p}_{\mathrm{B},k}} = \frac{2\breve{p}_{\mathrm{B},k}^{3/2} + 5\breve{p}_{\mathrm{B},k}\sqrt{\breve{p}_{\mathrm{H},k}} + 4\breve{p}_{\mathrm{H},k}\sqrt{\breve{p}_{\mathrm{B},k}} + \sqrt{\breve{p}_{\mathrm{H},k}} + \breve{p}_{\mathrm{H},k}^{3/2}}{\breve{p}_{\mathrm{B},k}^{3/2}(1+\breve{p}_{\mathrm{B},k}+2\sqrt{\breve{p}_{\mathrm{B},k}\breve{p}_{\mathrm{H},k}}+\breve{p}_{\mathrm{H},k})^2} \tag{3.27}$$

we conclude that the first term of the sum in (3.23) increases as $p_{\mathrm{B},k}$ increases (still it is always negative). This, in turn means that $\nu_N = B_k$ must be lower, in order to keep (3.23) equal to zero. In other words, as the power $p_{\mathrm{B},k}$ increases, the corresponding sum of Lagrangians B_k decreases, and viceversa. Likewise, $E_{\mathrm{B},T}^{(m)}$ is a monotonically decreasing function in ν_N as

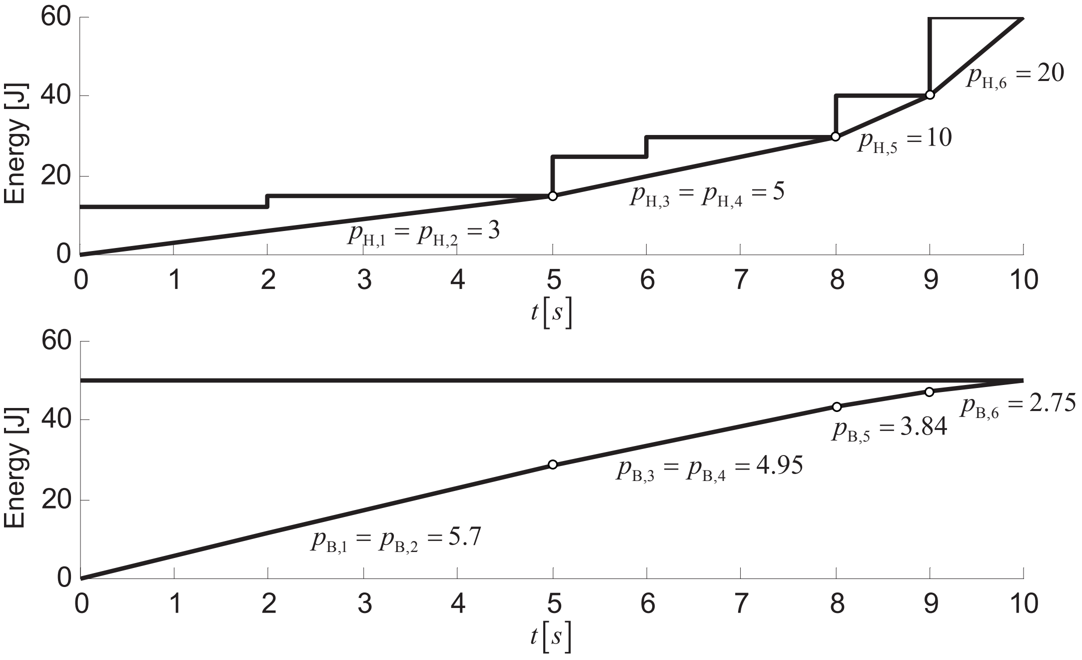

Figure 3.6: Optimal power allocation: EH and BO sensors ($T = 10s$, $E_{2,0} = 50$J).

well. In other words, there exists a *one-to-one mapping* function between the primal and dual solutions. This turns out to be a sufficient condition for the algorithm to converge, as long as a *sufficiently* small step size δ is used for the grid search over some range of ν_N values. Finally, Figure 3.6 depicts the optimal transmission policies corresponding to the EH and BO sensors for a specific realization of the energy arrivals. Clearly, (i) it satisfies all the lemmas and theorems; (ii) Lemma 3.5 on the monotonicity of the optimal power allocation does not hold for the BO sensor; and (iii) in order to collaboratively transmit data, the BO sensor must adopt an optimal transmission policy which is different from that of the single-sensor scenario, that is, constant transmit power within $[0 \dots T]$.

3.3.3 Simulations and numerical results

In this section, we assess the performance of the proposed power allocation algorithm in a scenario where solar energy is harvested from the environment. The energy storage system in the EH sensor comprises (i) a supercapacitor [16]; and (ii) a re-chargeable Lithium-Ion battery (see Figure 3.7). Upon being harvested, the energy is temporarily stored in the supercapacitor. When it is fully charged, the energy is transferred to the battery in a burst[8]. Clearly, this validates the event-based model of the energy harvesting process presented in Section 3.2. For such devices, the amount of energy harvested in each event is constant and it equals the

---

[8] Pulse charging is beneficial for Lithium-Ion batteries in terms of improved discharge capacity and longer life cycles [36].

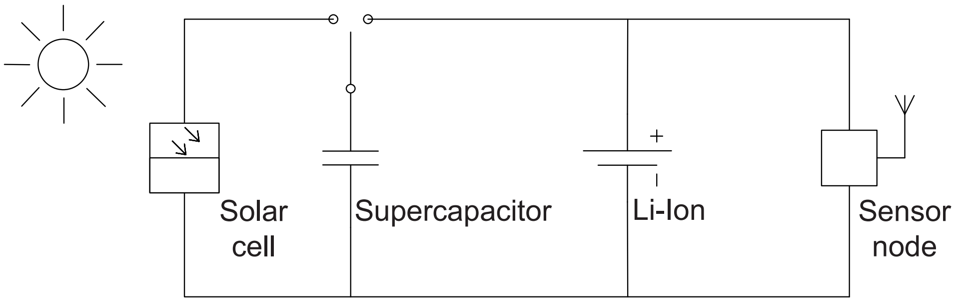

Figure 3.7: Hybrid energy storage with supercapacitor and battery.

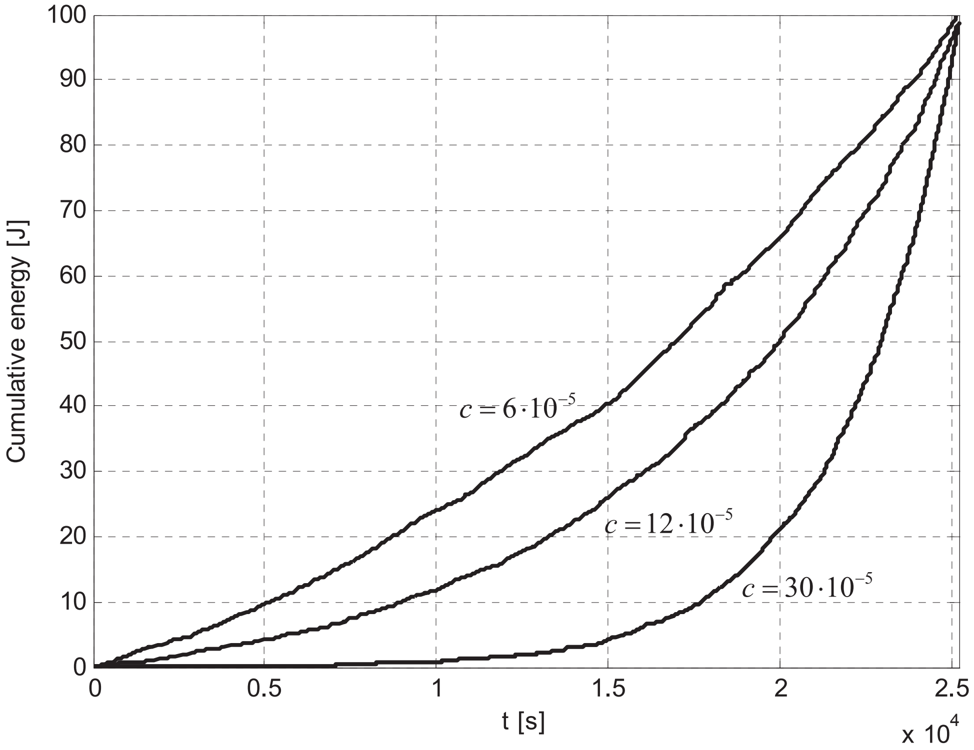

Figure 3.8: Typical cumulative energy curves parameterized by c.

maximum energy that can be stored in the supercapacitor. Since solar irradiation levels change over time (e.g. from dawn to noon, from winter to summer), so does the *average* number of energy arrivals (events). Consequently, the stochastic process that models energy arrivals is non-stationary. In the sequel, we adopt a Poisson process with time-varying mean given by $\lambda_E(t)$. From the solar irradiation data in [37], the mean arrival rate from 5 A.M. to 12 P.M. (i.e. dawn to noon, with $T = 7$ h) can be fitted by the following exponential function:

$$\lambda_E(t) = \beta_{E,c,T} e^{ct} \tag{3.28}$$

where parameter c models the variability of the energy harvested over time (i.e. the rate of energy transfers from the capacitor to the battery); and $\beta_{E,c,T}$ is a constant depending on the total amount of energy harvested E, parameter c, and the total harvesting time T. For the solar irradiation data in [37], it yields $\beta_{E,c,T} = 3.899 \cdot 10^{-2}$ and $c = 6 \cdot 10^{-5}$. Figure 3.8

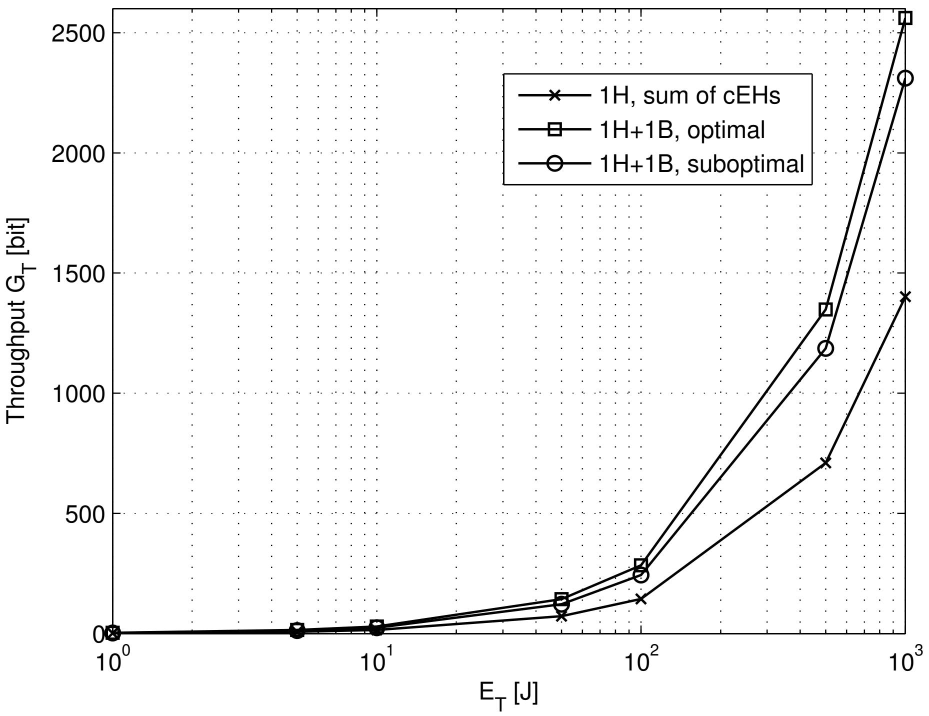

Figure 3.9: Throughput vs. total energy in the system ($c = 30 \cdot 10^{-5}$, $R_E = 1$).

shows a number of cumulative energy harvesting curves for different values of parameter c: the higher c, the higher the energy variability, i.e. the steeper the curves by the end of the observation interval. Hereinafter, we let $E_T^{\mathrm{H}} = \sum_{k=0}^{N-1} E_{1,k}$ and $E_T^{\mathrm{B}} = E_{2,0}$ denote the total energy harvested by/stored in the EH and BO sensors, respectively; whereas $E_T = E_T^{\mathrm{H}} + E_T^{\mathrm{B}}$ accounts for the total energy in the system. Further, we define $R_E = E_T^{\mathrm{B}}/E_T^{\mathrm{H}}$ as the ratio between the total energy in the BO and EH sensors, that is, for large R_E, the battery operated sensor dominates. In all plots, we have $T = 7$ h (from 5 A.M. to noon). Initially, we assume that the storage capacity of the aforementioned Lithium-ion battery is infinite. In Figure 3.9, we depict the throughput of the virtual array with the jointly optimal transmission policies defined by Theorem 3.1 and Theorem 3.2 for the EH and BO sensors, respectively. The amount of energy harvested by/stored in the EH and BO sensors is identical ($R_E = 1$) and results are shown as a function of the total energy E_T in the system. As benchmarks, we consider (i) a system with only one EH sensor, the cEH curve of which is given by the point-wise sum of the cEH curves for the EH and BO sensors in the virtual array (curve labeled with "1H, sum of cEHs"); and (ii) a two-sensor virtual array in which the transmission policies for the EH and BO sensors are optimized individually for each sensor as in [17], which is suboptimal for a virtual array ("1H+1B, suboptimal"). For (ii), the optimal policy for the BO sensor consists in a constant transmit power for $t = 0 \ldots T$. Unsurprisingly, for systems with multiple transmitters the beamforming gain translates into substantially higher throughputs. Besides, some additional throughput gain results from the *joint* optimization of the transmission

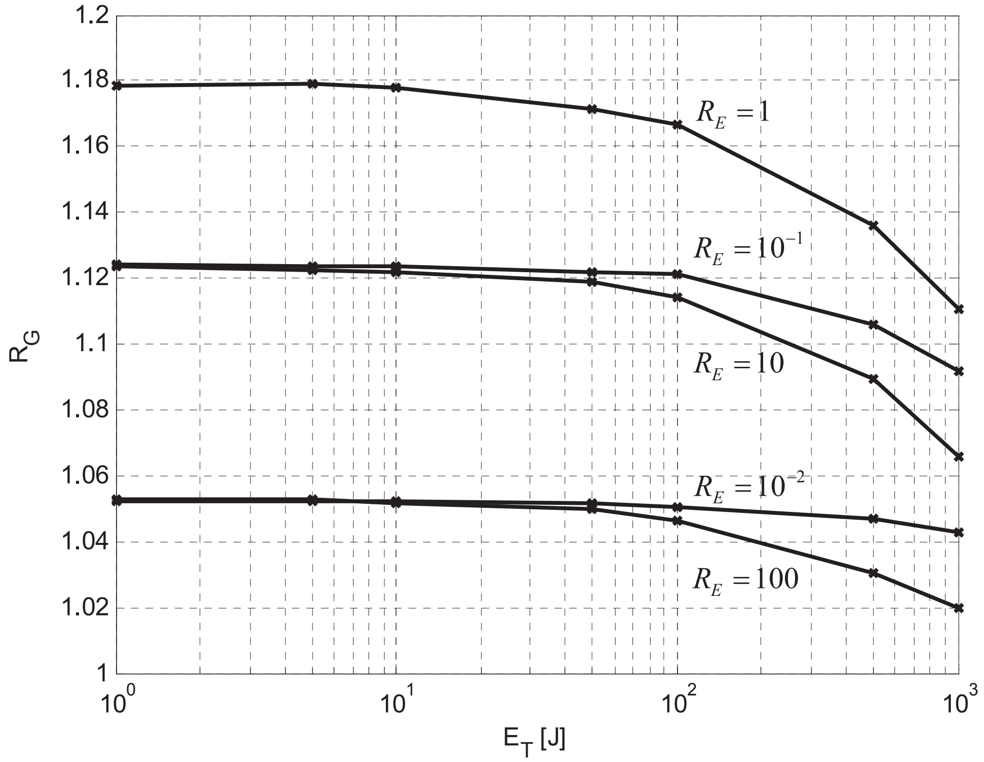

Figure 3.10: Throughput gain vs. total energy in the system ($c = 30 \cdot 10^{-5}$).

policies for the EH and BO sensors, that is, by forcing the BO sensor to adapt to the changes in transmit power in the EH sensor.

Figure 3.10 provides further insights on the throughput gains stemming from the *joint* optimization of transmission policies over sensors. More precisely, we depict the throughput gain by ratio $R_G = G_{T,\text{opt}}/G_{T,\text{subopt}}$ as a function of the total system energy. Interestingly, the highest gain is attained when the total energy harvested by the EH sensor equals that stored in the BO one, that is, for $R_E = 1$. Yet in a totally different context, this is consistent with [10] where the authors conclude that, in order to maximize the beamforming gain, the received signal levels from the opportunistically selected sensors must be comparable. Conversely, when either the EH or the BO sensors dominate ($R_E \ll 1$ or $R_E \gg 1$, respectively) the gain from a joint optimization becomes marginal ($R_G \to 1$) since the signal received from the other sensor is weak. We also observe that, in the case of unbalanced energy levels, throughput gains are lower when the BO sensor dominates. This is motivated by the fact that when $E_T^{\text{H}} \ll E_T^{\text{B}}$ the policy for the EH sensor has very little impact in the definition of the (jointly) optimal policy for the BO one. In other words, the energy consumption curves for the BO sensor with and without joint optimization are similar and, hence, the throughput gain approaches 1. It is also clear that throughput gains become negligible when E_T increases (i.e. in the high SNR regime). Let $\alpha = E_{T,\text{high}}/E_{T,\text{low}}$ denote the ratio of total system energies in the high and low SNR regimes. Since the total received power $p_{\text{BF}}(t)$ scales with α, from the score function in (3.5) and for

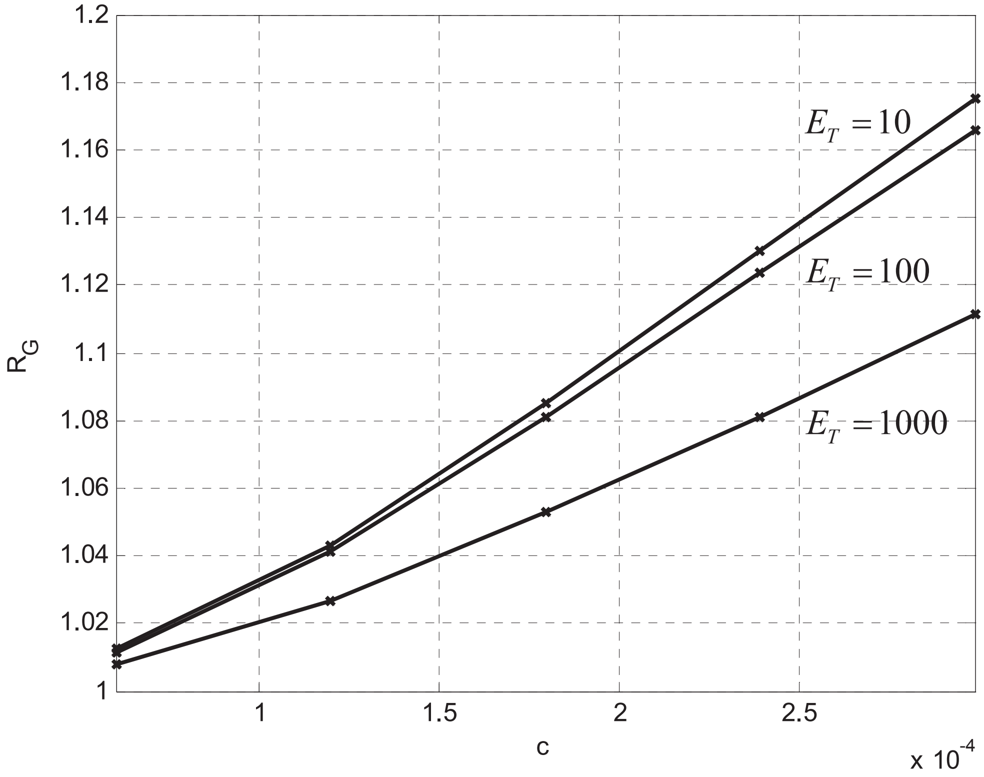

Figure 3.11: Throughput gain vs. variability of the energy harvested ($R_E = 1$).

large $E_{T,\text{high}}$ we can write,

$$R_G(E_{t,\text{high}}) = \frac{N\log(\alpha) + G_{T,\text{opt}}(E_{T,\text{low}})}{N\log(\alpha) + G_{T,\text{subopt}}(E_{T,\text{low}})}.$$

Clearly, for large α the impact of the specific transmission policies (optimal/ suboptimal) diminishes. In other words, joint optimization of transmission policies is more relevant in the low-SNR regime.

Next, Figure 3.11 illustrates the impact of the variability of energy arrivals in the throughput gain. Clearly, the higher the variability (i.e. for higher values of parameter c), the higher the gain: $R_G = 1.2$ (or $+20\%$ gain) for $c = 3 \cdot 10^{-4}$ and $E_T = 10$ J. On the contrary, if the average number of arrivals does not vary (increase) substantially in the observation interval, the gain stemming from a joint optimization of both transmission policies is marginal ($R_G \approx 1$). In conclusion, rapid variations of solar irradiation levels from dawn to noon (e.g. in high latitude locations, winter time) make joint optimization of transmission policies advisable.

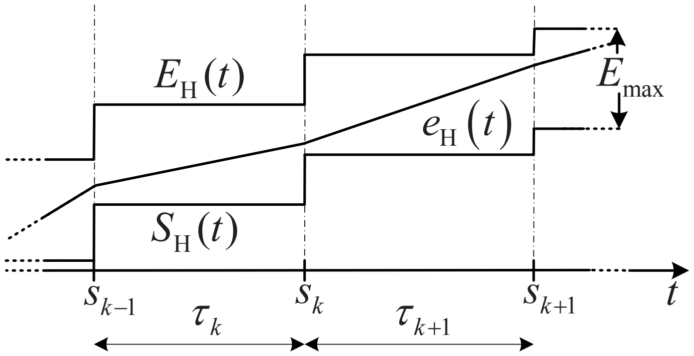

Figure 3.12: Cumulative energy harvesting and energy storage constraints.

3.4 Finite battery capacity

Unlike in previous sections, here we assume that the energy storage capacity of the EH sensor, $E_{\max}$, is *finite*. If, in the k^{th} event, the energy harvested by the EH sensor $E_{1,k}$ exceeds the remaining storage capacity at that time instant, a *battery overflow* occurs. That is, its rechargeable battery gets fully charged and the excess harvested energy is simply discarded. In Appendix 3.A.5, we prove that any transmission policy allowing battery overflows to occur is strictly suboptimal. Assuming that[9] $E_{1,k} \leq E_{\max}\ \forall k$, those suboptimal solutions can be removed from the feasible set by imposing that

$$e_H(t) \geq S_H(t) \triangleq \sum_{k:s_k<t} E_{1,k} - E_{\max} \tag{3.29}$$

for $0 \leq t \leq T$, where $S_H(t)$ denotes the cumulative energy *storage* (cES) constraint. One can easily verify that Lemmas 3.1-3.3 and Lemma 3.4 still hold for the case of finite storage capacity. On the contrary, Lemma 3.5 does not, as we will discuss in the proof of Lemma 3.7. Since, in particular, Lemma 3.1 does hold, the optimization problem can be posed again by the set of equations given by (3.5)-(3.9) in Section 3.3, along with the additional constraint (3.29), namely,

$$\sum_{k=1}^{n} \tau_k p_{H,k} \geq S_H^n = \sum_{k=0}^{n} E_{1,k} - E_{\max} \text{ for } n = 1 \ldots N. \tag{3.30}$$

A graphical representation for this additional constraint can be found in Figure 3.12. Clearly, a transmit policy is now feasible when the corresponding EC curve lies inside the *tunnel* defined by the cEH and cES curves. The additional constraint (3.30) is affine and therefore the optimization problem continues to be convex.

3.4.1 Computation of the optimal transmission policy

The next Lemma is an extension of Lemma 3.6 for the case of finite storage capacity:

---

[9] Otherwise, part of the energy in each arrival will be unavoidably wasted.

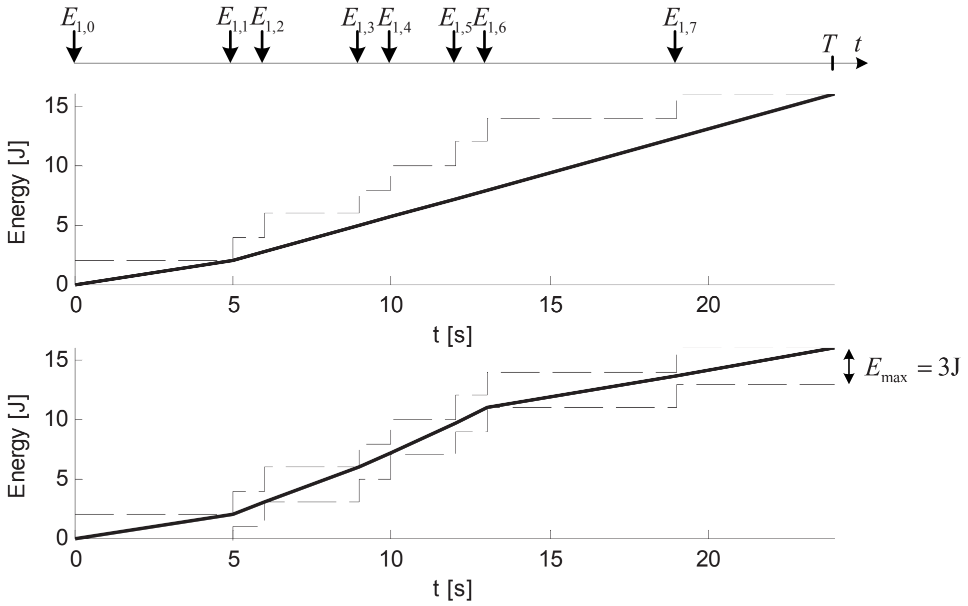

Figure 3.13: Optimal transmission policy for the EH sensor with infinite (top) and finite (bottom) battery capacity.

Lemma 3.7 *The jointly optimal power allocation policy when the storage capacity of the EH sensor is finite is such that, whenever the transmit power changes, its re-chargeable battery is either fully charged or completely depleted.*

Proof: The proof of this Lemma is based again on the Karush-Kuhn-Tucker (KKT) conditions associated with the new optimization problem and it can be found in Appendix 3.A.6. This Lemma can also be regarded as an extension of Lemma 4 in [18] for scenarios with *multiple* sensor nodes forming a virtual array. In essence, Lemma 3.7 states that changes in the slope of the EC curve can only occur when it hits either the cEH curve (depleted battery) or the cES curve (fully charged). Intuitively, this is the reason why Lemma 3.5 (on the monotonically increasing behavior of transmit powers for the EH sensor) does not hold anymore in scenarios with finite energy storage capacity. This extent is illustrated in Figure 3.13. ■

In the same vein of Theorem 3.1, one can easily verify that Lemmas 3.1-3.3, 3.4, and 3.7 unequivocally determine the optimal transmission policy for the EH harvesting sensor with finite storage capacity. Since those Lemmas are equivalent to the ones presented in [18] for the *single* sensor case, the (jointly) optimal transmission policy for the EH sensor here can be again *independently* computed on the basis of algorithm A1 proposed therein. Interestingly, the optimal EC curve turns out to be the shortest *feasible* string which, now, lies *inside* the tunnel given by the cEH and cES curves. Besides, the equation in Step 8 of Algorithm 1 in Section 3.3.2 continues to provide a connection between the primal and dual solutions of the problem with finite storage capacity. Since no additional constraints apply to the BO sensor, its optimal transmission policy can be computed from that of the EH one with Algorithm 1.

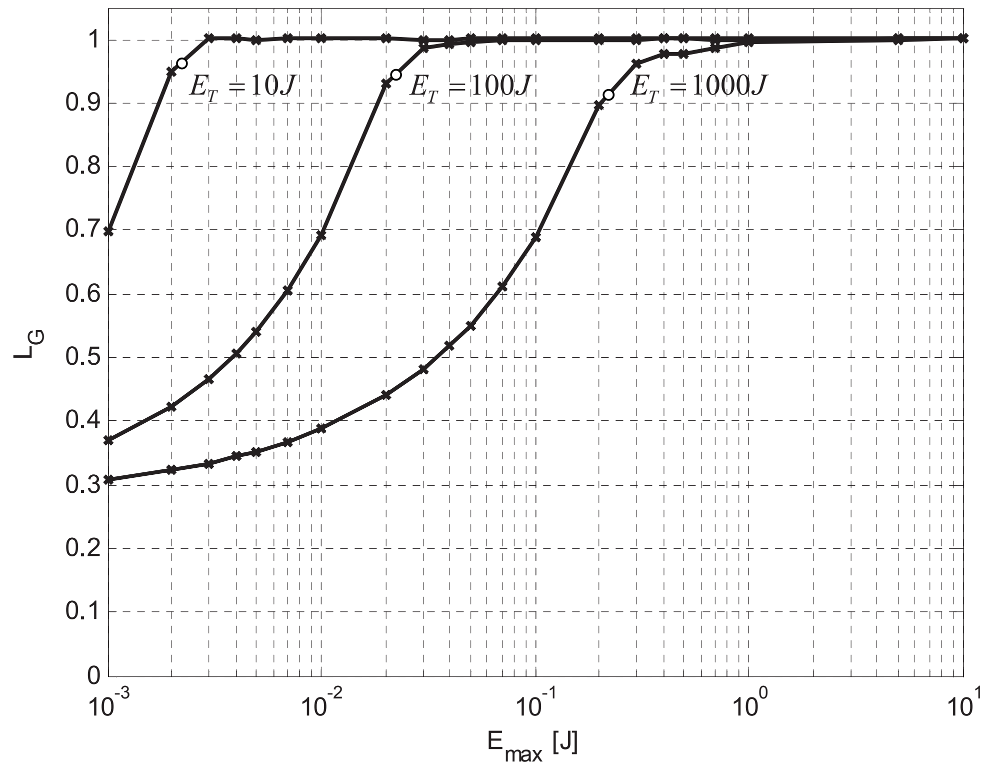

Figure 3.14: Throughput ratio (loss) as a function of battery capacity ($N = 2250$ epochs). Big round markers on the curve correspond to the operating points where the maximum storage capacity E_{max} equals the energy harvested in each arrival $E_{1,k}$ ($E_{1,k} = 2.21 \cdot 10^{-3}, 2.21 \cdot 10^{-2}, 2.21 \cdot 10^{-1}$ for the $E_T = 10, 100, 1000$ J curves, respectively).

3.4.2 Simulations and numerical results

Unlike in Section 3.3.3, here we assume the more realistic case where the energy storage capacity for the EH sensor is finite.

Figure 3.14 depicts the total loss in throughput with respect to the case of infinite storage capacity by throughput ratio L_G. Interestingly, as long as the maximum storage capacity is greater than the energy harvested in each arrival, the throughput loss is barely noticeable (the throughput ratio equals 1). In other words, the changes in the optimal transmission policy resulting from the introduction of the additional constraint (3.30), which avoids battery overflows, have a rather marginal impact on the achievable throughput. This is excellent news since, typically, storage capacity is well above individual harvested energy levels. On the contrary, throughput performance rapidly degrades for smaller storage capacities. This stems from the fact that now part of the energy in each arrival is unavoidably wasted in battery overflows. As a result, the total amount of energy stored with respect to the case of infinite capacity decreases, and so does the resulting throughput.

Next, we analyze the impact of battery degradation in the EH sensor on system performance.

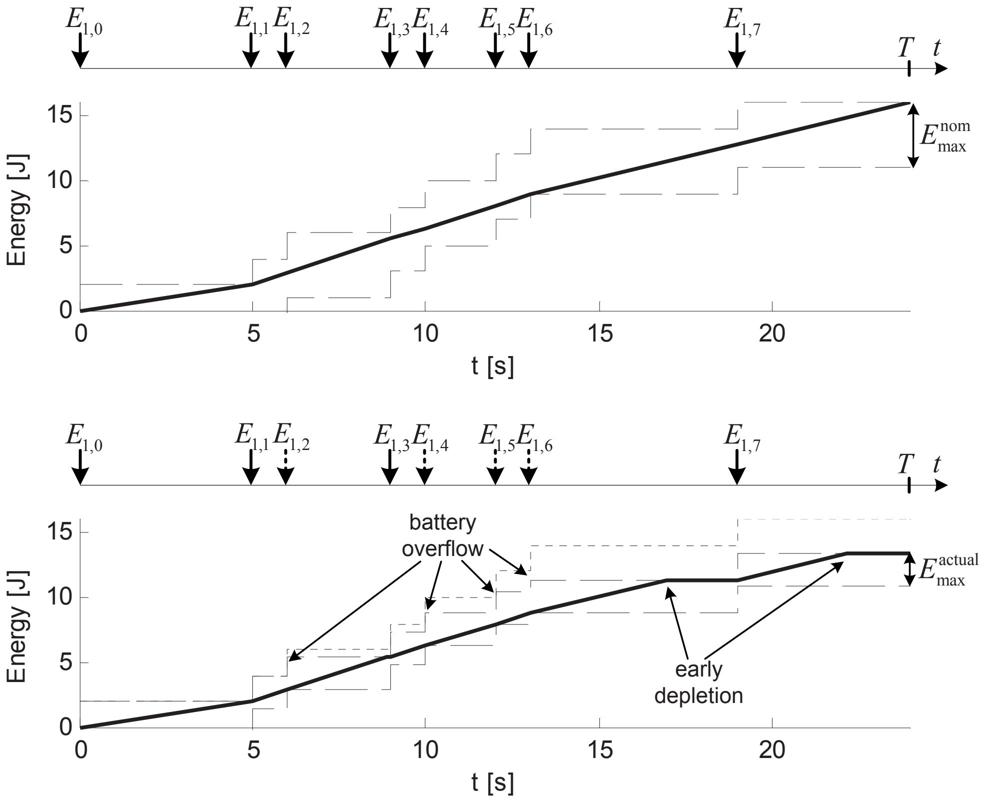

Figure 3.15: Battery overflow and early depletion phenomena: transmission policies for the EH sensor with nominal battery capacity (top, $E_{\max}^{\text{nom}} = 5$ J) and actual capacity (bottom, $E_{\max}^{\text{actual}} = 2.5$ J) for a given realization of energy arrivals. Dotted arrows indicate the arrivals in which part of the energy is wasted ($E_{1,k} = 2$ J). As a reference, the lower plot includes the cEH curve for the nominal capacity (dash-dotted line).

Our focus is on impairments due to *long-term* battery degradation due to e.g. aging. Accordingly, its storage capacity is assumed to take a constant value for the whole transmission period (i.e. no battery leakage between arrivals). The *nominal* storage capacity $E_{\max}^{\text{nom}}$, on which basis the optimal transmission policies for the EH and BO are computed, is assumed to be known. On the contrary, the *actual* capacity $E_{\max}^{\text{actual}} \leq E_{\max}^{\text{nom}}$, which enables data transmission, is unknown. The fact that the actual capacity is lower that its nominal value may result into *battery overflows* and *early battery depletion* (see Figure 3.15), both having a negative impact on the achievable throughput. Despite of the introduction of the additional constraint (3.30), now there is a risk to waste part of the energy arrivals in battery overflows since the remaining battery capacity is smaller than expected. As an example, for the particular realization in Figure 3.15, the total energy actually harvested within $0 \ldots T$ amounts to 13.375 J instead of 16 J. Likewise, the fact that the actual energy stored in the battery is lower than expected might lead to early battery depletions. This forces data transmission for the EH sensor to be suspended until the next energy arrival. Consequently, the beamforming gain vanishes for this period of time.

In Figure 3.16, we investigate the impact of battery overflows and early depletions on through-

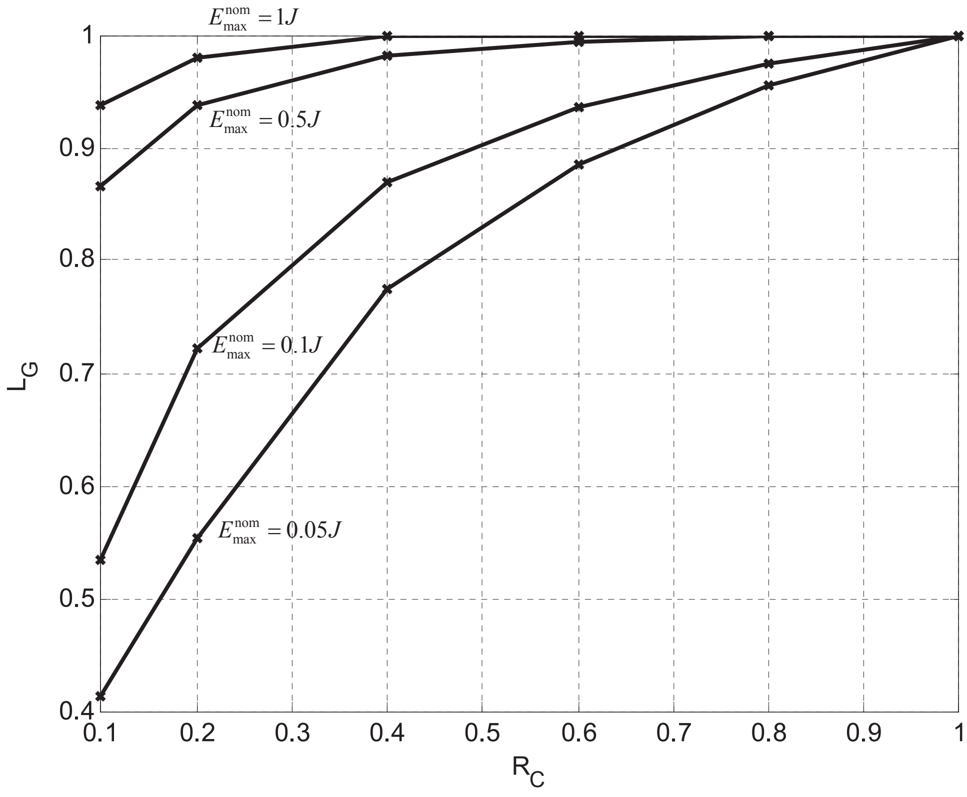

Figure 3.16: Throughput ratio (loss) vs. battery capacity degradation ($E_T = 100$ J, $c = 30 \cdot 10^{-5}, T = 7h$).

put. More specifically, we depict the throughput ratio $L_G = G_{T,\text{actual}}/G_{T,\text{nom}}$ as a function of the ratio between actual and nominal battery capacities, namely, $R_C = E_{\max}^{\text{actual}}/E_{\max}^{\text{nom}}$. Unsurprisingly, throughput degradation is particulary severe and faster for smaller values of nominal capacity (i.e. for $E_{\max}^{\text{nom}} = 0.05$ J). In this case, the amount of energy in each arrival ($E_{1,k} = 2.21 \cdot 10^{-2}$ J) is comparable to the nominal capacity. Consequently, many battery overflows and early depletions occur. Furthermore, for $R_{\text{C}} = 0.1$, the actual battery capacity amounts to $E_{\max}^{\text{actual}} = 5 \cdot 10^{-3}$ which is below $E_{1,k}$. Hence, every energy arrival causes a battery overflow which results into a throughput loss of 60%. It is also worth noting that for large nominal battery capacities ($E_{\max}^{\text{nom}} = 1$ J) and higher values of capacity degradation ($R_{\text{C}} = 0.1$) there is also a noticeable throughput loss (some 10%). Even though the actual battery capacity ($E_{\max}^{\text{actual}} = 0.1$ J) is well above $E_{1,k}$, the mismatch between nominal and actual capacities results into some battery overflows and early depletions too.

3.5 Computational complexity analysis

To recall, the computation of the optimal transmission policy for the EH sensor with infinite storage capacity entails the determination of a number of piece-wise linear functions with minimal slope which connect a *subset* of the N corner points on the cEH curve (see proof of Theorem 3.1 and [17]). In the worst case, the total number of corner points on the EC curve equals[10] N. For the first corner point (actually, the origin), the total number of slopes to be checked equals N, that is, as many as the number of corner points up to $t = T$. For the second corner point, the total number of slopes equals $N - 1$. The total number of operations is, thus, $N + (N-1) + \ldots 1 = \frac{N \cdot (N-1)}{2}$. Hence, the complexity associated with the computation of the optimal transmission policy for the EH sensor with infinite energy storage capacity is $\mathcal{O}(N^2)$. As for the BO sensor, each iteration of Algorithm 1 entails the computation of N transmit powers (Steps 6 to 10). When a bi-section scheme is adopted (rather than the grid search we actually used in Algorithm 1), the total number of iterations needed is on the order of $\log(\frac{1}{\epsilon})$ [38], where ϵ denotes the constraints prescribed tolerance. Hence, the complexity associated with the computations of the optimal transmission policy for the BO sensor is $\mathcal{O}(N \log(\frac{1}{\epsilon}))$. In conclusion, the computational complexity[11] of the proposed scheme is dominated by that of the algorithm presented in [17] and it reads $\mathcal{O}(N^2)$.

3.6 Chapter summary and conclusions

In this chapter, we have derived the *jointly* optimal transmission policy which allows an energy harvesting plus a battery operated sensor node to act as a virtual antenna array to maximize throughput for a given deadline. The necessary conditions for optimality that we have identified, for both scenarios, i.e. with infinite and finite energy storage capacity in the energy harvesting sensor, allowed us to prove that the optimal transmission policy for the energy harvesting sensor can be computed independently from that of the battery operated one according to the procedure described in [17] and [18], respectively. Interestingly enough, we have proved that such policies *continue* to be optimal for our *two*-sensor (vs. single-sensor) scenario. Moreover, we have shown that the optimal transmission policy for the battery operated sensor is unequivocally determined and can be iteratively computed from that of the energy harvesting one. The resulting policy is, in general, different from that of battery operated sensors in single-sensor scenarios (i.e. constant transmit power).

The performance of the jointly optimal transmission policy has been assessed by means of computer simulations in a realistic scenario where solar energy is harvested from the environment. Computer simulation results have revealed that, in scenarios with *infinite* storage capacity in the energy harvesting sensor, the joint optimization of transmit policies in combination with

---

[10] The actual number depends on the specific realization of energy arrivals.

[11] Likewise, for the scenario where EH sensor is equipped with an energy storage of finite capacity, the algorithm proposed in [18] checks two times more slopes. The order of number operations, however, continues to be the same, i.e. $\mathcal{O}(N^2)$. Consequently, the computational complexity for the optimization method proposed in Section 3.4 is dominated by that of the algorithm presented in [18], and it equals $\mathcal{O}(N^2)$.

beamforming yields substantial throughput gains. The highest gain is attained when the total energy in the energy harvesting and battery operated sensors are identical. However, the gain becomes negligible in high-SNR scenarios where large amounts of energy are harvested by/stored in sensors. In the case of unbalanced energy levels, throughput gains are lower when the BO sensor dominates. Besides, we have found that throughput gain is higher when solar irradiation levels vary rapidly.

We have also learnt that throughput losses stemming from finite storage capacity are only substantial when battery capacity is smaller than the amount of energy in each arrival. Finally, we have observed that a long-term degradation of battery capacity may result into battery overflows and early battery depletions. The associated throughput loss is particulary severe for smaller values of the nominal storage capacity. Still, the impact of the mismatch between nominal and actual capacities can also be noticeable for larger values.

3.A Appendix

3.A.1 Proof of Lemma 3.1

Assume that the optimal policy before s_{k-1} and after s_k is optimal. The total throughput in the k^{th} epoch is given by $G_{\tau_k} = \int_{s_{k-1}}^{s_k} \log(1 + p_{\text{BF}}(t))dt$ where, to recall, we defined $p_{\text{BF}}(t) = (\sqrt{p_{\text{H}}(t)} + \sqrt{p_{\text{B}}(t)})^2$ as the instantaneous power received at the base station from the two sensors. Besides, let $\Delta e_{\text{BF}} = \int_{s_{k-1}}^{s_k} p_{\text{BF}}(t)dt$ denote the total received energy in the k^{th} epoch of duration $\tau_k = s_k - s_{k-1}$. From Jensen's inequality [39, Section 7.2.5], we have that the following inequality:

$$\frac{\int_a^b g\left(f(t)\right) h(t)dt}{\int_a^b h(t)dt} \leq g\left(\frac{\int_a^b f(t)h(t)dt}{\int_a^b h(t)dt}\right)$$

holds as long as $g(\cdot)$ is a concave function, $f(t)$ is such that $\alpha \leq f(t) \leq \beta$, and $h(t) \geq 0$. Letting $g(p) = \log(1+p)$, $f(t) = p_{\text{BF}}(t)$ and $h(t) = 1$ yields

$$\begin{aligned} G_{\tau_k} &= \int_{s_{k-1}}^{s_k} \log(1 + p_{\text{BF}}(t))dt \\ &\leq \tau_k \log\left(1 + \left(\frac{\int_{s_{k-1}}^{s_k} p_{\text{BF}}(t)dt}{\int_{s_{k-1}}^{s_k} dt}\right)\right) \\ &= \tau_k \log\left(1 + \frac{\Delta e_{\text{BF}}}{\tau_k}\right). \end{aligned} \tag{3.31}$$

This last inequality evidences that for a given energy Δe_{BF}, the optimal power allocation policies for the k^{th} epoch must be such that the instantaneous received power at the BS is *constant* and equal to $p_{\text{BF}}(t) = \Delta e_{\text{BF}}/\tau_k$. In order to determine the optimal transmission policy for *each* sensor, we resort to Cauchy's inequality [39, Section 7.2.5] to learn that

$$\left(\int_{s_{k-1}}^{s_k} p_{\text{BF}}(t)dt\right)^{\frac{1}{2}} \leq \left(\int_{s_{k-1}}^{s_k} p_{\text{H}}(t)dt\right)^{\frac{1}{2}} + \left(\int_{s_{k-1}}^{s_k} p_{\text{B}}(t)dt\right)^{\frac{1}{2}}$$

or, equivalently (see Figure 3.17),

$$\int_{s_{k-1}}^{s_k} p_{\text{BF}}(t)dt \leq \left(\sqrt{\Delta e_{\text{H}}} + \sqrt{\Delta e_{\text{B}}}\right)^2. \tag{3.32}$$

By replacing (3.32) into (3.31), we finally get:

$$G_{\tau_k} \leq \tau_k \log\left(1 + \left(\sqrt{\frac{\Delta e_{\text{H}}}{\tau_k}} + \sqrt{\frac{\Delta e_{\text{B}}}{\tau_k}}\right)^2\right). \tag{3.33}$$

In other words, the individual power allocation policies that maximize the throughput in the k^{th} epoch consist in using a *constant* transmit power given by $p_{\text{H}}(t) = \Delta e_{\text{H}}/\tau_k$ and $p_{\text{B}}(t) = \Delta e_{\text{B}}/\tau_k$ for the EH and BO sensors, respectively. This concludes the proof.

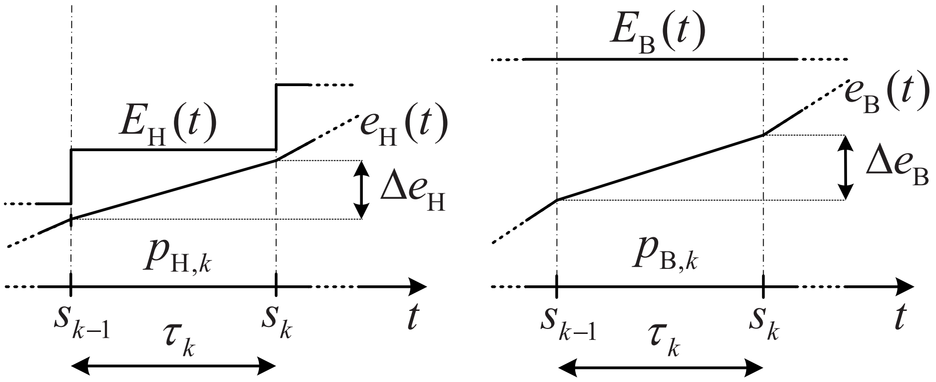

Figure 3.17: Transmit power in each sensor remains constant between consecutive events (Lemma 3.1).

3.A.2 Proof of strict concavity of the utility function

The utility function for the optimization problem is given by:

$$\sum_{k=1}^{N} \tau_k \log\left(1 + (\sqrt{p_{H,k}} + \sqrt{p_{B,k}})^2\right) \tag{3.34}$$

As it can be seen, it is represented as a weighted sum of terms, where all the terms have the same form. In addition, the k^{th} term only depends on the corresponding two variables, i.e. $p_{H,k}$ and $p_{B,k}$. Let us define the following function:

$$G_1(p_H, p_B) = \tau \log\bigl(1 + (\sqrt{p_H} + \sqrt{p_B})^2\bigr) \tag{3.35}$$

which represents the k^{th} term in the sum (indices k have been omitted for brevity). Hence, it suffices to show that $G_1(p_H, p_B)$ is strictly concave, or, alternatively that $G_2(p_H, p_B) = -G_1(p_H, p_B)$ is strictly convex. The latter can be verified by realizing that for $p_H > 0$ and $p_B > 0$, the Hessian

$$\nabla^2 G_2(p_H, p_B) = \begin{bmatrix} \frac{\partial^2 G_2}{\partial {p_H}^2} & \frac{\partial^2 G_2}{\partial p_H \partial p_B} \\ \frac{\partial^2 G_2}{\partial p_B \partial p_H} & \frac{\partial^2 G_2}{\partial {p_B}^2} \end{bmatrix} \tag{3.36}$$

is positive definite, i.e. $\nabla^2 G_2(p_H, p_B) \succ 0$. By using the Schur complement, it is equivalent to say that $A > 0$, $S > 0$, with A and S defined as follows:

$$A = \frac{\partial^2 G_2}{\partial {p_H}^2} \tag{3.37}$$

$$S = \frac{\partial^2 G_2}{\partial {p_B}^2} - \frac{\partial^2 G_2}{\partial p_B \partial p_H} \left(\frac{\partial^2 G_2}{\partial {p_H}^2}\right)^{-1} \frac{\partial^2 G_2}{\partial p_H \partial p_B} \tag{3.38}$$

Considering the definition of G_2, (3.37) and (3.38) can further be expressed as follows:

$$A = \frac{2p_H^{3/2} + 5p_H\sqrt{p_B} + 4\sqrt{p_H}p_B + \sqrt{p_B} + p_B^{3/2}}{2p_H^{3/2}(1 + p_H + 2\sqrt{p_H p_B} + p_B)^2} \tag{3.39}$$

$$\begin{aligned} S = {} & \frac{6\sqrt{p_{\mathrm{B}}}p_{\mathrm{H}}^{5/2} + p_{\mathrm{B}}^{3} + 6p_{\mathrm{H}}p_{\mathrm{B}} + 4p_{\mathrm{H}}^{3/2}\sqrt{p_{\mathrm{B}}} + p_{\mathrm{H}}^{3} + 6p_{\mathrm{B}}^{5/2}}{p_{\mathrm{B}}^{3/2}(2p_{\mathrm{H}}^{3/2} + 5p_{\mathrm{H}}\sqrt{p_{\mathrm{B}}} + 4\sqrt{p_{\mathrm{H}}}p_{\mathrm{B}} + \sqrt{p_{\mathrm{B}}} + p_{\mathrm{H}}^{3/2})(1 + p_{\mathrm{H}} + 2\sqrt{p_{\mathrm{H}}p_{\mathrm{B}}} + p_{\mathrm{B}})^2} \\ & + \frac{15p_{\mathrm{B}}^{2}p_{\mathrm{H}} + 15p_{\mathrm{B}}p_{\mathrm{H}}^{2} + 20p_{\mathrm{B}}^{3/2}p_{\mathrm{H}}^{3/2} + p_{\mathrm{H}}^{2} + p_{\mathrm{B}}^{2} + 4p_{\mathrm{B}}^{3/2}\sqrt{p_{\mathrm{H}}}}{p_{\mathrm{B}}^{3/2}(2p_{\mathrm{H}}^{3/2} + 5p_{\mathrm{H}}\sqrt{p_{\mathrm{B}}} + 4\sqrt{p_{\mathrm{H}}}p_{\mathrm{B}} + \sqrt{p_{\mathrm{B}}} + p_{\mathrm{H}}^{3/2})(1 + p_{\mathrm{H}} + 2\sqrt{p_{\mathrm{H}}p_{\mathrm{B}}} + p_{\mathrm{B}})^2} \end{aligned} \tag{3.40}$$

Since $p_{\mathrm{H}} > 0$ and $p_{\mathrm{B}} > 0$, as shown in Lemma 3.4, we conclude that $A > 0$ and $S > 0$, and therefore $\nabla^2 G_2(p_{\mathrm{H}}, p_{\mathrm{B}}) \succ 0$. This concludes the proof of *strict* concavity of the utility function.

3.A.3 Solution of third order equation

In order to find the optimal policy for BO sensor node, it is necessary to solve the third order equation (Step 8 in Algorithm 1), where, to recall, the optimal policy at the EH sensor $\breve{p}_{\mathrm{H},k}$ is known from Theorem 3.1. To that end, let us rewrite the equation (3.23) as follows:

$$ax^2 + bx^2 + cx + d = 0, \tag{3.41}$$

with variable x and coefficients $a, b, c,$ and d given by:

$$x = \sqrt{\breve{p}_{\mathrm{B},k}} \tag{3.42}$$

$$a = \breve{B}_k \tag{3.43}$$

$$b = 2\breve{B}_k\sqrt{\breve{p}_{\mathrm{H},k}} \tag{3.44}$$

$$c = \breve{B}_k\breve{p}_{\mathrm{H},k} + \breve{B}_k - 1 \tag{3.45}$$

$$d = -\sqrt{\breve{p}_{\mathrm{H},k}}. \tag{3.46}$$

Equation (3.41), known as *complete cubic equation* [39, Section 5.1.3], can be solved by introducing the following change of variable

$$x = y - \frac{b}{a}, \tag{3.47}$$

this resulting in an *incomplete cubic equation*, namely

$$y^3 + py + q = 0, \tag{3.48}$$

with the coefficients p and q given by

$$\begin{aligned} p &= -\frac{1}{3}\left(\frac{b}{a}\right)^2 + \frac{c}{a} \\ q &= \frac{2}{27}\left(\frac{b}{a}\right)^3 - \frac{bc}{3a^2} + \frac{d}{a}. \end{aligned} \tag{3.49}$$

The solutions of the incomplete cubic equation read:

$$\begin{aligned} y_1 &= \alpha + \beta \\ y_{2,3} &= -\frac{1}{2}(\alpha + \beta) \pm i\frac{\sqrt{3}}{2}(\alpha - \beta) \end{aligned} \tag{3.50}$$

with α and β given by:

$$\begin{aligned} \alpha &= \left(-\frac{q}{2} + \sqrt{D}\right)^{1/3} \\ \beta &= \left(-\frac{q}{2} - \sqrt{D}\right)^{1/3}, \end{aligned} \tag{3.51}$$

being D, the *discriminant*, namely:

$$D = \left(\frac{p}{3}\right)^3 + \left(\frac{q}{2}\right)^2. \tag{3.52}$$

The number of real-valued roots of a cubic equation depends on the sign of the discriminant D:

- $D > 0$: there is one real and two complex conjugate roots.
- $D < 0$: There are three real roots.
- $D = 0$: There is one real root and another real root of double multiplicity (for $p = q = 0$).

From the Viète theorem [39, Sec 5.1.3], the roots of a complete cubic equation (3.41) must satisfy

$$x_1 + x_2 + x_3 = -\frac{b}{a}, \tag{3.53}$$

$$x_1x_2 + x_1x_3 + x_2x_3 = \frac{c}{a}, \tag{3.54}$$

$$x_1x_2x_3 = -\frac{d}{a}. \tag{3.55}$$

Hence, from (3.43), (3.46) and (3.55), we know that:

$$\begin{aligned} x_1x_2x_3 &= \frac{\sqrt{\breve{p}_{\mathrm{H},k}}}{\breve{B}_k} \\ &> 0 \end{aligned} \tag{3.56}$$

where the strict positivity of (3.56) comes out of the fact that $\breve{p}_{\mathrm{H},k}, \breve{B}_k > 0$. When the discriminant D is positive, the single real (and positive) root will be the solution to (3.41). On the contrary, when there are multiple real roots (i.e.$D \leq 0$), only one of them can be positive and the other two must be negative in order for (3.56) to hold. Again, this single positive root will be chosen. Finally, by considering the change of variables (3.42), the power at the battery operated sensor during k^{th} epoch follows

$$\breve{p}_{\mathrm{B},k} = x_1^2, \tag{3.57}$$

where x_1 is the only positive solution to equation (3.41).

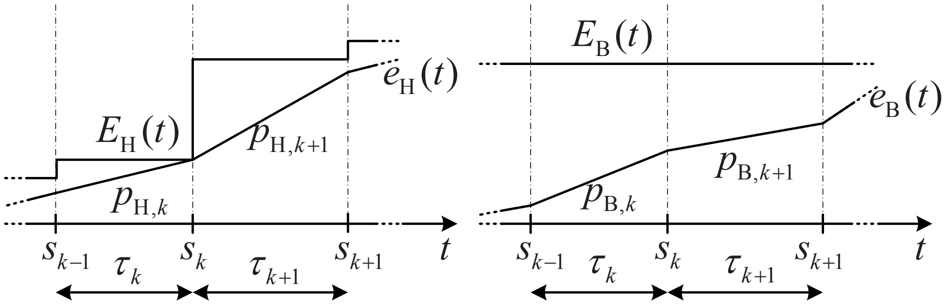

Figure 3.18: When transmit power changes, the energy consumed by the EH sensor equals the energy harvested (Lemma 3.6).

3.A.4 Proof of Lemma 3.6

Let us consider (3.25) and (3.26), which give us the connection between primal and dual optimal solutions. Since, as stated in Lemma 3.4 , $\breve{p}_{\text{H},k}, \breve{p}_{\text{B},k} \neq 0$, the complementary slackness conditions (3.18) and (3.19), force the corresponding Lagrangian multipliers to vanish, i.e. $\breve{\mu}_k, \breve{\xi}_k = 0$. When transmit power changes, due to Lemma 3.5 we have $\breve{p}_{\text{H},k} < \breve{p}_{\text{H},k+1}$. From (3.25) and the *Remark* below, this can only hold if $\breve{A}_k \neq \breve{A}_{k+1}$ or, equivalently, if $\breve{\lambda}_k \neq 0$ (to recall, $\breve{\mu}_k = 0$). From the complementary slackness condition in (3.16), we have that $\breve{\lambda}_k \neq 0 \Rightarrow \sum_{i=1}^{k} \tau_i \breve{p}_{\text{H},i} - E_{\text{H}}^k = 0$. That is, the energy consumed by the energy harvesting sensor up to s_k, equals the energy harvested by such sensor up to that instant (see Figure 3.18). This concludes the proof.

Remark: From Lemma 3.2, we know that $\sum_{k=1}^{N} \tau_k \breve{p}_{\text{B},k} = E_{2,0}$. Since, in addition $\breve{p}_{\text{B},k} \neq 0$ this yields $\sum_{k=1}^{n} \tau_k \breve{p}_{\text{B},k} - E_{2,0} < 0$ for all $n = 1 \dots N-1$. From the complementary slackness condition of (3.17), we conclude that, necessarily, $\breve{\nu}_k = 0$ for $k = 1 \dots N-1$. This, along with the fact that $\breve{\mu}_k = 0$ for all k, implies that $\breve{B}_k = \breve{B}_N = \nu_N, \forall k$, that is, all $\breve{B}_k$s are identical. This property is a cornerstone of Algorithm 1 since it turns an N-dimensional exhaustive search into a single-dimensional one.

3.A.5 Transmission policies with battery overflows are suboptimal

Here we show that any transmission policy resulting into battery overflows in the EH sensor is strictly suboptimal. We will prove this by contradiction. Assume that a transmission policy with battery overflow at s_k only (Figure 3.19 left) is optimal. Let $\Pi_{\text{H}} = \{p_{\text{H},1}, \dots, p_{\text{H},k}, \dots, p_{\text{H},N}\}$ and $\Pi_{\text{B}} = \{p_{\text{B},1}, \dots, p_{\text{B},k}, \dots, p_{\text{B},N}\}$ denote the corresponding *optimal* transmission policies for the EH and BO sensors, respectively. We can think of an alternative (and feasible) transmission policy $\dot{\Pi} = \{\dot{\Pi}_{\text{H}}, \dot{\Pi}_{\text{B}}\}$ such that, on the one hand, $\dot{\Pi}_{\text{H}} = \{p_{\text{H},1}, \dots, \dot{p}_{\text{H},k}, \dots, p_{\text{H},N}\}$ and, on the other, $\dot{\Pi}_{\text{B}} = \Pi_{\text{B}}$. That is, the new policy only differs from the optimal one in the power allocated to the EH sensor in the k^{th} epoch. By properly adjusting $\dot{p}_{\text{H},k}$, the battery over-

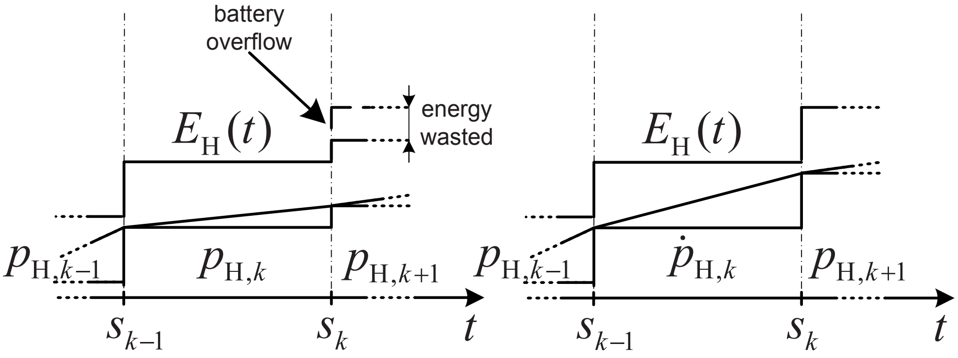

Figure 3.19: Transmission policies with battery overflows are strictly suboptimal.

flow at s_k can be avoided (Figure 3.19 right). Since, clearly, $\dot{p}_{\mathrm{H},k} > p_{\mathrm{H},k}$, the throughput in the k^{th} epoch is higher, this resulting into a higher total throughput in $[0 \ldots T]$. This contradicts the claim that the original policy $\Pi = \{\Pi_{\mathrm{H}}, \Pi_{\mathrm{B}}\}$ is optimal and concludes the proof.

3.A.6 Proof of Lemma 3.7

The Lagrangian $\mathcal{L}_2$ of the new optimization problem with finite battery capacity constraints is given by

$$\begin{aligned}\mathcal{L}_2 = &-\sum_{k=1}^{N} \tau_k \log\left(1 + (\sqrt{p_{\mathrm{H},k}} + \sqrt{p_{\mathrm{B},k}})^2\right) \\ &+ \sum_{n=1}^{N} \lambda_n \left(\sum_{k=1}^{n} \tau_k p_{\mathrm{H},k} - E_{\mathrm{H}}^n\right) - \sum_{n=1}^{N} \pi_n \left(\sum_{k=1}^{n} \tau_k p_{\mathrm{H},k} - S_{\mathrm{H}}^n\right) \\ &+ \sum_{n=1}^{N} \nu_n \left(\sum_{k=1}^{n} \tau_k p_{\mathrm{B},k} - E_{\mathrm{B}}^n\right) - \sum_{k=1}^{N} \mu_k p_{\mathrm{H},k} - \sum_{k=1}^{N} \xi_k p_{\mathrm{B},k}. \end{aligned} \tag{3.58}$$

The new KKT conditions thus read

$$\frac{\partial \mathcal{L}_2}{\partial p_{\mathrm{H},k}}, \frac{\partial \mathcal{L}_2}{\partial p_{\mathrm{B},k}} = 0 \tag{3.59}$$

$$\sum_{k=1}^{n} \tau_k \breve{p}_{\mathrm{H},k} \leq E_{\mathrm{H}}^n \text{ for } n = 1 \ldots N \tag{3.60}$$

$$\sum_{k=1}^{n} \tau_k \breve{p}_{\mathrm{H},k} \geq S_{\mathrm{H}}^n \text{ for } n = 1 \ldots N \tag{3.61}$$

$$\sum_{k=1}^{n} \tau_k \breve{p}_{\mathrm{B},k} \leq E_{\mathrm{B}}^n \text{ for } n = 1 \ldots N \tag{3.62}$$

$$\breve{p}_{\mathrm{H},k}, \breve{p}_{\mathrm{B},k} > 0 \tag{3.63}$$

$$\breve{\lambda}_n, \breve{\pi}_n, \breve{\nu}_n, \breve{\mu}_k, \breve{\xi}_k \geq 0 \tag{3.64}$$

$$\breve{\lambda}_n \left(\sum_{k=1}^{n} \tau_k \breve{p}_{\mathrm{H},k} - E_{\mathrm{H}}^n \right) = 0 \text{ for } n = 1 \dots N \tag{3.65}$$

$$\breve{\pi}_n \left(\sum_{k=1}^{n} \tau_k \breve{p}_{\mathrm{H},k} - S_{\mathrm{H}}^n \right) = 0 \text{ for } n = 1 \dots N \tag{3.66}$$

$$\breve{\nu}_n \left(\sum_{k=1}^{n} \tau_k \breve{p}_{\mathrm{B},k} - E_{\mathrm{B}}^n \right) = 0 \text{ for } n = 1 \dots N \tag{3.67}$$

$$-\breve{\mu}_k \breve{p}_{\mathrm{H},k} = 0 \text{ for } k = 1 \dots N \tag{3.68}$$

$$-\breve{\xi}_k \breve{p}_{\mathrm{B},k} = 0 \text{ for } k = 1 \dots N \tag{3.69}$$

where equation (3.66) accounts for the additional constraint given by (3.30), and $\{\pi_n\}$ denote the corresponding set of Lagrange multipliers. Since the additional constraint does not apply to the BO sensor, the partial derivative $\frac{\partial \mathcal{L}_2}{\partial p_{\mathrm{B},k}}$ is identical to that in Appendix 3.A.4, namely, $\frac{\partial \mathcal{L}_2}{\partial p_{\mathrm{B},k}} = \frac{\partial \mathcal{L}_1}{\partial p_{\mathrm{B},k}}$. On the contrary, $\frac{\partial \mathcal{L}_2}{\partial p_{\mathrm{H},k}}$ differs and, more specifically, it reads

$$\frac{\partial \mathcal{L}_2}{\partial p_{\mathrm{H},k}} = -\tau_k \frac{\sqrt{\breve{p}_{\mathrm{H},k}} + \sqrt{\breve{p}_{\mathrm{B},k}}}{\sqrt{\breve{p}_{\mathrm{H},k}} \left(1 + (\sqrt{\breve{p}_{\mathrm{H},k}} + \sqrt{\breve{p}_{\mathrm{B},k}})^2\right)} + \tau_k (\sum_{n=k}^{N} \breve{\lambda}_n - \breve{\pi}_n) - \breve{\mu}_k \tag{3.70}$$

From (3.59) and by introducing the change of variables $\breve{A}_k = \sum_{n=k}^{N} (\breve{\lambda}_n - \breve{\pi}_n) - \frac{\breve{\mu}_k}{\tau_k}$ and $\breve{B}_k = \sum_{n=k}^{N} \breve{\nu}_n - \frac{\breve{\xi}_k}{\tau_k}$, the optimal transmit powers in k^{th} epoch, $\breve{p}_{\mathrm{H},k}$ and $\breve{p}_{\mathrm{B},k}$, again yield

$$\breve{p}_{\mathrm{H},k} = \frac{\breve{B}_k (\breve{A}_k + \breve{B}_k - \breve{A}_k \breve{B}_k)}{\breve{A}_k (\breve{A}_k + \breve{B}_k)^2} \tag{3.71}$$

$$\breve{p}_{\mathrm{B},k} = \frac{\breve{A}_k (\breve{A}_k + \breve{B}_k - \breve{A}_k \breve{B}_k)}{\breve{B}_k (\breve{A}_k + \breve{B}_k)^2}. \tag{3.72}$$

Equation (3.63) and the complementary slackness conditions (3.68) and (3.69) again force the corresponding Lagrangian multipliers to vanish, i.e. $\breve{\mu}_k, \breve{\xi}_k = 0$. As in Appendix 3.A.4, the transmit power changes ($\breve{p}_{\mathrm{H},k} \neq \breve{p}_{\mathrm{H},k+1}$) iff $\breve{A}_k \neq \breve{A}_{k+1}$ or, equivalently, if $\breve{\lambda}_k - \breve{\pi}_k \neq 0$. This is only possible for the following combinations of values of the Lagrangian multiplier: (i) $\breve{\lambda}_k \neq 0, \breve{\pi}_k = 0$; (ii) $\breve{\lambda}_k = 0, \breve{\pi}_k \neq 0$; or (iii) $\breve{\lambda}_k \neq 0, \breve{\pi}_k \neq 0, \breve{\lambda}_k \neq \breve{\pi}_k$. The conditions (i) and (ii) accounts for cases in which the EC curve hits the cEH or cES curves at s_k respectively; whereas (iii) accounts for the case in which the cEH and cES curves coincide at time instant s_k (i.e. when energy harvested at s_k equals battery capacity, namely, $E_{1,k} = E_{\text{max}}$).

Chapter 4

Collaborative Beamforming with Energy Harvesting Sensors

In this chapter, we generalize the communication scenario from Chapter 3, by considering a system where *multiple* energy harvesting sensors cooperate to transmit a common message to a distant base station. As in the previous chapter, the aim is to identify the *jointly* optimal transmission policy such that the total data throughput for a given deadline is maximized. However, the fact that now, all the sensors are capable of harvesting ambient energy, renders this problem more involved. First, we address a scenario where the energy storage capacity of sensors is assumed to be *infinite*. In order to facilitate the presentation of the proposed optimization method, initially, we consider the case with only two EH sensors. For the given setup, we prove that the jointly optimal solution can be found in an iterative manner, where, in each iteration, the utility function is maximized by adjusting the powers at one of the sensors, whilst the policies at the other sensor(s) is(are) kept fixed. Next, we generalize the analysis for a scenario were the sensors are assumed to have *finite* energy storage capacity. The computational complexity of the proposed schemes is analyzed in detail and compared with that of interior point methods. The performance is extensively assessed by means of computer simulations in different scenarios with vibrational energy harvesting. As benchmarks, we consider the case where the transmission policies for each sensor are *separately* optimized, as well as other cluster-based suboptimal transmission strategies. Besides, for a finite storage capacity scenarios, we evaluate the effects of long-term battery aging.

4.1 Introduction

This chapter is a natural extension of Chapter 3. To recall, in the previous chapter, we considered a simple communication scenario with two sensor nodes, where only one of them was able to harvest energy from the environment. Although the given scenario is quite simple, the insights gained therein, along with the iterative method proposed in this chapter, will ultimately allow us to solve a more general problem with multiple energy harvesting sensors.

4.1.1 Contribution

In this chapter, the focus of our study is a communication scenario where *multiple* energy-harvesting-enabled sensor nodes collaborate to transmit a common message signal to a distant base station. As for the system model, we assume the setup identical to that of Chapter 3, i.e. the information on energy harvesting arrivals is perfectly known in advance and the sensor-to-BS channels are described by using the Gaussian model. Once again, the goal is to identify the *jointly* optimal transmission policy at all energy harvesting sensors such that the total throughput up to a given deadline is maximized. In contrast to Chapter 3, the transmission policies at *all* the sensor nodes are now constrained by the corresponding energy harvesting arrivals. Consequently, the optimal policies for the scenario considered here cannot be computed independently anymore.

Since Lemma 3.1 continues to hold for the multiple energy harvesting sensor case, once again, the problem of computing the jointly optimal transmission policy can be cast into a convex program. Furthermore, this allows us to derive a semi-analytical solution which leverages on (i) the computationally-efficient iterative coordinate descent method of [40, Section 2.7]; and (ii) algorithms that we propose for *infinite* and *finite* energy storage capacity cases, on which basis one can compute the optimal policy for one sensor whilst the policy(ies) for the remaining one(s) is (are) held fixed. We also rigorously prove the optimality of the proposed method for a virtual array with an *arbitrary* number of EH sensors. Besides, we analyze the computational complexity associated with the proposed optimization scheme. In this respect, interior point methods are used as a benchmark. Finally, we extensively assess the performance of the proposed algorithm in a realistic system scenario where vibrational energy is harvested from the environment.

The contents of this chapter have been partly published in references [41], [42] and [43].

The chapter is organized as follows. First, in Section 4.2, we introduce the signal and communication model for the two energy harvesting sensor case. Next, in Section 4.3 we address a scenario where EH sensors are equipped with energy storage of infinite capacity. Subsequently, we generalize the analysis to a scenario with an arbitrary number of energy harvesting sensors. Then, in Section 4.4, we provide the analysis for a case in which multiple sensors are equipped with energy storage of finite capacity. Finally, we outline the main findings of the chapter in Section 4.5.

4.2 Signal model

Let I denote the total number of EH sensors which cooperate to transmit a common message to a distant base station. Initially, we restrict the analysis to the *two*-sensor case[1] (i.e., $I = 2$) and, thus, the received signal reads

$$r(t) = m(t)\left(\sum_{i=1}^{2} g_i^*(t)e^{j\psi_i(t)}\right) + w(t) \tag{4.1}$$

where, to recall, the common message is given by $m(t) = \sum_l x_l u(t - lT_s)$, with $\{x_l\}$ denoting a sequence of zero-mean complex Gaussian symbols with unit variance (T_s is the symbol period) and $u(t)$ standing for the impulse response of a bandlimited pulse (unit bandwidth); function $g_i(t) = \sqrt{p_i(t)}e^{-j\theta_i(t)}$ accounts for the i^{th} time-varying complex transmit weight to be designed (in polar notation); $e^{j\psi_i(t)}$ stands for the phase shift of the Gaussian sensor-to-base station channels; and $w(t)$ is zero-mean complex additive white Gaussian noise with unit variance (i.e. $w(t) \sim \mathcal{CN}(0, 1)$). By properly designing $\theta_i(t)$ for $i = \{1, 2\}$, again, we assume that the aforementioned channel phase shifts and oscillator offsets can be ideally pre-compensated (frequency and time synchronization are assumed, as well). With these assumptions, the whole sensor network behaves as a virtual array capable of *beamforming* the message to the base station. The instantaneous received power at the base station is thus given by $p_{\text{BF}}(t) = (\sqrt{p_1(t)} + \sqrt{p_2(t)})^2$, and the total throughput for a given deadline T, G_T, then reads

$$G_T = G_T\big(p_1(t), p_2(t)\big) = \int_0^T \log\big(1 + p_{\text{BF}}(t)\big)dt. \tag{4.2}$$

Once again, the aim is to identify the jointly optimal transmission (power allocation) policies $p_1(t)$ and $p_2(t)$ such that the throughput G_T is maximized subject to the constraints imposed by the energy harvesting processes, namely,

$$e_1(t) \leq E_1(t) \triangleq \sum_{k:s_k<t} E_{1,k} \quad ; \quad 0 \leq t \leq T \tag{4.3}$$

$$e_2(t) \leq E_2(t) \triangleq \sum_{k:s_k<t} E_{2,k} \quad ; \quad 0 \leq t \leq T, \tag{4.4}$$

---

[1] This initial assumption, to be relaxed in Section 4.3.4, greatly facilitates the presentation of the proposed algorithm.

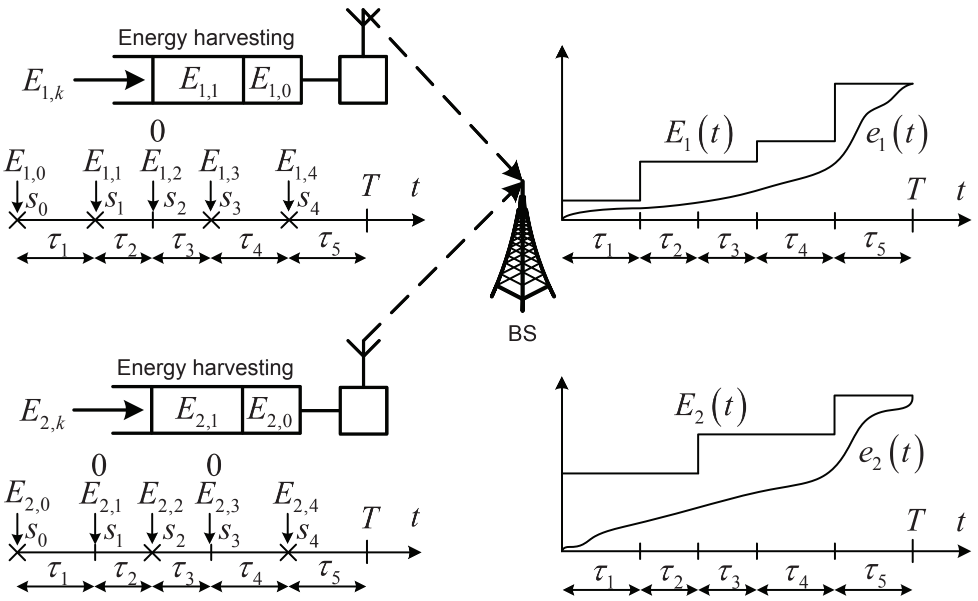

Figure 4.1: Network with two energy harvesting sensors (left); cumulative energy harvesting constraints and energy consumption curves (right).

where, again, $e_1(t) = \int_0^t p_1(\tau)d\tau$ and $e_2(t) = \int_0^t p_2(\tau)d\tau$ denote the energy *consumption* (EC) curves; and $E_1(t)$, $E_2(t)$ stand for the cumulative energy *harvesting* (cEH) constraints which, as Figure 4.1 illustrates, are both staircase functions. The rest of parameters, i.e. $E_{i,k}$, s_k and τ_k, were defined in Chapter 3.

4.3 Infinite battery capacity

In this section, we initially assume that the energy storage capacity of each sensor in the network is unlimited (infinite). In other words, each sensor is capable of storing all energy packets that arrive over time. Consequently, the transmission policy for each of them is only constrained by the corresponding cumulative energy harvesting curve. Furthermore, it can be shown that Lemmas 3.1 - 3.4 from Chapter 3 continue to hold, even for a more general scenario where all the sensors have energy harvesting capabilities. As shown in the previous chapter, this considerably simplifies the analysis, by allowing us to pose the original optimization problem given by the score function (4.2) and the causality constraints (4.3) and (4.4) into a convex optimization framework.

4.3.1 Computation of the optimal transmission policy

The problem of maximizing the throughput for a given deadline, such that energy causality constraints are satisfied[2], can be expressed as the following optimization problem:

$$
\begin{aligned}
&\max_{\{p_{1,k}\}_{k=1}^{N},\{p_{2,k}\}_{k=1}^{N}} \sum_{k=1}^{N} \tau_k \log\left(1+(\sqrt{p_{1,k}}+\sqrt{p_{2,k}})^2\right) && (4.5)\\
&\text{s.t.:}\\
&\sum_{k=1}^{n} \tau_k p_{1,k} \le E_1^n = \sum_{k=0}^{n-1} E_{1,k} \ \text{ for } n = 1\dots N && (4.6)\\
&\sum_{k=1}^{n} \tau_k p_{2,k} \le E_2^n = \sum_{k=0}^{n-1} E_{2,k} \ \text{ for } n = 1\dots N && (4.7)\\
&p_{1,k} \ge 0 \ \text{ for } k = 1\dots N && (4.8)\\
&p_{2,k} \ge 0 \ \text{ for } k = 1\dots N && (4.9)
\end{aligned}
$$

where $p_{i,k}$ account for the power at i^{th} sensor during k^{th} epoch, i.e. $p_i(t) = p_{i,k}$ for $s_{k-1} \le t < s_k$. Again, the optimization problem given by (4.5)-(4.9) turns out to be convex since the aim is to maximize a concave function subject to a set of affine constraints. In order to overcome the drawbacks associated with the numerical optimization (high computational complexity), in the remainder of this section we derive a semi-analytical solution which is computationally efficient. To that aim, we leverage on (i) the so-called iterative coordinate descent method (see Section 4.3.2); and (ii) the algorithm that we propose in Section 4.3.3, on which basis we can maximize the throughput by adjusting the policy for one sensor whilst the policy of the other sensor is held fixed.

4.3.2 Iterative coordinate descent method

Consider an optimization problem of the form:

$$
\begin{aligned}
&\max_{\mathbf{p}} f(\mathbf{p})\\
&\text{s.t.: } \mathbf{p} \in \mathcal{P}, && (4.10)
\end{aligned}
$$

where $f(\mathbf{p}) : \mathbb{R}^n \to \mathbb{R}$ is a continuously differentiable and concave function on a set $\mathcal{P}$ which, in turn, can be expressed as the Cartesian product of convex sets $\mathcal{P}_1, \dots, \mathcal{P}_n$.

In [44], the authors prove that as long as (i) f($\mathbf{p}$) is a strictly concave function of the i^{th} coordinate of vector $\mathbf{p}$ (i.e. it has a unique maximum in p_i when the remaining coordinates are held constant); and (ii) the sequence of said coordinates is generated according to an *almost cyclic rule* (or, more intuitively, every coordinate is iterated a *sufficient* number of times); an iterative

---

[2] The energy consumption curves lie below the cumulative energy harvesting constraints at all times.

procedure by which in each step a subset of coordinates in $\mathbf{p}$ are adjusted so as to minimize $f(\cdot)$ over $\mathcal{P}$ along this direction necessarily converges to the optimal solution. This procedure is referred to in the literature as the iterative coordinate descent method.

One can easily prove that the optimization problem (4.5)-(4.9) can be cast into the general framework described above and, hence, it can be solved in an iterative fashion. In this context, we let $\mathbf{p}_i = [p_{i,1}, p_{i,2}, \ldots, p_{i,N}]^T$ denote a column vector gathering the N components in the transmission policy $\{p_{i,k}\}_{k=1}^{N}$ of sensor $i \in \{1, 2\}$. Further, we define *transmission sub-policy* as the subset of transmit powers $\{p_{i,k}\}_{k=k_l}^{k_u}$ in epochs $k = k_l \ldots k_u$. Accordingly, vector $\mathbf{p}_{i,k_l:k_u} = [p_{i,k_l}, p_{i,k_l+1}, \ldots, p_{i,k_u}]^T$ gathers the transmit powers in such transmission sub-policy. Bearing all this in mind, the original optimization problem (4.5)-(4.9) can be decomposed in two individual sub-problems (one for each sensor in the network) and be iteratively solved. More precisely, in the m^{th} iteration of coordinate descent method, we update the transmission policy of the first sensor, $\mathbf{p}_1^{(m)}$, by solving the subproblem

$$\mathbf{p}_1^{(m)} = \arg\max_{\mathbf{p}_1} \sum_{k=1}^{N} \tau_k \log\left(1 + \left(\sqrt{p_{1,k}^{(m)}} + \sqrt{p_{2,k}^{(m-1)}}\right)^2\right) \tag{4.11}$$

s.t.:

$$\sum_{k=1}^{n} \tau_k p_{1,k}^{(m)} \le E_1^n = \sum_{k=0}^{n-1} E_{1,k} \quad \text{for } n = 1 \ldots N \tag{4.12}$$

$$p_{1,k}^{(m)} \ge 0 \quad \text{for } k = 1 \ldots N \tag{4.13}$$

while holding fixed the policy for the second sensor that was computed in the previous iteration, namely, $\mathbf{p}_2^{(m-1)}$. Next, we update the transmission policy of the second sensor, $\mathbf{p}_2^{(m)}$ by solving

$$\mathbf{p}_2^{(m)} = \arg\max_{\mathbf{p}_2} \sum_{k=1}^{N} \tau_k \log\left(1 + \left(\sqrt{p_{1,k}^{(m)}} + \sqrt{p_{2,k}^{(m)}}\right)^2\right) \tag{4.14}$$

s.t.:

$$\sum_{k=1}^{n} \tau_k p_{2,k}^{(m)} \le E_2^n = \sum_{k=0}^{n-1} E_{2,k} \quad \text{for } n = 1 \ldots N \tag{4.15}$$

$$p_{2,k}^{(m)} \ge 0 \quad \text{for } k = 1 \ldots N \tag{4.16}$$

while holding $\mathbf{p}_1^{(m)}$ fixed[3]. This procedure is iterated until a prescribed level of accuracy is attained or when the maximum number of iterations is reached. Since in *each* iteration *both* transmission policies are updated, the almost cyclic rule is clearly satisfied.

---

[3] Note that each subproblem includes only its own energy causality constraint. This follows from the fact that (i) causality for the other (fixed) transmission policy is enforced in the previous iteration; and (ii) causality constraints are not mutually coupled since both sensors harvest energy independently.

4.3.3 Updating the transmission policy of one sensor node

In this section, we propose an algorithm to *semi-analytically* find the (jointly) optimal transmission policy of one sensor whilst that of the other one is held fixed. Assume, without loss of generality, that we want to optimize the transmission policy of the first sensor. The Karush-Kuhn-Tucker (KKT) conditions for the sub-problem (4.11)-(4.13), read[4]:

$$\frac{\partial \mathcal{L}_1}{\partial \breve{p}_{1,k}} = 0 \tag{4.17}$$

$$\sum_{k=1}^{n} \tau_k \breve{p}_{1,k} \leq E_1^n = \sum_{k=0}^{n-1} E_{1,k} \ \text{ for } n = 1 \dots N \tag{4.18}$$

$$\breve{p}_{1,k} \geq 0 \tag{4.19}$$

$$\breve{\lambda}_n, \breve{\mu}_k \geq 0 \tag{4.20}$$

$$\breve{\lambda}_n \left(\sum_{k=1}^{n} \tau_k \breve{p}_{1,k} - E_1^n \right) = 0 \text{ for } n = 1 \dots N \tag{4.21}$$

$$-\breve{\mu}_k \breve{p}_{1,k} = 0, \tag{4.22}$$

where $\frac{\partial \mathcal{L}_1}{\partial \breve{p}_{1,k}}$ stands for the partial derivative of the Lagrangian associated with the sub-problem, namely,

$$\frac{\partial \mathcal{L}_1}{\partial \breve{p}_{1,k}} = -\tau_k \frac{\sqrt{\breve{p}_{1,k}} + \sqrt{p_{2,k}}}{\sqrt{\breve{p}_{1,k}} \left(1 + (\sqrt{\breve{p}_{1,k}} + \sqrt{p_{2,k}})^2\right)} + \tau_k \left(\sum_{n=k}^{N} \breve{\lambda}_n - \frac{\breve{\mu}_k}{\tau_k} \right). \tag{4.23}$$

In the previous chapter, it is shown that the optimal solution is such that all the powers must be strictly positive. This fact, along with the complementary slackness condition (4.22) implies that, at the optimal point $\breve{\mathbf{p}}_1$, all $\breve{\mu}_k$ must vanish, i.e. $\breve{\mu}_k = 0, \ \forall k$. Hence, by defining

$$A_k = \sum_{n=k}^{N} \lambda_n \tag{4.24}$$

the partial derivative of the Lagrangian in (4.23) can be conveniently re-written as

$$\frac{\partial \mathcal{L}_1}{\partial \breve{p}_{1,k}} = -\ \tau_k \frac{\sqrt{\breve{p}_{1,k}} + \sqrt{p_{2,k}}}{\sqrt{\breve{p}_{1,k}} \left(1 + (\sqrt{\breve{p}_{1,k}} + \sqrt{p_{2,k}})^2\right)} + \tau_k \breve{A}_k. \tag{4.25}$$

In order to compute the optimal transmission policy for the first sensor, we partly leverage on (and generalize) Algorithm 1 presented in Chapter 3. To recall, Algorithm 1 allows to analytically compute the optimal policy for a *battery operated* (BO) sensor in a virtual array composed of one EH plus one BO sensor. For a BO sensor, we have $E_{i,0} > 0$ whereas $E_{i,k} = 0$ for $k = 1 \dots N - 1$. In other words, no energy other than that initially stored in its battery is harvested during sensor operation. As a result, the cEH curve defined in (4.3) or (4.4) is no longer a staircase function. Instead, it takes a constant value for the whole $0 \leq t \leq T$ period.

---

[4] For brevity, hereinafter we omit the iteration index m.

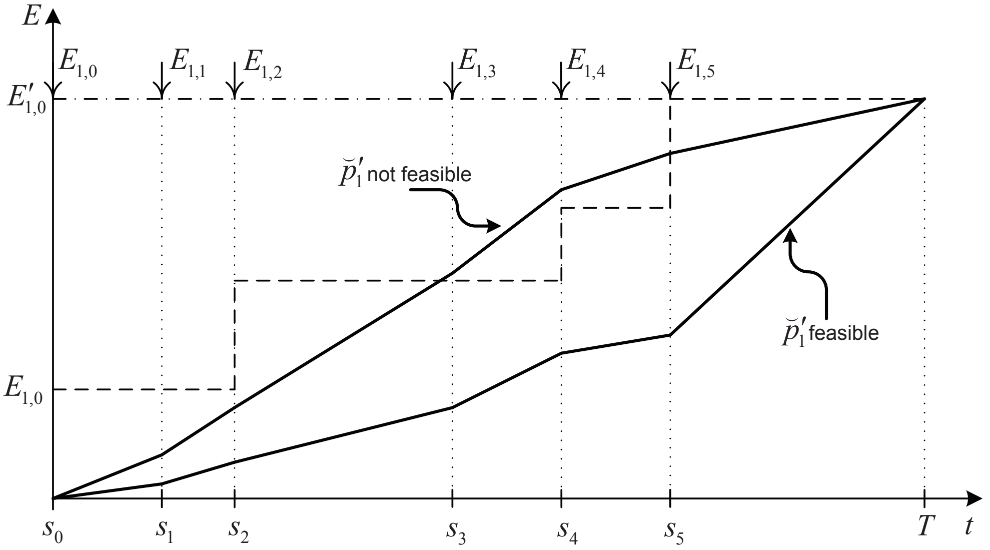

Figure 4.2: Original and virtual optimization problems. Dashed and dash-dotted lines account for the original and virtual cEH curves, respectively.

Specifically, in order to compute the optimal transmission policy for the first sensor we propose the following 4-step procedure:

1. *Check whether a BO-like solution for epochs $k = 1 \dots N$ is feasible*: To that aim, we assume that all the energy harvested by the first sensor during its operation is available from $t = 0$ (see Figure 4.2). This is equivalent to solve an optimization sub-problem where we replace the set of *actual* harvested energies $E_{1,k}$ by the following *virtual* ones

$$E'_{1,0} = \sum_{k=0}^{N-1} E_{1,k} \tag{4.26}$$

$$E'_{1,k} = 0 \tag{4.27}$$

for $k = 1 \dots N-1$. The corresponding virtual transmission policy $\breve{\mathbf{p}}'_1$ can thus be computed by using the procedure given in Algorithm 1. If such virtual transmission policy verifies the constraints (4.12)-(4.13) of the *original* sub-problem (i.e. it is feasible) then it is solved and the procedure terminated. This follows from the facts that (i) the score function optimized in the virtual and original sub-problems are identical; (ii) the sub-problem is strictly convex and, hence, the optimal solution is unique; and (iii) the solution of the virtual sub-problem is feasible for the original one too[5]. In other words, we have $\breve{\mathbf{p}}_1 = \breve{\mathbf{p}}'_1$. Interestingly enough, if the BO-like solution is feasible (and, thus, optimal) then $\breve{\mathbf{p}}_1$ is not affected by the causality constraints for $n = 1 \dots N-1$ which could well be dismissed. More formally, this is equivalent to say that, in the Lagrange dual we have $\breve{\lambda}_n = 0$ for $n = 1 \dots N-1$ (still, we must have $\breve{\lambda}_N > 0$ in order to fulfill

---

[5] Intuitively, since in a BO-like policy all the energy harvested is available from the *onset* the throughput it attains is necessarily higher than that of any other policy computed with the *actual* energy arrivals.

the necessary optimality condition given by Lemma 3.2 and, thus, enforce $\sum_{k=1}^{N} \tau_k \breve{p}_{1,k} = E_1^N$ in the KKT condition given by (4.21)).

On the contrary, if the resulting virtual policy $\breve{\mathbf{p}}_1'$ violates *one or more* causality constraint given by (4.12) then it is not feasible. In order to enforce those constraints, we necessarily have $\breve{\lambda}_n > 0$ for one or more epochs in $n = 1 \ldots N-1$ (in addition to having $\breve{\lambda}_N > 0$). Consequently, the optimal policy $\breve{\mathbf{p}}_1$ is such that the EC curve touches[6] the cEH constraints in one or more corner points of the cEH curve in $n = 1 \ldots N-1$. This case is addressed in Step 2.

2. *Find the largest $L < N$ such that a BO-like solution for epochs $k = 1 \ldots L$ is feasible and, simultaneously, the energy harvested by that sensor in s_L is non-zero*: If the BO-like *virtual* sub-policy $\mathbf{p}_{1,1:L}'$ is feasible for *original* problem, then it verifies the causality constraints for $k = 1 \ldots L$ (or, equivalently, the KKT conditions for such epochs). Hence, $\mathbf{p}_{1,1:L}'$ is a *good candidate* for the optimal transmission policy $\breve{\mathbf{p}}_1$ since, at least, it verifies the problem constraints up to the L^{th} epoch. As soon as this happens, we move to Step 3 below (otherwise, we try a smaller value of L). It is worth noting that, analogously to Step 1, the fact that this virtual sub-policy is feasible implies that, in the Lagrange dual, we have $\lambda_n = 0$ for $n = 1 \ldots L-1$ and[7] $\lambda_L > 0$. In other words, in the first L epochs the EC curve associated with this candidate hits the cEH curve in s_L *only*.

   The reason why we impose the sensor to effectively harvest some energy in s_L (i.e., $E_{1,L} > 0$) will be clarified in Step 4 below. For the time being, it suffices to say that imposing $E_{1,L} > 0$ is equivalent impose that the cEH curve has a corner point in s_L.

3. *Retain sub-policy $\mathbf{p}_{1,1:L}'$ and repeat Steps 1 and 2 for epochs $k = L+1 \ldots N$ only (instead of $k = 1 \ldots N$).* Steps 1 to 3 are iterated until all the transmit powers for epochs $k = 1 \ldots N$ have been computed as BO-like feasible solutions.

4. *Construct the optimal transmission policy as a concatenation of the BO-like sub-policies computed and retained in Steps 1-3.* This extent is illustrated in Figure 4.3 where, as an example, we have $\breve{\mathbf{p}}_1 = [\mathbf{p}_{1,1:L}^{\prime T}, \mathbf{p}_{1,L+1:M}^{\prime T}, \mathbf{p}_{1,M+1:N}^{\prime T}]^T$ with $L, M < N$. The intuition behind this approach is that, as previously discussed, each BO-like policy attains the highest possible throughput in its *own* epoch subset, which is determined in Steps 1-2. However, its *overall* optimality needs to be proved.

   As a final remark, note that should the sub-policy $\mathbf{p}_{1,1:L}'$ hit the cEH curve in a non-corner point, we would unavoidably have $p_{1,L+1}' = 0$ which contradicts the necessary optimality condition that the powers must be strictly positive. This is why in Step 2 above we imposed $E_{1,L} > 0$.

---

[6] This occurs due to the complementary slackness constraint (4.21).

[7] This is consistent with the fact that, from Step 1, we know that there exists at least one $n < N$ such that $\breve{\lambda}_n > 0$.

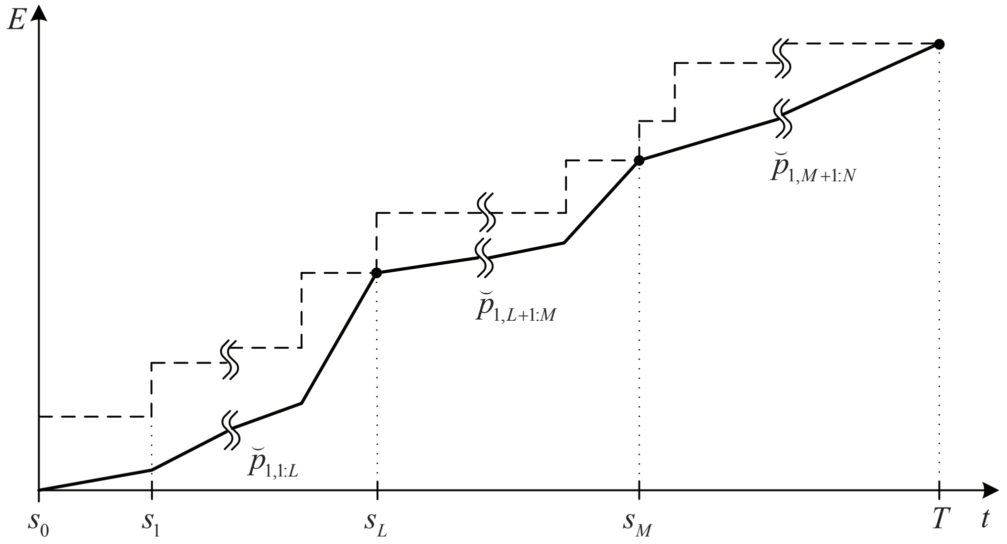

Figure 4.3: Concatenation of sub-policies.

In the remainder of this section, we prove our claim that the resulting transmission policy is indeed optimal. This motivates the following two lemmas and theorem.

Lemma 4.1 *If $L \leq N$ is the largest value for which a candidate BO-like transmission sub-policy $\mathbf{p}_{1,1:L}$ ending in a corner point of the cEH curve is feasible, then there exists no other BO-like transmission sub-policy $\mathbf{p}_{1,1:R}$ with $R < L$ such that it is part of the optimal transmission policy.*

This lemma implies that, as soon as the aforementioned largest L has been identified, there is no need to search for additional candidate sub-policies in which the EC curve touches the cEH one in a corner point at a *previous* time instant s_R (since, for sure, the overall optimal transmission policy will not include those corner points). This avoids conducting an exhaustive search over events and, hence, allows us to move from Step 2 to Step 3 as described in the procedure above without compromising optimality. This lemma can be easily proved by contradiction, as we will see next.

Proof: Consider *two* candidate transmission policies, $\mathbf{p}_1$ and $\dot{\mathbf{p}}_1$, the first L or R (respectively) elements of which, namely, $\mathbf{p}_{1,1:L}$ and $\dot{\mathbf{p}}_{1,1:R}$ with $R < L$, have been computed as BO-like solutions (see Figure 4.4). From the discussions in Steps 1 and 2 above, we know that $\mathbf{p_1}$ verifies

$$\lambda_n = 0,\ n = 1, \ldots, L-1;\ \lambda_L > 0$$

and, as long as $L < N$,

$$\lambda_n \geq 0,\ n = L+1, \ldots, N \tag{4.28}$$

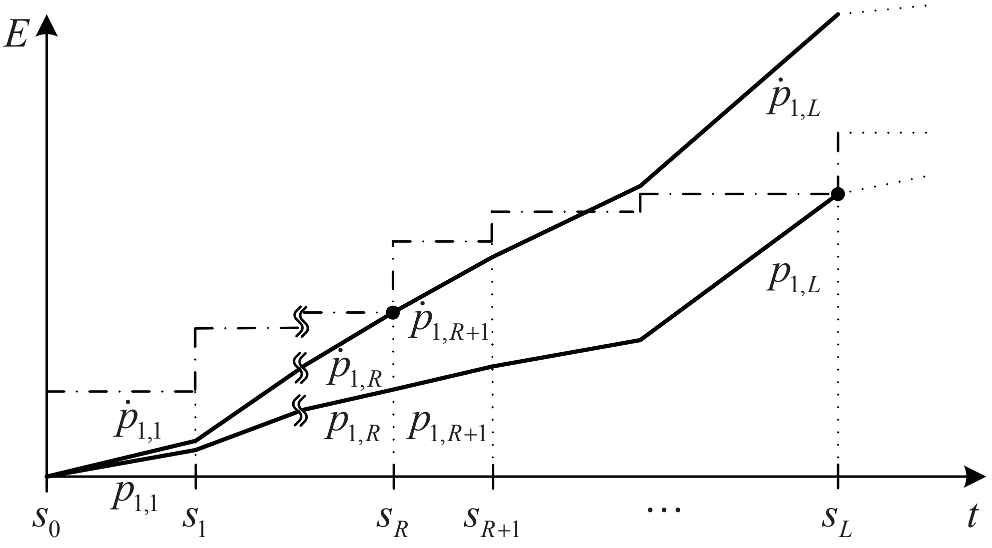

Figure 4.4: Lemma 4.1: A sub-policy consuming all the harvested energy in s_R is not feasible and, thus, is not part of the overall optimal policy.

where (4.28) follows from the KKT conditions. From this, the corresponding sums of Lagrangian multipliers A_k verify in turn

$$A_1 = A_2 = \ldots = A_L = \sum_{n=L}^{N} \lambda_n. \tag{4.29}$$

Likewise, for $\dot{\mathbf{p}}_1$ we have

$$\begin{aligned} &\dot{\lambda}_n = 0,\ n = 1, \ldots, R-1;\ \dot{\lambda}_R > 0 \\ &\dot{\lambda}_n \geq 0,\ n = R+1, \ldots, N \end{aligned} \tag{4.30}$$

and, hence,

$$\dot{A}_1 = \dot{A}_2 = \ldots = \dot{A}_R = \sum_{n=R}^{N} \dot{\lambda}_n. \tag{4.31}$$

Since in s_R the EC curve associated with $\dot{\mathbf{p}}_1$ lies above that of $\mathbf{p}_1$ (see Figure 4.4), there necessarily exists at least one epoch $k_o \in \{1 \ldots R\}$ such that $\dot{p}_{1,k_o} > p_{1,k_o}$. Besides, a necessary condition for either candidate sub-policy to qualify as optimal, is that the corresponding derivative of the Lagrangian given by (4.25) must vanish for *all* $k \in \{1 \ldots R\}$, namely, $\frac{\partial \mathcal{L}_1}{\partial \breve{p}_{1,k}} = 0$. In particular, for $k = k_o$ the fact that $\dot{p}_{1,k_o} > p_{1,k_o}$ implies that $\dot{A}_{k_o} < A_{k_o}$ (and vice-versa: if $\dot{p}_{1,k_o} < p_{1,k_o}$ then $\dot{A}_{k_o} > A_{k_o}$). Moreover, from (4.29) and (4.31), we conclude that $\dot{A}_k < A_k$ for *all* $k \in \{1 \ldots R\}$ which, in turn, implies $\dot{p}_{1,k} > p_{1,k}$ for those epochs. In other words, the EC curve associated with the candidate sub-policy $\dot{\mathbf{p}}_{1,1:R}$ lies *strictly* above that of $\mathbf{p}_{1,1:R}$ for *all* those epochs, as Figure 4.4 illustrates. This holds true in particular for $k = R$, namely, $\dot{p}_{1,R} > p_{1,R}$. For the next epoch, we have that either $\dot{p}_{1,R+1} < p_{1,R+1}$ or $\dot{p}_{1,R+1} \geq p_{1,R+1}$. The former would hold if (and only if)

$$\dot{A}_R < A_R = A_L \tag{4.32}$$

$$\dot{A}_{R+1} > A_{R+1} = A_L \tag{4.33}$$

which renders $\dot{\lambda}_R = \dot{A}_R - \dot{A}_{R+1} < 0$. Since this contradicts one KKT condition then, necessarily, $\dot{p}_{1,R+1} \geq p_{1,R+1}$. By applying the same reasoning to the subsequent consecutive epoch pairs, we conclude that $\dot{p}_{1,k} \geq p_{1,k}$ for all $k \in \{R+1, L\}$. Hence, the EC curve associated with the candidate sub-policy $\dot{\mathbf{p}}_{1,1:L}$ lies strictly above that of $\mathbf{p}_{1,1:L}$ not only for the first R epochs but for *all* epochs $k \in \{1 \ldots L\}$. Since, to recall, at s_L the EC associated with the candidate sub-policy $\dot{\mathbf{p}}_{1,1:L}$ hits the cEH curve, this means that the candidate sub-policy $\dot{\mathbf{p}}_{1,1:L}$ is necessarily not feasible and, thus, cannot be part of the overall optimal policy (see Figure 4.4). This concludes the proof.

To insist, this Lemma does not state that $\mathbf{p}_{1,1:L}$ *is* part of the overall optimal policy (to that aim we need Lemma 4.2 next) but, instead, that $\dot{\mathbf{p}}_{1,1:L}$ *cannot* be part of it. ■

Lemma 4.2 *If $L \leq N$ is the largest value for which a candidate BO-like sub-policy $\mathbf{p}_{1,1:L}$ ending in a corner point of the cEH curve is feasible then such sub-policy is necessarily part of the optimal transmission policy $\breve{\mathbf{p}}_1$.*

Proof: For the $L = N$ case, the proof is trivial. In order to prove the lemma for $L < N$, notice that from Step 1 we know that there exists one (or more) $\breve{\lambda}_k > 0$ for $k = 1 \ldots N-1$. In other words, the EC curve hits the cEH curve in some corner point(s) at s_k with $k = 1 \ldots N-1$. Assume that this occurs for the first time at $k = N-1$. If so, the corresponding BO-like sub-policy is feasible and $\lambda_{N-1} > 0$. Otherwise, we know that the EC curve hits the cEH one for the first time in some corner point(s) at s_k for $k = 1 \ldots N-2$ for which $\lambda_k > 0$. We recursively apply this procedure and, for $k = L+1$, we realize that the corresponding BO-like policy is again not feasible and, thus, the first $\lambda_k > 0$ is necessarily in the range $k = 1 \ldots L$. Finally, for $k = L$ the BO-like policy is feasible and, from Lemma 4.1, we know that the EC curve associated with the optimal transmission policy does not touch the cEH one in a corner point at a *previous* time instant. Therefore only the BO-like transmission sub-policy $\mathbf{p}_{1,1:L}$ is in a position to satisfy the $\lambda_k > 0$ for some $k = 1 \ldots L$ and, thus, it *must* be part of the overall optimal transmission policy. This concludes the proof. ■

Theorem 4.1 *When the transmission policy for the second sensor is held fixed, the jointly optimal transmission policy for the first sensor, $\breve{\mathbf{p}}_1$, can be computed with the procedure given in Algorithm 2.*

Algorithm 2 is nothing but a more formal representation of the 4-step procedure described above. The corresponding proof of its optimality follows.

Algorithm 2 Optimal policy for sensor 1 with infinite storage capacity (m^{th} iteration)

```
$m$                                          ▷ Current iteration index
$k_l = 1$                                    ▷ Transmission sub-policy starts in epoch 1
$k_u = N$                                    ▷ Transmission sub-policy ends in epoch $N$
$\mathbf{p}_2 := \mathbf{p}_2^{(m-1)}$       ▷ Let the transmission policy for sensor 2
                                             ▷ be the one computed in the previous iteration.
repeat
    Compute BO-like sub-policy $\mathbf{p}'_{1,k_l:k_u}$ as per Algorithm 1
    if ($\mathbf{p}'_{1,k_l:k_u}$ is feasible) then
        $\mathbf{p}_1^{(m)}[k_l : k_u] \leftarrow \mathbf{p}'_{1,k_l:k_u}$
        $k_l \leftarrow k_u + 1$
        $k_u \leftarrow N$
    else
        repeat
            $k_u \leftarrow k_u - 1$
        until $E_{1,k_u} > 0$                ▷ Sub-policy ends in corner point
    end if
until $k_l > k_u$
```

Proof: After computing and retaining the candidate sub-policy $\mathbf{p}_{1,1:L}$, we only need to compute the remaining elements of the optimal transmission policy, namely, $\breve{p}_{1,k}$ for $k = L+1 \ldots N$. Since at s_L the total energy spent equals the energy harvested, the elements $k = L+1 \ldots N$ exclusively depend on the energy harvested in *subsequent* events (i.e. not in the previous ones, or on the optimal transmit powers for the preceding epochs). Thus, we can simply re-start the 4-step procedure above for epoch $L+1$ onwards, as it is done in Step 3. The overall optimal transmission policy is finally computed as a concatenation of the BO-like sub-policies computed in Steps 1-3, which is accomplished in Step 4. ■

To conclude this section, in Figure 4.5 we depict the transmission policies of both sensors when (i) both policies are *jointly* optimized (JO); and (ii) such policies are separately optimized (SO) as in the single-sensor scenario addressed in [17], which is suboptimal for a virtual antenna array. The corresponding transmission policies are clearly different. The impact in terms of throughput will be assessed in detail in Section 4.3.6.

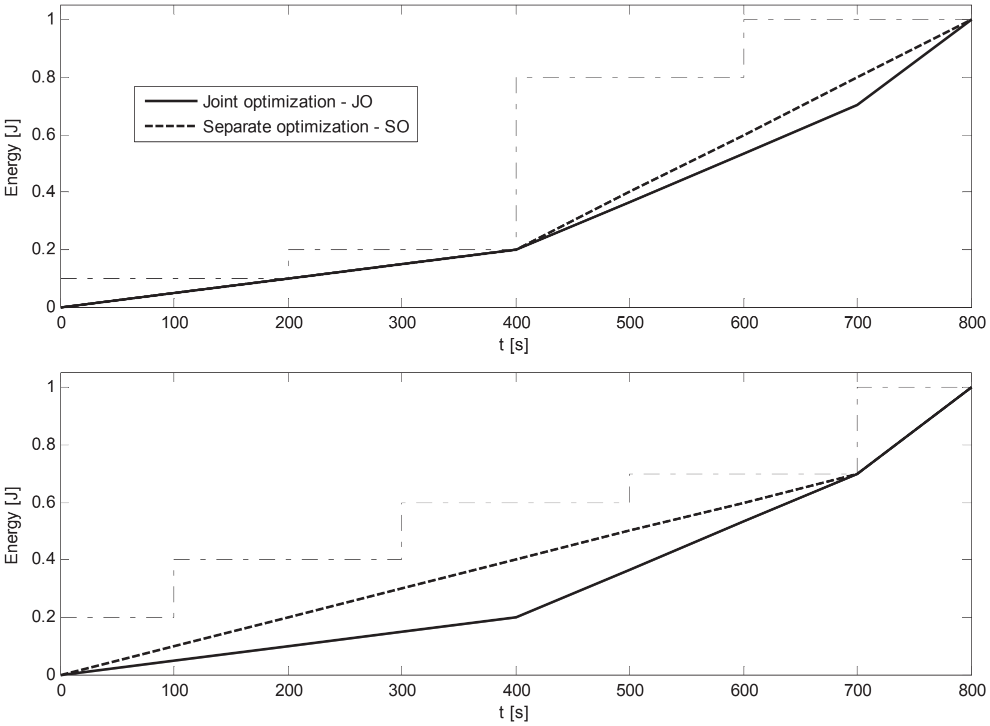

Figure 4.5: Joint vs. separate optimization of transmission policies ($I = 2$).

4.3.4 Generalization to networks with an arbitrary number of sensors

For the general case of a network with I energy-harvesting sensors, the optimization problem reads

$$\max_{\mathbf{p}_1,\mathbf{p}_2,\cdots\mathbf{p}_I} \sum_{k=1}^{N} \tau_k \log\left(1+\left(\sum_{i=1}^{I}\sqrt{p_{i,k}}\right)^2\right) \tag{4.34}$$

s.t.:

$$\sum_{k=1}^{n} \tau_k p_{i,k} \leq E_i^n = \sum_{k=0}^{n-1} E_{i,k};\ i = 1\ldots I \tag{4.35}$$

$$n = 1\ldots N$$

$$p_{i,k} > 0;\ i = 1\ldots I \tag{4.36}$$

$$k = 1\ldots N.$$

In order to generalize the results from the previous sections, it suffices to (i) show that the score function (4.34) is *strictly* concave as well; and (ii) ensure that the sequence of transmission policy updates of the iterative coordinate descent method is almost cyclic. The latter can be enforced by e.g. sequentially updating all sensor transmission policies in *each* iteration (namely, $\mathbf{p}_1^{(m)} \rightarrow \mathbf{p}_2^{(m)} \rightarrow \ldots \rightarrow \mathbf{p}_I^{(m)} \rightarrow \mathbf{p}_1^{(m+1)} \rightarrow \ldots$). As for the former, it is worth noting again that the k^{th} term in the summation, namely

$$G_k(p_{1,k}...p_{I,k}) = \tau_k \log\left(1 + \left(\sum_{i=1}^{I} \sqrt{p_{i,k}}\right)^2\right), \tag{4.37}$$

exclusively depends on the vector of transmit powers in the k^{th} epoch. In other words, there are no cross variables. In these circumstances, it suffices to show that for *any* k, $G_k(\cdot)$ is a strictly concave function. This holds true if its Hessian $\nabla^2 G_k$ is negative definite (namely, $\nabla^2 G_k \prec 0$) in its domain, that is, if $\mathbf{y}^T \nabla^2 G_k \mathbf{y} < 0$ for all *non-zero* vectors $\mathbf{y} \in \mathbb{R}^I$.

Let us define functions $f(\cdot)$ and $h(\cdot)$ as

$$f(h) = \log(1 + h) \tag{4.38}$$

$$h(\mathbf{p}) = \left(\sum_{i=1}^{I} \sqrt{p_i}\right)^2 \tag{4.39}$$

From these definitions, we can write $G(\mathbf{p}) = f(h(\mathbf{p}))$ where we have omitted the epoch index k for brevity. Its Hessian can thus be expressed as[8]:

$$\nabla^2 G = \nabla h \frac{\partial^2 f}{\partial h^2}\Big|_{h=h(\mathbf{p})} \nabla h^T + \frac{\partial f}{\partial h}\Big|_{h=h(\mathbf{p})} \nabla^2 h \tag{4.40}$$

with

$$\nabla h = \left(\sum_{i=1}^{I} \sqrt{p_i}\right) \cdot \left[\ \tfrac{1}{\sqrt{p_1}} \tfrac{1}{\sqrt{p_2}} \cdots \tfrac{1}{\sqrt{p_I}}\ \right]^T, \tag{4.41}$$

$$\frac{\partial^2 f}{\partial h^2}\Big|_{h=h(\mathbf{p})} = -\frac{1}{\left(1 + \left(\sum_{i=1}^{I} \sqrt{p_i}\right)^2\right)^2}, \tag{4.42}$$

$$\frac{\partial f}{\partial h}\Big|_{h=h(\mathbf{p})} = \frac{1}{1 + \left(\sum_{i=1}^{I} \sqrt{p_i}\right)^2}, \tag{4.43}$$

and

$$\nabla^2 h = \frac{1}{2} \begin{bmatrix} -\frac{\sum_{i=1}^{I} \sqrt{p_i} - \sqrt{p_1}}{\sqrt{p_1}^3} & \cdots & \frac{1}{\sqrt{p_1}\sqrt{p_I}} \\ \frac{1}{\sqrt{p_1}\sqrt{p_2}} & \ddots & \frac{1}{\sqrt{p_2}\sqrt{p_I}} \\ \vdots & \ddots & \vdots \\ \frac{1}{\sqrt{p_1}\sqrt{p_I}} & \cdots & -\frac{\sum_{i=1}^{I} \sqrt{p_i} - \sqrt{p_I}}{\sqrt{p_I}^3} \end{bmatrix}. \tag{4.44}$$

---

[8] The composition of *strictly* concave functions is not necessarily a *strictly* concave function [32]. This is why, in the sequel, we derive a specific proof for the function of interest.

After some tedious manipulations, it yields

$$\begin{aligned}\mathbf{y}^T\nabla^2 G\,\mathbf{y} = -\frac{1}{1+h(\mathbf{p})}\cdot\Bigg[&\underbrace{\frac{h(\mathbf{p})}{1+h(\mathbf{p})}\cdot\left(\sum_{i=1}^{I}\frac{y_i}{\sqrt{p_i}}\right)^2}_{L_1}\\ &-\underbrace{\frac{1}{2}\left(\sum_{i=1}^{I}\frac{y_i}{\sqrt{p_i}}\right)^2}_{L_2}\\ &+\underbrace{\frac{1}{2}\left(\sum_{i=1}^{I}\frac{y_i^2}{\sqrt{p_i}^2}\cdot\frac{1}{\sqrt{p_i}}\sum_{j=1}^{I}\sqrt{p_j}\right)}_{L_3}\Bigg]\end{aligned} \tag{4.45}$$

Interestingly, from Cauchy-Schwartz's inequality [39, Section 1.6.2], the following relationship between the L_2 and L_3 terms can be established:

$$\begin{aligned}L_3 &= \frac{1}{2}\left(\sum_{i=1}^{I}\frac{y_i^2}{\sqrt{p_i}^2}\cdot\frac{1}{\sqrt{p_i}}\right)\cdot\left(\sum_{j=1}^{I}\sqrt{p_j}\right)\\ &\geq \frac{1}{2}\left(\sum_{i=1}^{I}\frac{y_i}{\sqrt{p_i}}\cdot\frac{\sqrt[4]{p_i}}{\sqrt[4]{p_i}}\right)^2 = \frac{1}{2}\left(\sum_{i=1}^{I}\frac{y_i}{\sqrt{p_i}}\right)^2 = L_2\end{aligned} \tag{4.46}$$

where the equality holds if (and only if) $y_i = \alpha p_i$ for all i, that is, if vectors $\mathbf{y}$ and $\mathbf{p}$ are co-linear. Besides, we know that all transmit powers p_i are strictly positive and, hence, from (4.39) we have $h(\mathbf{p}) > 0$. Thus, from (4.45) it follows that $\nabla^2 G$ is negative definite iff $L_1 - L_2 + L_3 > 0$. Since vector $\mathbf{y}$ is different from zero, this implies $L_1, L_2 > 0$, and $L_3 > 0$. If vectors $\mathbf{y}$ and $\mathbf{p}$ are not co-linear then $L_3 > L_2$ and, consequently, $L_1 - L_2 + L_3 > 0$. If, on the contrary, vectors $\mathbf{y}$ and $\mathbf{p}$ are co-linear then $L_2 = L_3$ which yields $L_1 - L_2 + L_3 = L_1$. Since $y_i = \alpha p_i$ this means that all y_i are either strictly positive or negative. Consequently, $L_1 > 0$ and, again, this yields $\mathbf{y}^T\nabla^2 G\,\mathbf{y} < 0$, which concludes the proof.

4.3.5 Computational complexity analysis

In this section, we analyze the computational complexity of the proposed joint optimization scheme, and compare it with that of the popular interior point methods [45]. More precisely, we focus on the number of operations needed in order to determine the (jointly) optimal transmission policy of one sensor while holding the rest fixed. This renders the comparison independent of the number of iterations of the coordinate descent method described in Section 4.3.2 which depends inter-alia on the required precision.

To recall, we construct the jointly optimal transmission policy as the concatenation of a number of feasible BO-like sub-policies. Necessarily, each sub-policy starts and ends in a corner point of its cEH curve (see Figure 4.3). For large I, the average number of corner points in *each* cEH curve reads $P = N/I$. The total number of corner points in the optimal policy is, thus, within the $1 \ldots P$ range. The *maximum* (worst-case) number of BO-like sub-policies that need to be checked for feasibility (i.e. pseudo-instructions 6 to 15 in Algorithm 2) equals $P + (P-1) + (P-2) + ... + 1 = \frac{P(P-1)}{2}$. The *minimum* number (best-case) is, clearly, 1 (when the EH sensor behaves as a BO one), whereas the actual number depends on the specific realization of energy arrivals. In all cases, though, the number of epochs in each sub-policy is upper-bounded by N. For each of those epochs, the BO-like transmit power is computed according to the *iterative* procedure given by Algorithm 1, which essentially entails solving the third order equation in pseudo-instruction 8. Still, the number of operations that solving it entails, Ω, does *not* depend on the problem dimensionality (e.g. N, or I). Finally, the total number of times that such third order equation needs to be solved depends on χ, namely, the required accuracy with which the constraint in pseudo-instruction 11 of Algorithm 1 is enforced. When a bi-section scheme is adopted (rather than the grid search actually used in Algorithm 1), the total number of iterations needed scales as $\log(\frac{1}{\chi})$ [38]. Bearing all the above in mind, the computational complexity of the proposed scheme is upper-bounded by

$$\mathcal{O}\left(P^2 \cdot N \cdot \Omega \cdot \log\left(\frac{1}{\chi}\right)\right) = \mathcal{O}\left(\frac{N^3}{I^2} \cdot \Omega \cdot \log\left(\frac{1}{\chi}\right)\right) \tag{4.47}$$

and lower-bounded by

$$\mathcal{O}\left(N \cdot \Omega \cdot \log\left(\frac{1}{\chi}\right)\right). \tag{4.48}$$

The computational complexity of interior point methods reads [45]

$$\mathcal{O}\left(N^3 \cdot \log\left(\frac{1}{\epsilon}\right)\right). \tag{4.49}$$

where parameter ϵ is directly related with the accuracy with which the optimization problem is solved. Clearly, even for the upper bound of (4.47), the computational complexity savings are on the order of I^2. This is of utmost importance since the number of sensors in such networks is typically high. Furthermore, Figure 4.6 reveals that the *actual* number of times that a BO-like policy needs to be checked for feasibility (averaged over realizations) is substantially below the $\frac{P \cdot (P-1)}{2}$ figure of the worst case. For this particular yet representative setting, it was empirically found to be $\mathcal{O}\left(NP\right)$. Consequently, the actual savings are much larger than those predicted by the upper bound (4.47).

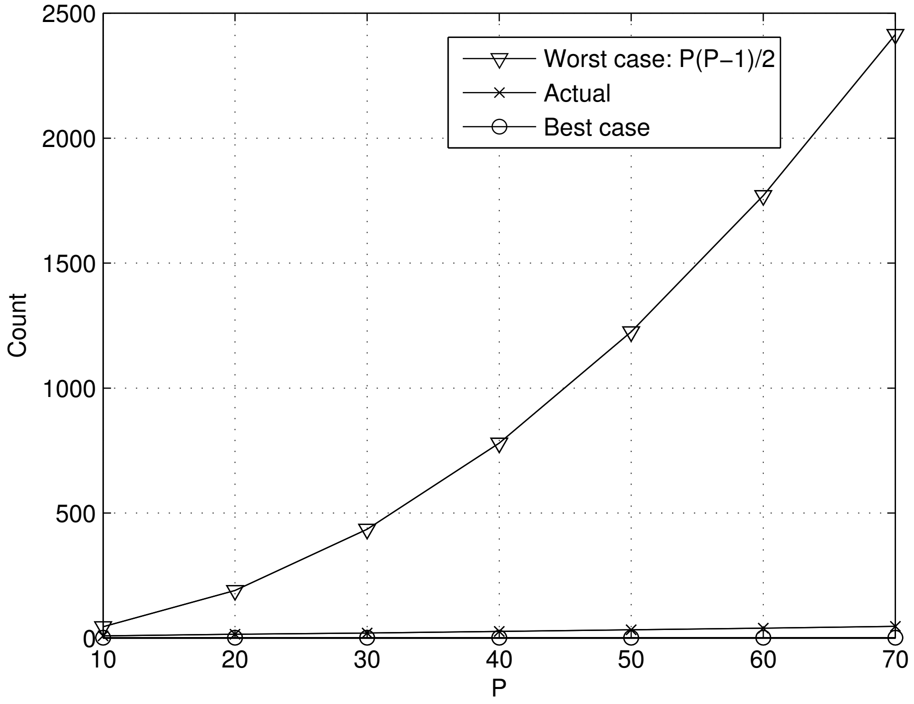

Figure 4.6: Number of times that a BO-like sub-policy needs to be checked for feasibility: worst-case, best-case, and actual number averaged over realizations ($I = 32$, $E_T = 1$ J).

4.3.6 Simulations and numerical results

In this section, we assess the performance of the proposed power allocation algorithm in a scenario where vibrational energy is harvested from the environment. More precisely, sensors are assumed to be deployed along a roadside and the energy they harvest is generated by passing-by vehicles (see Figure 4.7). As for the energy storage device, we use the model introduced in

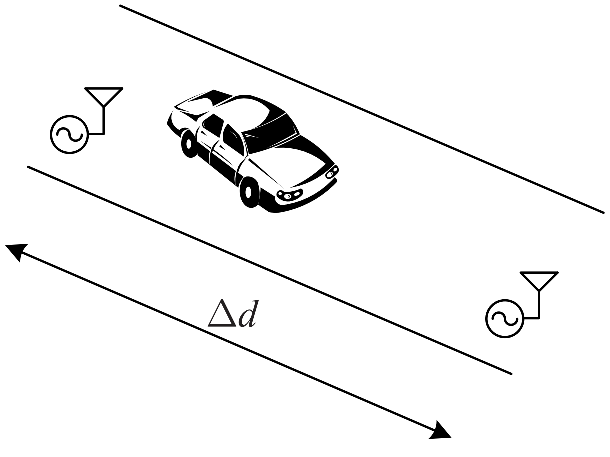

Figure 4.7: Vibration energy harvesting, two sensor nodes.

Section 3.3.3. Except in very dense traffic conditions, the levels of vibrational energy change over time (e.g. when a vehicle passes by), and so does the *average* number of energy arrivals (events). Consequently, the stochastic process that models energy arrivals is non-stationary. In the sequel, we adopt a Poisson process with time-varying mean given by $\lambda_E(t)$. For simplicity, we assume that sensors harvest energy at a *constant* rate $\lambda_E(t) = \lambda_o$ when the vehicle is in its vicinity, and $\lambda_E(t) = 0$ otherwise (i.e. $\lambda_E(t)$ is given by a sequence of rectangular pulses).

Hereinafter, we let $E_T^i = \sum_{k=0}^{N-1} E_{i,k}$ denote the total energy harvested by the i^{th} sensor; whereas $E_T = \sum_{i=1}^{I} E_T^i$ accounts for the total energy in the system. In all plots, we have set $T = 320$ s.

Two-sensor case

Here, we assume that two sensors have been deployed at normalized locations $d_1 = 0.05$ and $d_2 \geq d_1$. The normalized inter-sensor distance is denoted by $\Delta d = d_2 - d_1$. Each sensor $i \in \{1, 2\}$ is assumed to harvest energy when the passing vehicle is within a road segment centered in d_i and total normalized length[9] 0.1. Further, we define $R_E = E_T^1 / E_T^2$ as the ratio between the total energy harvested by the first and second sensors, respectively (i.e. for large R_E, the first sensor dominates).

In Figure 4.8, we depict the throughput attained by the virtual array when using the jointly optimal (JO) transmission policy described in Sections 4.3.1 and 4.3.3.

As a benchmark, we consider a system in which the transmission policy for each sensor is separately optimized (SO) as in [17], which is suboptimal for a virtual array. The total energy harvested by each sensor is identical ($R_E = 1$) and the results are shown as a function of normalized inter-sensor distance Δd. For small E_T, the throughput attained by the JO transmission policy is approximately constant for the whole range of Δd values. On the contrary, the performance exhibited by the SO policy degrades when inter-sensor distance increases: since the first sensor ignores that the second one is idle for most of the time, its harvested energy is mostly wasted *before* the second sensor starts transmitting. In other words, the JO transmission policy tends to allocate (shift) more energy to the period of time where *both* sensors are active. The beamforming gain that it entails, results into a higher throughput. For this range of E_T values, the larger the inter-sensor distance, the more noticeable this effect becomes. This extent is illustrated for a particular realization in Figure 4.9.

On the contrary, for large E_T the jointly optimal and suboptimal transmission policies are almost identical, as shown in Figure 4.10. This is due to the fact that throughput scales *logarithmically* in the transmit power (and, thus, on the total harvested energy) and *linearly* in the transmission time. Hence, for large E_T it makes no sense for sensor 1 to *wait* until sensor

---

[9] Ultimately, this value depends on the sensitivity of the EH device

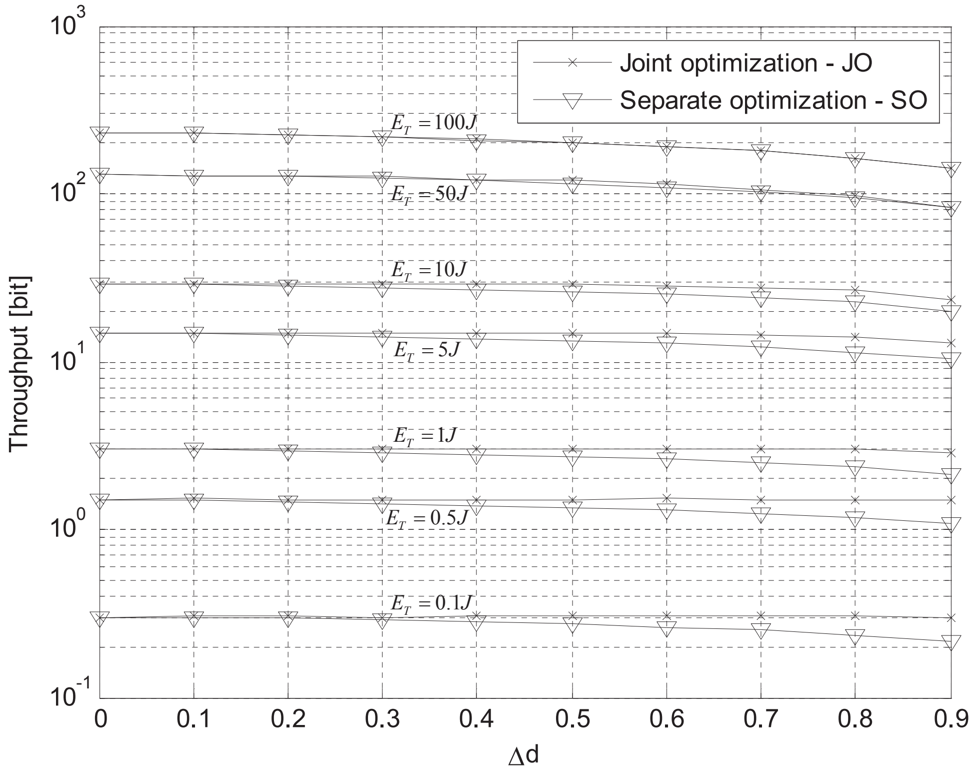

Figure 4.8: Throughput vs. normalized inter-sensor distance for several levels of total energy harvested E_T ($R_E = 1$, $I = 2$).

2 starts transmitting: the additional beamforming gain (and instantaneous throughput) cannot compensate the *saturation* effect of the concave $\log$ function and the reduced transmission time. Instead, it is optimal to let sensor 1 transmit for most of the time, as the SO solution does. In other words, joint optimization of transmission policies is particularly useful in the low-SNR regime (i.e. for small E_T). Indeed, for large inter-sensor distances and large E_T, the throughput achievable by the jointly optimal policy decreases as well, since the contribution of the second sensor vanishes. The larger E_T, the more noticeable this effect is for smaller values of inter-sensor distance, as Figure 4.8 illustrates.

Figure 4.11 provides further insights on the throughput *gain* stemming from the joint optimization of transmission policies. More precisely, we depict the throughput ratio $R_G = \frac{G_{T,\text{opt}}}{G_{T,\text{subopt}}}$ as a function of inter-sensor distance. The throughput gain can be as high as 40% when the total amount of energy harvested is small ($E_T = 0.1$ J) and inter-sensor distance high ($\Delta d = 0.9$). For large E_T values and, in particular, in the case of distant sensors, the gain vanishes, as discussed in the previous paragraph.

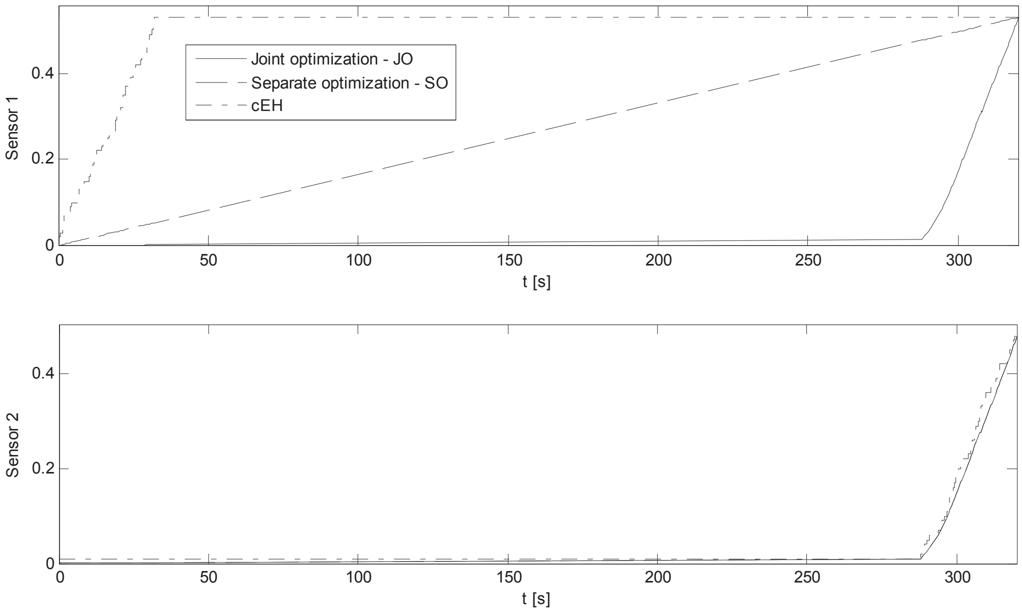

Figure 4.9: Joint and separate optimization of transmission policies for one particular realization of energy arrivals ($E_T = 1J$, $\Delta d = 0.9$, $I = 2$, $R_E = 1$).

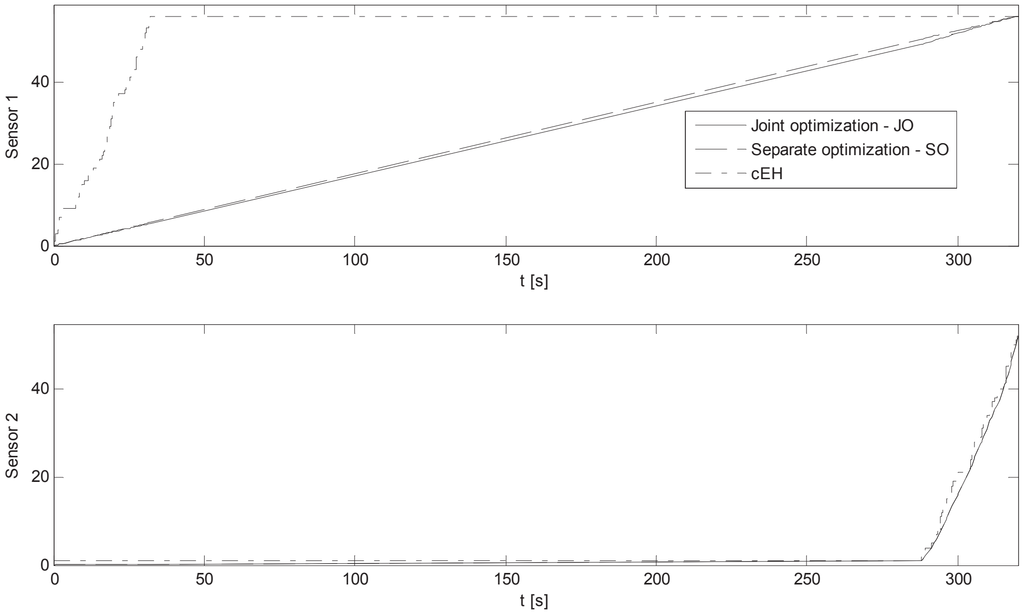

Figure 4.10: Joint and separate optimization of transmission policies for one particular realization of energy arrivals ($E_T = 100J$, $\Delta d = 0.9$, $I = 2$, $R_E = 1$).

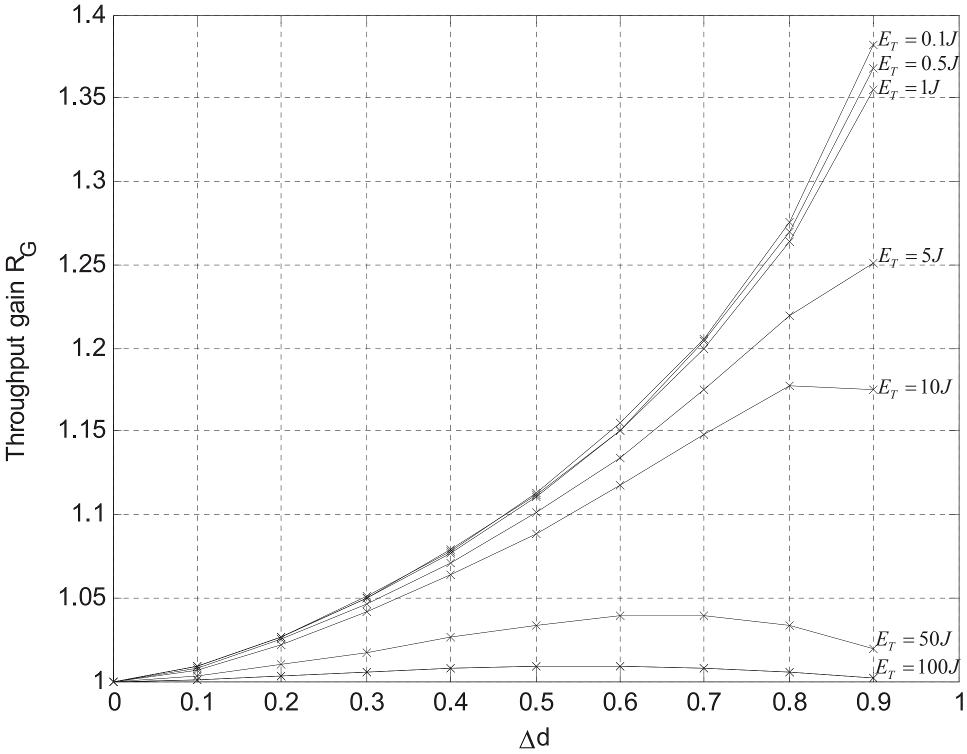

Figure 4.11: Throughput gain vs. normalized inter-sensor distance ($R_E = 1$, $I = 2$).

Next, in Figure 4.12, we depict the throughput gain vs. total system energy, for a number of energy ratios $R_E = E_T^1/E_T^2$ between the first and second sensors. Interestingly enough, the highest gain for most scenarios is attained when the energies harvested by the first and second sensors are identical, that is, for $R_E = 1$. Conversely, when either the first or second sensor dominate ($R_E \ll 1$ or $R_E \gg 1$, respectively) the gain from the joint optimization becomes marginal ($R_G \to 1$) since the signal received from the other sensor is weak. We also observe that, in the case of unbalanced energy levels[10], the throughput gain is lower when the first sensor dominates. In other words, when $E_T^1 \gg E_T^2$ the transmission policy of the second (weak) sensor has very little impact in that of the first (strong) one, which is close to that resulting from a separate optimization over sensors. Finally, and as it was discussed earlier, all throughput gains vanish in the high-SNR regime (i.e. for large E_T).

---

[10] Such an imbalance might result e.g. from differences in the transduction efficiency of the two energy harvesting devices.

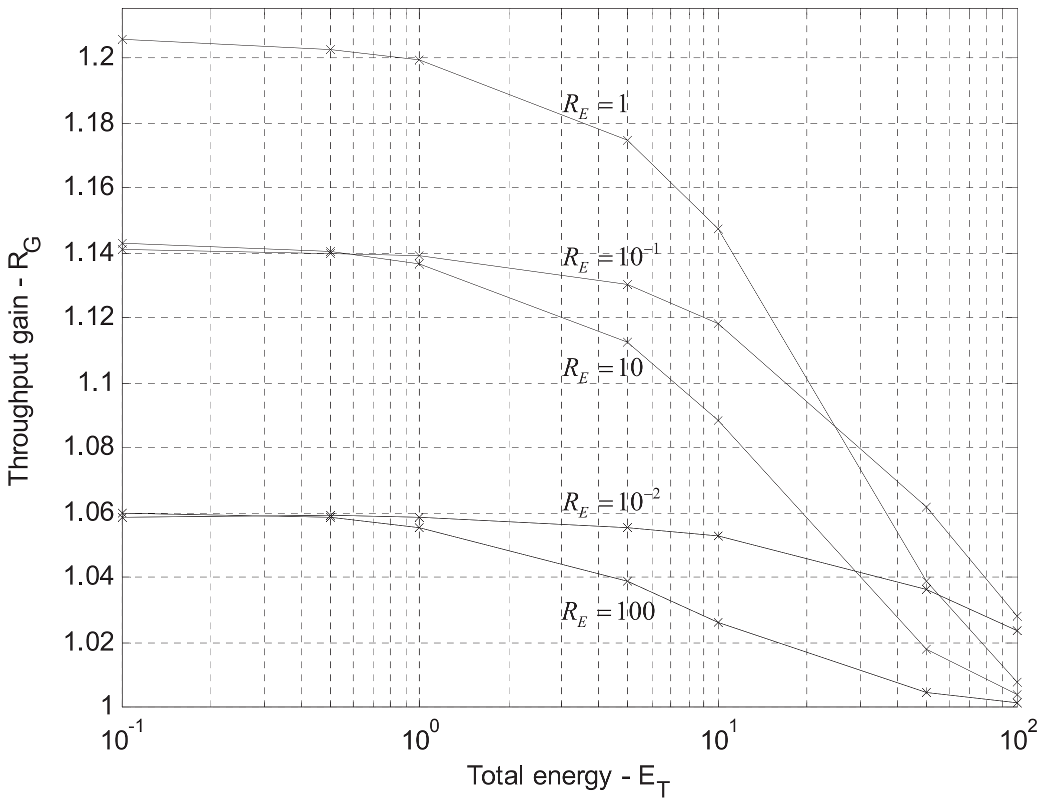

Figure 4.12: Throughput gain vs. total energy harvested ($\Delta d = 0.7$, $I = 2$).

Multiple-sensor case

Hereinafter, we consider a deployment scenario where the $I > 2$ sensors in the network are grouped into N_c non-overlapping and homogeneous clusters, each with I/N_c sensors, as shown in Figure 4.13.

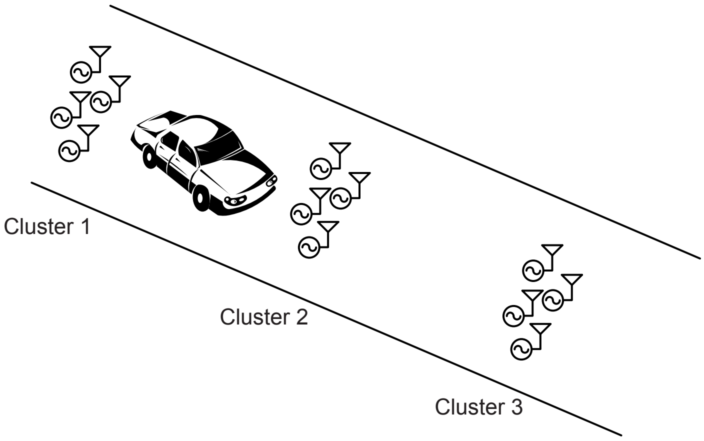

Figure 4.13: Vibration energy harvesting, multiple sensor nodes grouped into N_c clusters.

The sensors in the i^{th} cluster are deployed in the vicinity of the normalized location $d_i =$

Table 4.1: Optimization mechanisms and parameter set-up for each strategy.

Strategy	Optimiz.	Max. Nr. sensors	Max. Tx time
Joint Optimization	Joint	I	T
Separate Optimization	Separate	I	T
Cluster-by-cluster	Joint	I/N_c	T/N_c
All sensors, last cluster	Joint	I	T/N_c

$0.05 + i/N_c$ for $i = 0 \ldots N_c - 1$ and, again, they harvest energy when the passing vehicle is within a road segment centered in d_i and total normalized length equal to 0.1. It is assumed that all the sensing devices are identical and, thus, we have $E_T^i = E_T/I$ for all i. As far as the computation of the transmission policy for each sensor is concerned, we consider four possible strategies, namely,

- **Joint Optimization (JO)**: Here, again, we compute the jointly optimal transmission policy for each sensor as proposed in Section 4.3.4. Hence, the maximum number of active sensors in the virtual array and, thus, the maximum beamforming gain is I. All sensors are allowed to transmit data at any time instant in $[0 \ldots T]$ (of course, as long as some energy has been harvested before). Clearly, this strategy will attain the highest possible throughput. Subsequent ones are suboptimal and will be used as benchmarks.

- **Separate Optimization (SO)**: As in the two-sensor case, here the transmission policy for each sensor is separately optimized (vs. jointly).

- **Cluster-by-cluster (CbC)**: In this strategy, the sensors in the i^{th} cluster are allowed to transmit data until the first sensor in the $(i+1)^{\text{th}}$ cluster becomes active. As a result, (i) the maximum number of simultaneously active sensors is I/N_c; and, (ii) the maximum transmission time for a specific sensor is, roughly, T/N_c. That is, the beamforming gain is lower and the transmission time is shorter than in the previous strategies.

- **All sensors, last cluster (ASLC)**: Here, we assume that the sensors in the first $N_c - 1$ clusters harvest some energy, they store it in their respective batteries, and postpone data transmissions until the first sensor in the N_c cluster harvests some energy (i.e. the time instant in which data transmission for the last cluster can start). As a result, the maximum transmission time for a given sensor is, again, T/N_c; and the maximum number of active sensors equals I.

For the sake of comparison, Table 4.1 summarizes the mechanisms to compute the transmission policy and provides details on the parameter set-up for each strategy. In Figure 4.14, we depict the throughput attained by the various strategies in a low to mid-SNR scenario ($E_T = 1$ J). Unsurprisingly, throughput is a monotonically increasing function in the number of sensors for

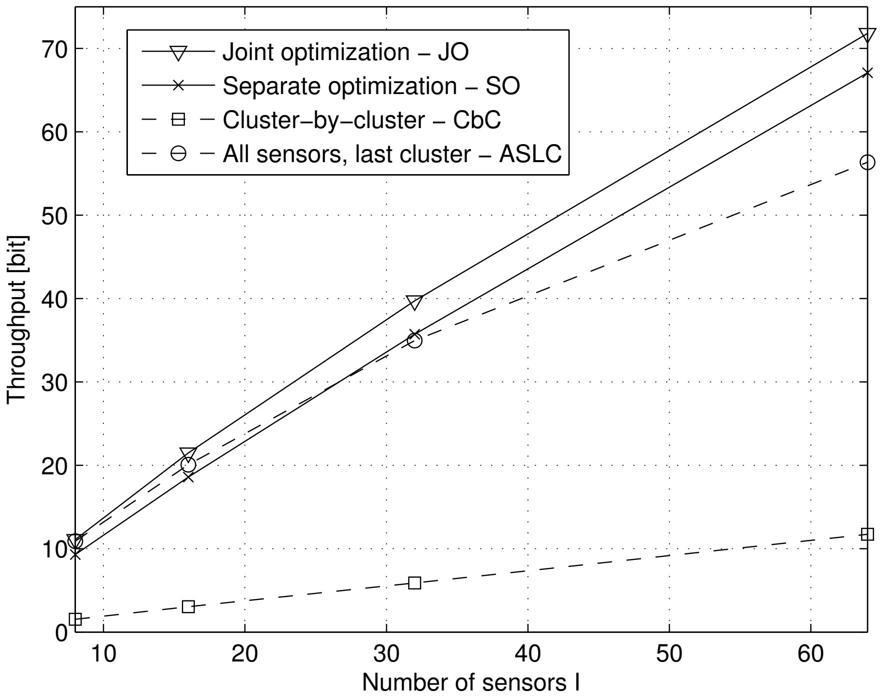

Figure 4.14: Throughput vs. number of sensors ($N_c = 8$, $E_T = 1$ J).

all the strategies considered. When the number of sensors increases, so does the beamforming gain and the SNR of the received signal (and, thus, throughput) becomes higher. In other words, by deploying more sensors, we drive the network towards high-SNR regime. Unsurprisingly too, the JO strategy attains the highest throughput. However and as we will see next, the fact that some suboptimal strategies outperform others will ultimately depend on a number of system parameters.

Next, we show some results in terms of the throughput ratio (i.e., loss) between the JO strategy and the suboptimal ones, namely, $L_{G,\{\text{SO,CbC,ASLC}\}} = G_{T,\{\text{SO,CbC,ASLC}\}}/G_{T,\text{JO}} \leq 1$. In Figure 4.15 we depict the corresponding losses as a function of the number of sensors, and for diverse conditions in terms of cluster number and amount of energy harvested. In brief, by moving from (i) the top to the bottom subplot, or (ii) from left to right in each subplot, we drive the system towards the high-SNR regime. By moving from the first to the second subplot, we increase the number of clusters as well. Interestingly, in the low to mid-SNR regime (top and middle subplots, left), the ASLC strategy outperforms all suboptimal ones and, in particular, separate optimization (SO). Hence, forcing *all* sensors to simultaneously transmit with those in the last cluster (which leads to an increased beamforming gain) is definitely better than allowing them to transmit at any time in an uncoordinated manner (at the risk of wasting the scarce energy harvested without really acting as a virtual array). As already discussed in the two-sensor case, the performance gap for the JO and SO strategies vanishes in the high-SNR regime.

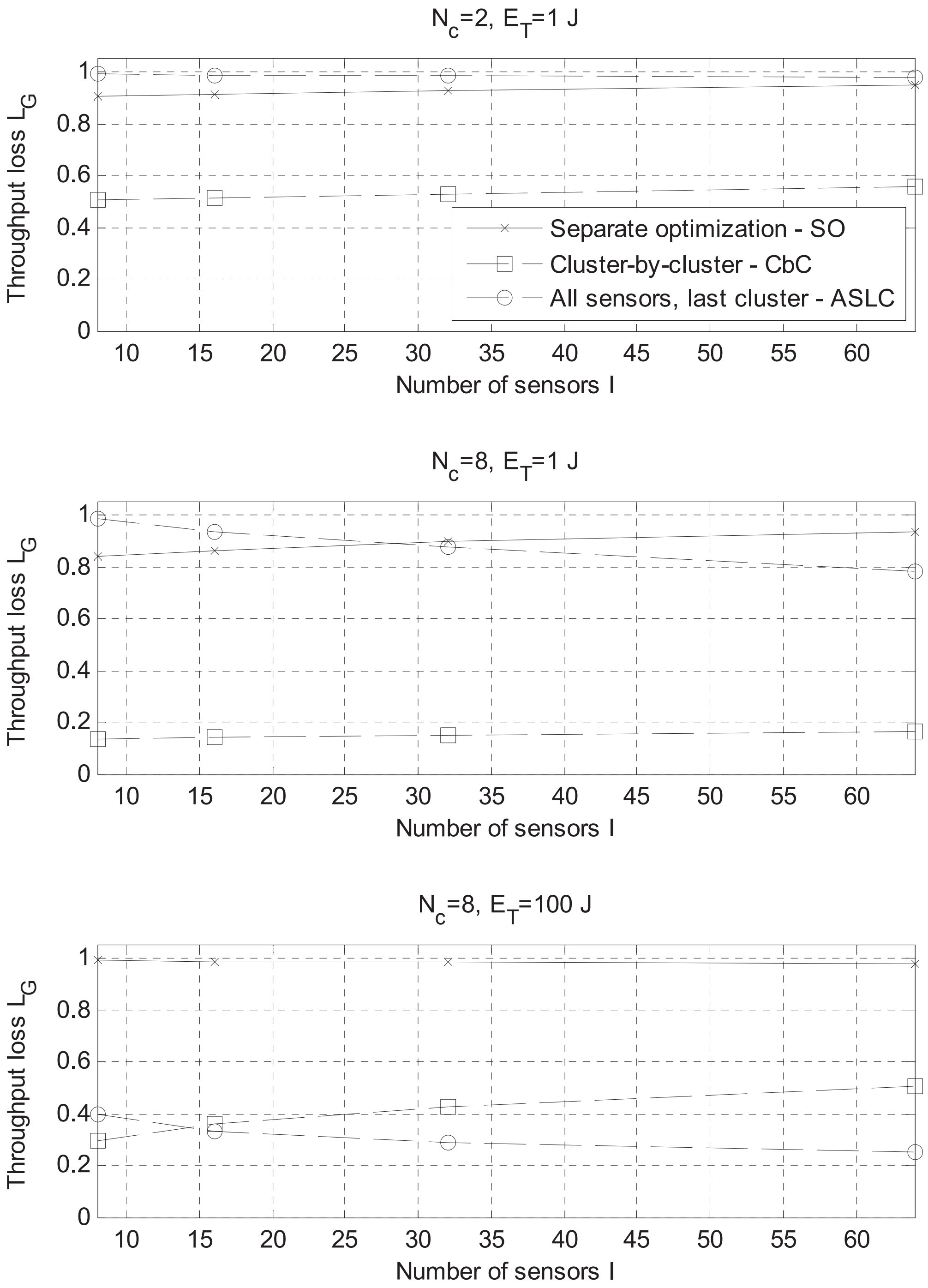

Figure 4.15: Throughput ratio (loss) vs. number of sensors. Top: Low-SNR, low number of clusters. Middle: low-SNR, high number of clusters. Bottom: high-SNR, high number of clusters.

Consequently, $L_{G,\text{SO}} \approx 1$ in the bottom subplot (high E_T or in the rightmost part of the top and middle ones. It is also worth noting that, in the low-SNR regime, increasing the number of clusters results into a wider performance gap between the CbC and ASLC strategies (c.f. upper and middle subplots). Since the number of sensors per cluster is lower and no inter-cluster coordination takes place (clusters transmit one after the other), this results into a lower beamforming gain for CbC and, thus, poorer performance (to stress, the maximum transmission time for each sensor is identical in the CbC and ASLC cases). Finally, we also observe that if we sustainedly drive the sensor network towards higher SNRs (bottom, right), the CbC strategy finally outperforms ASLC, as the crossing point indicates. Interestingly, this is despite of the fact that the former exhibits a lower beamforming gain (I/N_c vs. I). This, again, is motivated by the fact that throughput is a concave function which increases slowly in the high-SNR regime. In other words, it is more efficient to split the sensors into higher number of clusters and, hence, increase the transmission time linearly (CbC); rather than increasing the beamforming gain and shortening the transmission time (ASLC).

Finally, Figure 4.16 provides further insights into the performance of the various strategies as a function of the total energy harvested. The main conclusions are as follows: (i) the JO strategy proposed in this section is particularly useful for the low-SNR regime; (ii) in the mid-to-high SNR regime, on the contrary, separate optimization results into a marginal loss (SO is virtually identical to JO); and (iii) the CbC and ASLC strategies exhibit substantial performance losses in the mid-to-high SNR regime.

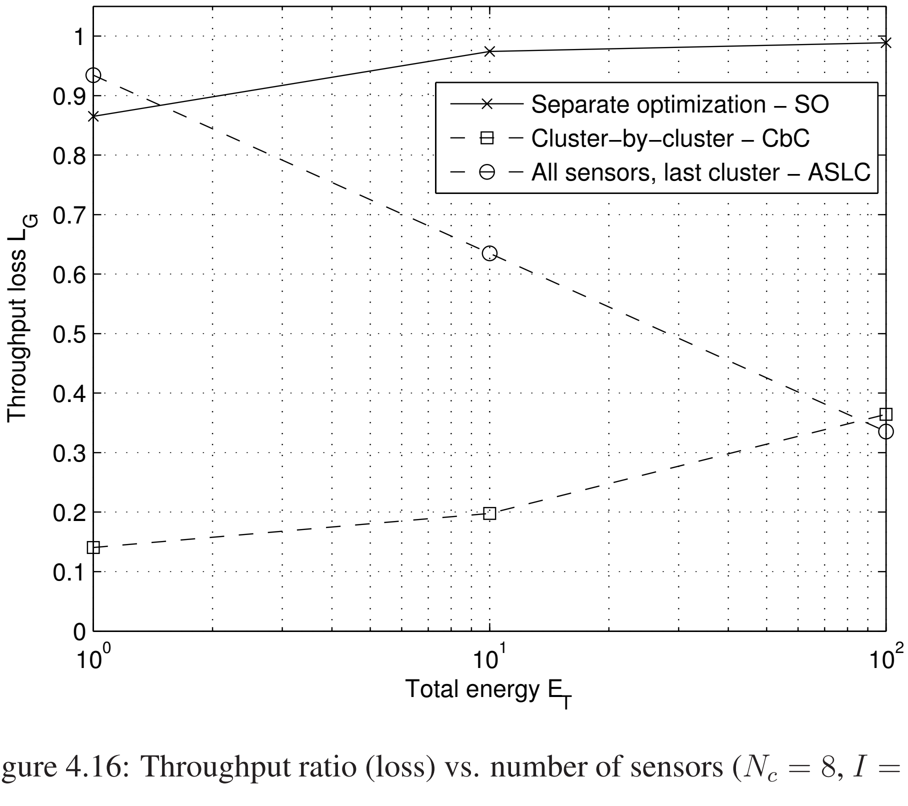

Figure 4.16: Throughput ratio (loss) vs. number of sensors ($N_c = 8$, $I = 16$) .

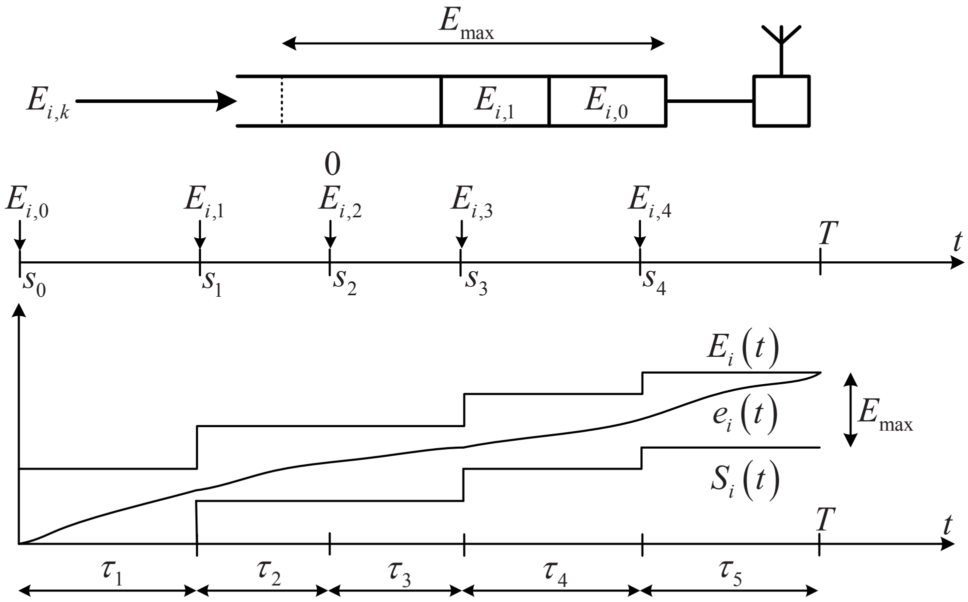

Figure 4.17: Energy harvesting process (top). Cumulative energy harvesting and storage curves, and energy consumption curve (bottom).

4.4 Finite battery capacity

In the sequel, we further generalize the communication scenario from Section 4.3, by realistically assuming that all the energy harvesting sensors are equipped with energy storage (ES) devices of *finite* capacity, denoted by E_{max}. The goal remains to be the same, i.e. we aim to identify the *jointly* optimal power allocation strategy which maximizes the total throughput for a given deadline. Hence, whenever the energy harvested by i^{th} EH sensor in the k^{th} event, $E_{i,k}$, exceeds the remaining storage capacity at that time instant, a *battery overflow* occurs. To avoid that[11], similarly to Section 3.4, we introduce the additional set of constraints:

$$e_i(t) \geq S_i(t) = \sum_{k:s_k<t} E_{i,k} - E_{\text{max}} \text{ for } i = 1 \dots I \tag{4.50}$$

where $S_i(t)$ denotes the cumulative energy *storage* (cES) constraints for the i^{th} sensor. In general, both the cEH and cES curves are given by a staircase functions. For this scenario, a given transmission policy is said to be *feasible* if, as imposed by (4.35) and (4.50), the energy consumption curves for each sensor lie *inside* the tunnel defined by the corresponding cEH and cES curves at all times, as shown in Figure 4.17.

---

[11] To recall, in Appendix 3.A.5, it is shown that any transmission policy that results in battery overflow is strictly suboptimal.

4.4.1 Computation of the optimal transmission policy

The original problem given by the score function (4.34), causality constraints (4.35) along with the associated energy storage capacity constraints (4.50) can be cast into following convex optimization framework:

$$\max_{\{p_{i,k}\}_{k=1,i=1}^{N,I}} \sum_{k=1}^{N} \tau_k \log\left(1+(\sum_{i=1}^{I}\sqrt{p_{i,k}})^2\right) \tag{4.51}$$

s.t.:

$$\sum_{k=1}^{n} \tau_k p_{i,k} \leq E_i^n = \sum_{k=0}^{n-1} E_{i,k} \tag{4.52}$$

$$\sum_{k=1}^{n} \tau_k p_{i,k} \geq S_i^n = \sum_{k=0}^{n} E_{i,k} - E_{\text{max}} \tag{4.53}$$

$$\text{for } n = 1\ldots N,\ i = 1\ldots I$$

$$p_{i,k} \geq 0 \ \text{ for } i = 1\ldots I,\ k = 1\ldots N \tag{4.54}$$

where we defined $E_i^n \triangleq E_i(t)$ and $S_i^n \triangleq S_i(t)$ for $t \in [s_{n-1}, s_n)$. The problem (4.51)-(4.54) is strictly convex, since it only adds a new set of affine constraints (4.53) to the problem considered before, in Section 4.3. In an attempt to determine its *unique* solution without resorting to computationally intensive numerical methods, we hereinafter generalize the *semi-analytical* approach presented in Section 4.3 to a scenario where EH sensors are equipped with ES devices of *finite* capacity. To that aim, once again we leverage on (i) the iterative coordinate descent method given in Section 4.3.2 ; and (ii) the algorithm that we propose in the Section 4.4.2 ahead. Similarly to Section 4.3.3, the latter allows to compute the optimal policy for one sensor whilst the policies of the other sensors are held fixed. However, the difference is that the proposed algorithm now has to specifically take into account the fact that sensors are equipped with an energy storage device of finite capacity.

By employing the coordinate descent method, we decompose the original problem (4.51)-(4.54) into a number of individual sub-problems (one for each sensor in the network) which, in turn, can be solved in an iterative fashion. More specifically, in the m^{th} iteration of the coordinate descent method the transmission policies of all sensors $\mathbf{p}_i^{(m)}$ are sequentially updated by solving

$$\mathbf{p}_j^{(m)} = \arg\max_{\{p_{j,k}\}_{k=1}^{N}} \sum_{k=1}^{N} \tau_k \log\left(1 + \left(\sqrt{p_{j,k}} + \sum_{i\neq j}\sqrt{p_{i,k}^{(m-1)}}\right)^2\right) \tag{4.55}$$

s.t.:

$$\sum_{k=1}^{n} \tau_k p_{j,k} \leq E_j^n = \sum_{k=0}^{n-1} E_{j,k} \ \text{ for } n = 1 \dots N \tag{4.56}$$

$$\sum_{k=1}^{n} \tau_k p_{j,k} \geq S_j^n = \sum_{k=0}^{n} E_{j,k} - E_{\text{max}} \ \text{ for } n = 1 \dots N \tag{4.57}$$

$$p_{j,k} \geq 0 \ \text{ for } k = 1 \dots N \tag{4.58}$$

where, in the above expression, $\mathbf{p}_j^{(m)} = [p_{j,1}^{(m)}, \dots, p_{j,N}^{(m)}]^T$ denotes a column vector gathering the N components in the transmission policy $\{p_{j,k}\}_{k=1}^{N}$ of the j^{th}sensor computed in the *current* iteration. Likewise, $\mathbf{p}_i^{(m-1)}$ denotes the transmission policies computed for the other sensors in the *previous* iteration which are held fixed. This procedure is iterated until a prescribed level of accuracy is attained or when the maximum number of iterations is reached.

4.4.2 Updating the transmission policy of one sensor node

To recall, we define *transmission sub-policy* $\{p_{i,k}\}_{k=k_l}^{k_u}$ as the subset of transmit powers associated with epochs $k = k_l \dots k_u$, which can be gathered in vector[12] $\mathbf{p}_{i,k_l:k_u} = [p_{i,k_l}, p_{i,k_l+1}, \dots, p_{i,k_u}]^T$. In Section 4.3, we rigorously proved that, in scenarios with *infinite* energy storage capacity, the optimal transmission policy for the i^{th} sensor, $\breve{\mathbf{p}}_i$, can be constructed as the concatenation of a number of battery operated (BO)-like (see definitions below) and feasible sub-policies $\mathbf{p}'_{i,k_l:k_u}$ starting and ending in *certain* corner points of the *cEH* curve. This extent was illustrated in Figure 4.3 where we have $\breve{\mathbf{p}}_1 = [\mathbf{p}_{1,1:L}^{'T}, \mathbf{p}_{1,L+1:M}^{'T}, \mathbf{p}_{1,M+1:N}^{'T}]^T$. As discussed in Section 4.3, the intuition behind is that (i) each BO-like sub-policy attains the highest possible throughput in its *own* epoch subset; and (ii) the transmission sub-policies in different epoch subsets can be computed independently (when the EC curve hits the cEH constraint, the battery becomes completely depleted and, hence, transmit powers in *subsequent* epochs exclusively depend on the energy harvested in those epochs).

As a reminder, a BO-like policy $\mathbf{p}'_i$ is the solution to an optimization problem where we replace the set of *actual* harvested energies $E_{i,k}$ by the following *virtual* ones: $E'_{i,0} = \sum_{k=0}^{N-1} E_{i,k}$, and $E'_{i,k} = 0$ for $k = 1 \dots N-1$. That is, as if all the harvested energy had been available from $t = 0$, as in battery-operated devices. Likewise, we define a BO-like policy $\mathbf{p}''_i$ as the one resulting from the set of virtual energies $E''_{i,0} = \sum_{k=0}^{N} E_{i,k} - E_{\text{max}}$, and $E''_{i,k} = 0$ for $k =$

---

[12] In the sequel, we omit the iteration index m for brevity.

$1 \dots N-1$. Interestingly, BO-like solutions can be very efficiently computed with Algorithm 1 from Chapter 3.

In the sequel, we generalize the results from Section 4.3, by presenting an algorithm to *semi-analytically* find the optimal transmission policy of one sensor with *finite* energy storage capacity while those of the other sensors are held fixed. More specifically, we propose a procedure to determine the (new) set of starting and ending corner points for each BO-like sub-policy. Differently from our previous work, those corner points can now be located either on the cEH or the cES curves (to recall, the optimal energy consumption curve must lie inside the tunnel defined by those two sets of causality constraints).

Let us assume, without loss of generality, that we aim to optimize the transmission policy of the first sensor node (i.e., $j=1$). The KKT conditions associated with the sub-problem (4.55) - (4.58) read

$$\frac{\partial \mathcal{L}_1}{\partial \breve{p}_{1,k}} = 0 \tag{4.59}$$

$$\sum_{k=1}^{n} \tau_k \breve{p}_{1,k} \leq E_1^n = \sum_{k=0}^{n-1} E_{1,k} \ \text{ for } n = 1 \dots N \tag{4.60}$$

$$\sum_{k=1}^{n} \tau_k \breve{p}_{1,k} \geq S_1^n = \sum_{k=0}^{n} E_{1,k} - E_{\text{max}} \ \text{ for } n = 1 \dots N \tag{4.61}$$

$$\breve{p}_{1,k} \geq 0 \tag{4.62}$$

$$\breve{\lambda}_n, \breve{\pi}_n, \breve{\mu}_k \geq 0 \tag{4.63}$$

$$\breve{\lambda}_n \left(\sum_{k=1}^{n} \tau_k \breve{p}_{1,k} - E_1^n \right) = 0 \ \text{ for } n = 1 \dots N \tag{4.64}$$

$$-\breve{\pi}_n \left(\sum_{k=1}^{n} \tau_k \breve{p}_{1,k} - S_1^n \right) = 0 \ \text{ for } n = 1 \dots N \tag{4.65}$$

$$-\breve{\mu}_k \breve{p}_{1,k} = 0, \tag{4.66}$$

where $\frac{\partial \mathcal{L}_1}{\partial \breve{p}_{1,k}}$ accounts for the partial derivative of the Lagrangian associated with the sub-problem:

$$\frac{\partial \mathcal{L}_1}{\partial \breve{p}_{1,k}} = -\tau_k \frac{\sqrt{\breve{p}_{1,k}} + \sum_{i \neq 1} \sqrt{\breve{p}_{i,k}}}{\sqrt{\breve{p}_{1,k}} \left(1 + \left(\sqrt{\breve{p}_{1,k}} + \sum_{i \neq 1} \sqrt{\breve{p}_{i,k}} \right)^2 \right)} + \tau_k \left(\sum_{n=k}^{N} \breve{\lambda}_n - \breve{\pi}_n - \frac{\breve{\mu}_k}{\tau_k} \right). \tag{4.67}$$

The fact that powers are strictly positive along with the complementary slackness condition (4.66) implies that, at the optimal point, all $\breve{\mu}_k$ must vanish, i.e. $\breve{\mu}_k = 0$. Thus, by defining

$$A_k = \sum_{n=k}^{N} \lambda_n - \pi_n, \tag{4.68}$$

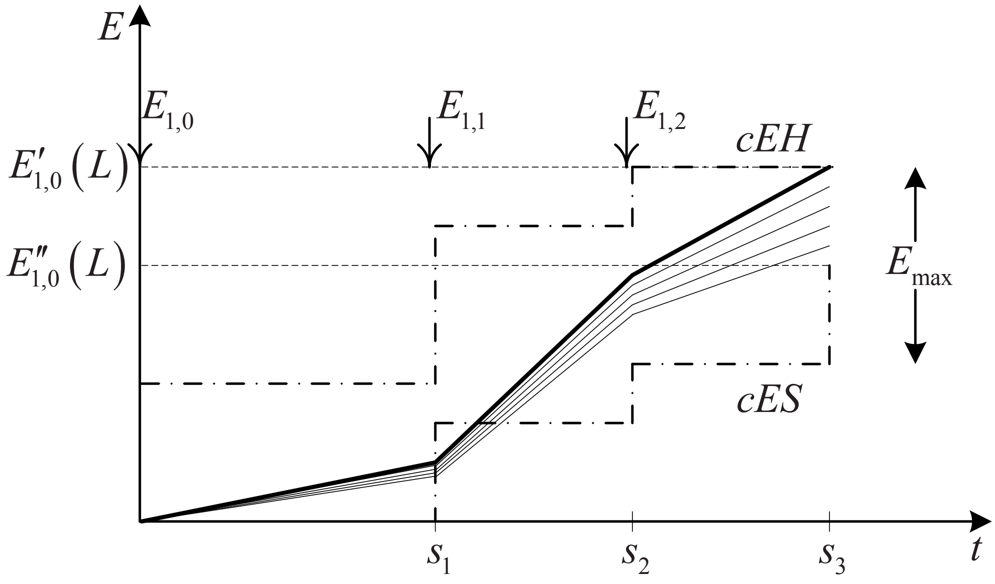

Figure 4.18: Violation of cES constraints - Case (i).

the partial derivative of the Lagrangian in (4.23) can be conveniently re-written as

$$\frac{\partial \mathcal{L}_1}{\partial \breve{p}_{1,k}} = -\tau_k \frac{\sqrt{\breve{p}_{1,k}} + \sum_{i \neq 1} \sqrt{\breve{p}_{i,k}}}{\sqrt{\breve{p}_{1,k}} \left(1 + \left(\sqrt{\breve{p}_{1,k}} + \sum_{i \neq 1} \sqrt{\breve{p}_{i,k}}\right)^2\right)} + \tau_k A_k. \tag{4.69}$$

In order to find the points where the EC curve hits either cEH or cES constraint (or, in other words, where corresponding Lagrangian multipliers in (4.68) are positive), we start the following four-step procedure:

1. *Check whether a BO-like solution* $\mathbf{p}'_1$ *for epochs* $k = 1 \ldots N$ *is feasible. If such virtual transmission policy verifies the causality constraints* (4.56)-(4.57) *of the original sub-problem (i.e. it is feasible) then it is optimal, the problem is solved and the procedure terminated.* In other words, we have $\breve{\mathbf{p}}_1 = \mathbf{p}'_1$. Similarly to procedure given in Section 4.3, if the BO-like solution is feasible (and, thus, optimal) then $\breve{\mathbf{p}}_1$ is not affected by the energy causality and energy storage constraints for $n = 1 \ldots N-1$ which could well be removed (or, equivalently, the corresponding Lagrange multipliers vanish). On the contrary, if the resulting virtual policy $\mathbf{p}'_1$ violates *one or more* causality constraints, then it follows from basic concepts in convex optimization theory [32] that $\breve{\mathbf{p}}_1$ is such that the EC curve hits the cEH and/or cES constraints in one or more corner points in $n = 1 \ldots N-1$ (or, more formally, the corresponding Lagrange multipliers are positive). This case is addressed in Step 2 and Step 3.

2. *Identify the first event* s_L *such that either (i) a BO-like sub-policy* $\mathbf{p}'_{1,1:L}$ *ending in a corner point of the cEH curve at* s_L *violates the cES constraints at some previous time*

instant(s); or (ii) a BO-like sub-policy $\mathbf{p}''_{1,1:L}$ *ending in a corner point of the cES curve violates the cEH constraints*[13].

As an example, Figure 4.18 illustrates a case where (i) holds for $s_L = s_3$ since, clearly, the EC curve violates the cES constraint in s_1. Interestingly, from Section 4.3.3 and the proof of convergence of Algorithm 1 in Section 3.3.2, *any* other EC curve associated with some candidate policy $\dot{\mathbf{p}}_1$ (see Figure 4.18) which in s_3 lies in between the corner points of the cEH and cES curves will necessarily *not* be feasible. This follows from the fact that, in order for such candidate EC curve to take a smaller value than that of the cEH curve, we must have $\dot{\mathbf{p}}_{1,1:L} \preccurlyeq \mathbf{p}'_{1,1:L}$, where $\preccurlyeq$ denotes component-wise inequality. Thus, if $\mathbf{p}'_{1,1:L}$ violates the cES constraints, so does $\dot{\mathbf{p}}_{1,1:L}$ and, hence, it is not feasible. As a result, now we know that the optimal transmission policy is such that the associated EC curve necessarily hits the cES curve in some previous corner point (or the cEH curve for case (ii) above)[14].

3. *Identify the first corner point where the optimal EC curve hits the cES or cEH curves (cases (i) and (ii), respectively).* The previous step allows us to restrict the search for the *first* corner point. For the given example, we just need to check events s_1 and s_2. Actually, it suffices to search for the event s_R with *largest* $R < L$ such that a BO-like policy $\mathbf{p}''_{1,1:R}$ (or $\mathbf{p}'_{1,1:R}$, for the (ii) case) ending in such corner point of the cES (or cEH) curve is feasible. The reason why is that, according to Lemma 4.3, there exists no other sub-policy $\mathbf{p}_{1,1:Q}$ with $Q < R$ such that it is part of the optimal transmission policy[15].

4. *Retain the corner points computed in the previous step and repeat Steps 1, 2, and 3 for epochs* $k = R + 1 \dots N$ *only (instead of* $k = 1 \dots N$*).* In each iteration, the associated sub-policy $\mathbf{p}''_{1,1:R}$ (or $\mathbf{p}'_{1,1:R}$) is retained as well.

Steps 1 to 4 are iterated until all the transmit powers for epochs $k = 1 \dots N$ have been computed as BO-like feasible solutions. In the sequel, we prove our claim that the resulting transmission policy is in fact optimal. This motivates the following lemma and theorem.

Lemma 4.3 *If* $R < L$ *is the largest value for which a candidate BO-like transmission sub-policy* $\mathbf{p}'_{1,1:R}$ ($\mathbf{p}''_{1,1:R}$) *ending in a corner point of the cEH (cES) curve is feasible, then there exists no other BO-like transmission sub-policy* $\mathbf{p}'_{1,1:Q}$ ($\mathbf{p}''_{1,1:Q}$) *with* $Q < R$ *such that it is part of the optimal transmission policy.*

---

[13] Likewise, we define the virtual BO-like sub-policy $\mathbf{p}''_{1,1:L}$ as the one that results from solving an optimization problem with the virtual *energies* $E''_{1,0}(L) = \sum_{k=0}^{L} E_{1,k} - E_{\text{max}}$ and $E''_{1,k}(L) = 0$ for $k = 1 \dots L-1$

[14] However, nothing could be inferred from a scenario where a BO-like sub-policy $\mathbf{p}'_{1,1:L}$ ending in a corner point of the cEH curve violates the same constraint at some previous time instant. This is why this case is not analyzed.

[15] Lemma 4.3 extends Lemma 4.1 for the case with sensors of finite energy storage capacity.

Proof: This lemma is an extension of Lemma 4.1 for the case where sensors have limited energy storage capacity. The proof is given in Appendix 4.A.1. ■

Theorem 4.2 *When the transmission policies at the other sensors is held fixed, the jointly optimal transmission policy for the first sensor (with finite energy storage capacity),* $\breve{\mathbf{p}}_1$, *can be computed with the procedure given in Algorithm 3.*

Proof: Algorithm 3 is in fact a more formal representation of the 4-step procedure given above. Step 2 allow us to restrict the search of the first "touching" corner to either cEH or cES curve. When such curve is identified, from Lemma 4.3, we realize that the first touching point corresponds to the ending point of the longest feasible BO-like policy. Once this point is found, the procedure can be restarted until the overall optimal policy is found as a concatenation of BO-like policies starting and ending at the corresponding corners of cEH and/or cES curves[16]. ■

4.4.3 Simulations and numerical results

In this section, we assess the performance of the proposed algorithm in a scenario where vibrational energy is harvested from the environment. As for the energy harvesting scenario, we take the setup given in Section 4.3.6.

We present results for a two-sensor scenario ($I = 2$) only, being those sensors deployed at normalized locations $d_1 = 0.05$ and $d_2 \geq d_1$. The normalized inter-sensor distance is denoted by $\Delta d = d_2 - d_1$. Each sensor $i \in \{1, 2\}$ harvests energy when the passing vehicle is within a road segment centered in d_i and total normalized length[17] 0.1. This, of course, means that collaborative transmission can only start in practice when the vehicle reaches the second sensor. To recall, we define $R_E = E_T^1/E_T^2$ as the ratio between the total energy harvested by the first and second sensors, respectively (i.e. for large R_E, the first sensor dominates).

Figure 4.19 depicts the ratio (loss) of achievable throughputs for sensors with finite and infinite energy storage capacities, $L_G = \frac{G_{T,E_{\max}}}{G_{T,\infty}}$. Three main regions can be observed for each curve, accounting for situations with rapid, slow and, no throughput degradation (left to right, with vertical lines on the curves denoting region boundaries). Indeed, when the capacity of the ES device is above the *total* amount of energy harvested by each sensor ($E_{\max} > E_T/2$, rightmost region) no loss in throughput results: energy storage constraints here are inactive. On the

---

[16] It can been shown that the complexity of Algorithm 3 is equal to that of Algorithm 2. This stems from the fact that, although Algorithm 3 checks the points on the cES curve as well, the order of number operations continues to be the same.

[17] Ultimately, this value depends on the sensitivity of the EH device

Algorithm 3 Optimal policy for sensor 1 with finite storage capacity (m^{th} iteration)

```
$m$                                                       ▷ Current iteration index
$\mathbf{p}_2 \leftarrow \mathbf{p}_2^{(m-1)}$            ▷ Let the transmission policy for sensor 2
                                                          ▷ be the one computed in the previous iteration.
$k_l \leftarrow 1$                                        ▷ Sub-policy starts in epoch 1
$k_u \leftarrow N$                                        ▷ Sub-policy ends in epoch $N$
repeat
    Compute BO-like sub-policy $\mathbf{p}'_{1,k_l:k_u}$
    if ($\mathbf{p}'_{1,k_l:k_u}$ is feasible) then
        $\mathbf{p}_1^{(m)}[k_l : k_u] \leftarrow \mathbf{p}'_{1,k_l:k_u}$
    else
        $k_u \leftarrow k_l + 1$
        $C_{out} \leftarrow$ false
        repeat
            Compute BO-like sub-policy $\mathbf{p}'_{1,k_l:k_u}$, $\mathbf{p}''_{1,k_l:k_u}$
            $C_1 \leftarrow$ ($\mathbf{p}'_{1,k_l:k_u}$ violates cES)
            $C_2 \leftarrow$ ($\mathbf{p}''_{1,k_l:k_u}$ violates cEH)
            if ($C_1$ or $C_2$) then                      ▷ Find first corner point
                if $C_1$ then
                    Find $\max_{k<k_u} k$ such that $\mathbf{p}''_{1,k_l:k}$ feasible
                    $\mathbf{p}_1^{(m)}[k_l : k] \leftarrow \mathbf{p}''_{1,k_l:k}$
                else
                    if $C_2$ then
                        Find $\max_{k<k_u} k$ s.t. $\mathbf{p}'_{1,k_l:k}$ feasible
                        $\mathbf{p}_1^{(m)}[k_l : k] \leftarrow \mathbf{p}'_{1,k_l:k}$
                    end if
                end if
                $k_l \leftarrow k + 1$
                $k_u \leftarrow N$
                $C_{out} \leftarrow$ true
            else                                          ▷ Check violations from next event
                $k_u \leftarrow k_u + 1$
            end if
        until $C_{out}$
    end if
until (Optimal transmission policy computed)
```

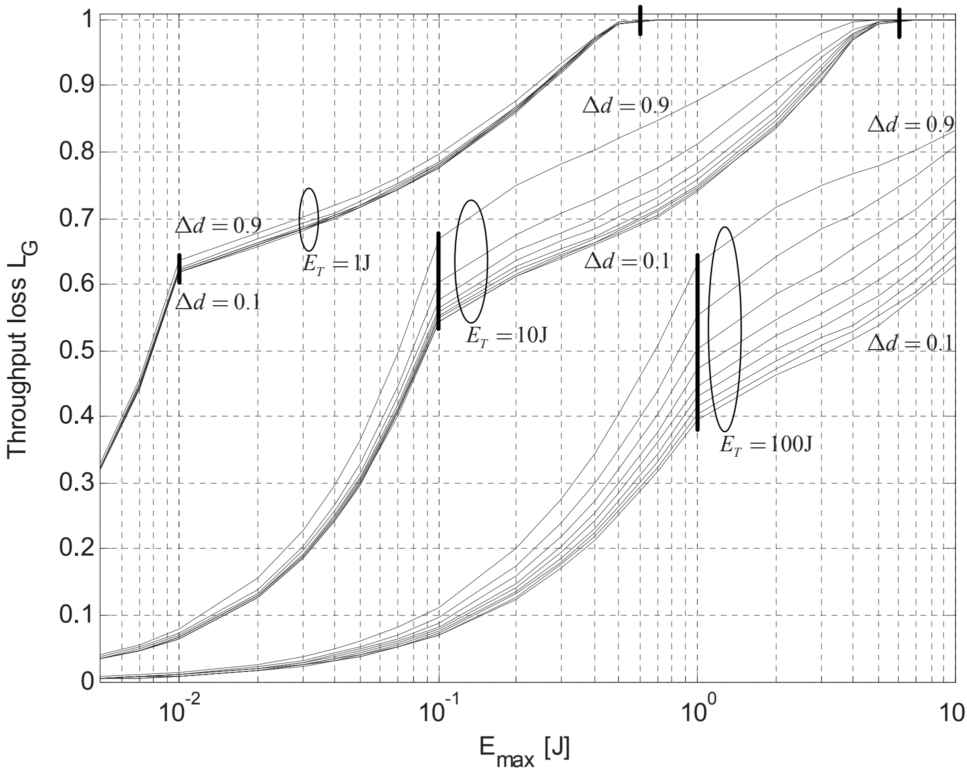

Figure 4.19: Throughput ratio (loss) as a function of energy storage capacity ($N = 100$, $E_{i,k}$ ($E_{i,k} = 10^{-2}, 10^{-1}, 1$J for $E_T = 1, 10, 100$J respectively).

contrary, throughput rapidly degrades when the storage capacity is smaller than the energy harvested in *each* arrival ($E_{\text{max}} < E_{\text{ev}}$, leftmost region) since part of the energy in each arrival is unavoidably wasted. As a result, throughput rapidly decreases. Finally, when $E_{\text{ev}} \leq E_{\text{max}} \leq E_T/2$ (central region), throughput experiences a graceful degradation for decreasing values of E_{max}. This is in stark contrast with our previous results in Figure 3.16 where throughput loss was barely noticeable as long as the maximum storage capacity exceeded the energy harvested in each arrival (i.e. no central region). This is attributed to the fact that in Figure 3.16 one of the two sensors was battery-operated. Hence, only the EH sensor was affected by the additional energy storage constraints. When computing its transmission policy, the BO sensor (partly) compensated the penalty due to the additional constraints imposed to the EH one.

From Figure 4.19, we also conclude that throughput loss is far more sensitive to changes in inter-sensor distance when the amount of energy harvested E_T is large. Ultimately, this is due to the fact that throughput scales *logarithmically* in the transmit power and *linearly* in the transmission time. For small E_T, the optimal transmission policy tends to allocate (shift) more energy to the period of time where *both* sensors are active: the additional beamforming gain that it entails, results into a higher throughput. Besides, in this region the log function exhibits an approximately linear behavior. As a result, the total throughput $G_{T,\infty}$ resulting from the integration of the instantaneous throughput over the actual transmission time (which, clearly, depends on inter-sensor distance) is approximately constant. The introduction of energy storage constraints renders the period of time when the harvested energy is usable potentially shorter and, thus, may turn collaborative transmission into sequential transmissions (i.e., each sensor uses its energy as soon as it is harvested). Yet, unavoidably, this results into lower $G_{T,E_{\max}}$ values, again this barely depend on inter-sensor distance. Being both $G_{T,\infty}$ and $G_{T,E_{\max}}$ barely sensitive to inter-sensor distance, it renders $L_G = \frac{G_{T,E_{\max}}}{G_{T,\infty}}$ barely sensitive to it, as well. For large E_T, on the contrary, it makes no sense for sensor 1 to *wait* until sensor 2 can start transmitting: the additional beamforming gain cannot compensate the *saturation* effect of the concave $\log$ function and the reduced transmission time. Instead, it is optimal to let sensor 1 (and sensor 2) transmit for most of the time. The transmission time for sensor 2, however, decreases linearly in the inter-sensor distance and, thus, the resulting throughput exhibits substantial variations in Δd. In the presence of energy storage constraints, on the contrary, throughput sensitivity to inter-sensor distance is far more limited. As a result, the sensitivity of L_G to inter-sensor distance is quite high, as Figure 4.19 illustrates.

Finally, in Figure 4.20 we depict $R_G = \frac{G_{T,\text{JO}}}{G_{T,\text{SO}}}$, namely, the ratio (gain) of achievable throughputs resulting from (i) the *Joint* Optimization (JO) of sensors' transmission policies (by means of Algorithm 3); and (ii) the Separate Optimization (SO) of those policies, as in the single-sensor scenario addressed in [18], which is suboptimal. In the leftmost part of the plot, the *total* amount of energy harvested by each sensor is well below its energy storage capacity ($E_{\max} = 5$ J). Hence, the curves with infinite and finite storage capacity are identical. Consistently with results in the previous sections, the highest gain is attained when the energies harvested by the first and second sensors are identical, that is, for $R_E = 1$ (some 20% gain). Besides, all throughput gains vanish when E_T increases, as discussed earlier. In the rightmost part of the plot, on the contrary, energy storage constraints do have some impact on throughput gains and, thus, curves split. Interestingly, the throughput gain in all cases verifies $R_G > 1$, that is, a joint optimization of transmission policies continues to pay-off. This holds in particular when $R_E \geq 1$ (i.e., the first sensor dominates or both sensors harvest the same amount of energy) since the throughput gain is even larger that that of a system with infinite energy storage capacity.

4.5 Chapter summary and conclusions

In this chapter, we have proposed a semi-analytical algorithm that allows to compute the *jointly* optimal transmission policy for a virtual array of energy harvesting sensors in such a way that the throughput for a given deadline is maximized. For both infinite and finite energy storage capacity cases, the optimality of the resulting policy has been rigorously proved. We have also found that the computational complexity of the proposed scheme is upper-bounded by $\mathcal{O}\left(\frac{N^3}{I^2}\right)$ for infinite and finite energy storage capacity. Consequently, the computational savings with

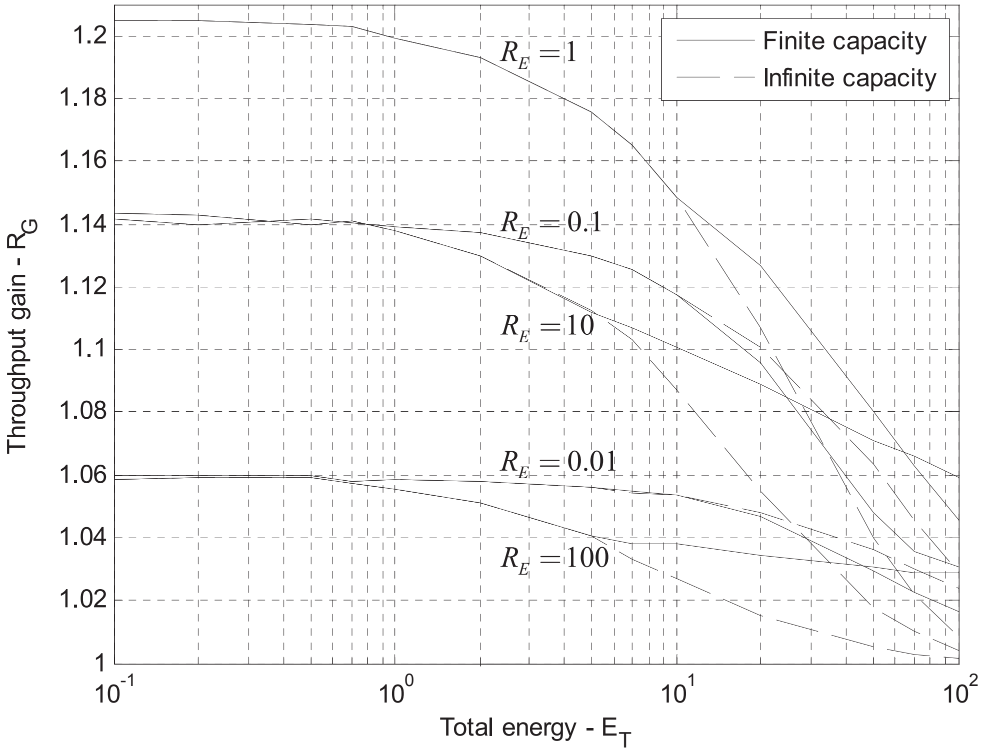

Figure 4.20: Throughput gain vs. total energy ($\Delta_d = 0.7$, $E_{\text{max}} = 5\text{J}$).

respect to interior point methods are, at least, of an I^2 factor (yet, in practice, much higher).

Performance has been assessed by means of computer simulations in a realistic scenario where vibrational energy is harvested from the environment. Computer simulation results revealed that, for infinite capacity scenario, in the low-SNR regime, the gain resulting from the joint optimization (vs. separate optimization) of the transmission policies can be as high as 40% when inter-sensor distance is high. This is achieved by favoring simultaneous sensor transmissions which result into a higher beamforming gain (and, thus, throughput). On the contrary, in the high-SNR regime the jointly and separately optimal transmission policies are almost identical and, hence, such gain vanishes. This follows from the fact that throughput scales logarithmically in the transmit power and linearly in the transmission time. We have also concluded that, for most scenarios, the throughput is higher when each sensor in the virtual array harvests the same amount of total energy. As for the other suboptimal transmissions strategies (cluster-by-cluster, all sensors-last cluster), we have learnt that, in the low-to-mid SNR regime the all sensors-last cluster policy outperforms all the rest and, in particular, separate optimization. Besides, the performance gap between between the cluster-by-cluster and all sensors-last cluster strategies becomes wider when the number of cluster increases. In the high-SNR regime, on the contrary, the cluster-by-cluster strategy outperforms the all sensors-last cluster one.

In the realistic scenario, where the energy storage capacity is assumed to be finite, we specifically evaluate the effects of limited capacity on the system performance. Namely, for intermediate values of the energy storage capacity, the throughput ratio w.r.t. to a system with *infinite* energy storage capacity, experiences a graceful degradation. When the total energy harvested by the group of sensors is large, performance is more sensitive to inter-sensor distance. Finally, we have also found that, in the presence of strict energy storage constraints, joint (vs. separate) optimization of transmission policies continues to pay-off, in particular when both sensors harvest the same amount of energy or the first sensor dominates.

4.A Appendix

4.A.1 Proof of Lemma 4.3

Since the case for the sub-policy $\mathbf{p}'_{1,1:R}$ ending in a corner point of cEH curve has already been addressed in Lemma 4.1, here we only consider the proof related to sub-policy $\mathbf{p}''_{1,1:R}$. Again, the proof is based on contradiction.

Let us consider *two* candidate transmission policies, $\mathbf{p}_1$ and $\dot{\mathbf{p}}_1$, the first R or Q (respectively) elements of which, namely, $\mathbf{p}_{1,1:R}$ and $\dot{\mathbf{p}}_{1,1:Q}$ with $Q < R$, have been computed as BO-like solutions (see Figure 4.21). From the discussions in Steps 1 and 2 above, we know that the Lagrangian multipliers associated with $\mathbf{p_1}$ verify

$$\begin{aligned}&\lambda_n = 0,\ n = 1, \ldots, R\\&\pi_n = 0,\ n = 1, \ldots, R-1;\ \pi_R > 0\end{aligned} \tag{4.70}$$

and, as long as $R < N$,

$$\lambda_n \geq 0, \pi_n \geq 0\ n = R+1, \ldots, N \tag{4.71}$$

where (4.70) and (4.71) follow from the KKT conditions. From this, the corresponding sums of Lagrangian multipliers A_k verify in turn

$$A_1 = A_2 = \ldots = A_R = \sum_{n=R}^{N} \lambda_n - \pi_n. \tag{4.72}$$

Similarly, for $\dot{\mathbf{p}}_\mathbf{1}$ we have

$$\begin{aligned}&\dot{\lambda}_n = 0,\ n = 1, \ldots, Q\\&\dot{\pi}_n = 0,\ n = 1, \ldots, Q-1;\ \dot{\pi}_Q > 0\\&\dot{\lambda}_n \geq 0, \dot{\pi}_n \geq 0,\ n = Q+1, \ldots, N\end{aligned} \tag{4.73}$$

and, accordingly,

$$\dot{A}_1 = \dot{A}_2 = \ldots = \dot{A}_Q = \sum_{n=Q}^{N} \dot{\lambda}_n - \dot{\pi}_n. \tag{4.74}$$

Since in s_Q the EC curve associated with $\dot{\mathbf{p}}_1$ lies below that of $\mathbf{p}_1$ (see Figure 4.21), there necessarily exists at least one epoch $k_o \in \{1 \ldots Q\}$ such that $\dot{p}_{1,k_o} < p_{1,k_o}$. Besides, a necessary condition for either candidate sub-policy to qualify as optimal, is that the corresponding derivative of the Lagrangian given by (4.69) must vanish for *all* $k \in \{1 \ldots Q\}$, namely, $\frac{\partial \mathcal{L}_1}{\partial \breve{p}_{1,k}} = 0$. In particular, for $k = k_o$ the fact that $\dot{p}_{1,k_o} < p_{1,k_o}$ implies that $\dot{A}_{k_o} > A_{k_o}$ (and vice-versa: if $\dot{p}_{1,k_o} > p_{1,k_o}$ then $\dot{A}_{k_o} < A_{k_o}$). Furthermore, from (4.72) and (4.74), we conclude that $\dot{A}_k > A_k$ for *all* $k \in \{1 \ldots Q\}$ which, in turn, implies $\dot{p}_{1,k} < p_{1,k}$ for those epochs. In other words, the

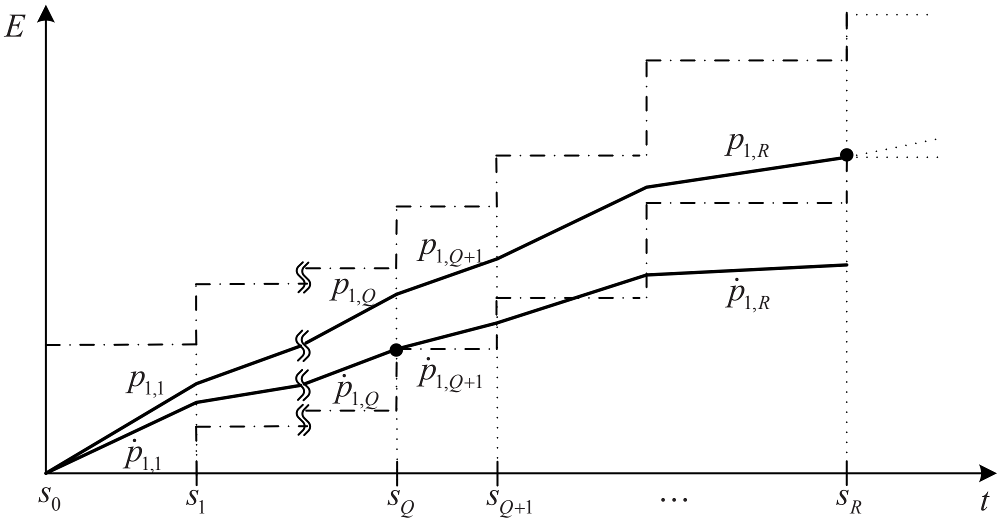

Figure 4.21: Lemma 4.3: A sub-policy touching the cES (cEH) curve at point s_Q is not feasible and, thus, it cannot be part of the overall optimal policy.

EC curve associated with the candidate sub-policy $\dot{\mathbf{p}}_{1,1:Q}$ lies *strictly below* that of $\mathbf{p}_{1,1:Q}$ for *all* those epochs, as Figure 4.21 illustrates. In particular, this holds true for $k = Q$, namely, $\dot{p}_{1,Q} < p_{1,Q}$. For the subsequent epoch, we have that either $\dot{p}_{1,Q+1} > p_{1,Q+1}$ or $\dot{p}_{1,Q+1} \leq p_{1,Q+1}$. The former would hold if (and only if)

$$\dot{A}_Q > A_Q = A_R \tag{4.75}$$

$$\dot{A}_{Q+1} < A_{Q+1} = A_R \tag{4.76}$$

which translate to $\dot{\pi}_Q = \dot{A}_{Q+1} - \dot{A}_Q < 0$. Since this violates one KKT condition then, necessarily, $\dot{p}_{1,Q+1} \leq p_{1,Q+1}$. By applying the same reasoning to the subsequent consecutive epoch pairs, we conclude that $\dot{p}_{1,k} \leq p_{1,k}$ for all $k \in \{Q+1, R\}$. Hence, the EC curve associated with the candidate sub-policy $\dot{\mathbf{p}}_{1,1:R}$ lies strictly below that of $\mathbf{p}_{1,1:R}$ not only for the first Q epochs but for *all* epochs $k \in \{1 \ldots R\}$. Since, to recall, at s_R the EC associated with the candidate sub-policy $\dot{\mathbf{p}}_{1,1:R}$ hits the cEH curve, this means that the candidate sub-policy $\dot{\mathbf{p}}_{1,1:R}$ is necessarily not feasible and, thus, cannot be part of the overall optimal policy (see Figure 4.21). This concludes the proof.

Chapter 5

Distributed Carrier Synchronization Schemes for Collaborative Beamforming

In previous chapters, we designed jointly optimal transmission strategies for scenarios where a number of sensors cooperate to transmit (beamform) a common message to a distant base station. To make the problem more tractable, we assumed full carrier and time synchronization over sensors. In particular, we assumed that, by properly designing the set of transmit weights, both the channel phase shifts and oscillator offsets could be ideally pre-compensated. In this chapter, instead, we focus on the design of the (decentralized) carrier synchronization schemes behind our initial assumption. For instance, we propose a phase synchronization scheme which does not require base stations to coordinate the allocation of sensors to the training timeslots or poll them individually, which can be burdensome for large networks. We also analyze the impact of additive noise on the behavior of an iterative phase synchronization scheme, and propose new synchronization schemes capable of maximizing the beamforming gain in the direction of the main base station while keeping the sidelobe levels in the direction of unintended base stations reasonably low.

5.1 Introduction

In Chapters 3 and 4, we have addressed scenarios where energy harvesting and/or battery operated sensors employ collaborative beamforming in order to reach a distant base station. Nevertheless, in order to implement this idea into a practical scenario, accurate frequency and phase carrier *synchronization* over sensors is a must.

A simple *phase* synchronization scheme, with low feedback requirements is proposed in [8]. At each iteration, all the sensors in the network add some random perturbation to the carrier phase. Then, based on the change in resulting received signal strength, the BS informs the sensors in the network whether they should keep (if RSS increased) or discard (otherwise) the introduced phase perturbation. The authors show that in an idealized scenario where noise is neglected, and therefore the RSS estimation is perfect, the proposed algorithm almost surely converges to full phase synchronization. The proposed scheme is further generalized in [9], where the authors explicitly include simultaneous *frequency* synchronization as well.

Employing the fact that collaborative transmission where sensors are not perfectly synchronized can still provide significant beamforming gain, the authors in [10] propose an algorithm which is based on the *selection* of a subset of sensor nodes whose signals combine in a quasi-coherent manner at the base station. In order to relieve the BS from the burden associated with exhaustive search among all the possible combinations, they propose different suboptimal selections schemes, which result in small performance loss with respect to the optimal scheme. Still, the fact that only a subset of sensor nodes is selected for beamforming results in an unequal energy consumption among the sensors, which may have adverse effects on the network lifetime.

The main challenge when computing the resulting *beampattern* stems from the fact that sensor nodes are randomly deployed, and therefore their precise locations are usually not known. In such situations, it is natural to consider stochastic measures such as *average* beampattern or sidelobe distribution. For uniform and Gaussian sensor node distributions, in [12] and [13], the authors find the mathematical expressions for average beampattern. From these two papers, we learn that both uniform and Gaussian sensor node deployments provide similar conclusions with respect to the relation between network diameter and beamwidth. Nevertheless, the Gaussian distributed antenna array was shown to result in the beampattern with wider mainlobe and lower probability of high sidelobes.

Due to random deployment of sensor nodes, the sidelobe locations and levels for a particular network realization can not be predicted. This, in turn, may lead to high interference levels that the given network is causing to the neighboring ones. One possible approach to deal with this problem is given in [14], where the authors propose a *sidelobe control* mechanism based on the node selection method. In the proposed scheme, the authors assume that all the nodes in the network have already achieved perfect phase synchronization. Then, they employ an iterative algorithm, where in each iteration, a new subset of nodes is added to a group of selected nodes if the resulting sidelobe levels for specific directions is kept below the prescribed threshold. Although this method is of low complexity and requires low rate feedback, only a subset of all the nodes is selected for beamforming. This, however, may not be suitable for some applications, where higher received signal is needed, thus requiring all the sensors to be active.

5.1.1 Contribution

In this chapter, we carry out an analysis of distributed carrier synchronization schemes. In Section 5.3, we focus on the so called one bit of feedback algorithm proposed in [8]. First, we generalize the analysis given therein, for a more realistic scenario with additive noise. With this assumption we ask ourselves what is the impact of imperfect RSS estimation on the algorithm convergence. To answer this question, we derive an analytical expression for expected increase in RSS as a function of algorithm iteration. Furthermore, we also prove that for the noisy scenario, the algorithm does not converge to full phase synchronization. In order to maximize the resulting RSS, we numerically optimize the number of samples per RSS estimate. Next, we generalize the one bit of feedback algorithm from [8] to a scenario with multiple base stations. Namely, the goal is not only to increase the received signal level at the base station of interest (main BS), but also to keep the received signal level at the unintended base stations below some prescribed threshold. In some scenarios, this may result in decreased RSS levels at the main base station. Furthermore, we compare the resulting beampattern obtained by the one bit of feedback algorithm with the one obtained by centralized numerical optimization solution. The impact of number and relative positions of unintended base stations on system performance is considered, as well.

Finally, in Section 5.4, we propose a novel decentralized phase synchronization scheme for collaborative beamforming with wireless sensor networks. The proposed scheme does not require the base station to coordinate the allocation of sensors to the training timeslots or poll them individually (which can be burdensome for large networks), and, instead, sensors randomly choose their respective training timeslots. In this context, we ask ourselves whether there exists an optimal number of training timeslots, and about the optimal split for the training and data transmission periods. To answer this question, we analytically derive upper bounds of the resulting beamforming gain with ideal and noisy phase shift estimation. Computer simulation results are mainly given in terms of (normalized) beamforming gain and achievable throughput. The contents of this chapter have been partly published in references [46–49].

The chapter is organized as follows. First, in Section 5.2, we present the signal model. Next, in Section 5.3 we present the analysis of one bit of feedback algorithm for noisy and multiple

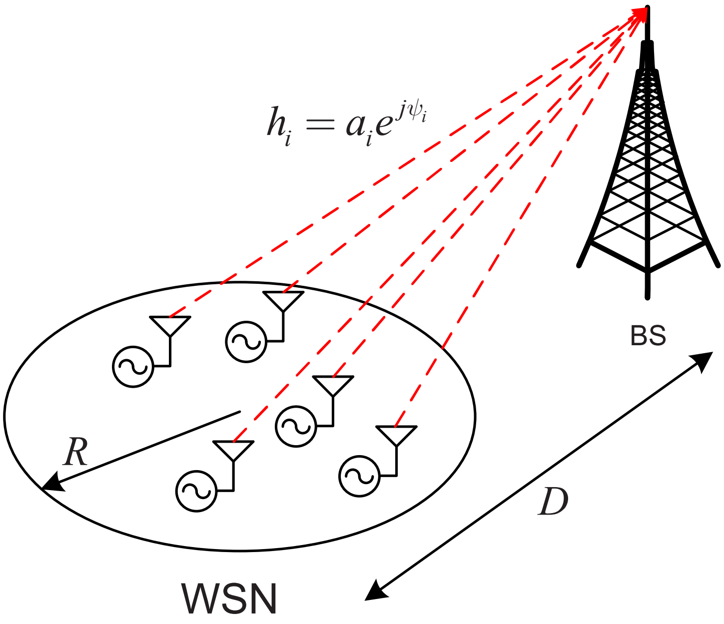

Figure 5.1: Distributed beamforming in wireless sensor networks.

base station scenarios, and provide some computer simulation results. Next, in Section 5.4 we propose a novel decentralized phase synchronization scheme. The algorithm's performance is given with the special emphasis on ideal and noisy phase estimation. The main findings for both synchronization schemes are given at the end of this chapter.

5.2 Signal model

Consider a wireless sensor network consisting of I sensor nodes randomly placed over a disk of radius R according to a uniform distribution, as shown in Figure 5.1. We assume that the base station is located far apart and outside the coverage area of each individual sensor node, i.e. $D \gg R$. The goal is to collaboratively transmit a common narrowband message signal $m(t)$ to the BS. For simplicity, we assume that nodes have already shared the message signal and that $\mathbb{E}\left[|m(t)|^2\right] = 1$. In order to save energy, sensors are in the sleep state (i.e. transceiver circuits are turned off) for most of the time. When new data have to be collected, the BS sends an RF signal, which activates the energy detectors in the sensor nodes and wakes them up (see [50] for details). After the sleep period, all sensors are assumed to remain frequency-locked to the reference carrier frequency f_c (i.e., negligible frequency drift). The signal transmitted by the i-th sensor node reads:

$$s_i(t) = g_i^* m(t)\, e^{j(2\pi f_c t + \gamma_i)} \tag{5.1}$$

where $g_i = b_i e^{-j\theta_i}$ denotes the corresponding complex transmit weight (to be designed), whereas γ_i stands for the initial phase offset. The phase offset of each oscillator, however, is unknown, and we model it as a uniformly distributed (i.e. $\gamma_i \sim \mathcal{U}(-\pi, \pi)$) and i.i.d. random variable. The complex channel from the i-th sensor to the base station is denoted by $h_i = a_i e^{j\psi_i}$, where a_i and ψ_i account for the channel gain and phase shift associated with the Euclidean distance between the sensor and the BS. Accordingly, the signal received at the BS is given by:

$$\begin{aligned} r(t) &= \mathcal{R}\left(\sum_{i=1}^{I} s_i(t)h_i + w(t)\right) \\ &= \mathcal{R}\left(m(t)e^{j2\pi f_c t}\sum_{i=1}^{I} a_i b_i e^{j(\gamma_i+\theta_i+\psi_i)} + w(t)\right) \end{aligned} \tag{5.2}$$

with $w(t) \sim \mathcal{N}(0, \sigma_w^2)$ denoting additive white Gaussian noise. To further simplify the analysis, we assume that the transmit power at each sensor node is constant and, hence, the transmit weights become $g_i = e^{-j\theta_i}$. We also assume that $a_i = 1$ for all sensors or, in other words, that the distance between the BS and the sensors is much larger than inter-sensor distances (in addition to line-of-sight conditions). After down-conversion and sampling, the received signal strength (RSS) at the BS in time instant n reads:

$$\text{RSS}\,[n] = R[n] = \left|\sum_{i=1}^{I} e^{j\Phi_i[n]} + w\,[n]\right|, \tag{5.3}$$

where $\Phi_i[n] = \gamma_i + \psi_i + \theta_i[n]$ denotes the overall phase rotation of the signal received at the BS from the i-th sensor node. Likewise, we define the beamforming gain $Y[n]$ as:

$$Y[n] = \left|\sum_{i=1}^{I} e^{j\Phi_i[n]}\right| \in \mathbb{R}^+ \cup \{0\}. \tag{5.4}$$

5.3 One bit of feedback scheme for collaborative beamforming

Clearly, for the given signal model, the beamforming gain $Y[n]$ is maximized when the individual signals from all the sensors are coherently combined at the BS, namely, $\gamma_i + \psi_i - \theta_i = C; \forall i$ (where C is a constant) which yields $Y[n] = Y_{\max} = |\sum_{i=1}^{I} e^{jC}| = I$. To that aim, sensors must pre-compensate the unknown oscillator and channel phase offsets by properly adjusting the θ_i term during e.g. a training period. The distributed beamforming scheme of [8] achieves that in an iterative manner. To recall, in [8], the authors *neglect* the impact of noise, i.e. $w(t) = 0$. With this assumption, the RSS and beamforming gain $Y[n]$ turn out to be *identical*. As a reminder, we outline the one bit of feedback algorithm proposed in [8]:

Initially, the phases of the received signals at the base station, $\Phi_i[0] = \gamma_i + \psi_i - \theta_i[0] = \gamma_i + \psi_i$, are uniformly distributed in $[-\pi, \pi]$[1]. At all times, each transmitter keeps track of the *best* value

---

[1] This follows from the fact that, on the one hand, the oscillators run independently and, on the other, $R \ll D$

of $\theta_{\text{best},i}[n]$. At each iteration, $\theta_{\text{best},i}[n]$ is adjusted with a random perturbation $\delta_i[n]$ drawn from a suitable probability distribution $f_\delta(\delta_i)$. Next, all the sensor nodes transmit their signals with the incremental phase rotations, namely, $\theta_i[n+1] = \theta_{\text{best},i}[n] + \delta_i[n]$ and the BS measures the RSS again[2]. By comparing $Y[n+1]$ with $Y_{\text{best}}[n] = \max_{m \leq n} Y[m]$ (i.e. the largest RSS until time instant n), the BS determines whether the set of perturbations $\Delta[n] = [\delta_1[n], \ldots, \delta_N[n]]$ should be kept (if RSS increases) or discarded (otherwise). The sensor nodes are notified about this decision by sending one bit of feedback over an error-free common signalling channel. More formally,

$$Y_{\text{best}}[n+1] = \begin{cases} Y[n+1] & \text{if } Y[n+1] \geq Y_{\text{best}}[n] \\ Y_{\text{best}}[n] & \text{otherwise} \end{cases} . \tag{5.5}$$

Accordingly, the bit in the feedback channel is set to:

$$z_{\text{FB}}[n+1] = \begin{cases} 1 & \text{if } Y[n+1] \geq Y_{\text{best}}[n] \\ 0 & \text{otherwise} \end{cases} , \tag{5.6}$$

and, finally, the sensor nodes update their phases according to:

$$\theta_{\text{best},i}[n+1] = \begin{cases} \theta_{\text{best},i}[n] + \delta_i[n] & \text{if } z_{\text{FB}}[n+1] = 1 \\ \theta_{\text{best},i}[n] & \text{otherwise} \end{cases} . \tag{5.7}$$

5.3.1 Distributed beamforming with noisy RSS measurements

In this section, we generalize the algorithm's convergence analysis from [8], by explicitly taking into account the impact of additive noise in RSS measurements. As a consequence, the decisions on whether to accept or discard the phase perturbations are based on the *noisy* RSS estimates $R[n]$, given by (5.3) and, thus,

$$z_{\text{FB}}[n+1] = \begin{cases} 1 & \text{if } R[n+1] \geq R_{\text{best}}[n] \\ 0 & \text{otherwise} \end{cases} . \tag{5.8}$$

$$\theta_{\text{best},i}[n+1] = \begin{cases} \theta_{\text{best},i}[n] + \delta_i[n] & \text{if } z_{\text{FB}}[n+1] = 1 \\ \theta_{\text{best},i}[n] & \text{otherwise} \end{cases} . \tag{5.9}$$

Note that in (5.8), the RSS estimates $R[n]$ are different from the corresponding beamforming gain $Y[n]$. This, in turn, means that, even if $R[n+1] \geq R_{\text{best}}[n]$, the system could experience a decrease in terms of beamforming gain (i.e. $Y[n+1] < Y_{\text{best}}[n]$). This has a number of implications that we will discuss in the sequel.

---

[2] To recall, in the absence of additive noise, we have $R[n] = Y[n]$.

Evolution of the expected beamforming gain

Let us rewrite equation (5.3) as follows

$$\begin{aligned} R[n] &= \left|Y[n] + w\left[n\right]e^{-j\alpha}\right| \\ &\triangleq \left|Y[n] + w_\alpha\left[n\right]\right|, \end{aligned} \tag{5.10}$$

with $\alpha = \arg\left\{\sum_{i=1}^{I} e^{j\Phi_i[n]}\right\}$ and where $w_\alpha \sim \mathcal{CN}(0, \sigma_w^2)$. Clearly, the random variable R is *Ricean* distributed. However, for $Y \gg \sigma_w$, its pdf can be approximated by a *Gaussian* pdf [51], namely,

$$R \sim \mathcal{N}(\sqrt{Y^2[n] + \frac{\sigma_w^2}{2}}, \frac{\sigma_w^2}{2}). \tag{5.11}$$

From [8], we know that the following equality holds for the expected value of the normalized beamforming gain in n-th iteration:

$$\frac{1}{I}\mathbb{E}\left[Y_{\text{best}}[n+1]\right] = \frac{1}{I}\mathbb{E}\left[Y_{\text{best}}[n]\right] + \mathbb{E}\left[h_n\left(y\right)\right], \tag{5.12}$$

with the random variable y being defined as $y = \frac{1}{I}Y_{\text{best}}[n]$. For the sake of clarity, the expectations in the above equation are taken with respect to the random perturbations and the measured received signal strength in time instants n and $n+1$, where relevant; and the function $h_n(y)$ denotes the *conditional* expectation of the increment in the normalized beamforming gain, namely,

$$h_n(y) \triangleq \frac{1}{I}\mathbb{E}\left[\left(Y[n+1] - Y_{\text{best}}[n]\right) \times \mathcal{H}\left(R[n+1] - R_{\text{best}}[n]\right) \middle| \frac{1}{I}Y_{\text{best}}[n] = y\right], \tag{5.13}$$

with $\mathcal{H}(x)$ denoting the Heaviside step function:

$$\mathcal{H}(x) \quad = \left\{\begin{array}{ll} 1 & x > 0 \\ 0 & \text{otherwise} \end{array}\right., \tag{5.14}$$

which models the phase perturbation acceptance rule given by (5.8) and (5.9). From (5.12) and based on the observation that $Y_{\text{best}}[n]$ is highly concentrated around its expected value when I is large, we have that

$$\frac{1}{I}\mathbb{E}\left[Y_{\text{best}}[n+1]\right] \approx \frac{1}{I}\mathbb{E}\left[Y_{\text{best}}[n]\right] + h_n\left(\frac{1}{I}\mathbb{E}\left[Y_{\text{best}}[n]\right]\right). \tag{5.15}$$

This last equation suggests that we can model the evolution of the expected (and normalized) beamforming gain through function $h_n(y)$. In the sequel, we attempt to derive an expression for such function that, unlike in previous works, explicitly takes into consideration the impact of noise.

The authors in [8] showed that, given $\frac{1}{I}Y_{\text{best}}[n] = y$, the following holds for normalized beamforming gain in the $(n+1)$-th iteration

$$\frac{1}{I}Y_{\text{best}}[n+1] \underset{p}{\rightarrow} \chi_n y + x, \tag{5.16}$$

where $\chi_n = 1 - \frac{1}{2}\mathrm{Var}[\delta_i[n]]$ is constant, and x denotes a zero-mean Gaussian r.v. with variance:

$$\sigma^2_{\mathcal{R}}[n] = \frac{1 - \chi_n^2 - \rho_n \kappa_n(y)}{2I}, \tag{5.17}$$

being $\kappa_n(y)$ a function of the normalized beamforming gain y only which can be approximated as

$$\kappa_n(y) \approx e^{-4(1-y)}. \tag{5.18}$$

Next, $\rho_n \approx \mathrm{Var}[\delta_i[n]]$ in (5.17) is a constant that exclusively depends on the pdf of the perturbation, i.e. $f_\delta(\delta_i)$. From all this, we can approximately re-write (5.13) as

$$h_n(y) \triangleq \mathbb{E}\left[(\chi_n y + x - y) \times \mathcal{H}\left(r_{n+1} - r_n\right) \left| \frac{1}{I} Y_{\text{best}}[n] = y \right.\right] \tag{5.19}$$

where, to simplify notation, we have re-defined $r_n = \frac{1}{I} R_{\text{best}}[n]$ and $r_{n+1} = \frac{1}{I} R[n+1]$. From (5.11) and bearing in mind that noise is stationary, it follows that

$$r_{n+1} \sim \mathcal{N}\left(\sqrt{(\chi_n y + x)^2 + \frac{\sigma_w^2}{2I^2}}, \frac{\sigma_w^2}{2I^2} \right), \tag{5.20}$$

$$r_n \sim \mathcal{N}\left(\sqrt{y^2 + \frac{\sigma_w^2}{2I^2}}, \frac{\sigma_w^2}{2I^2} \right), \tag{5.21}$$

and, consequently, $z_{n+1} \triangleq r_{n+1} - r_n$ verifies

$$z_{n+1} \sim \mathcal{N}\left(\sqrt{(\chi_n y + x)^2 + \frac{\sigma_w^2}{2I^2}} - \sqrt{y^2 + \frac{\sigma_w^2}{2I^2}}, \frac{\sigma_w^2}{I^2} \right). \tag{5.22}$$

Finally, from (5.19) and (5.22), we conclude that the conditional expectation of the increase in beamforming gain equals:

$$\begin{aligned} h_n(y) &= \int_{-\infty}^{\infty} \int_{A(x)}^{\infty} (x - y(1-\chi_n)) \frac{1}{\sqrt{2\pi\sigma^2_{\mathcal{R}}[n]}} e^{-\frac{x^2}{2\sigma^2_{\mathcal{R}}[n]}} \times \\ &\quad \times \frac{1}{\sqrt{2\pi\sigma_w^2/I^2}} e^{-\frac{z^2}{2\sigma_w^2/I^2}} dz\, dx \\ &= \int_{-\infty}^{\infty} (x - y(1-\chi_n)) \frac{1}{\sqrt{2\pi\sigma^2_{\mathcal{R}}[n]}} e^{-\frac{x^2}{2\sigma^2_{\mathcal{R}}[n]}} \times \\ &\quad \times \mathcal{Q}\left(\frac{\sqrt{y^2 + \frac{\sigma_w^2}{2I^2}} - \sqrt{(\chi_n y + x)^2 + \frac{\sigma_w^2}{2I^2}}}{\sigma_w / I} \right) dx, \end{aligned} \tag{5.23}$$

where the lower limit of the second integral equals: $A(x) = \sqrt{y^2 + \frac{\sigma_w^2}{2I^2}} - \sqrt{(\chi_n y + x)^2 + \frac{\sigma_w^2}{2I^2}}$, and $\mathcal{Q}(x)$ stands for the Q-function, namely, $Q(x) = \int_x^\infty \exp(-u^2/2) du$. Since a closed-form solution of (5.23) is difficult to obtain, in the sequel we will resort to numerical integration methods.

Asymptotic behavior

In [8], the authors proved that in a noiseless scenario the expected value of the normalized beamforming gain when $n \to \infty$ is $y = 1$. Here, we show that in noisy scenarios such limit is not achievable. We start by noting that the increment of the normalized beamforming gain $h_n(y)$ is, by definition, a continuous function (actually, an integral of a continuous function). In Appendix 5.A.1, we prove on the one hand that $h_n(y) < 0$ for $y = 1$; and, on the other, that $h_n(y) > 0$ for $y = 0$. Hence, there exists a value of $y \in (0 \ldots 1)$ for which expected increase of the normalized beamforming gain turns out to be $h_n(y) = 0$. At this point, the expected normalized beamforming saturates. Besides, when the recursive algorithm is initialized (i.e. *before* running the algorithm), the set of overall phase rotations $\Phi_i[n]$ are uniform i.i.d. random variables (over sensors). In these circumstances, one can easily show that the expected value of the beamforming gain is $1/\sqrt{I}$. In other words, $1/\sqrt{I}$ can be regarded as a lower bound which results when no control is exerted on the phases. For this reason, we conjecture that, in noisy scenarios, the maximum achievable value of the expected beamforming gain actually lies in the range $(1/\sqrt{I} \ldots 1)$. Computer simulation results confirm this extent.

Numerical results

Next, we present some numerical and computer simulation results aimed to illustrate the impact of channel noise on the behavior of the algorithm. The total number of sensors equals $I = 300$. Sensors are deployed over a disk of radius R according to a uniform distribution. The base station is located at a distance $D \gg R$ (i.e. far field conditions). The phase perturbations are chosen independently from a uniform distribution, that is, $\delta_i \sim \mathcal{U}(-\frac{\pi}{20}, \frac{\pi}{20})$.

In Figure 5.2, we depict the evolution of the expected beamforming gain (normalized). Several curves are shown for a collection of values of the noise variance. As a benchmark, the curve corresponding to a noiseless scenario ($\sigma_w^2 = 0$) is included, as well. First of all, we observe a close match between computer simulations results (solid lines) and the prediction from our analysis (dashed lines). Next, and as previously discussed, the algorithm does not achieve full beamforming gain in noisy scenarios (i.e. $\sigma_w^2 > 0$). Beyond some point, the fact that the variable upon which the decisions on keeping or rejecting perturbations is corrupted by noise prevents the algorithm from fully aligning sensor phases (and, of course, the higher the noise, the lower the beamforming gain after convergence). This also has an impact on the initial rate at which the algorithm converges which is also lower (i.e. less steep curves around $n = 0$) when the variance of the noise increases.

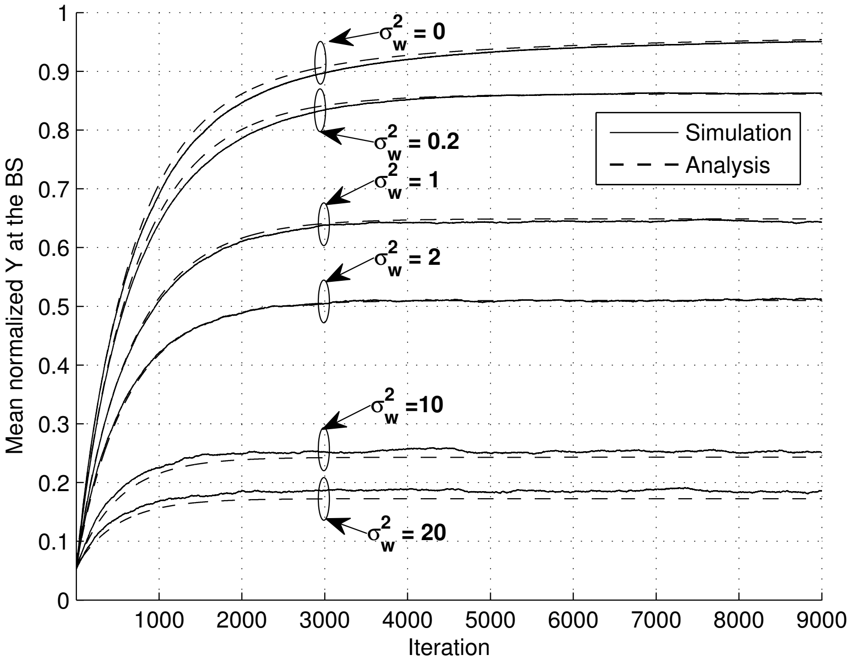

Figure 5.2: Mean normalized beamforming gain vs. number of iterations ($I = 300$).

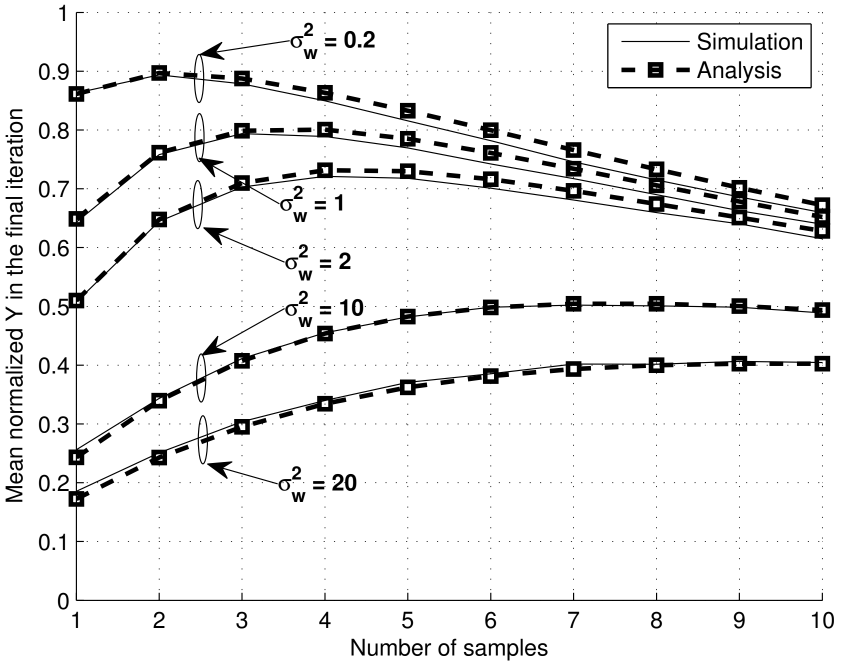

Figure 5.3: Mean normalized beamforming gain after $M = \lfloor L_T/L \rfloor$ iterations vs. number of samples per iteration, L. ($I = 300$, $L_T = 9000$).

Indeed, one can increase the reliability of the measured received signal strength ($R[n]$) by averaging out L consecutive samples. By doing so, the effective noise variance becomes σ_w^2/L.

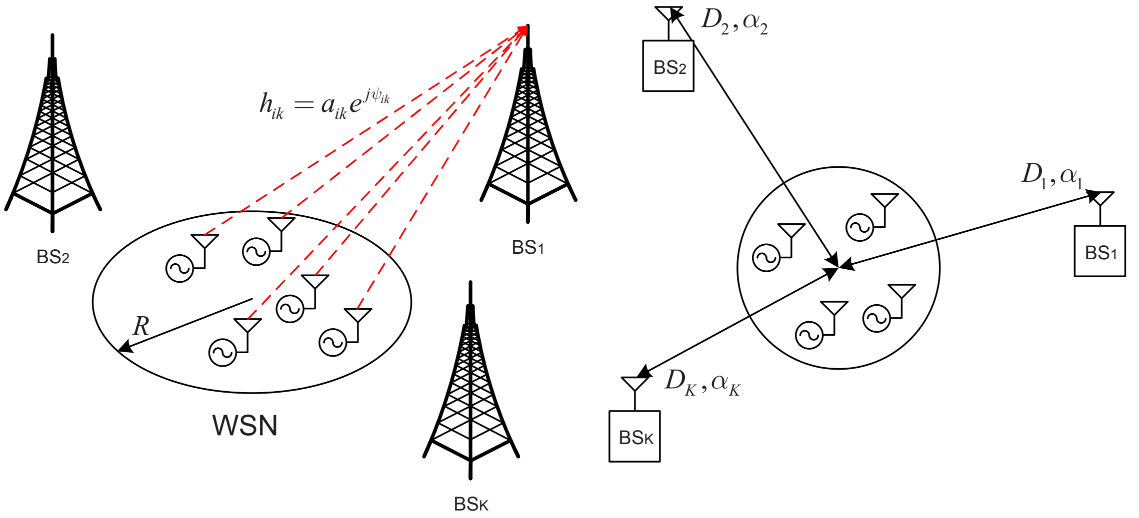

Figure 5.4: A WSN cluster with multiple base stations.

However, the total number of iterations M for a given number of samples L_T yields $M = \lfloor L_T/L \rfloor$. In other words, decisions are more reliable now but the number of iterations available is smaller. This suggests that an optimal value of L could exist. Figure 5.3 illustrates this extent. Clearly, the higher the variance of the observation noise, the higher the optimal number of samples per iteration.

5.3.2 Distributed beamforming with sidelobe control mechanisms

In this section, we generalize the one bit of feedback algorithm of [8] to encompass sidelobe control mechanisms. As in the previous section, we consider a wireless sensor network consisting of I sensor nodes randomly placed over a disk of radius R according to a uniform distribution. In contrast to the original scenario given in [8], here we assume that the WSN is surrounded by K Base Stations (BS) located on the XY plane at directions $\mathcal{A} = \{\alpha_1, \alpha_2, \ldots, \alpha_K\}$ and distances $\mathcal{D} = \{D_1, D_2, \ldots, D_K\}$ (see Figure 5.4). As in Section 5.2, we assume that BSs are far apart and outside the coverage area of each individual sensor node. In the given scenario, the goal is to collaboratively transmit a common message signal $m(t)$ to the BS of interest (referred to in the sequel as *main* BS) without causing unacceptable interference levels to the remaining $K - 1$ base stations which are assigned to other clusters of sensor nodes (*interfered* or *unintended* ones). We make the same assumptions for the common message and transmitted signal as those given in Section 5.2.

As for the complex channel from the i-th sensor to the k-th BS, it is now denoted by $h_{ik} = a_{ik}e^{j\psi_{ik}}$, where a_{ik} and ψ_{ik} account for the channel gain and phase shift associated with the Euclidean distance between the sensor and the k-th base station. Accordingly, the signal received at the k-th BS is given by:

$$\begin{aligned} r_k(t) &= \mathcal{R}\left(\sum_{i=1}^{I} s_i(t)h_{ik} + w(t)\right) \\ &= \mathcal{R}\left(m(t)e^{j2\pi f_c t}\sum_{i=1}^{I} a_{ik}b_i e^{j(\gamma_i+\theta_i+\psi_{ik})} + w(t)\right) \end{aligned} \tag{5.24}$$

with $w(t) \sim \mathcal{N}(0, \sigma_w^2)$. Due to hardware limitations, we assume that the transmit power at each sensor node is constant and, hence, the transmit weights become $g_i = e^{-j\theta_i}$. Besides, for simplicity, we assume that $a_{ik} = 1$ for all sensors, i.e. the distance between each BS and the sensors is much larger than inter-sensor distance. After down-conversion and sampling and by neglecting the noise term in (5.24), the received signal strength (RSS) at the k-th BS in the current timeslot reads:

$$\begin{aligned} \mathrm{RSS}_k\,[n] &= Y_k[n] \\ &= \left|\sum_{i=1}^{I} e^{j\Phi_{ik}[n]}\right|, \end{aligned} \tag{5.25}$$

where $\Phi_{ik} = \gamma_i + \theta_i + \psi_{ik}$ denotes the overall phase rotation of the signal received at the k-th BS from the i-th sensor node.

Optimization problem

From all the above, the problem of distributed beamforming with sidelobe control can be posed as follows (without loss of generality, we assume that $k = 1$ indexes the main BS):

$$\begin{aligned} &\max && Y_1 \\ &\text{subject to} && Y_k \leq \Gamma_k,\ k = 2, \ldots, K, \end{aligned} \tag{5.26}$$

where the Γ_k thresholds are system parameters. By resorting to vector notation, and defining $\mathbf{a}_k = [a_{1k}e^{j(\gamma_1+\psi_{1k})}, \ldots, a_{Nk}e^{j(\gamma_N+\psi_{Nk})}]^T$ $\mathbf{g} = [e^{-j\theta_1}, \ldots, e^{-j\theta_N}]^T$, the problem can be posed as:

$$\begin{aligned} &\max_{\mathbf{g}} && \left|\mathbf{g}^H\mathbf{a_1}\right| \\ &\text{subject to} && \left|\mathbf{g}^H\mathbf{a}_k\right| \leq \Gamma_k,\ k = 2, \ldots, K. \\ & && \mathsf{diag}\left[\mathbf{g}\mathbf{g}^H\right] \leq \mathbf{1}, \end{aligned} \tag{5.27}$$

where $\mathbf{1}$ denotes an $I \times 1$ vector with all entries equal[3] to 1. In this way, vector g gathers the beamforming weights to be optimized, whereas $\mathbf{a}_k$ accounts for the phase offset *and* channel propagation effects. This formulation is particularly useful in order to numerically solve the problem.

---

[3] This is a relaxed optimization problem. Note, that for the iterative solution, we assume that the powers at all the sensors are constant and *equal* to one.

Iterative solution with partial channel state information

The enhancement of the original DBF scheme by including sidelobe control mechanisms (DBF-SC) is motivated by the fact that a subset of the sequence of perturbations $\{\Delta[n]\}$ is capable of *simultaneously* increasing $Y_1[n]$ and decreasing $Y_k[n]$ for $k = 2 \ldots K$, bringing us one step closer to the solution of the constrained problem (5.26). To enforce this behavior, not only the main BS but also the unintended ones need to measure the RSS and generate the corresponding feedback messages, that is,

$$z_{\text{FB},1}[n+1] = \begin{cases} 1 & \text{if } Y_1[n+1] \geq Y_{\text{best},k}[n] \\ 0 & \text{otherwise} \end{cases}, \tag{5.28}$$

$$z_{\text{FB},k}[n+1] = \begin{cases} 1 & \text{if } (Y_k[n+1] < Y_{\text{best},k}[n] \text{ or } Y_k[n+1] < \Gamma_k) \\ 0 & \text{otherwise} \end{cases}, \text{for } k = 2, \ldots, K. \tag{5.29}$$

The sensor nodes will only keep their perturbations if positive feedback is received from *all* the BSs, namely,

$$\theta_{\text{best},i}[n+1] = \begin{cases} \theta_{\text{best},i}[n] + \delta_i[n] & \text{if } z_{\text{FB},k}[n+1] = 1 \text{ for } k = 1, \ldots, K. \\ \theta_{\text{best},i}[n] & \text{otherwise} \end{cases} \tag{5.30}$$

This algorithm is iterated until the desired RSS level at the main BS stabilizes while the RSS at the unintended BS are kept below the corresponding set of Γ_k thresholds (or until the maximum number of iterations is reached).

Clearly, the introduction of constraints into the problem leads to a decreased convergence rate: only a subset of the perturbations of the unconstrained problem will be kept now. This can be particularly harmful when the directions of main and unintended BSs are close to each other, or when the number of unintended BSs is high. In order to investigate these challenges, in the sequel, we propose to check the validity of the solutions against those obtained via convex optimization methods, which will be used as a benchmark.

Numerical solution with full channel state information

The optimization problem (5.27) is not convex because the goal is to *maximize* a convex objective function subject to a set of convex inequality constraint functions. Besides, the objective function is invariant to an arbitrary phase rotation applied to vector g. To transform the problem into a convex one, we force the solution vector to fulfill[4] $\mathcal{I}\left(\mathbf{g}^H \mathbf{a_1}\right) = 0$, this leading to the

---

[4] This can be done by appropriately selecting the phase rotation term.

following equivalent optimization problem:

$$\begin{aligned}
\max_{\mathbf{g}} \quad & \mathcal{R}\left(\mathbf{g}^H \mathbf{a_1}\right) \\
\text{subject to} \quad & \mathcal{I}\left(\mathbf{g}^H \mathbf{a_1}\right) = 0 \\
& \mathcal{R}^2\left(\mathbf{g}^H \mathbf{a}_k\right) + \mathcal{I}^2\left(\mathbf{g}^H \mathbf{a}_k\right) \leq \Gamma_k^2, \; k = 2, \ldots, K \\
& \mathsf{diag}\left[\mathbf{g}\mathbf{g}^H\right] \leq \mathbf{1},
\end{aligned} \tag{5.31}$$

where the third constraint in (5.31) becomes active for large I. Next, we apply the following change of variables:

$$\hat{\mathbf{g}} = \begin{bmatrix} \mathcal{R}(\mathbf{g}) \\ \mathcal{I}(\mathbf{g}) \end{bmatrix}; \; \hat{\mathbf{a}}_k = \begin{bmatrix} \mathcal{R}(\mathbf{a}_k) \\ \mathcal{I}(\mathbf{a}_k) \end{bmatrix}; \; \mathring{\mathbf{a}}_k = \begin{bmatrix} \mathcal{I}(\mathbf{a}_k) \\ -\mathcal{R}(\mathbf{a}_k) \end{bmatrix}; \tag{5.32}$$

and, bearing all the above in mind, the optimization problem can be finally re-written as:

$$\begin{aligned}
\max_{\hat{\mathbf{g}}} \quad & \hat{\mathbf{g}}^T \hat{\mathbf{a}}_1 \\
\text{subject to} \quad & \hat{\mathbf{g}}^T \mathring{\mathbf{a}}_1 = 0 \\
& \left(\hat{\mathbf{g}}^T \hat{\mathbf{a}}_k\right)^2 + \left(\hat{\mathbf{g}}^T \mathring{\mathbf{a}}_k\right)^2 \leq \Gamma_k^2, \; k = 2, \ldots, K. \\
& \mathsf{diag}\left[(\mathbf{M}\hat{\mathbf{g}})(\mathbf{M}\hat{\mathbf{g}})^H\right] \leq \mathbf{1},
\end{aligned} \tag{5.33}$$

where we have defined $\mathbf{M} = [\mathbf{I}_I, j\mathbf{I}_I]$ with $\mathbf{I}_I$ denoting an $I \times I$ identity matrix. Clearly, the problem (5.33) is convex, since the goal is to maximize[5] a linear objective function (which, by definition, is convex *and* concave), the inequality constraint functions are convex (quadratic), and the equality constraint ones are affine (actually, linear). Consequently, it can be numerically solved using e.g. interior points methods. To that aim, *full* Channel State Information (CSI) is required at the BS, which is impractical in particular for large networks. On the contrary, the iterative algorithm proposed previously only requires partial CSI knowledge (essentially, SNR measurements at the BS plus one bit of feedback from every BS) and, interestingly, operates in a decentralized manner.

Numerical results

In the sequel, we present some computer simulation results which illustrate the behavior of the iterative distributed beamforming scheme with sidelobe control. Where appropriate, the numerical optimization solution will be used as a benchmark. The total number of sensor nodes is $I = 100$ and they are deployed in a disk or radius R (normalized to the wavelength). The main and the $K - 1$ unintended BS are located in the far-field of the cluster WSN at identical distances (i.e. $D_k = D \gg R$). Without loss of generality, we assume that the main

---

[5] Out of the two phase rotations for which $\mathbf{g}^H \mathbf{a_1} = \mathcal{R}(\mathbf{g}^H \mathbf{a_1})$, this formulation naturally leads to the one resulting in $\mathcal{R}(\mathbf{g}^H \mathbf{a_1}) > 0$.

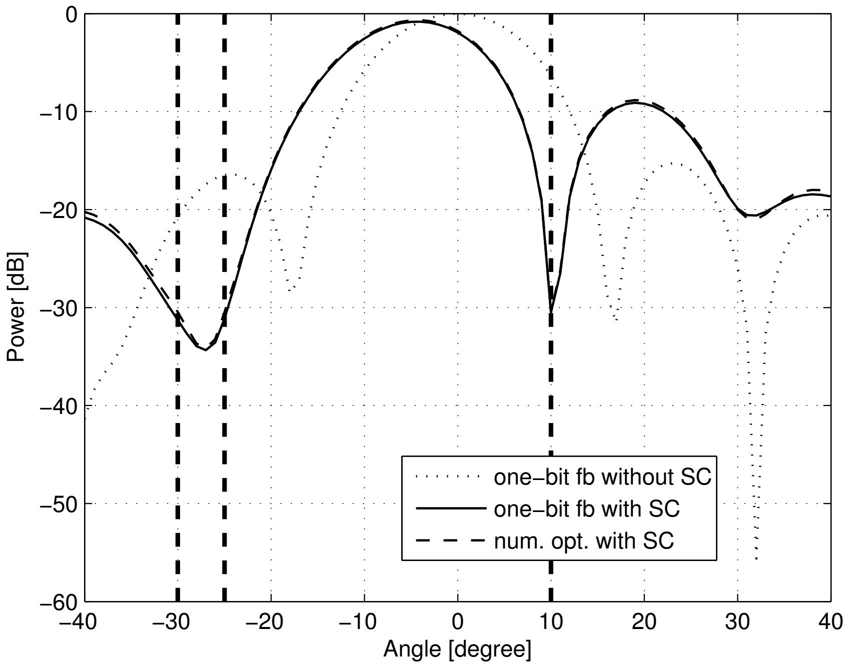

Figure 5.5: Average radiation pattern of beamforming schemes with and without sidelobe control mechanisms ($K = 4$, $R = 2$, $\alpha_{\text{main}} = 0°$, $\alpha_{\text{un}} = [-30°, -25°, 10°]$, $\Gamma_{dB} = -30$ dB).

.

BS is located at $\alpha_1 = \alpha_{\text{main}} = 0°$. The phase perturbations are chosen independently from a uniform distribution, that is, $\delta_i \sim \mathcal{U}(-\frac{\pi}{50}, \frac{\pi}{50})$. Unless otherwise stated, the maximum number of iterations allowed to the DBF-SC scheme is $L = 5 \cdot 10^4$ and the (normalized) thresholds for the unintended BS are set to $\Gamma_2 = \ldots = \Gamma_K = -30$ dB.

Figure 5.5 illustrates the impact of sidelobe control mechanisms on the resulting beampattern. Clearly, the DBF-SC scheme succeeds in reducing the received signal strength in the direction of the unintended BSs (denoted by dashed vertical lines in the plot) at levels of -30 dB or less, whereas in the original beampattern they were substantially above. However, we also observe that the maximum of the beampattern is shifted away from α_{main}. This is due to the fact that one of the unintended BSs falls within the mainlobe of the original beampattern ($\alpha_2 = 10°$). Besides, Figure 5.5 reveals that the beampatterns obtained with the iterative DBF-SC scheme and numerical optimization tools are identical, which empirically validates the proposed distributed beamforming scheme.

Figure 5.6 shows the average beampattern for different WSN radii R in the presence of one unintended BS at $\alpha_2 = 10°$. As expected, the larger radius, the narrower the mainlobe. For $R = 4$ (or larger), this allows the mainlobe to continue to point at the main BS whereas for smaller radii its maximum is again shifted away. Clearly, this results into an RSS loss at the main BS. This effect can be readily observed in Figure 5.7 where we depict the evolution of the mean normalized RSS for the main BS in the same scenario (averaged over 100 algorithm

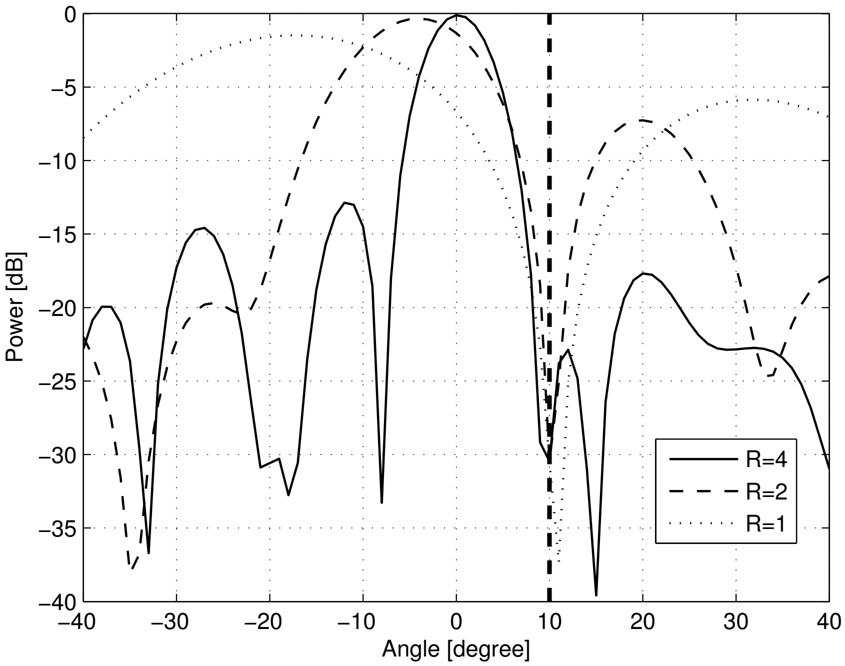

Figure 5.6: Average radiation pattern of beamforming schemes with sidelobe control mechanisms ($K = 2$, $\alpha_{\text{main}} = 0°$, $\alpha_{\text{un}} = 10°$, $\Gamma_{dB} = -30$ dB).

runs). After convergence, the penalty in terms of normalized RSS for the $R = 1$ case is on the order of 7 dB. Interestingly, the rate at which the DBF-SC converges to the optimal solution is also affected by the network size. Whereas for larger radii the loss is marginal with respect to the unconstrained case (dotted curve), for smaller radii the slope of the curves is substantially smaller. Indeed, for broader mainlobes it is more difficult to find perturbations that simultaneously increase the RSS at the main BSS and decrease the RSS at the interfered ones. This can also be observed in Figure 5.8 where we show the evolution of the normalized RSS at the *unintended* BS. Clearly, the interference level decreases more slowly for smaller radii. The inspection of the upper and bottom plots also gives some insights on how the DBF-SC scheme exploits the available degrees of freedom to find an optimal balance. Although the interference level temporarily goes below the prescribed threshold (see the first 500 iterations of the $R = 4$ curve), finally it converges to $\Gamma = -30$ dB since, otherwise, it would not be possible to maximize the RSS at the main BS.

Next, in Figure 5.9, we analyze the impact of the angle difference $\Delta\alpha$ between the main and the unintended BS on the normalized RSS at the main BS. We observe that, as soon as the unintended BS enters the mainlobe region, the normalized RSS degrades rapidly. Of course, the angle difference at which such degradation starts depends on the network radius. Besides, the fact that for some directions of the unintended BS it coincides with the maximum of a sidelobe (that needs to be canceled) and for some other with a deep null of the radiation pattern motivates the slight fluctuations in the upper part of the plot.

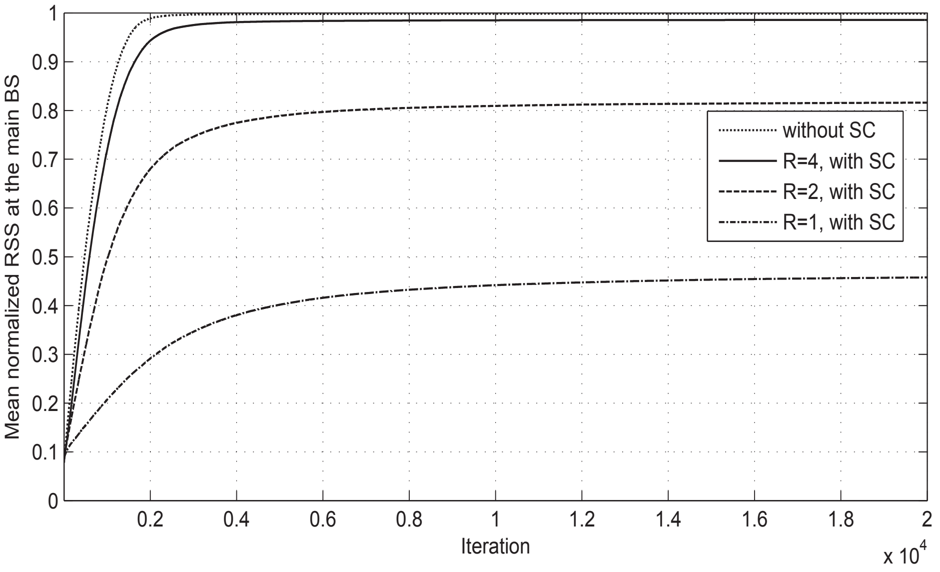

Figure 5.7: Mean normalized RSS for the main BS vs. number of iterations ($\alpha_{\text{main}} = 0°$, $\alpha_{\text{un}} = 10°$, $\Gamma_{dB} = -30$ dB).

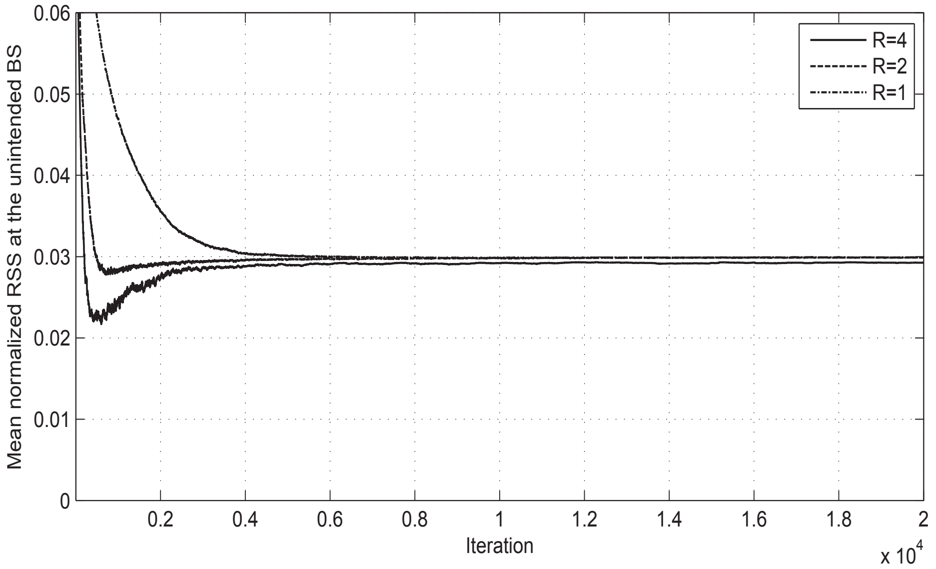

Figure 5.8: Mean normalized RSS for the unintended BS vs. number of iterations ($\alpha_{\text{main}} = 0°$, $\alpha_{\text{un}} = 10°$, $\Gamma_{dB} = -30$ dB).

Interestingly, the results (which are averaged over a large number of realizations) are identical for both the iterative DBF-SC scheme and the numerical solution. This, again, validates the proposed distributed beamforming scheme.

Complementarily, Figure 5.10 shows the normalized RSS at the main BS as a function of the threshold associated with the unintended one ($K = 2$ case). For this scenario, the impact of Γ is

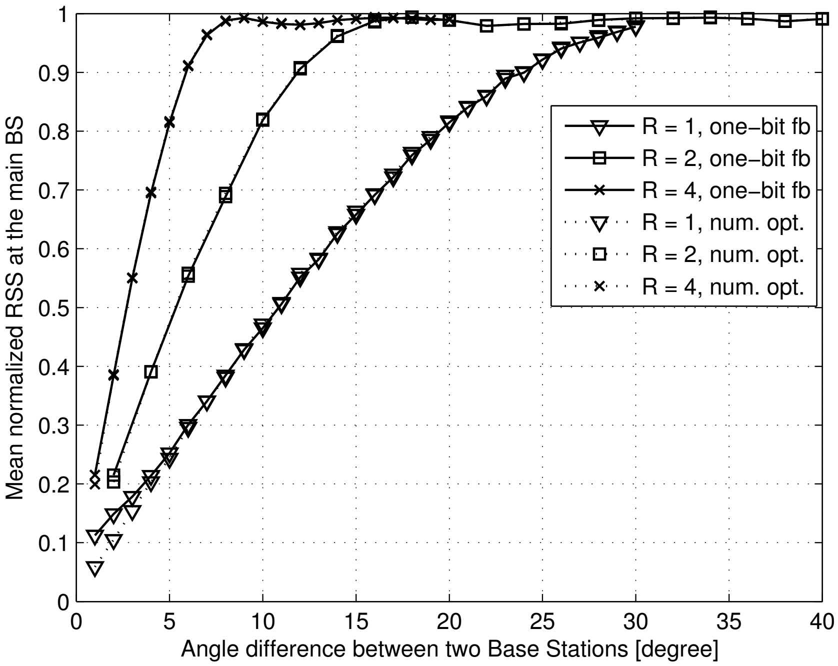

Figure 5.9: Mean normalized received signal strength vs. angle difference main-unintended BS ($K = 2$, $\Gamma_{dB} = -30$ dB).

relatively mild: it slightly degrades in the $-20 \ldots -40$ dB range and, interestingly, it virtually saturates for values below -40 dB. In other words, beyond a certain point there is no penalty associated with making nulls deeper and, by doing so, increasing the SINR in the unintended BSs. Curves can be significantly different (RSS saturation levels, ranges) for networks with a diverse number of sensor nodes since the average value of sidelobe peaks (and, the effort needed to keep them under control) strongly depends on I.

Finally, in Figure 5.11 we depict the *hitting time* which is defined as the number of iterations needed until the average RSS at the main BS reaches 90% of its maximum value, for a varying number of unintended BSs. Results are averaged over the directions of the interfered BSs and sensor locations. As expected, when the number of BSs increases, the time needed for the algorithm to converge increases, as well (chances are higher for one of those BS to lie in the mainlobe of the main BS). Consequently, the degradation is particulary severe for networks with smaller disk radii with almost a 10-fold increase of the hitting time when the number of unintended BSs increases from 1 to 3.

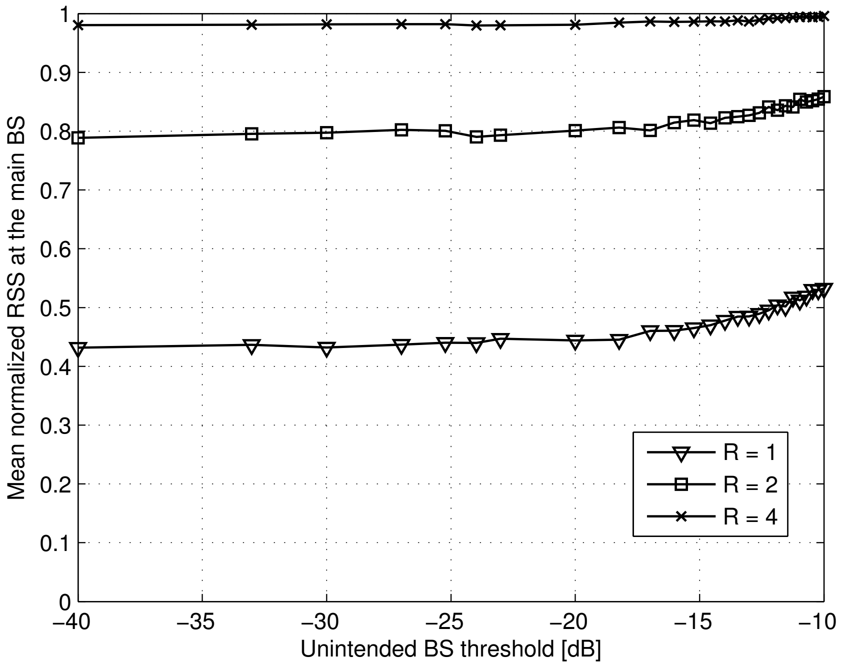

Figure 5.10: Mean normalized received signal strength vs. RSS threshold at the unintended BS ($K = 2$, $\Delta\alpha = 10°$).

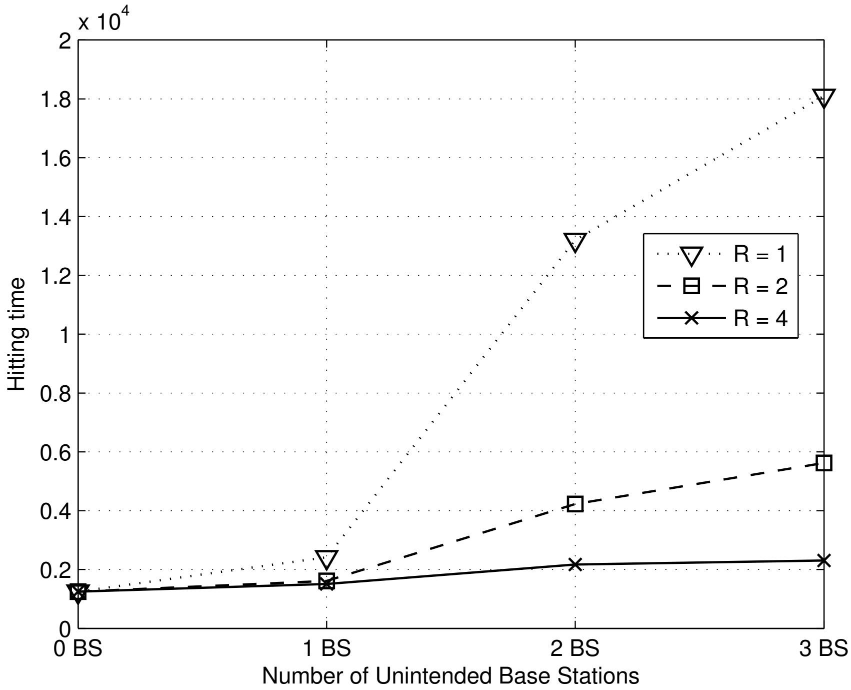

Figure 5.11: Hitting time ($\Gamma_{dB} = -30$ dB).

5.4 Decentralized phase synchronization scheme for collaborative beamforming

In this section, we propose a novel distributed phase synchronization scheme, which turns out to be particularly suitable for communication scenarios where the total duration of the training plus data transmission period is fixed irrespectively of the number of sensors (unlike the iterative schemes proposed in [8,9]). In the proposed scheme, we let all sensors participate in the beamforming process since, unlike in [10], we count with mechanisms to pre-compensate the oscillator phase offset and the channel phase shift.

5.4.1 Communication protocol

To recall, the signal model in Section 5.2 assumes that I sensors collaborate to send a common message signal $m(t)$ to a distant base station. In order to maximize the received signal strength at the base station, the sensor must precompensate the oscillator and channel phase offsets by properly adjusting the θ_i term. In the sequel, we take an approach different from that of Section 5.3. Namely, upon BS request, nodes wake up for T seconds during which a data packet will be transmitted. Typically, T is predefined and turns out to be a small percentage of the time elapsed between consecutive requests (i.e. low duty-cycle). Within this period of time, sensors need to (i) estimate θ_i; (ii) share the common message $m(t)$; and (iii) actually transmit the message. For simplicity, we assume that (ii) is carried out transparently to (i) and (iii) and, hence, the packet consists of one training block and one data transmission block only. Their respective durations are T_T and T_D, with $T = T_\mathrm{T} + T_\mathrm{D}$. The training block, in turn, consists of M timeslots of duration T_M (see Figure 5.12). Each timeslot is used by a sensor (or group of sensors) in order to estimate the corresponding pre-compensation phase. In order to relieve the BS from the burden of allocating sensors to timeslots[6], we allow sensors to randomly choose training timeslots according to a uniform distribution, namely, $p_j = 1/M$; $j = 1 \dots M$. Let $\mathcal{S}_j$ denote the subset of sensors in timeslot j of cardinality $|\mathcal{S}_j| = I_j$. Clearly, I_j is a binomial random variable and it fulfills $\sum_{j=1}^{M} I_j = I$. Whenever $I_j > 1$, the phase pre-compensation will be carried out for the *group* of sensors rather than for *individual* ones. Because of that, the overall received signal strength in the subsequent data transmission period will be lower. However, arbitrarily increasing the number of timeslots M (to avoid sensors to overlap) is detrimental, as well.

---

[6] Note that, in realistic settings, the BS should first learn about which sensors woke up. Since the number is potentially large, the associated signalling needs would also be.

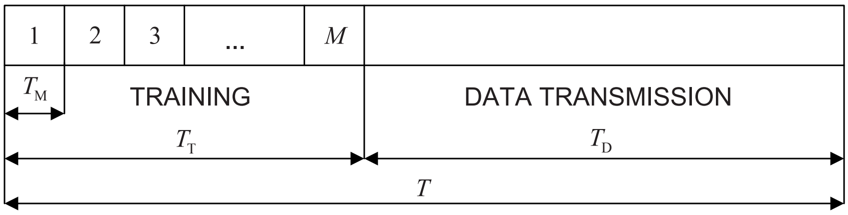

Figure 5.12: Training and data transmission phases.

The amount of information conveyed (i.e., throughput) in the transmit period is given by:

$$R(T_\mathrm{D}) = T_\mathrm{D} \log_2 \left(1 + \frac{\mathrm{RSS}^2\left(T_\mathrm{T}\right)}{\sigma_w^2}\right) \;\text{[bits]}. \tag{5.34}$$

If T_M is pre-defined, then increasing M results into a shorter data transmission block ($T_\mathrm{D} = T - M \cdot T_\mathrm{M}$) and, consequently, lower throughput. If, on the contrary, the duration of the training period T_T is fixed, then timeslots become shorter ($T_\mathrm{M} = \frac{T_\mathrm{T}}{M}$) which results into poorer phase estimates (and, thus, lower RSS in the data transmission period). Consequently, the optimal split between the training and data transmission periods, and the optimal number of timeslots in the training phase should be identified. A more detailed analysis follows.

RSS analysis: ideal phase shift estimation

In the training period, sensors merely transmit an unmodulated carrier. From (5.1) and by defining $\phi_i = \gamma_i + \psi_i$, the received signal in the j-th timeslot reads[7]:

$$r_j(t) = e^{j2\pi f_c t} \sum_{i \in \mathcal{S}_j} e^{j\phi_i} + w(t); \quad t \in [(j-1)T_\mathrm{M}, jT_\mathrm{M}) \tag{5.35}$$

The summation term can be conveniently expressed as

$$\sum_{i \in \mathcal{S}_j} e^{j\phi_i} = \mathrm{RSS}_j e^{j\xi_j} \tag{5.36}$$

with $\mathrm{RSS}_j \geq 0$ denoting the received signal strength in j-th timeslot[8] and ξ_j standing for the aggregated phase shift (see Figure 5.13). For the time being, we assume that ξ_j can be *perfectly* estimated and fedback to all the I_j sensors in timeslot j. Upon completion of the training period, each sensor node pre-compensates its carrier phase by setting $\theta_i = -\xi_j; \forall i \in \mathcal{S}_j$ and, hence, the received signal strength during the data transmission period yields:

$$\mathrm{RSS} = \left| \sum_{j=1}^{M} \sum_{i \in \mathcal{S}_j} e^{j(\phi_i - \xi_j)} \right|, \tag{5.37}$$

---

[7] Time synchronization is already achieved.

[8] For simplicity, the contribution of the additive noise to the resulting RSS will be neglected throughout this section.

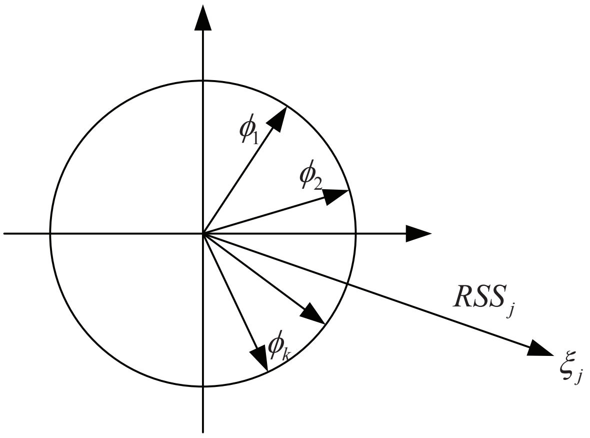

Figure 5.13: Aggregated phase shift in a training slot.

and the expected value of the *normalized* RSS then reads

$$\overline{\mathrm{RSS}} = \frac{1}{I}\mathbb{E}_{\{I_j\}_{j=1}^{M},\{\phi_i\}_{i=1}^{I}}[\mathrm{RSS}]. \tag{5.38}$$

From (5.36), it follows that $\sum_{i\in\mathcal{S}_j} e^{j(\phi_i-\xi_j)} = \mathrm{RSS}_j \in \{\mathbb{R}^+, 0\}$. If, in addition, we define $\Phi_I \triangleq \{\phi_i\}_{i=1}^{I}$ then we can write:

$$\overline{\mathrm{RSS}} = \frac{1}{I}\sum_{j=1}^{M}\mathbb{E}_{I_j,\Phi_I}\left[\mathrm{RSS}_j\right], \tag{5.39}$$

where:

$$\begin{aligned}
\mathbb{E}_{I_j,\Phi_I}[\mathrm{RSS}_j] &= \mathbb{E}_{I_j,\Phi_I}\left[\left|\sum_{k\in\mathcal{S}_j} e^{j(\phi_k-\xi_j)}\right|\right] && (5.40)\\
&= \mathbb{E}_{I_j,\Phi_I}\left[\sqrt{\sum_{k\in\mathcal{S}_j} e^{j(\phi_k-\xi_j)}\sum_{l\in\mathcal{S}_j} e^{-j(\phi_l-\xi_j)}}\right] && (5.41)\\
&= \mathbb{E}_{I_j,\Phi_I}\left[\sqrt{I_j + \sum_{k\in\mathcal{S}_j}\sum_{\substack{l\in\mathcal{S}_j\\ l\neq k}} e^{j(\phi_k-\phi_l)}}\right] && (5.42)\\
&= \mathbb{E}_{I_j,\Phi_I}\left[\sqrt{I_j + \sum_{k\in\mathcal{S}_j}\sum_{\substack{l\in\mathcal{S}_j\\ l> k}} 2\mathcal{R}\{e^{j(\phi_k-\phi_l)}\}}\right] && (5.43)\\
&= \mathbb{E}_{I_j,\Phi_I}\left[\sqrt{I_j + \sum_{k\in\mathcal{S}_j}\sum_{\substack{l\in\mathcal{S}_j\\ l> k}} 2\cos(\phi_k-\phi_l)}\right] && (5.44)
\end{aligned}$$

$$\tag{5.45}$$

The expectation in this last expression is difficult to compute in closed form. Hence, we resort to the following upper bound:

$$\mathbb{E}_{I_j,\Phi_I}[\text{RSS}_j] \leq \mathbb{E}_{I_j}\left[\sqrt{I_j + \sum_{k\in\mathcal{S}_j}\sum_{\substack{l\in\mathcal{S}_j\\ l>k}} 2\mathbb{E}_{\phi_k,\phi_l}[\cos(\phi_k-\phi_l)]}\right], \tag{5.46}$$

which follows from Jensen's inequality and the fact that I_j is statistically independent of Φ_I. With the change of variables $z = \phi_k - \phi_l$, the inner expectation term yields

$$\begin{aligned}\mathbb{E}_{\phi_k,\phi_l}[\cos(\phi_k-\phi_l)] &= \mathbb{E}_z[\cos(z)]\\ &= \frac{1}{2\pi}\int_{-\pi}^{\pi}\cos(z)dz\\ &= 0.\end{aligned} \tag{5.47}$$

which follows from the fact that z is uniformly distributed in $[-\pi,\pi]$ since so are both ϕ_k and ϕ_l[9].

From (5.46) and (5.47), we conclude that the contribution of the sensors in the j-th slot to the resulting RSS can be upper-bounded as follows:

$$\mathbb{E}_{I_j,\Phi_I}[\text{RSS}_j] \leq \mathbb{E}_{I_j}\left[\sqrt{I_j}\right]. \tag{5.48}$$

and, hence, the *normalized* RSS of (5.39) can in turn be upper-bounded by:

$$\overline{\text{RSS}} \leq \frac{M}{I}\mathbb{E}_{I_j}\left[\sqrt{I_j}\right]. \tag{5.49}$$

Unfortunately, this expectation cannot be computed in closed-form and, as such, is not very informative. We can gain some insight by letting M and I grow without bound at a constant ratio $\alpha = \frac{M}{I}$. In this case, the (binomial) random variable I_j is well approximated by a Poisson r.v. of mean α^{-1} [52](Ch.3). From all the above, the upper bound for *normalized* RSS in (5.49) yields:

$$\overline{\text{RSS}} \leq e^{-\frac{1}{\alpha}}\sum_{k=0}^{\infty}\alpha^{1-k}\frac{\sqrt{k}}{k!}. \tag{5.50}$$

This expression reveals that, with perfect phase-shift estimation, the normalized RSS exclusively depends on α, that is, the ratio of the number of available timeslots to the number of sensors. In Figure 5.14, we depict the actual RSS (for a scenario with $I = 100$ sensors) along with the corresponding upper bound. The bound is particularly tight for large α (i.e. $M \gg I$) since, in this case, the upper bound in (5.46) is tight as well (essentially, the cross terms in the summations vanish). Besides, we also realize that, for large α, the system achieves full beamforming gain. This follows from the fact that, for large M, the probability of having more than one sensor in a time slot is low. Consequently, the phase shift can be ideally estimated and pre-compensated for each individual sensor rather than for the whole group.

---

[9] The pdf of $z = \phi_k - \phi_l$ is given by the convolution of the individual pdfs and, thus, it exhibits a triangular shape within $[-2\pi, 2\pi]$. Phase wrapping effects, render this pdf equivalent to a uniform one within $[-\pi,\pi]$.

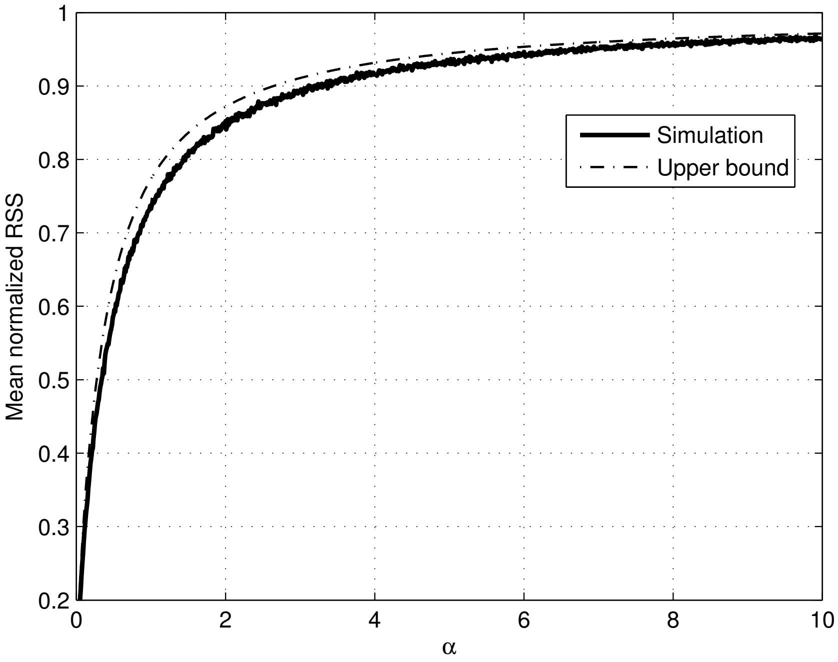

Figure 5.14: Mean normalized RSS vs. $\alpha = \frac{M}{I}$ (I = 100).

RSS analysis: noisy phase shift estimation

Here, we assume that the duration of the training period is fixed (e.g. defined as a percentage of the data transmission time). Consequently, the higher the number of timeslots, the shorter their duration. This has an impact on the quality of the corresponding phase estimates $\hat{\xi}_j$ that we analyze next.

Let f_s be the sampling frequency. Consequently, the total number of samples in the training period and in each timeslot are $L_\mathrm{T} = f_s T_\mathrm{T}$ and $L = L_\mathrm{T}/M$, respectively. The maximum-likelihood (ML) estimate of the aggregated phase shift in the j-th slot is given by [53](Ch.7)

$$\hat{\xi}_j = -\arctan \frac{\sum_{n=0}^{L-1} r_j[n] \sin(2\pi f_c n)}{\sum_{n=0}^{L-1} r_j[n] \cos(2\pi f_c n)}. \tag{5.51}$$

where $r_j[n]$ denotes the sampled version of the received signal. For large L, the estimation error $\Delta\xi_j = \xi_j - \hat{\xi}_j$ turns out to be a zero-mean Gaussian r.v. of variance

$$\begin{aligned} \sigma^2_{\Delta\xi_j} &= \frac{\sigma_w^2}{L \cdot \mathrm{RSS}_j^2} \\ &= \frac{M\sigma_w^2}{L_\mathrm{T} \cdot \mathrm{RSS}_j^2}. \end{aligned} \tag{5.52}$$

which indicates that the quality of the estimate is a function of the number of samples L in the timeslot. To recall, the instantaneous RSS at the BS after phase pre-compensation by all sensors reads

$$\mathrm{RSS} = \left| \sum_{j=1}^{M} \sum_{i \in \mathcal{S}_j} e^{j(\phi_i - \hat{\xi}_j)} \right|, \tag{5.53}$$

and, from (5.36), we can write

$$\begin{aligned} \frac{1}{I}\mathrm{RSS} &= \frac{1}{I}\left| \sum_{j=1}^{M} \mathrm{RSS}_j e^{j\Delta\xi_j} \right| \\ &= \alpha \left| \frac{1}{M} \sum_{j=1}^{M} \mathrm{RSS}_j e^{j\Delta\xi_j} \right|. \end{aligned} \tag{5.54}$$

From the weak law of large numbers, for large M and I we have that

$$\alpha \left| \frac{1}{M} \sum_{j=1}^{M} \mathrm{RSS}_j e^{j\Delta\xi_j} \right| \xrightarrow{P} \alpha \left| \mathbb{E}_{I_j,\Phi_I,\Delta\xi_j}[\mathrm{RSS}_j e^{j\Delta\xi_j}] \right|, \tag{5.55}$$

where P denotes convergence in probability. With a slight abuse of notation, the normalized RSS asymptotically reads:

$$\overline{\mathrm{RSS}} = \frac{M}{I} \left| \mathbb{E}_{I_j,\Phi_I,\Delta\xi_j}[\mathrm{RSS}_j e^{j\Delta\xi_j}] \right| \tag{5.56}$$

or, equivalently,

$$\overline{\mathrm{RSS}} = \frac{M}{I} \left| \mathbb{E}_{I_j,\Phi_I}\left[\mathrm{RSS}_j \mathbb{E}_{\Delta\xi_j | I_j,\Phi_I}[e^{j\Delta\xi_j}] \right] \right|. \tag{5.57}$$

Since the phase estimation errors are Gaussian-distributed, this implies that

$$\begin{aligned} \mathbb{E}_{\Delta\xi_j | I_j,\Phi_I}\left[e^{j\Delta\xi_j} \right] &= e^{-\frac{1}{2}\sigma^2_{\Delta\xi_j}} \\ &= e^{-\frac{M\sigma_w^2}{2L_\mathrm{T}\cdot\mathrm{RSS}_j^2}}. \end{aligned} \tag{5.58}$$

From the last two equations and by resorting again to Jensen's inequality, we can thus write

$$\begin{aligned} \overline{\mathrm{RSS}} &= \frac{M}{I} \left| \mathbb{E}_{I_j,\Phi_I}\left[\mathrm{RSS}_j e^{-\frac{M\sigma_w^2}{2L_\mathrm{T}\cdot\mathrm{RSS}_j^2}} \right] \right| && (5.59) \\ &= \frac{M}{I} \mathbb{E}_{I_j,\Phi_I}\left[\mathrm{RSS}_j e^{-\frac{M\sigma_w^2}{2L_\mathrm{T}\cdot\mathrm{RSS}_j^2}} \right] && (5.60) \\ &\leq \frac{M}{I} \mathbb{E}_{I_j}\left[\sqrt{I_j} e^{-\frac{M\sigma_w^2}{2L_\mathrm{T}\cdot I_j}} \right] && (5.61) \end{aligned}$$

where in the second equality we have exploited the fact that all the terms in the expectation are real-valued and positive. Again, for $M, I \to \infty$ and $\alpha = \frac{M}{I}$ constant, the random variable I_j is approximately Poisson distributed and, thus,

$$\overline{\mathrm{RSS}} \leq e^{-\frac{I}{M}} \sum_{k=0}^{\infty} \left(\frac{M}{I} \right)^{1-k} \frac{\sqrt{k}}{k!} e^{-\frac{M\sigma_w^2}{2L_\mathrm{T}k}} \tag{5.62}$$

Interestingly, the exponential term in the summation models the decrease in RSS resulting from the use of imperfect phase estimates.

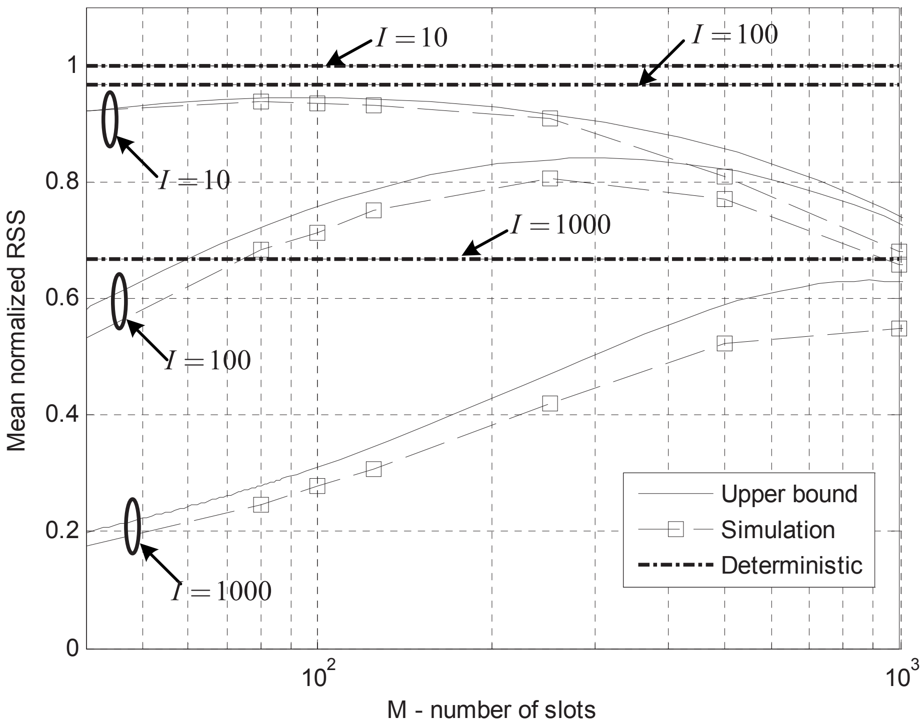

Figure 5.15: Mean normalized RSS vs. number of timeslots M ($\sigma_w^2 = 6$, $T_\mathrm{T} = 10^4$).

Numerical results

In this section, we present some computer simulation and numerical results which illustrate the behavior of the proposed distributed beamforming scheme. In all cases, the duration of the training slots is inversely proportional to M and, hence, we address the scenario with imperfect (noisy) phase estimates. Without loss of generality, time is normalized to the sampling period (i.e. $T_s = 1$).

Figure 5.15 depicts the normalized RSS as a function of the number of timeslots M. For benchmarking purposes, we also indicate the RSS attainable when the BS allocates sensors to timeslots in a centralized manner ($M = I$ case, curves labeled as 'deterministic') and the corresponding upper bounds of (5.62). The plot reveals that the upper bound is, in general, tight. However, it is worth noting that it is not valid for very small or large values of M. For small M, on the one hand, the bound (5.61) is loose and, besides, the approximation of a binomial distribution by a Poisson one is not accurate. For large M, on the other, the assumption of large $L = L_\mathrm{T}/M$ in the computation of the asymptotic variance of (5.52) does not hold. We also observe that the optimal number of timeslots increases for larger networks (see maxima for the curves with $I = 10$, 100 and 1000 sensors). Intuitively, the higher the number of sensors, the higher the number of timeslots needed to minimize the risk of having more than one sensor in one timeslot (even if this comes at a price of experiencing higher variance in the phase estimates). Besides, we observe that the loss (in terms of normalized RSS) for schemes with decentralized allocation of timeslots is moderate (some 5% to 15%).

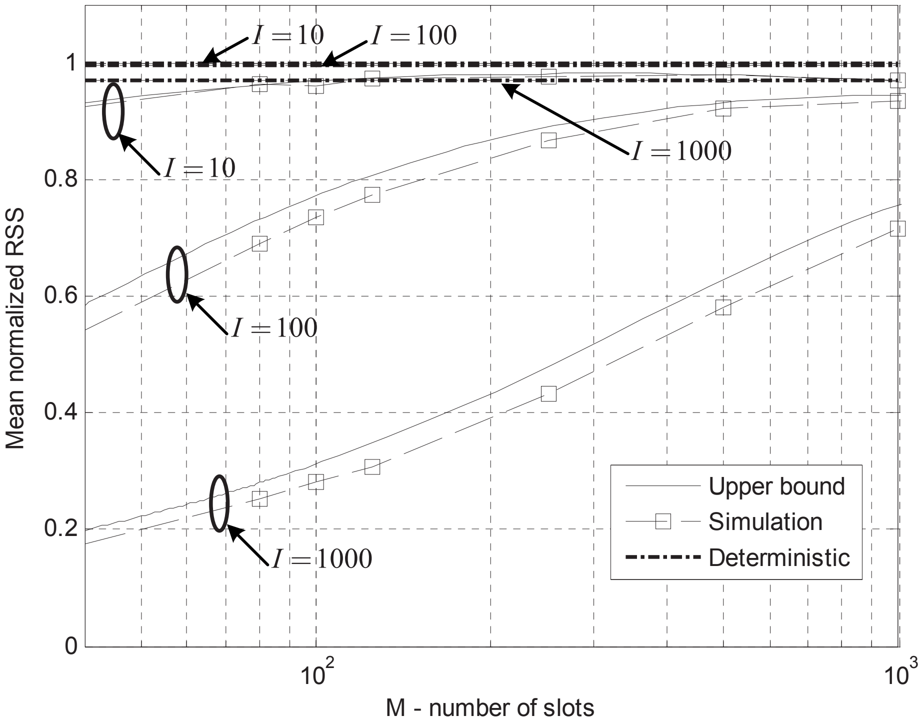

Figure 5.16: Mean normalized RSS vs. number of timeslots M ($\sigma_w^2 = 6$, $T_\mathrm{T} = 10^5$).

In other words, the lack of coordination can be in part compensated with a sufficiently high (and optimally designed) number of training timeslots. Complementarily, Figure 5.16 shows some additional results in scenarios with longer training periods ($T_\mathrm{T} = 10^5$ vs. $T_\mathrm{T} = 10^4$). Unsurprisingly, the resulting RSS is higher and so is the optimal number of timeslots.

Next, in Figure 5.17, we plot the optimal number of timeslots M^* as a function of the variance of the channel noise σ_w^2. Clearly, M^* is a monotonically decreasing function of σ_w^2: in noisy scenarios, more samples per timeslot ($L = L_\mathrm{T}/M$) are needed to average out channel noise. It also reveals that the optimal number of timeslots increases for an increasing duration of the training period T_T. Since the number of sensors is fixed ($I = 100$), for larger T_T the probability of having more than one sensor per timeslot decreases without impairing too much the quality of the estimates. As a remark, the curves saturate in the low-noise region because the lowest possible number of samples per timeslot (namely, $L = 1$) is reached there.

Finally, in Figure 5.18 we depict the throughput given by (5.34) vs. the total duration of the data transmission period (for fixed $T = 10^4$). For the training period, we (numerically) optimize on the number of timeslots. For benchmarking purposes, we also include data on the theoretical throughput achievable if the (channel and oscillator) phase shifts were known and, consequently, no training period were needed (i.e. $T_\mathrm{D} = T$ and RSS $= I$, dashed lines). As expected, there exists an optimal operating point for each curve where the best trade-off in terms of the beamforming gain after phase adjustments vs. time left for data transmission is reached. Interestingly, the duration of the training period amounts to less than 10% of the wake up time

T only. Moreover, the gap with respect to the highest theoretical throughput is on the order of some 25%, in all cases.

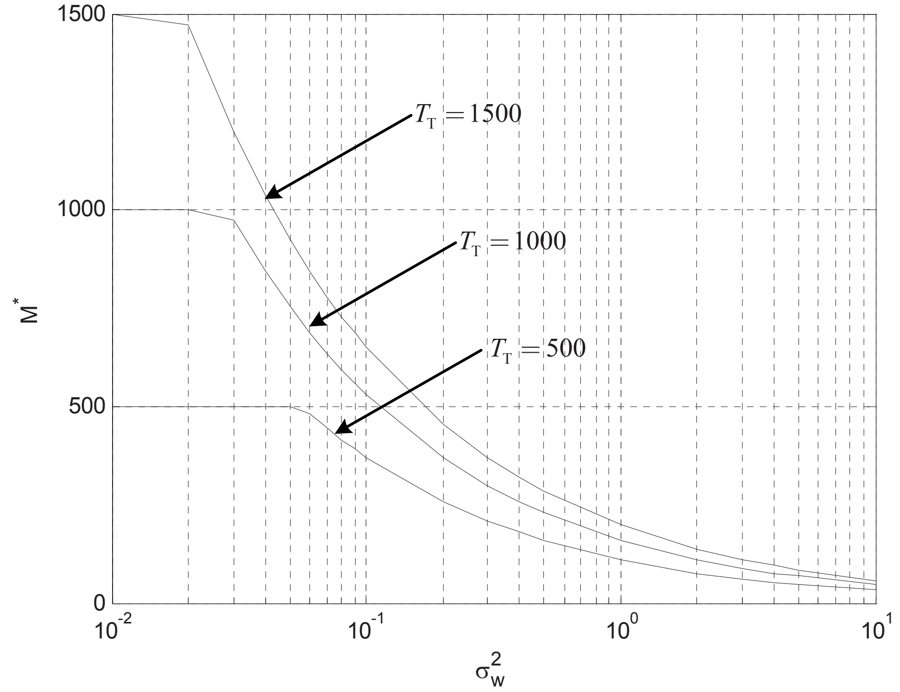

Figure 5.17: Optimal number of timelots vs. variance of the channel noise ($N = 100$).

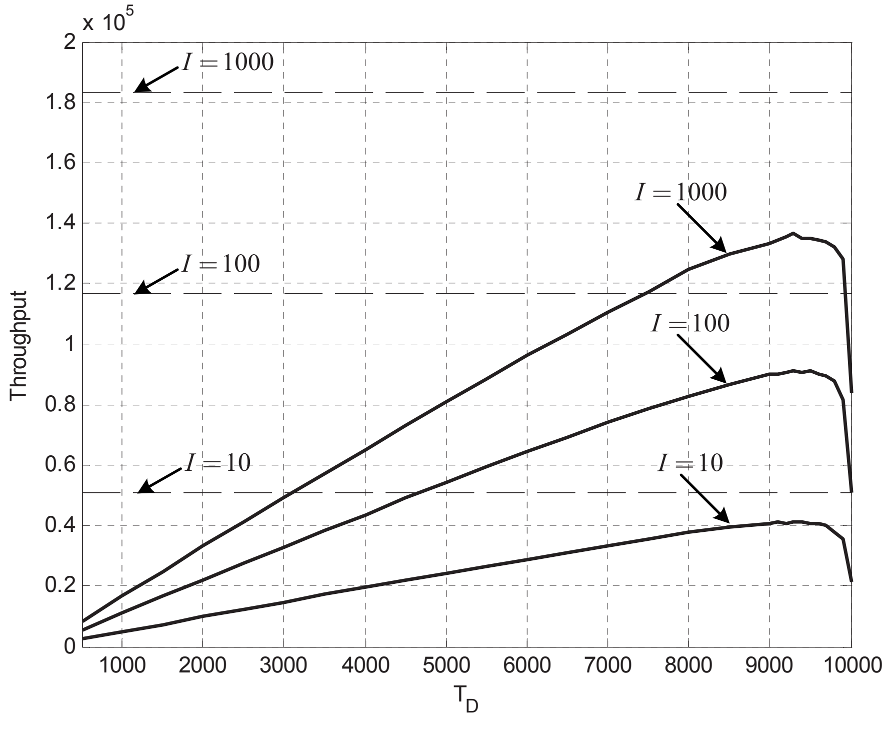

Figure 5.18: Throughput vs. data transmission time ($\sigma_w^2 = 6$, $T = 10^4$). Dashed lines indicate the throughput with known channel and oscillator phase shifts.

5.5 Chapter summary and conclusions

In this chapter, we have studied the problem of distributed carrier synchronization in wireless sensor networks. In particular, we have addressed two carrier phase synchronization schemes: (i) the one bit of feedback synchronization scheme, and (ii) the novel distributed phase synchronization scheme that we propose.

As for the one bit of feedback scheme, we have learned that the impact of noise on the behavior is two-fold: on the one hand, it prevents the algorithm from achieving full beamforming gain; on the other, it exhibits a slower convergence rate. This effect can be partly mitigated by averaging out over a number of RSS samples at each iteration. An optimal value of such number of samples exists and it is a function of the noise variance. In addition, we have also addressed an enhanced version of one bit of feedback scheme with sidelobe control (DBF-SC). It is shown that after a sufficient number of iterations, DBF-SC maximizes the beamforming gain at the main BS and, simultaneously, it keeps the sidelobe levels in the directions of the unintended BSs below some prescribed threshold. The proposed algorithm operates with partial CSI (namely, the RSSs measured at the main and unintended BSs), its signalling requirements are minimal (essentially, one bit of feedback per BS) and it exhibits a very low computational complexity. In spite of that, its performance and the associated radiation patterns are virtually identical to those of other centralized solutions obtained via convex optimization tools (i.e. numerically) which require full CSI and exhibit a much higher computational complexity. Computer simulation results reveal that, in scenarios where the unintended BS lies in the mainlobe of the original beampattern, the maximum of the radiation pattern shifts away from the direction of the main BS. Clearly, this results into degradation of the RSS at the main BS. On the contrary, when the interfered BS lie in the sidelobe region, we find only minor fluctuations in the RSS. Moreover, for the scenarios considered, the impact of the actual threshold value is relatively mild and, interestingly, it virtually saturates for values below -40 dB. Finally, we observed that increasing the number of unintended BSs has a substantial impact on the hitting time. For networks with small radii, increasing from 1 to 3 unintended BSs results into a 10-fold increase in the hitting time.

In this chapter, we have also proposed a novel decentralized phase synchronization scheme for collaborative beamforming with wireless sensor networks. This scheme does not require the BS to coordinate the allocation of sensors to the training timeslots or poll them individually. For the given scenario, we have derived (in general, tight) closed-form expressions for the upper bound of the resulting received signal strength (i.e., beamforming gain) in two scenarios of interest: ideal, and noisy phase shift estimates. For the ideal scenario, we have learnt that, asymptotically, the normalized received signal strength exclusively depends on the ratio of the number of timeslots to sensors in the network (and it is a monotonically increasing function). For the noisy phase shift estimates, numerical results reveal that there exists an optimal number of timeslots maximizing the overall received signal strength for the data transmission period. The optimal number of timeslots increases with the number of sensors in the network and the duration of the training period, and it decreases with the variance of the channel noise. The loss, in terms of normalized RSS, with respect to centralized schemes is moderate (some 5% to 20%). In terms of achievable throughput, there also exists an optimal split for the duration of the training and data transmission periods which attains the best trade-off in terms of beamforming gain vs. time left for data transmission. The gap with respect to the theoretical throughput with ideal knowledge on channel and oscillator phase shifts is on the order of 25%.

5.A Appendix

5.A.1 Proof of the convergence of one bit of feedback algorithm

In (5.23), we show that, the expected increase of the normalized RSS in the presence of AWGN can be expressed as :

$$\begin{aligned} h_n(y) &= \int_{-\infty}^{\infty} (x - y(1-\chi_n)) \frac{1}{\sqrt{2\pi\sigma^2_{\mathcal{R}}[n]}} e^{-\frac{x^2}{2\sigma^2_{\mathcal{R}}[n]}} \times \\ &\quad \times \mathcal{Q}\left(\frac{\sqrt{y^2 + \frac{\sigma_w^2}{2I^2}} - \sqrt{(\chi_n y + x)^2 + \frac{\sigma_w^2}{2I^2}}}{\frac{\sigma_w}{I}} \right) dx \\ &= \int_{-\infty}^{\infty} g(x,y)\, dx, \end{aligned} \tag{5.63}$$

Given $y = y_n$, the evolution of the mean normalized RSS (see eq. (5.15)) is modeled by the following recursion:

$$y_{n+1} \triangleq y_n + h_n(y), \text{ with the initialization}^{10}\ y_0 \triangleq \frac{1}{\sqrt{I}}. \tag{5.64}$$

We note that, the algorithm convergence in mean implies that $y_{n+1} = y_n$ for $n \to \infty$, or that the expected RSS increase equals zero ($h_n(y) = y_{n+1} - y_n = 0$). In the sequel, we prove that in the presence of AWGN, the algorithm converges to $\tilde{y}$, such that $\tilde{y} = \underset{y}{\arg}\{h_n(y) = 0\}$, with $\tilde{y} \in [\frac{1}{\sqrt{I}}, 1)$. To that end, we show that:

- The function $h_n(y)$ is continuous on the interval $y \in [0,1]$. This follows from the fact that, the derivative of expected RSS increase in (5.63) $\frac{dh_n(y)}{dy} = \frac{d}{dy}\int_{-\infty}^{\infty} g(x,y)dx$ is continuous function, since $\frac{d}{dy}\int_a^b g(x,y)dx = \int_a^b \frac{dg(x,y)}{dy}dx$ (see [54]) and $\frac{dg(x,y)}{dy}$ in (5.63) is continuous.
- At $y = 1$ the expected RSS increase is negative (namely, $h_n(y) < 0$).
- At $y = 0$ the expected RSS increase is positive (namely, $h_n(y) > 0$) and and the expected RSS is lower bounded by $\frac{1}{\sqrt{I}}$.

Based on the previous facts, since the function $h_n(y)$ is continuous, and inside the interval $[0,1]$ it changes its sign from positive to negative, we know that it must have zero somewhere inside this interval. Since $h_n(y)$ cannot be zero for $y < \frac{1}{\sqrt{I}}$, we conclude that, its zero must lie in the interval $[\frac{1}{\sqrt{I}}, 1)$, and therefore, the algorithm, on average converges to the normalized RSS value $\tilde{y} \in [\frac{1}{\sqrt{I}}, 1)$.

Proof that expected RSS increase is negative for $y = 1$

First, we replace the $\mathcal{Q}$ function inside the integral (5.63) with the function $f(x)$ defined as:

$$f(x) \triangleq \mathcal{Q}\left(\frac{\sqrt{y^2 + \frac{\sigma_w^2}{2I^2}} - \sqrt{(\chi_n y + x)^2 + \frac{\sigma_w^2}{2I^2}}}{\frac{\sigma_w}{I}}\right), \tag{5.65}$$

where for I large and σ_w^2 constant (i.e. $y \gg \frac{\sigma_w}{I}$) here, the function $f(x)$ can be approximated as follows:

$$\begin{aligned} f(x) &\approx \mathcal{Q}\left(-\frac{x - y(1-\chi_n)}{\frac{\sigma_w}{I}}\right) \\ &= 1 - \mathcal{Q}\left(\frac{x - y(1-\chi_n)}{\frac{\sigma_w}{I}}\right) \end{aligned} \tag{5.66}$$

Next, we express (5.63) as a sum of two integrals as follows:

$$\begin{aligned} h_n(y) &= \int_{-\infty}^{\infty} (x - y(1-\chi_n)) \frac{1}{\sqrt{2\pi\sigma_{\mathcal{R}}^2[n]}} e^{-\frac{x^2}{2\sigma_{\mathcal{R}}^2[n]}} f(x) dx \\ &= \int_{-\infty}^{y(1-\chi_n)} (x - y(1-\chi_n)) \frac{1}{\sqrt{2\pi\sigma_{\mathcal{R}}^2[n]}} e^{-\frac{x^2}{2\sigma_{\mathcal{R}}^2[n]}} f(x) dx \\ &\quad + \int_{y(1-\chi_n)}^{\infty} (x - y(1-\chi_n)) \frac{1}{\sqrt{2\pi\sigma_{\mathcal{R}}^2[n]}} e^{-\frac{x^2}{2\sigma_{\mathcal{R}}^2[n]}} f(x) dx. \end{aligned} \tag{5.67}$$

Now, by introducing the variable change $t = 2y(1-\chi_n) - x$ to the first integral of (5.67) which we denote by I_0, and by exploiting the fact that $f(t) = 1 - f(x)$, we obtain the following expression for I_0:

$$\begin{aligned} I_0 &= \int_{-\infty}^{y(1-\chi_n)} (x - y(1-\chi_n)) \frac{1}{\sqrt{2\pi\sigma_{\mathcal{R}}^2[n]}} e^{-\frac{x^2}{2\sigma_{\mathcal{R}}^2[n]}} f(x) dx \\ &= -\int_{\infty}^{y(1-\chi_n)} (-t + y(1-\chi_n)) \frac{1}{\sqrt{2\pi\sigma_{\mathcal{R}}^2[n]}} e^{-\frac{(2y(1-\chi_n)-t)^2}{2\sigma_{\mathcal{R}}^2[n]}} (1 - f(t))\, dt \\ &= -\int_{y(1-\chi_n)}^{\infty} (t - y(1-\chi_n)) \frac{1}{\sqrt{2\pi\sigma_{\mathcal{R}}^2[n]}} e^{-\frac{(t-2y(1-\chi_n))^2}{2\sigma_{\mathcal{R}}^2[n]}} (1 - f(t)) dt \\ &= -\int_{y(1-\chi_n)}^{\infty} (x - y(1-\chi_n)) \frac{1}{\sqrt{2\pi\sigma_{\mathcal{R}}^2[n]}} e^{-\frac{(x-2y(1-\chi_n))^2}{2\sigma_{\mathcal{R}}^2[n]}} (1 - f(x)) dx. \end{aligned} \tag{5.68}$$

Then, by plugging (5.68) into (5.67), we have that:

$$h_n(y) = \int_{y(1-\chi_n)}^{\infty} f_1(x) f(x) dx - \int_{y(1-\chi_n)}^{\infty} f_2(x)\,(1 - f(x))\, dx, \tag{5.69}$$

where $f_1(x)$ and $f_2(x)$ are functions defined in the sequel:

$$f_1(x) \triangleq (x - y(1-\chi_n))\frac{1}{\sqrt{2\pi\sigma^2_{\mathcal{R}}[n]}}e^{-\frac{x^2}{2\sigma^2_{\mathcal{R}}[n]}}, \tag{5.70}$$

$$f_2(x) \triangleq (x - y(1-\chi_n))\frac{1}{\sqrt{2\pi\sigma^2_{\mathcal{R}}[n]}}e^{-\frac{(x-2y(1-\chi_n))^2}{2\sigma^2_{\mathcal{R}}[n]}}. \tag{5.71}$$

$$\tag{5.72}$$

Therefore, the expected RSS increase of (5.69) can be rewritten as follows

$$\begin{aligned} h_n(y) &= \int_{y(1-\chi_n)}^{\infty} (f_1(x)+f_2(x))f(x)dx - \int_{y(1-\chi_n)}^{\infty} f_2(x)dx && (5.73)\\ &= I_1 - I_2 && (5.74)\end{aligned}$$

where

$$\begin{aligned} I_1 &\triangleq \int_{y(1-\chi_n)}^{\infty} (f_1(x)+f_2(x))f(x)dx, && (5.75)\\ I_2 &\triangleq \int_{y(1-\chi_n)}^{\infty} f_2(x)dx. && (5.76)\end{aligned}$$

On the one hand, integral I_2 can be lower bounded as follows:

$$\begin{aligned} I_2 &\triangleq \int_{y(1-\chi_n)}^{\infty} f_2(x)dx\\ &\overset{(a)}{>} \int_{-\infty}^{\infty} f_2(x)dx\\ &= \int_{-\infty}^{\infty}(x-y(1-\chi_n))\frac{1}{\sqrt{2\pi\sigma^2_{\mathcal{R}}[n]}}e^{-\frac{(x-2y(1-\chi_n))^2}{2\sigma^2_{\mathcal{R}}[n]}}dx\\ &= y(1-\chi_n), && (5.77)\end{aligned}$$

where (a) follows from the fact that $f_2(x) < 0$ for $x \in (-\infty, y(1-\chi_n))$. On the other hand, integral I_1 can be upper bounded as follows:

$$\begin{aligned} I_1 &= \int_{y(1-\chi_n)}^{\infty} (f_1(x)+f_2(x))f(x)dx\\ &\overset{(b)}{<} \int_{y(1-\chi_n)}^{\infty} (f_1(x)+f_2(x))dx\\ &= \int_{y(1-\chi_n)}^{\infty} f_1(x)dx + \int_{y(1-\chi_n)}^{\infty} f_2(x)dx\\ &= I_3 + I_4, && (5.78)\end{aligned}$$

where inequality (b) in (5.78) follows from the fact that that $f(x) \leq 1$ for $x \in \mathbb{R}$, and

$$\begin{aligned} I_3 &\triangleq \int_{y(1-\chi_n)}^{\infty} f_1(x)dx, && (5.79)\\ I_4 &\triangleq \int_{y(1-\chi_n)}^{\infty} f_2(x)dx. && (5.80)\end{aligned}$$

After some algebra manipulations integral I_3 reads

$$\begin{aligned}
I_3 &= \int_{y(1-\chi_n)}^{\infty} f_1(x)dx \\
&= \int_{y(1-\chi_n)}^{\infty} (x - y(1-\chi_n)) \frac{1}{\sqrt{2\pi\sigma_{\mathcal{R}}^2[n]}} e^{-\frac{x^2}{2\sigma_{\mathcal{R}}^2[n]}} dx \\
&= \int_{y(1-\chi_n)}^{\infty} x \frac{1}{\sqrt{2\pi\sigma_{\mathcal{R}}^2[n]}} e^{-\frac{x^2}{2\sigma_{\mathcal{R}}^2[n]}} dx - y(1-\chi_n) \int_{y(1-\chi_n)}^{\infty} \frac{1}{\sqrt{2\pi\sigma_{\mathcal{R}}^2[n]}} e^{-\frac{x^2}{2\sigma_{\mathcal{R}}^2[n]}} dx \\
&\overset{(c)}{=} \sigma_{\mathcal{R}} \frac{1}{\sqrt{2\pi}} \int_{\frac{y(1-\chi_n)}{\sigma_{\mathcal{R}}}}^{\infty} t e^{-\frac{t^2}{2}} dt - y(1-\chi_n) \int_{\frac{y(1-\chi_n)}{\sigma_{\mathcal{R}}}}^{\infty} \frac{1}{\sqrt{2\pi}} e^{-\frac{t^2}{2}} dt \\
&= \sigma_{\mathcal{R}} \left[\frac{1}{\sqrt{2\pi}} e^{-\frac{x^2}{2}} - x\mathcal{Q}(x) \right] \Bigg|_{x=\frac{y(1-\chi_n)}{\sigma_{\mathcal{R}}}}, \qquad (5.81)
\end{aligned}$$

where we have introduced the variable change $t = \frac{x}{\sigma_{\mathcal{R}}}$ in (c). Similarly to (5.81), integral I_4 can be computed as follows:

$$\begin{aligned}
I_4 &= \int_{y(1-\chi_n)}^{\infty} f_2(x)dx \\
&= \int_{y(1-\chi_n)}^{\infty} (x - y(1-\chi_n)) \frac{1}{\sqrt{2\pi\sigma_{\mathcal{R}}^2[n]}} e^{-\frac{(x-2y(1-\chi_n))^2}{2\sigma_{\mathcal{R}}^2[n]}} dx \\
&= \int_{y(1-\chi_n)}^{\infty} (x - 2y(1-\chi_n)) \frac{1}{\sqrt{2\pi\sigma_{\mathcal{R}}^2[n]}} e^{-\frac{(x-2y(1-\chi_n))^2}{2\sigma_{\mathcal{R}}^2[n]}} dx \\
&\quad + y(1-\chi_n) \int_{y(1-\chi_n)}^{\infty} \frac{1}{\sqrt{2\pi\sigma_{\mathcal{R}}^2[n]}} e^{-\frac{(x-2y(1-\chi_n))^2}{2\sigma_{\mathcal{R}}^2[n]}} dx \\
&\overset{(d)}{=} \sigma_{\mathcal{R}} \frac{1}{\sqrt{2\pi}} \int_{-\frac{y(1-\chi_n)}{\sigma_{\mathcal{R}}}}^{\infty} u e^{-\frac{u^2}{2}} du + y(1-\chi_n) \int_{-\frac{y(1-\chi_n)}{\sigma_{\mathcal{R}}}}^{\infty} \frac{1}{\sqrt{2\pi}} e^{-\frac{u^2}{2}} du \\
&= \sigma_{\mathcal{R}} \left[\frac{1}{\sqrt{2\pi}} e^{-\frac{x^2}{2}} - x\mathcal{Q}(x) \right] \Bigg|_{x=\frac{-y(1-\chi_n)}{\sigma_{\mathcal{R}}}} \qquad (5.82)
\end{aligned}$$

where we have introduced the variable change $u = \frac{x-2y(1-\chi_n)}{\sigma_{\mathcal{R}}}$ in (d). Therefore, from (5.78), (5.81) and (5.82) we have that:

$$\begin{aligned}
I_1 &< I_3 + I_4 \\
&= \sigma_{\mathcal{R}} \left[\frac{1}{\sqrt{2\pi}} e^{-\frac{x^2}{2}} - x\mathcal{Q}(x) \right] \Bigg|_{x=\frac{y(1-\chi_n)}{\sigma_{\mathcal{R}}}} + \sigma_{\mathcal{R}} \left[\frac{1}{\sqrt{2\pi}} e^{-\frac{x^2}{2}} - x\mathcal{Q}(x) \right] \Bigg|_{x=\frac{-y(1-\chi_n)}{\sigma_{\mathcal{R}}}} \\
&= \sigma_{\mathcal{R}} \left[2\frac{1}{\sqrt{2\pi}} e^{-\frac{x^2}{2}} - x\mathcal{Q}(x) + x(1-\mathcal{Q}(x)) \right] \Bigg|_{x=\frac{y(1-\chi_n)}{\sigma_{\mathcal{R}}}} \\
&= 2\sigma_{\mathcal{R}} \left[\frac{1}{\sqrt{2\pi}} e^{-\frac{x^2}{2}} - x\mathcal{Q}(x) \right] \Bigg|_{x=\frac{y(1-\chi_n)}{\sigma_{\mathcal{R}}}} + \frac{y(1-\chi_n)}{\sigma_{\mathcal{R}}} \sigma_{\mathcal{R}} \\
&= 2\sigma_{\mathcal{R}} h_n^* + y(1-\chi_n), \qquad (5.83)
\end{aligned}$$

where $h_n^* = \left[\frac{1}{\sqrt{2\pi}} e^{-\frac{x^2}{2}} - x\mathcal{Q}(x)\right]\Big|_{x=\frac{y(1-\chi_n)}{\sigma_{\mathcal{R}}}}$ corresponds to the expected increase when no noise is present in the system (see [8, eq.(23)]) and, hence, this term turns out to be zero (i.e. $h_n^* = 0$) for $y = 1$. Finally, from (5.74), (5.77) and (5.83) we have that

$$
\begin{aligned}
h_n(y) &= I_1 - I_2 && (5.84)\\
&< 0, && (5.85)
\end{aligned}
$$

which concludes the proof.

Proof that expected RSS increase is zero for $\tilde{y} \geq \frac{1}{\sqrt{I}}$

When $y = 0$, the BS observes only noise, whose signal strength on average is always greater than zero. Based on that non-accurate measurement, the algorithm accepts any given perturbation, which results in the average RSS increase greater than zero.
Even more, at the algorithm's starting point, all the carrier phases are uniformly distributed, resulting in the expected RSS equal to $y = \frac{1}{\sqrt{I}}$.When the noise variance is very high, the average RSS remains the same over time. This happens since, based on non-reliable RSS measurements, the algorithm accepts or discards phase perturbation randomly, maintaining the initial uniform distribution of phases. On the other hand, when the noise is not that much high, the RSS can be improved, leading to positive expected RSS increase. Based on these two facts and the continuity of $h_n(y)$, we conclude that the expected RSS *increase* can be zero only for some normalized RSS $\tilde{y} \geq \frac{1}{\sqrt{I}}$.

Chapter 6

Conclusions and Future Work

In this PhD dissertation, we have focused on the design of collaborative beamforming schemes for energy harvesting wireless sensor networks. First, in Chapter 3, we have addressed the case where one energy harvesting and one battery operated sensor collaborate to transmit data to a distant base station. This scenario is further generalized in Chapter 4, where we have considered the collaborative transmission with multiple energy harvesting nodes. In both Chapters 3 and 4, we have assumed that the signals from all the sensors involved in collaborative transmission are coherently added at the destination. This assumption is justified in Chapter 5, where we have addressed the problem of distributed carrier phase synchronization. In the sequel, we summarize the main findings of each chapter of this dissertation.

6.1 Conclusions

Chapter 3

In this chapter, we have addressed the scenario where two sensors (one of them with energy harvesting capabilities) collaboratively transmit a common message to a distant base station. In this setting, we have identified the optimal transmission policy such that the throughput for a given deadline is maximized. To do so, we have proposed a semi-analytical solution for the cases of infinite and finite energy storage capacity. More specifically, we have shown that the optimal transmission policy for the energy harvesting sensor can be computed independently (without the knowledge of the optimal policy for the battery operated sensor) by using the algorithms proposed in [17] and [18], respectively. Next, we have shown that the optimal policy at the battery operated sensor can be computed by means of the iterative algorithm that we propose. The performance of the jointly optimal transmission policy is compared to that of the suboptimal one, in the realistic scenario where solar energy is harvested. The computer simulation results have shown that the optimal transmission policy yields substantial throughput gains with respect to the suboptimal policy, especially when small amounts of energy are harvested or solar irradiation levels vary faster.

Regarding the case of finite energy storage capacity, numerical results have revealed that the loss due to limited capacity turns out to be significant, only when the storage capacity is smaller than the amount of energy harvested in each arrival. Finally, by considering long-term energy storage capacity degradation, the throughput loss is shown to be particularly severe for smaller values of nominal energy storage capacity.

Chapter 4

In this chapter, we have generalized the analysis of Chapter 3 by considering a scenario with multiple energy harvesting sensor nodes. In this setting, we have proposed an algorithm that finds the jointly optimal transmission policy in an iterative manner. More specifically, in each iteration, the algorithm optimizes the policy of a given sensor node, whilst the policies at other sensors are held fixed.

Next, we have assessed the system performance in a realistic scenario where vibrational energy is harvested from the environment. Computer simulation results have shown that for the infinite energy storage capacity case and for the low-SNR regime, the gain resulting from the joint optimization can be as high as 40% when the distance between sensors is high. Conversely, in the high-SNR regime such gain vanishes, since the jointly and separately optimal transmission policies turn out to be almost identical. Furthermore, we have found that for most of the scenarios, the throughput is higher when all sensors in the network harvest the same amount of energy.

Finally, by evaluating the impact of finite energy storage capacity, we have shown that the throughput gracefully degrades for intermediate values of the storage capacity. Moreover, for large energy storage capacities, the performance is more sensitive to inter-sensor distance.

Chapter 5

In this chapter, we have addressed two decentralized schemes for carrier phase synchronization. The proposed schemes perform in a distributed manner, which renders them particularly suitable for collaborative beamforming scenarios considered in Chapters 3 and 4.

First, we have considered the so-called one bit of feedback algorithm proposed in [8]. More particularly, we have generalized the analysis of [8] to the scenario with noisy received signal strength estimates. In such setting, we have found that the impact of noise on the algorithm's behavior is twofold: (i) the noise prevents the algorithm from achieving full beamforming gain; (ii) the algorithm exhibits a slower convergence rate. Besides, we have also proposed an enhanced version of one bit of feedback algorithm by including sidelobe control (DBF-SC). We have shown that after a sufficient number of iterations, DBF-SC is capable of maximizing the beamforming gain at the main BS while keeping the sidelobe levels in the directions of the unintended BSs below some prescribed threshold. The performance and the associated radiation patterns are practically identical to those of other centralized solutions obtained via convex relaxations, which, however, require full CSI.

In the second part of this chapter, we have proposed a novel decentralized phase synchronization scheme. Unlike the one bit of feedback algorithm considered before, this scheme is particularly suitable for scenarios where the total duration of the training plus data transmission period is fixed irrespectively of the number of sensors. In addition, similarly to the one bit of feedback algorithm, the proposed scheme does not require the centralized allocation of the sensors to the training timeslots. Initially, we have derived the closed-form expressions for the upper bound of the resulting received signal strength in two scenarios: ideal, and noisy phase shift estimates. For the ideal scenario, we have found that the normalized received signal strength exclusively depends on the ratio of the number of timeslots and the number of sensors. As for the noisy phase shift estimates, numerical simulations have revealed that there exists an optimal number of timeslots which maximizes the received signal strength during data transmission period. The RSS loss with respect to centralized schemes ranges from 5% to 20%. Besides, we have shown that there exists an optimal split for the duration of the training and data transmission periods, which attains the best trade-off in terms of beamforming gain vs. time left for data transmission. The performance gap with respect to the theoretical throughput with global CSI and full knowledge of the oscillator phase shifts turns out to be in the order of 25%.

6.2 Future work

In this section, we discuss a number of research areas and related topics for further work in the field of distributed beamforming and decentralized carrier synchronization in wireless sensor networks.

- **Energy harvesting sensors with causal knowledge of energy arrivals.** For the communication system considered in this dissertation, we assume that energy arrivals are known in advance. With this assumption, one can model quite accurately the energy harvesting process of predictable ambient energy sources. However, in the case where the amounts of energy and/or harvesting events cannot be predicted with sufficient accuracy, stochastic models are required. In this case, the convex optimization framework used in this dissertation cannot be used. Instead, one should resort to stochastic optimization and dynamic programming tools.
- **Energy required for data processing tasks.** In this dissertation, we assume that all the harvested energy is used for data transmission only. This assumption is only valid when the energy needed for data transmission dominates in the overall energy consumption. However, when the sensor node employs more complex data processing/modulation schemes, the processing energy cost must be included in the signal model, as well.
- **Convergence analysis of DBF-SC algorithm.** In this dissertation, we have analyzed the one bit of feedback algorithm for carrier phase synchronization with sidelobe control mechanisms. It is shown that the proposed method achieves the beampattern virtually identical to that of the centralized numerical optimization. Nevertheless, since the algorithm performs in an iterative manner, it still remains to verify the algorithm's convergence properties.
- **Soft keep/reject decisions for phase perturbations DBF-SC algorithm.** The proposed DBF-SC method performs quite well with respect to sidelobe control when the number of unintended base stations is small. However, when this number grows large, the probability that all the base stations give positive feedback becomes very small. This, in turn, results in significantly slower algorithm's convergence rate. Therefore, it is necessary to consider different rules on accepting/rejecting the phase perturbation, which may possibly lead to better performance in terms of convergence rate.
- **Message sharing.** In this dissertation we do not pay particular attention to the required message sharing stage. However, in scenarios with sensor nodes deployed over larger areas, a significant amount of energy is needed for this task. Consequently, those scenarios require the impact of the sharing overhead to be considered, as well.

Bibliography

[1] "Crossbow technologies," `http://www.xbow.com`.

[2] Thomas M. Cover and Joy A. Thomas, *Elements of information theory*, A John Wiley and Sons, Ltd, 2006.

[3] H. Sato, "The capacity of the gaussian interference channel under strong interference (corresp.)," *IEEE Transactions on Information Theory*, vol. 27, no. 6, pp. 786–788, November 1981.

[4] Xiaohu Shang, G. Kramer, and Biao Chen, "A new outer bound and the noisy-interference sum–rate capacity for gaussian interference channels," *IEEE Transactions on Information Theory*, vol. 55, no. 2, pp. 689–699, February 2009.

[5] Yung-Szu Tu and G.J. Pottie, "Coherent cooperative transmission from multiple adjacent antennas to a distant stationary antenna through awgn channels," in *IEEE 55th Vehicular Technology Conference (VTC Spring 2002)*, 2002, vol. 1, pp. 130–134 vol.1.

[6] III Brown, D.R., G.B. Prince, and J.A. McNeill, "A method for carrier frequency and phase synchronization of two autonomous cooperative transmitters," June 2005, pp. 260–264.

[7] D.R. Brown and H.V. Poor, "Time-slotted round-trip carrier synchronization for distributed beamforming," *IEEE Transactions on Signal Processing*, vol. 56, no. 11, pp. 5630–5643, November 2008.

[8] R. Mudumbai, J. Hespanha, U. Madhow, and G. Barriac, "Distributed transmit beamforming using feedback control," *IEEE Transactions on Information Theory*, vol. 56, no. 1, pp. 411–426, January 2010.

[9] Munkyo Seo, M. Rodwell, and U. Madhow, "A feedback-based distributed phased array technique and its application to 60-ghz wireless sensor network," *IEEE MTT-S International Microwave Symposium Digest*, pp. 683–686, June 2008.

[10] Man-On Pun, D.R. Brown, and H. Vincent Poor, "Opportunistic collaborative beamforming with one-bit feedback," *IEEE 9th Workshop on Signal Processing Advances in Wireless Communications (SPAWC 2008)*, pp. 246–250, July 2008.

[11] Y. Lo, "A mathematical theory of antenna arrays with randomly spaced elements," *IEEE Transactions on Antennas and Propagation*, vol. 12, no. 3, pp. 257–268, May 1964.

[12] H. Ochiai, P. Mitran, H.V. Poor, and V. Tarokh, "Collaborative beamforming for distributed wireless ad hoc sensor networks," *IEEE Transactions on Signal Processing*, vol. 53, no. 11, pp. 4110–4124, November 2005.

[13] M.F.A. Ahmed and S.A. Vorobyov, "Collaborative beamforming for wireless sensor networks with gaussian distributed sensor nodes," *IEEE Transactions on Wireless Communications*, vol. 8, no. 2, pp. 638–643, February 2009.

[14] M.F.A. Ahmed and S.A. Vorobyov, "Sidelobe control in collaborative beamforming via node selection," *IEEE Transactions on Signal Processing*, vol. 58, no. 12, pp. 6168–6180, December 2010.

[15] Stephen Beeby and Neil White, *Energy Harvesting for Autonomous Systems*, Artech House, 2010.

[16] S. Saggini, F. Ongaro, C. Galperti, and P. Mattavelli, "Supercapacitor-based hybrid storage systems for energy harvesting in wireless sensor networks," in *Twenty-Fifth Annual IEEE Applied Power Electronics Conference and Exposition (APEC 2010)*, February 2010, pp. 2281–2287.

[17] Jing Yang and S. Ulukus, "Optimal packet scheduling in an energy harvesting communication system," *IEEE Transactions on Communications*, vol. 60, no. 1, pp. 220–230, January 2012.

[18] K. Tutuncuoglu and A. Yener, "Optimum transmission policies for battery limited energy harvesting nodes," *IEEE Transactions on Wireless Communications*, vol. 11, no. 3, pp. 1180–1189, March 2012.

[19] O. Ozel, K. Tutuncuoglu, Jing Yang, S. Ulukus, and A. Yener, "Transmission with energy harvesting nodes in fading wireless channels: Optimal policies," *IEEE Journal on Selected Areas in Communications*, vol. 29, no. 8, pp. 1732–1743, September 2011.

[20] Maria Gregori and Miquel Payaró, "Throughput maximization for a wireless energy harvesting node considering the circuitry power consumption," in *IEEE Vehicular Technology Conference (VTC Fall 2012)*, September 2012, pp. 1–5.

[21] Oner Orhan, Deniz Gunduz, and Elza Erkip, “Throughput maximization for an energy harvesting communication system with processing cost,” in *IEEE Information Theory Workshop (ITW 2012)*, September 2012, pp. 84–88.

[22] B. Devillers and D. Gunduz, “A general framework for the optimization of energy harvesting communication systems with battery imperfections,” *Journal of Communications and Networks*, vol. 14, no. 2, pp. 130–139, April 2012.

[23] K. Tutuncuoglu and A. Yener, “Communicating using an energy harvesting transmitter: Optimum policies under energy storage losses,” *ArXiv*, 2012.

[24] D. Gunduz and B. Devillers, “Two-hop communication with energy harvesting,” in *4th IEEE International Workshop on Computational Advances in Multi-Sensor Adaptive Processing (CAMSAP 2011)*, December 2011, pp. 201–204.

[25] O. Orhan and E. Erkip, “Optimal transmission policies for energy harvesting two-hop networks,” *ArXiv*, 2012.

[26] Jing Yang and S. Ulukus, “Optimal packet scheduling in a multiple access channel with energy harvesting transmitters,” *Journal of Communications and Networks*, vol. 14, no. 2, pp. 140–150, April 2012.

[27] K. Tutuncuoglu and A. Yener, “Sum-rate optimal power policies for energy harvesting transmitters in an interference channel,” *Journal of Communications and Networks*, vol. 14, no. 2, pp. 151–161, April 2012.

[28] Jing Yang, O. Ozel, and S. Ulukus, “Broadcasting with an energy harvesting rechargeable transmitter,” *IEEE Transactions on Wireless Communications*, vol. 11, no. 2, pp. 571–583, February 2012.

[29] O. Ozel, Jing Yang, and S. Ulukus, “Optimal broadcast scheduling for an energy harvesting rechargeable transmitter with a finite capacity battery,” *IEEE Transactions on Wireless Communications*, vol. 11, no. 6, pp. 2193–2203, June 2012.

[30] O. Ozel, Jing Yang, and S. Ulukus, “Optimal scheduling over fading broadcast channels with an energy harvesting transmitter,” in *4th IEEE International Workshop on Computational Advances in Multi-Sensor Adaptive Processing (CAMSAP 2011)*, December 2011, pp. 193–196.

[31] K. Tutuncuoglu and A. Yener, “Communicating with energy harvesting transmitters and receivers,” in *Information Theory and Applications Workshop (ITA 2012)*, February 2012, pp. 240–245.

[32] S. Boyd and L. Vandenberghe, *Convex Optimization*, Cambridge University Press, 2004.

[33] M.A. Zafer and E. Modiano, "A calculus approach to energy-efficient data transmission with quality-of-service constraints," *IEEE/ACM Transactions on Networking*, vol. 17, no. 3, pp. 898–911, June 2009.

[34] L. Berbakov, J. Matamoros, and C. Anton-Haro, "Optimal transmission policy for distributed beamforming with energy harvesting and battery operated sensor nodes," in *International Symposium on Wireless Communication Systems (ISWCS 2012)*, August 2012, pp. 441–445.

[35] L. Berbakov, C. Anton-Haro, and J. Matamoros, "Optimal transmission policy for cooperative transmisssion with energy harvesting and battery operated sensor nodes," *submitted to Elsevier Signal Processing*.

[36] Jun Li, Edward Murphy, Jack Winnick, and Paul A Kohl, "The effects of pulse charging on cycling characteristics of commercial lithium-ion batteries," *Journal of Power Sources*, vol. 102, no. 1–2, pp. 302 – 309, 2001.

[37] "National solar radiation data base," 1991-2005, `http://rredc.nrel.gov/solar/old_data/nsrdb/1991-2005/tmy3/`.

[38] Richard L. Burden and J. Douglas Faires, *Numerical Analysis*, Brooks/Cole, 2011.

[39] Andrei D. Polyanin and Alexander V. Manzhirov, *Handbook of Mathematics for Engineers and Scientists*, Chapman & Hall/CRC, 2007.

[40] Dimitri P. Bertsekas, *Nonlinear programming*, Athena Scientific, 2nd edition, 1999.

[41] L. Berbakov, J. Matamoros, and C. Anton-Haro, "Greedy transmission strategies for collaborative beamforming with energy harvesting sensors," in *7th International ITG Workshop on Smart Antennas (WSA 2013)*, March 2013.

[42] L. Berbakov, J. Matamoros, and C. Anton-Haro, "Optimal transmission policy for collaborative beamforming with finite energy storage capacity," in *submitted to IEEE International Workshop on Signal Processing Advances in Wireless Communications (SPAWC 2013)*, June 2013.

[43] L. Berbakov, C. Anton-Haro, and J. Matamoros, "Joint optimization of transmission policies for collaborative beamforming with energy harvesting sensors," *submitted to IEEE Transactions on Wireless Communications*.

[44] Dimitri P. Bertsekas and John N. Tsitsklis, *Parallel and Distributed Computation: Numerical Methods*, Athena Scientific, 1989.

[45] Yinyu Ye, *Interior Point Algorithms: Theory and Analysis*, John Wiley & Sons, Inc, 1997.

[46] L. Berbakov, C. Anton-Haro, and J. Matamoros, “Distributed beamforming using one bit of feedback: Awgn analysis,” in *18th European Wireless Conference (EW 2012)*, April 2012.

[47] L. Berbakov, C. Anton-Haro, and J. Matamoros, “Distributed beamforming with sidelobe control using one bit of feedback,” in *IEEE 73rd Vehicular Technology Conference (VTC Spring 2011)*, May 2011, pp. 1–5.

[48] L. Berbakov, J. Matamoros, and C. Anton-Haro, “Decentralized phase synchronization scheme for collaborative beamforming in wireless sensor networks,” in *19th European Signal Processing Conference (EUSIPCO 2011)*, September 2011.

[49] L. Berbakov, C. Anton-Haro, and J. Matamoros, “Decentralized phase synchronization scheme for distributed beamforming in wsn with quantized phase feedback,” in *Future Network Mobile Summit (FUNEMS 2012)*, July 2012, pp. 1–8.

[50] G. Mergen, Qing Zhao, and L. Tong, “Sensor networks with mobile access: Energy and capacity considerations,” *IEEE Transactions on Communications*, vol. 54, no. 11, pp. 2033–2044, November 2006.

[51] R. Mark Henkelman, “Measurement of signal intensities in the presence of noise in MR images,” *Medical Physics*, vol. 12, no. 2, pp. 232–233, March 1985.

[52] A. Papoulis, *Probability, Random Variables, and Stochastic Processes*, pub-mcgraw-hill, pub-mcgraw-hill:adr, 3rd edition, 1991.

[53] Steven M. Kay, *Fundamentals of Statistical Signal Processing: Estimation Theory*, Prentice Hall PTR, 1993.

[54] Harley Flanders, “Differentiation under the integral sign,” *The American Mathematical Monthly*, vol. 80, no. 6, pp. pp. 615–627, 1973.